

Tip support

Microtubule stabilizing complexes
in cells and in vitro



Cyntha van den Berg

Tip support

Microtubule stabilizing complexes
in cells and in vitro

Cyntha van den Berg

ISBN: 978-94-6458-717-3

DOI: 10.33540/1540

The studies described in this thesis were performed at the division of Cell Biology, Neurobiology and Biophysics at the Faculty of Science of Utrecht University in Utrecht, The Netherlands.

The printing of this thesis is financially supported by Tjeenz B.V., H. Caelers and R. Roodbol.

Cover: Cyntha van den Berg

Layout: Cyntha van den Berg

Printing: Ridderprint

Tip support

Microtubule stabilizing complexes in cells and in vitro

Uiteinde ondersteuning

Microtubuli-stabiliserende complexen in cellen en in vitro

(met een samenvatting in het Nederlands)

Proefschrift

ter verkrijging van de graad van doctor aan de
Universiteit Utrecht
op gezag van de
rector magnificus, prof.dr. H.R.B.M. Kummeling,
ingevolge het besluit van het college voor promoties
in het openbaar te verdedigen op

maandag 16 januari 2023 des middags te 12.15 uur

door

Cyntha Melissa van den Berg

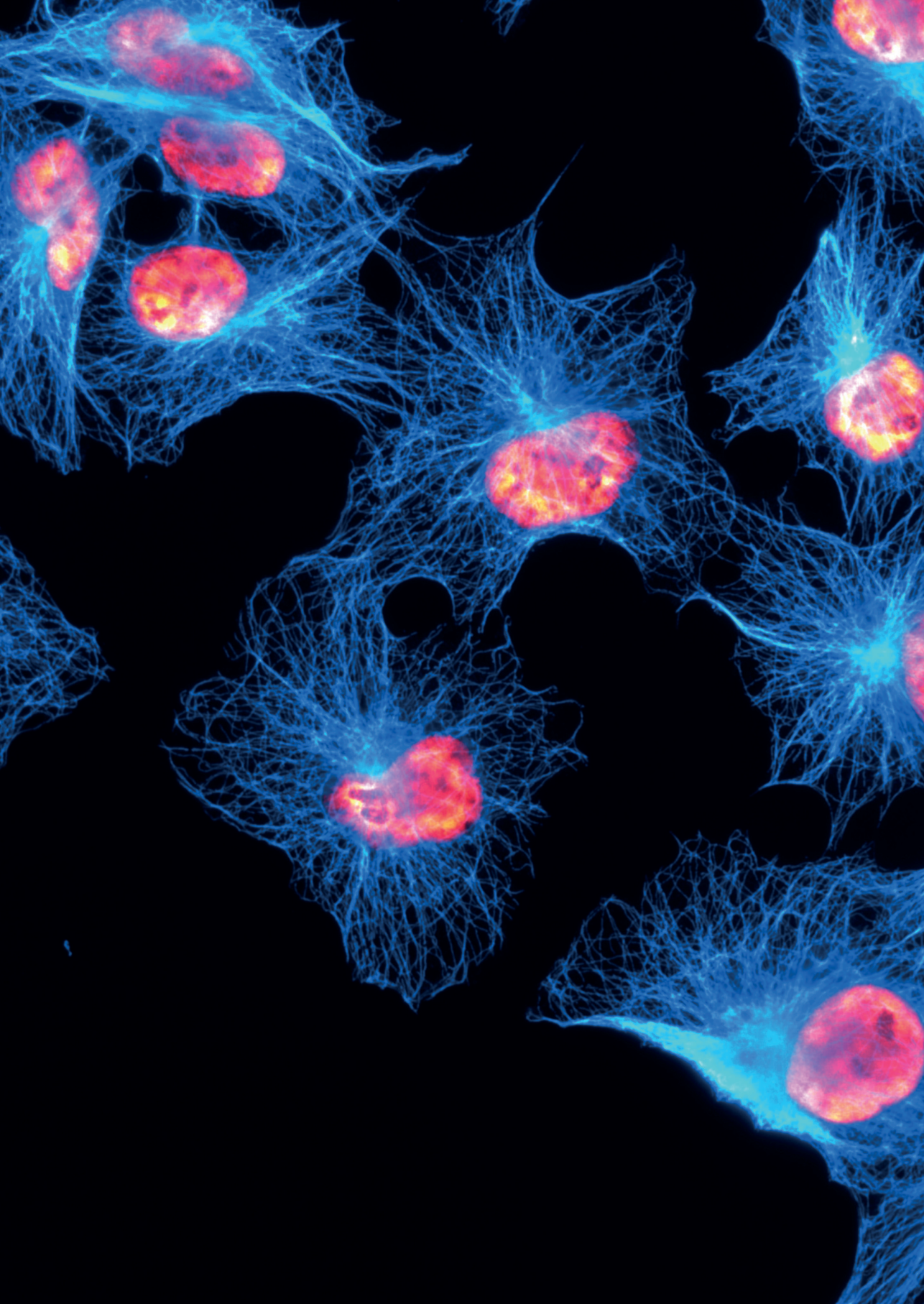
geboren op 9 juli 1994
te Gouda

Promotor:

Prof. dr. A.S. Akhmanova

Table of contents

Chapter 1	General Introduction	6
Chapter 2	Organization and dynamics of the cortical complexes controlling insulin secretion in β -cells	32
Chapter 3	CSPP1 stabilizes growing microtubule ends and damaged lattices from the luminal side	70
Chapter 4	Slow and steady: combined action of ciliary tip module proteins with opposing activities imparts slow microtubule growth	110
Chapter 5	General Discussion	136
Addendum	Nederlandse samenvatting	162
	Curriculum Vitae	164
	List of publications	164
	Dankwoord	165



1

General Introduction

Cyntha M. van den Berg¹

¹Cell Biology, Neurobiology and Biophysics, Department of Biology, Faculty of Science, Utrecht University, Padualaan 8, 3584 CH Utrecht, The Netherlands.

Cells are referred to as ‘the building blocks of life’, and to function properly, they require a cytoskeleton. In eukaryotic cells, the cytoskeleton is composed of four major polymeric networks: F-actin, microtubules, intermediate filaments and septins. These networks are involved in cellular processes such as the establishment and maintenance of cell polarity and cell shape, reorganization and transport of organelles and vesicles, and migration and division of cells. Here, we focus on the microtubule cytoskeleton. We will discuss the dynamic nature of microtubules and the ways how cells are able to stabilize microtubules when required.

Microtubule dynamics

Microtubules are hollow, cylindrical polymers that are formed from subunits called tubulin dimers, or simply tubulin. Tubulin dimers are heterodimers composed of proteins called α -tubulin and β -tubulin. Tubulin associates longitudinally creating a protofilament and multiple protofilaments associate laterally to create a closed tube (Brouhard and Rice, 2018). In mammalian cells, the majority of microtubules have an outer diameter of 25 nm and are composed of thirteen protofilaments. However, depending on species, cell type and cell stage, microtubules ranging from four to forty protofilaments have been observed (Chaaban and Brouhard, 2017). Longitudinal association of tubulin always occurs via interaction between α -tubulin of one subunit and β -tubulin of another subunit, also described as binding in a ‘head-to-tail’ fashion, creating a polarized tube. Association of tubulin at the β -tubulin-exposed end of the tube is much faster, and this end is referred to as the plus end. The α -tubulin-exposed end is referred to as the minus end and tubulin addition is much slower. In cells, microtubules usually form on a template called γ -tubulin ring complex (γ TuRC). The γ TuRC consists of γ -tubulin, a specialized tubulin isoform, and gamma-tubulin complex component proteins (GCPs) (Aher and Akhmanova, 2018; Brouhard and Rice, 2018). This template caps and stabilizes the minus ends. Nucleation can also occur spontaneously in presence of a (local) high concentration of soluble tubulin, but this is mainly observed *in vitro* (Brouhard and Rice, 2018).

For various cellular processes, microtubule depolymerization is required. This can be facilitated and regulated by microtubule associated proteins (MAPs), but also microtubules by themselves can switch to depolymerization. Microtubules can randomly switch between polymerization and depolymerization phases. This phenomenon has been defined as ‘dynamic instability’ (Fig. 1) (Desai and Mitchison, 1997). The transition of polymerization to depolymerization is known as catastrophe and the reverse transition is known as rescue. Experimental evidence showed that the switch to a depolymerizing state does not occur completely randomly, as longer-lived microtubules are more likely to undergo catastrophe (Coombes et al., 2013; Odde et al., 1995). Dynamic instability is facilitated by the guanosine triphosphate (GTP) to guanosine diphosphate (GDP) transition that occurs during microtubule polymerization. Both α -tubulin and β -tubulin have binding sites for GTP and both sites require binding to GTP for efficient polymerization. GTPs bound to α -tubulin are non-hydrolysable and non-exchangeable, but β -tubulin has the capability to hydrolyse its bound GTP to GDP a short while after incorporation into a protofilament. Addition of GTP-tubulin to a polymerizing microtubule is generally faster than the hydrolysis of GTP to GDP. This creates a cap at the microtubule plus end, also known as the GTP cap, which has stabilizing properties. The structure of a growing microtubule plus end with a GTP cap can be quite diverse and ranges from short, blunt ends to ends with long outwardly curved protofilaments. However, the tip is mainly characterized by differences in protofilament length and the more distal protofilaments curve somewhat outward (Brouhard and Rice, 2018). The microtubule shaft is a relatively straight tube composed of GDP-tubulin and is intrinsically unstable (Akhmanova and Steinmetz, 2015).

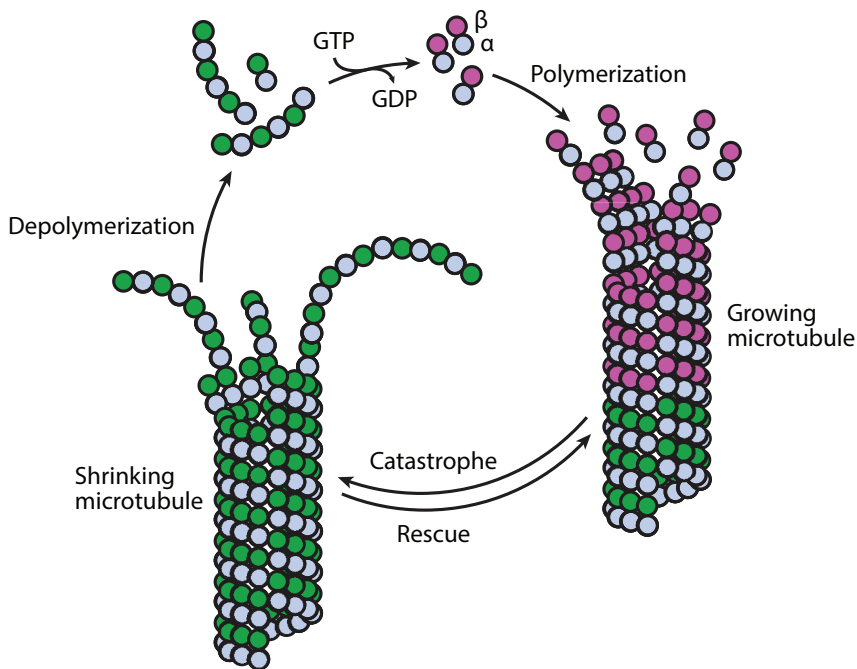


Figure 1: Microtubule dynamic instability. Microtubule can grow through the addition of GTP-bound soluble tubulin dimers, a process called polymerization. Soon after incorporation of the GTP-bound tubulin dimers, GTP gets hydrolyzed to GDP, and this results in a microtubule containing a GTP cap and a GDP-tubulin lattice. The loss of the GTP cap creates a catastrophe where the protofilaments peel away from the tube followed by depolymerization. Depolymerizing microtubules can switch back to a polymerizing state (rescue) with the help of MAPs. The GDP that is bound to depolymerized tubulin dimers gets exchanged to GTP and the cycle can start again. Figure adapted from Akhmanova & Steinmetz, 2015 and Brouhard & Rice, 2018.

The GDP-tubulin lattice is determined to be intrinsically unstable due to accumulating strain in the lattice, because tubulin dimers are forced into an energetically unfavorable conformation (Brouhard and Rice, 2014; Brouhard and Rice, 2018). GTP-bound tubulin dimers in solution are in a relaxed and curved conformation named 'curved GTP'. After addition to the microtubule tip, the tubulin dimer is forced into a strained and straight conformation known as 'expanded GTP'. Hydrolysis of GTP into GDP reorders the α -tubulin conformation creating a compacted tubulin dimer which is even more strained, termed 'compacted GDP'. When the strain reaches a certain threshold, in absence of MAPs, the microtubule undergoes a catastrophe. This is due to GDP-dimers relaxing back to the curved state and the protofilaments starting to peel outward in a characteristic way, the so-called 'ram's horns' (Mandelkow et al., 1991). This releases the stored energy, and protofilaments start to depolymerize (Brouhard and Rice, 2018). Depolymerization can also be initiated when hydrolysis catches up with microtubule polymerization resulting in the absence of the protective GTP cap.

The minimum requirements for microtubules to exhibit dynamic instability are high tubulin concentration (above a certain critical concentration), appropriate temperature, and presence of GTP and magnesium (Baas et al., 2016). However, to be able to partake in the

required cellular processes, more factors come into play. Microtubules can be composed of different α -tubulin or β -tubulin isoforms, or they can be modified by enzymes or MAPs. These microtubule modifications can directly affect the tubulin dimer conformation or have an indirect effect by tuning binding affinities of MAPs for regulatory purposes. These modifications can stabilize or destabilize microtubules, or microtubule segments, depending on the modification. Here, we will go into more detail into modifications that are considered to induce microtubule stabilization.

Stabilizing microtubule modifications

When microtubules are described as being stable, this does not necessarily mean that they are non-dynamic. Stability of microtubules is linked to the rate at which a microtubule exchanges tubulin dimers with the soluble tubulin pool (Baas et al., 2016). In the case of stable microtubules, this exchange is very slow. This can present itself in two ways. Either a microtubule is continuously growing because catastrophes are inhibited, or microtubules undergo catastrophes and subsequent rescues. In the latter scenario, they are only considered stable when the average length lost during shrinkage is smaller than the average length gained during growth (Akhmanova and Kapitein, 2022). In these descriptions, microtubules are still dependent on the presence or reacquisition of the GTP cap. In a more generally used definition, microtubules are considered stable when they resist depolymerization after the loss of the GTP cap induced by cold, severing or treatment with small molecules like nocodazole (Akhmanova and Kapitein, 2022). However, microtubules that are resistant to these treatments are usually dependent on the presence of lattice-associated modifications. Microtubule modifications can be divided into those belonging to the concept 'tubulin code', MAPs and microtubule-targeting agents (MTAs). MTAs are a group of chemical compounds that affect microtubule dynamics, but they will not be discussed here.

The tubulin code

The 'tubulin code' is a concept that was already proposed in the 1970s, but recent technical advances were required for a thorough functional characterization. The 'tubulin code' is now viewed as a fine regulator of microtubule dynamics and consists of tubulin isoforms and post-translational modifications (PTMs).

Tubulin isoforms

In most species, multiple genes encode variants (isoforms) of α -tubulin and β -tubulin. The number of tubulin isoforms varies between species. In humans, nine α -tubulin isoforms and ten β -tubulin isoforms have been identified so far (Tweedie et al., 2021). These tubulin isoforms can freely incorporate into microtubule lattices, but they are differentially expressed. The more common tubulin isoforms are highly conserved between evolutionary distant species, while the less common tubulin isoforms are found to have evolved for species-specific functions (Janke and Magiera, 2020). One example for this, which also implicates that tubulin isoforms can be involved in microtubule stabilization, is the requirement of $\beta 1$ -tubulin in mammalian platelets (Schwer et al., 2001). This isoform of β -tubulin shows the most sequence divergence of all β -tubulin isoforms and is not found in species which lack platelets. To function, platelets require a 'marginal band' (a circular bundle) composed of extremely bent microtubules. Microtubules built from more general tubulin isoforms will break under this extreme bending. Therefore, it could be that $\beta 1$ -tubulin has specifically evolved to create microtubules that can persist under strong curvature, also because mutation or absence of $\beta 1$ -tubulin leads to severe defects in the platelet microtubule array (Janke and Magiera, 2020; Kunishima et al., 2009; Schwer et al., 2001). However, it is not yet known if microtubules containing $\beta 1$ -tubulin are

really more flexible and more resistant to deformation or that they recruit MAPs that create or recognize curved regions.

Tubulin isotypes can directly affect microtubule stabilization, which has been shown in a study using recombinant human tubulin with a defined isotype composition in *in vitro* reconstitution assays with dynamic microtubules. Pure $\alpha 1\text{B}-\beta 2\text{B}$ tubulin dimers were observed to generate microtubules which were more resistant against spontaneous or catalyzed depolymerization than microtubules grown from $\alpha 1\text{B}-\beta 3$ -tubulin (Pamula et al., 2016; Ti et al., 2018).

Post-translational modifications

Both α -tubulin and β -tubulin have highly negatively charged, unstructured carboxy-terminal (C-terminal) tails, and these are exposed on the surface of microtubules. These tails are hotspots of post-translational modifications (PTMs) (Janke and Magiera, 2020). These tails can get polyglutamylated, polyglycylated, tyrosinated and detyrosinated by specific enzymes. Additionally, residues of the structured tubulin domains can get acetylated, methylated, phosphorylated and polyaminated (Fig. 2). Multiple PTMs can be found on the same microtubule, providing an additional regulatory layer for cellular processes. Acetylation, detyrosination and polyamination are modifications which are linked to stable microtubules. For a long time, it was not clear if stable microtubules were simply longer-lived and therefore acquired specific PTMs, or if PTMs were actively stabilizing the microtubule. Recently, it has been shown that both concepts can be true.

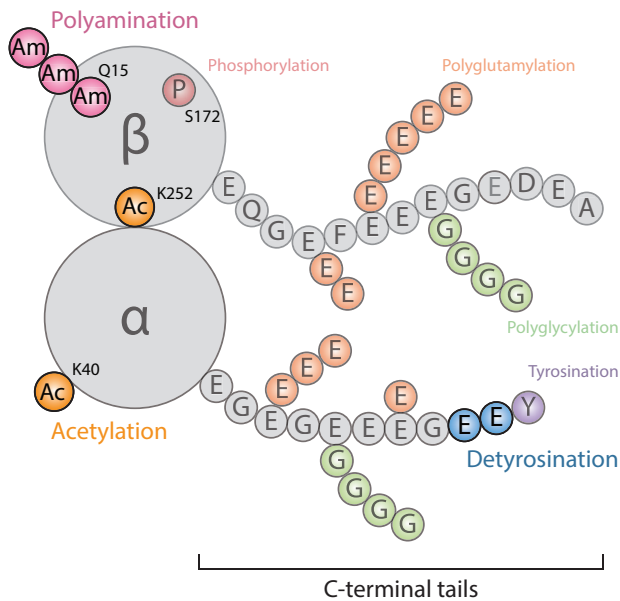


Figure 2: Post-translational modifications on microtubules. Tubulin monomers have a highly structured ‘tubulin body’ and an unstructured C-terminal tail which is exposed at the microtubule surface. C-terminal tails can acquire many post-translational modifications such as polyglutamylation, polyglycylation, tyrosination and detyrosination. Phosphorylation, polyamination and acetylation are modifications that occur on the ‘tubulin body’. Modifications that are known to directly or indirectly induce microtubule stabilization are shown in bright colors, while the other modifications are shown in more transparent colors. Figure adapted from Janke & Magiera, 2020.

Acetylation is the enzymatic addition of an acetyl group to a lysine residue on a protein. The best characterized tubulin acetylation sites are lysine-40 (K40) on α -tubulin and lysine-252 (K252) on β -tubulin. Acetylation of K40 on α -tubulin is catalyzed by α -tubulin N-acetyltransferase 1 (α TAT1) and occurs on the luminal side of polymerized microtubules (Shida et al., 2010). This is remarkable because it is the only luminal modification whereby catalysis takes place on polymerized microtubules, implying that the enzyme needs to somehow reach the lumen. K40 can also be methylated, but the methylase prefers tubulin dimers (Kearns et al., 2021). Acetylation of β -tubulin occurs solely on soluble tubulin dimers, is catalyzed by acetyltransferase San1 and has been shown to slow down microtubule polymerization (Chu et al., 2011). Acetylation of K40 always correlated with long-lived microtubules but it was unclear whether it just marked stable microtubules or if it actively stabilized microtubules. Recently, cryo-electron microscopy combined with molecular dynamics simulations showed that there are structural differences between acetylated and non-acetylated microtubules (Eshun-Wilson et al., 2019). Acetylation changes the conformation of the flexible loop in which K40 is located and this change results in weakening of the interaction between lateral α -tubulins. This explains earlier findings where acetylated microtubules were found to be less rigid and more resilient to mechanical stress, making them more stable (Portran et al., 2017). This direct effect of a PTM on the microtubule structure is so far unique among microtubule PTMs. Acetylation is reversible, and deacetylation occurs on tubulin dimers when tubulin dimers come back in the soluble tubulin pool to allow the re-use of dimers.

Detyrosination is the enzymatic removal of the last residue at the C-terminal tail of α -tubulin, and it is the major occurring PTM. Tyrosine removal is catalyzed by vasohibin proteins (VASH1/2) in complex with small vasohibin-binding protein (SVBP) or by MATCAP (Aillaud et al., 2017; Landskron et al., 2022; Nieuwenhuis et al., 2017). Newly added tubulin dimers still contain their C-terminal tyrosine, therefore detyrosination is linked to longer-lived microtubules. Unlike acetylation, detyrosination or tyrosination alone have no effect on microtubule dynamics indicating that these reactions do not change the conformation of tubulin dimers (Chen et al., 2021). However, detyrosination can indirectly affect microtubule stability. Detyrosinated microtubules can recruit stabilizing MAPs or prevent binding of destabilizing MAPs with high affinity for tyrosinated microtubules. The latter is illustrated by members of the kinesin-13 family which exhibit a high affinity for tyrosinated C-terminal tails of α -tubulin. These motor proteins actively disassemble tyrosinated microtubules, making them less stable, but detyrosinated microtubules are protected from these motors resulting in more stable microtubules (Peris et al., 2009). Like acetylation, detyrosination is reversible and preferentially occurs on soluble tubulin (Prota et al., 2013; Szyk et al., 2011).

Polyamination is the addition of polyamines to the γ -carboxy group of glutamine side chains catalyzed by transglutaminases (Janke and Magiera, 2020). Polyamination is the only PTM known to completely block depolymerization by making microtubules insoluble and resistant to proteolysis. This is most likely because amine addition makes tubulin tails more basic (Song et al., 2013). Polyamination is abundant in the axons of neurons, but in polyamination levels in non-neuronal cells are very low (Song et al., 2013). It has been shown that polyamination of neuronal microtubules contributes to microtubule stability and that it is important for neuronal development and maturation (Song et al., 2013). Various polyamination sites have been mapped suggesting that this modification might stabilize microtubules by modulation of GTP binding or hydrolysis, or lateral contacts, but biochemical evidence is lacking (Song et al., 2013). Additionally, no MAPs with affinity for polyaminated microtubules have been identified to date.

In summary, the 'tubulin code' can directly affect microtubule stability, but it is mostly viewed as having a regulatory function in the recruitment of MAPs to specific subsets of microtubules. Subsequently, the recruited MAPs can execute their function and thereby modulate microtubule stability.

Microtubule-associated proteins

MAPs can be categorized in stabilizers, such as capping proteins, polymerization enhancers and catastrophe inhibitors, and destabilizers, such as severing proteins and depolymerization-inducing motor proteins. Here, we will discuss the microtubule stabilizers based on their preferred localization on the microtubule.

At the minus end

Stabilization of the microtubule minus end is usually achieved by proteins or protein complexes that anchor microtubules at microtubule organizing centers (MTOC). Therefore, they have to execute two functions simultaneously; specifically bind to microtubule minus ends and interact with an MTOC (Vineethakumari and Lüders, 2022). Additionally, in cellular environments they need to inhibit minus-end growth because microtubules polymerized from pure tubulin in *in vitro* assays are actually dynamic, while this is not the case in cells (Akhmanova and Steinmetz, 2015; Hendershott and Vale, 2014; Jiang et al., 2014). Microtubule nucleators can also act as microtubule anchors, which is the case for the γ -tubulin ring complex (γ TuRC). After nucleation, this complex can remain bound to the microtubule minus end and acts as a cap (Wiese and Zheng, 2000). In vertebrate cycling cells, the centrosome is the main MTOC, and microtubule nucleation is facilitated by γ TuRC in the closely localized pericentriolar material (PCM) (Delgehr et al., 2005; Hori et al., 2014). It has been shown that the γ TuRC complex alone cannot efficiently nucleate microtubules, so additional factors such as ch-TOG, TPX2 and CLASPs are recruited to promote polymerization or inhibit catastrophes. Anchoring of microtubules at the centrosome involves the activity of the protein ninein at the subdistal appendages (Vineethakumari and Lüders, 2022). This would suggest that γ TuRC would be transferred together with the newly nucleated microtubule to the subdistal appendages (Delgehr et al., 2005; Hori et al., 2014). However, there is some evidence that γ TuRC also localizes to the subdistal appendages and potentially directly nucleate microtubules there (Schweizer and Lüders, 2021). Ninein has been shown to be able to bind to γ TuRC and the centrosome simultaneously, mediating anchoring (Delgehr et al., 2005; Lin et al., 2006). Another centrosomal protein, FSD1, has also been shown to facilitate microtubule anchoring by directly binding to both the mother centriole of the centrosome and microtubules (Tu et al., 2018). Its localization is more proximal than the subdistal appendages and future work will clarify if microtubules remain anchored there, or if they get transferred to the subdistal appendages.

Even when centrosomes function as the main MTOC, microtubules can be nucleated at the cis-Golgi, contributing to cellular microtubule organization. Like the centrosome, γ TuRC acts as a template for microtubule nucleation but here it does not stay bound to the newly nucleated microtubule. At the Golgi, CAMSAP2 binds to and stabilizes the microtubule minus end. Anchoring is facilitated by myomegalin, which links CAMSAP2 to AKAP450 on the Golgi membranes (Wu et al., 2016). CAMSAP2 and CAMSAP3 (another CAMSAP family member) slow down, but do not completely block minus-end growth by the formation of stable stretches which can promote repeated plus-end outgrowth (Hendershott and Vale, 2014; Jiang et al., 2014). CAMSAP2 and ninein have also been shown to play a role in microtubule anchoring in differentiated cells where MTOCs are non-centrosomal and more broadly distributed (Vineethakumari and Lüders, 2022).

During mitosis, microtubule minus ends of the kinetochore fibers need to be stabilized at the spindle poles. This is facilitated by the microspherule protein 1 (MCRS1) which does not show a preference for minus ends on its own, but it does have this preference when it is part of a complex containing KAT8-associated nonspecific lethal (KANSL) proteins (Meunier et al., 2015). KANSL component KANSL3 was shown to preferentially bind to stabilized microtubule minus ends *in vitro*, but it is not yet known if this is also true for dynamic microtubule minus

ends (Akhmanova and Steinmetz, 2019; Meunier et al., 2015). Plant-specific protein SPIRAL2 (SPR2) has been shown to bind and stabilize dynamic microtubule minus ends *in vitro* and in cells (Fan et al., 2018; Leong et al., 2018; Nakamura et al., 2018). SPR2 autonomously recognizes minus ends and dramatically decreases their dynamics (Fan et al., 2018; Leong et al., 2018). In cells and *in vitro*, both polymerization and depolymerization at the minus end were slowed down. Additionally, pauses started to occur in cells, all indicating a stabilizing function of SPR2. Interestingly, SPR2 also binds to microtubule plus ends and affects their dynamics in specific plant cells, but this is possibly dependent on additional binding partners (Fan et al., 2018).

Along the lattice

During early biochemical studies of microtubules, tubulin was purified from brain extracts or HeLa cell lysates. During these purifications, strong microtubule binders were co-purified and they were named MAPs. The well-studied MAPs that were purified at that time are MAP1, MAP2, MAP4, MAP6, MAP7, tau, and DCX. These proteins bind along the microtubule lattice, and they are usually referred to as classical or structural MAPs. These MAPs promote microtubule polymerization, and they can generate very stable microtubules. It has been quite challenging to experimentally study these MAPs, because overexpression or non-physiological concentrations resulted in microtubule artefacts like bundling and overstabilization. As already mentioned before, MAPs are tightly regulated by PTMs on microtubules. Additionally, MAPs themselves can be post-translationally modified and competition can play a role in regulation of MAP-microtubule binding. These types of regulations are usually absent *in vitro*, and overexpression in cells can lead to dysregulation.

Microtubule bundling by MAPs can be explained by a characteristic feature of MAPs. They are usually positively charged proteins which bind to the negatively charged C-terminal tubulin tails. This results in a decreased electrostatic repulsion between microtubules, causing them to form bundles. This concept has been illustrated by the removal of C-terminal tails by the protease subtilisin. Even in the absence of MAPs, subtilisin-treated microtubules were more prone to form bundles (Sackett et al., 1985). For some cellular processes, microtubule bundling is a requirement, and several MAPs have been identified to serve this purpose. Protein regulator of cytokinesis 1 (PRC1) is found to autonomously generate antiparallel microtubule bundles in anaphase required for midzone assembly (Bieling et al., 2010; Subramanian et al., 2013). In contrast, tripartite motif containing 46 (TRIM46) generates evenly spaced, parallel microtubule bundles in the axon initial segment (van Beuningen et al., 2015). TRIM46 acts as a microtubule rescue factor and is required for neuronal polarity and axon formation (Fréal et al., 2019; van Beuningen et al., 2015).

The structural MAPs have been extensively studied in neurons and are found to play major roles in neuronal development, activity, and maintenance. MAP1 family members are predominantly expressed in neurons and bind to the microtubule lattice resulting in stable microtubules (Halpain and Dehmelt, 2006; Tegha-Dunghu et al., 2014). Each family member contains non-overlapping actin-binding and microtubule-binding domains, and it is speculated that they can interact simultaneously with both cytoskeletal networks (Halpain and Dehmelt, 2006; Noiges et al., 2002). MAP2 isoforms are almost exclusively expressed in neurons and have been experimentally shown to cross-link microtubules and actin. MAP2 isoforms were shown to stabilize microtubules by inducing rescues or bundling (Gamblin et al., 1996). MAP4, expressed in all cell types, can also potentially cross-link microtubules and actin. This protein has been shown to stabilize microtubules by enhancing tubulin polymerization and overall microtubule stability (Nguyen et al., 1997; Nguyen et al., 1998; Xiao et al., 2012). MAP4 has been shown to protect microtubules from the depolymerizing kinesin MCAK and microtubule-severing enzyme katanin (Holmfeldt et al., 2002; McNally et al.,

2002). Additionally, a MAP4 isoform identified in muscle cells is required for the alignment of antiparallel microtubule bundles (Mogessie et al., 2015). MAP6 is expressed in many tissues and was initially shown to protect microtubules from depolymerization in cold- or drug treatment (Delphin et al., 2012). MAP6 has been recently identified as a MAP which can bind to the microtubule surface as well as to the microtubule luminal side (Cuveillier et al., 2020). Proteins binding to the microtubule lumen are a subgroup of MAPs termed microtubule inner proteins (MIP). MIPs have been observed in conventional electron microscopy studies, but the level of detail has been greatly improved recently. Increasing numbers of intraluminal proteins are observed with cryo-electron microscopy and tomography studies, particularly in cilia and flagella, and their identification has been greatly improved by structural analysis (Gui et al., 2021; Ma et al., 2019). MAP6 has been one of the exceptions that has not been identified in cilia. It has been shown to induce microtubules to coil and it creates apertures in the lattice, potentially to relieve mechanical stress (Cuveillier et al., 2020). MAP7 is widely expressed and promotes microtubule polymerization during mitosis (Gallaud et al., 2014). Additionally, MAP7 enhances kinesin-1 binding and processivity and it directly competes with tau *in vitro* (Hooikaas et al., 2019; Monroy et al., 2018; Sung et al., 2008). Tau is another neuronal MAP, which is associated with many neurodegenerative diseases such as Alzheimer's disease. The tau protein is largely disordered, and it has been shown to enhance microtubule stability and polymerization and it can control microtubule PTMs (Drechsel et al., 1992; Ramkumar et al., 2018). All previous described structural MAPs bind to the ridges of the microtubule filament, but there is one protein family which attaches to the valley between protofilaments. This family includes doublecortin (DCX) and doublecortin-like kinase (DCLK). These proteins stimulate microtubule polymerization and stabilize microtubules by binding to the protofilament groove, and this is thought to provide lateral and longitudinal stability to the microtubules (Bechstedt et al., 2014; Moores et al., 2004).

There are many more MAPs identified to be directly or indirectly involved in microtubule stabilization, but their mechanisms still remain unclear. One interesting concept about MAP-driven microtubule stabilization involves tubulin exchange in microtubule shafts. Motor proteins walking along microtubules induce damage to the lattice, and microtubule severing proteins have been found to contribute to the stabilization of microtubules. This is quite counterintuitive, as damaging and severing are events that are viewed to be destabilizing. It has been shown that damages in the microtubule lattice can incorporate GTP-tubulin dimers to facilitate microtubule repair, creating 'GTP-islands' (de Forges et al., 2016; Dimitrov et al., 2008; Schaedel et al., 2015; Schaedel et al., 2019). These islands can promote microtubule growth by creating points for reinitiating growth, called rescue sites, during subsequent catastrophe events (Aumeier et al., 2016; Dimitrov et al., 2008; Rai et al., 2020). Additionally, these islands can recruit growth-promoting MAPs which specifically recognize GTP-tubulin (Aher et al., 2020; de Forges et al., 2016). Microtubules with repaired damage sites are found to have longer lifetimes, longer lengths and increased number of rescues compared to microtubules which did not acquire defects (Aumeier et al., 2016).

At the plus end

MAPs that specifically localize to the microtubule plus end in cells are referred to as +TIPs. They generally only target polymerizing microtubule ends which contain the GTP cap. The central player in microtubule plus-tip recognition is the family of end binding (EB) proteins. These proteins can autonomously bind to the plus ends and track their growth. Most of the other MAPs belonging to the +TIP network interact with microtubules via binding to EB proteins. In mammalian cells, three EB proteins are expressed: EB1, EB2 and EB3. They all have an N-terminal calponin homology domain (CH domain), followed by a variable linker region, a coiled-coil domain for homo- or heterodimerization (together with the CH

domain and linker known as the EB-homology domain; EBH), and a C-terminal domain with binding sites for components of the +TIP network (Akhmanova and Steinmetz, 2015). EB proteins can be post-translationally modified to regulate their involvement in various cellular processes (Iimori et al., 2012; Xia et al., 2012). EBs bind to growing microtubule plus ends in a comet-like fashion at a short distance from the outermost end. It has been shown that the CH domain binds to the corners of four tubulin GTP-dimers (Maurer et al., 2011; Zhang et al., 2015). This enables the protein to sense conformational changes due to GTP hydrolysis, illustrating why it tracks growing microtubule ends. Upon catastrophe due to GTP-cap loss, EB proteins are also lost. Therefore, EB proteins are frequently used as markers of growing microtubule plus end in cells and *in vitro*. *In vitro*, they can also label growing microtubule minus ends. Interestingly, EBs are found to promote microtubule catastrophes *in vitro* while in cells they mostly promote elongation (Komarova et al., 2009; Zanic et al., 2013). This illustrates that binding partners and regulation play a key role in EB function.

EB proteins have two main binding sites for proteins belonging to the +TIP network: the EBH domain and the C-terminal EEY/F motif. Proteins that interact with the C-terminal EEY/F motif contain a cytoskeleton-associated protein glycine-rich (CAP-Gly) domain which has a hydrophobic cavity for this C-terminal motif as well as the C-terminal motif of α -tubulin. Two major +TIP proteins binding to this motif are CLIP-170 and p150Glued, the large subunit of the dynein assessor factor dynactin (Akhmanova and Hoogenraad, 2015). To interact with the EBH domain, proteins contain one or more SxIP amino acid motifs (x stands for any amino acid). Many proteins have been identified which contain this motif such as the CLASP (CLIP-associating protein) family (Jiang et al., 2012). These proteins have TOG domains which are known to be involved in microtubule plus-end polymerization by binding to soluble tubulin (Al-Bassam and Chang, 2011). CLASPs can indeed stimulate microtubule polymerization, but their TOG domains cannot bind to soluble tubulin (Aher et al., 2018). To date, it is not yet known how CLASPs can stimulate microtubule polymerization. Additionally, CLASPs can promote rescues and it has been shown that a single TOG domain is sufficient to achieve this (Aher et al., 2018; Bouchet et al., 2016b; Mimori-Kiyosue et al., 2005).

There is another major group of autonomous plus-end binding proteins which are members of the XMAP215 family. They are known as microtubule polymerases and they contain multiple TOG domains and a basic region with affinity for the microtubule lattice (Widlund et al., 2011). TOG domains bind to the curved conformational state of the GTP-bound tubulin dimers and because XMAP215 family proteins are localized at the outermost tip of growing microtubules, it is believed that they facilitate tubulin dimer addition while being bound to the plus tip (Ayaz et al., 2012).

TPX2 is another protein which is sensitive to the GTP/GDP state of tubulin. It prefers the extended GTP-bound microtubule lattice and is enriched at growing microtubule plus ends (Roostalu et al., 2015). TPX2 stabilizes the lattice potentially by slowing down the GTP hydrolysis speed. This suppresses catastrophes and it has been shown to promote microtubule nucleation (Roostalu et al., 2015; Zhang et al., 2017). CPAP/SAS-4 is a centriolar protein which prevents depolymerization and acts as a cap on the plus ends of centrioles to inhibit elongation. Stabilization of microtubules can be achieved by the presence of two or three CPAP dimers at the plus end (Sharma et al., 2016). CPAP slows down the growth rate several fold and reduces the catastrophe frequency by an order of magnitude (Sharma et al., 2016). Capping is achieved by a specific domain of CPAP (termed LID-domain), which binds to the exposed surface of β -tubulin (Sharma et al., 2016; Zheng et al., 2016).

Microtubule stabilizing complexes

As described above, microtubules can be stabilized in many different ways and for many different purposes. Stabilization can be achieved by single proteins or large multi-protein

assemblies. Here, two multi-protein assemblies will be discussed in more detail. The first one is the cortical microtubule stabilizing complex (CMSC), which anchors microtubules near focal adhesions for vesicle transport and exocytosis. The second one is the ciliary tip module (CTM), which is essential for microtubule elongation and maintenance of microtubule length in the axonemes of primary cilia, required for diverse signalling processes.

Cortical Microtubule Stabilizing Complex (CMSC)

For microtubule organization, but also for processes like focal adhesion (FA) turnover and exocytosis, microtubule plus ends need to be stabilized at the cell cortex. Stable microtubule tracks enable kinesins and their cargo to reach the cell cortex. Different plus-end tracking proteins have been identified as linkers between microtubules and the cell cortex. These proteins include APC, CLASPs, CLIP-170, dynein/dynactin and spectraplakins (Akhmanova and Steinmetz, 2015; Stehbens et al., 2014). From this group, CLASPs were found to attach dynamic microtubules to certain cortical regions through binding to EB1 (Mimori-Kiyosue et al., 2005). On the cortical side, CLASPs dependent on the direct interaction with LL5 β , or its homologue LL5 α , for cortical accumulation and microtubule stabilization (Hotta et al., 2010; Lansbergen et al., 2006). LL5 β is part of a larger protein complex which is known as the cortical microtubule stabilizing complex (CMSC). Aside from LL5 β , the CSMC consists of the proteins ELKS, liprin- α 1, liprin- β 1 and KANK1 (Fig. 3).

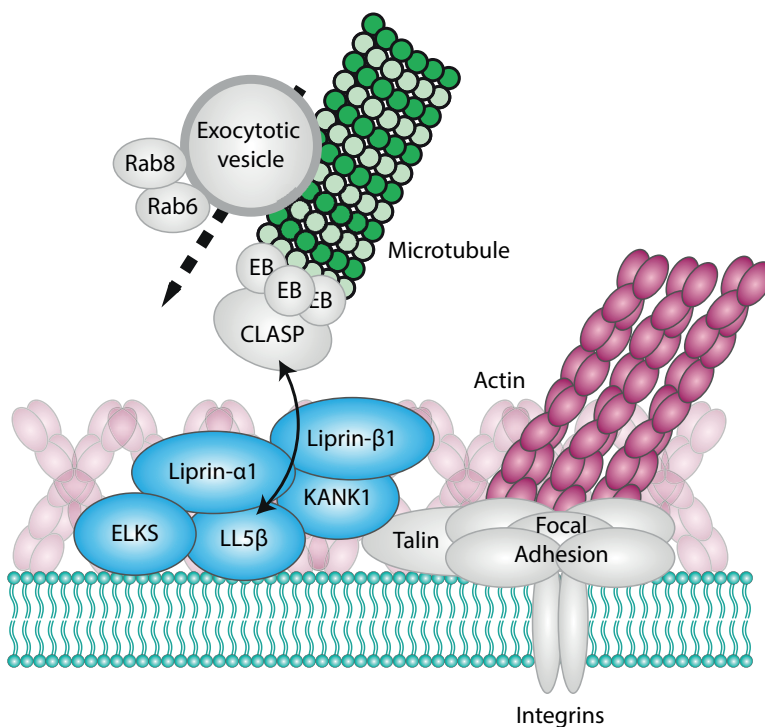


Figure 3: Cortical microtubule stabilizing complex (CMSC) near focal adhesions. Microtubule plus ends attach to the cell cortex via the interaction of +TIP CLASP and LL5 β from the CMSC (components shown in blue). KANK1 interacts with talin, the core component of focal adhesions. This interaction facilitates constitutive exocytosis at focal adhesion sites. Figure adapted from Noordstra & Akhmanova, 2017.

LL5 β contains a pleckstrin homology (PH) domain which binds to PIP3 (phosphatidylinositol-3,4,5-triphosphate) and its recruitment to the cell cortex, as well as the localization of the whole CMSC, is influenced by PI3 kinase activity (Lansbergen et al., 2006; Paranaivitane et al., 2003). LL5 β directly interacts with the scaffolding protein ELKS (also known as ERC1, for ELKS/RAB6-interacting/CAST family member 1) and this interaction is essential for cortical localization of ELKS. ELKS on the other hand, is necessary for the clustering of LL5 β and subsequently of CLASPs. LL5 β and ELKS both localize to the rim of focal adhesions (FAs), but they never overlap (Lansbergen et al., 2006). FAs are mature integrin-mediated cell attachment complexes. More than fifty different proteins are organized in macromolecular assemblies at the plasma membrane, which link the extracellular matrix to the actin cytoskeleton. This linkage is essential for many biological processes where FAs need to be assembled, matured, or disassembled. Examples of these processes are cell migration, tissue integrity, and wound healing. Alterations in FAs can cause human disease including cancer and developmental disorders (Byron et al., 2015; Winograd-Katz et al., 2014). Assembly and disassembly of FAs requires components to be transported to and from the cell cortex via the microtubule network, illustrating why it is beneficial to attach microtubules to the cell cortex near FAs. There are multiple ways microtubules can affect FA dynamics. For example, microtubules are involved in the local modulation of Rho GTPase signalling that controls actomyosin-based contractility (Stehbens and Wittmann, 2012). Moreover, alteration of the microtubule network, for example by addition of the drug nocodazole, also has been shown to affect FA turnover (Ezratty et al., 2005; Ren et al., 1999). Interestingly, it was shown that knockdown of LL5 β or ELKS resulted in smaller FAs, independently of microtubule organization (Lansbergen et al., 2006). This indicated a functional interplay between the LL5 β -ELKS structures, microtubules, and FAs. Additionally, this indicated LL5 β and ELKS could be part of a larger complex that links them to FAs.

Biochemical assays showed that liprin- α 1, liprin- β 1, KANK1 and KIF21A are part of the same cortical structures (van der Vaart et al., 2013). Liprin- α 1 directly binds to ELKS and liprin- β 1, and liprin- β 1 itself directly binds to another scaffolding protein called KANK1 (KN motif and ANKyrin repeat domain-containing protein 1) (Ko et al., 2003; van der Vaart et al., 2013). KANK1 interacts with the core FA protein talin, serving as the direct link between the CMSC to FAs (Bouchet et al., 2016a). Inhibition of the KANK1-talin or the liprin- β 1-KANK1 interaction leads to the loss of CMSC clusters around FAs and subsequent loss of localized cortical microtubule capture (Bouchet et al., 2016a; van der Vaart et al., 2013). KANK1 also recruits KIF21A to the cell cortex. KIF21A is a plus-end-directed motor (kinesin-4 family member), which cooperates with CLASPs in promoting microtubule stability at the cortex. It strongly inhibits microtubule growth as well as catastrophes (van der Vaart et al., 2013). Because it is localizing on microtubules, KIF21A is not considered a core component of the CMSC. Even though the CMSCs directly interact with FAs via the KANK1-talin bond, the two cortical structures do not overlap and intermix, for reasons that are not yet clear (van der Vaart et al., 2013). It is proposed that talin binding to actin and KANK family members is mutually exclusive, possibly explaining why the CMSC does not overlap with the actin-rich core of FAs (Noordstra and Akhmanova, 2017; Sun et al., 2016).

As mentioned before, ELKS is a scaffolding protein required for clustering of the other CMSC components. Additionally, ELKS can recruit other proteins to the CMSC clusters and has been shown to be a key component in constitutive calcium independent exocytosis in non-neuronal cells (Grigoriev et al., 2007; Grigoriev et al., 2011; Stehbens et al., 2014). Constitutive exocytosis is the process of continuous transport of newly synthesized lipids, membrane proteins and extracellular matrix components to the plasma membrane. ELKS directly binds to all isoforms of the small GTPase Rab6 which are localized to the outside of exocytotic vesicles (Grigoriev et al., 2007). Rab6A-positive vesicles dock and fuse at the

CMSC and fusion is inhibited when ELKS is depleted. This shows that ELKS is not involved in targeting of the vesicles to the CMSC, but it is involved in facilitating vesicle fusion (Grigoriev et al., 2007). Apart from binding to ELKS, Rab6 can also control the recruitment of GTPase Rab8A to exocytotic vesicles. This is important for subsequent docking at the CMSC, as Rab8A depletion led to accumulation of exocytotic vesicles in cortical regions devoid of ELKS (Grigoriev et al., 2011). It was shown that Rab8A binds to MICAL3, another binding partner of ELKS. MICAL3 is a multidomain oxidative enzyme which acts as a scaffold and promotes disassembly of actin filaments. It was shown that the monooxygenase activity of MICAL3 is required for vesicle fusion with the plasma membrane (Grigoriev et al., 2011).

ELKS is not only involved in constitutive exocytosis at focal adhesions, but it is also localized together with Liprin- α 1 family members in the cytomatrix at the active zone (CAZ) in neuronal cells. The active zone is the principal site of calcium-dependent exocytosis of neurotransmitters in neuronal synapses (Gundelfinger and Fejtova, 2012; Spangler and Hoogenraad, 2007; Sudhof, 2012). There is some overlap between the CMSC involved in constitutive exocytosis and calcium-dependent exocytosis at the CAZ, but there are many non-overlapping components. LL5 or KANK homologues are not found at the active zone and there are no direct connections to microtubules (Noordstra and Akhmanova, 2017).

In summary, cortical microtubule attachment in the vicinity of FAs is facilitated by the CMSC. The CMSC is involved in the formation and dynamics of FAs by regulating microtubule-dependent signaling and trafficking. Further understanding of this interplay will be important for diagnosis and development of treatment strategies for diseases involving one or more components of FAs or the CMSC.

Ciliary Tip Module (CTM)

Microtubules can also serve as a physical support in stable cellular structures such as cilia. Cilia are microtubule-based structures that protrude from plasma membrane. Motile cilia are a class of cilia which can generate movement. They are mostly known for the movement of single-celled eukaryotes or sperm cells, then referred to as flagella, or for driving fluid flow over apical surface in mammalian brain ependyma and trachea cells. Primary cilia, the other class of cilia and often referred to as cellular antennas, are usually found as single protrusions on the cellular surface and they are involved in signalling (Berbari et al., 2009; Klena and Pigino, 2022). Dysfunction of both classes of cilia is associated with diseases affecting multiple organ systems and developmental disorders, which are collectively called ciliopathies (Hildebrandt et al., 2011; Klena and Pigino, 2022).

Primary cilia are assembled during interphase, and they are generated from the mother centriole. Centrioles are microtubule-based structures, which are symmetrically organized in nine microtubule triplets. Every triplet is composed of an A-tubule, which is a fully closed 13-protofilament microtubule, and two incomplete microtubules, the B-tubule and the C-tubule, consisting of ten protofilaments and sharing a part of the microtubule wall with their neighbor tubule (Breslow and Holland, 2019; Wang and Stearns, 2017). There are two possible pathways to generate primary cilia (also called ciliogenesis), the extracellular pathway and the intracellular pathway (Breslow and Holland, 2019; Sorokin, 1962). The extracellular pathway starts with migration of the mother centriole to the plasma membrane where it docks using its centriolar distal appendages and is converted to a basal body. Then, the A- and B-tubules get extended to form the ciliary axoneme, creating a symmetric structure of nine microtubule doublets. Next, the transition zone is formed, creating a separation between the cytosol and the cilium. All materials required for cilium extension, maintenance and signalling machinery are delivered to the transition zone to be transported into the cilium by intraflagellar transport (IFT) (Keeling et al., 2016). The second pathway is the intracellular pathway, which shows quite some similarities to the extracellular pathway but docking to the plasma membrane

occurs much later. First, vesicles are recruited, docked, and fused at the distal appendages of the mother centriole creating a ciliary vesicle. Then, the axonemal microtubules are elongated, and the transition zone starts to form, creating a growing cilium fully inside the cell. Finally, the ciliary vesicle migrates, docks and fuses with the plasma membrane to expose the cilium on the cell surface where it can continue to grow. It is not well understood what determines which pathway the cell will use to generate cilia, but it seems to be cell type- and therefore also function-specific. For example, polarized epithelial cells are found to primarily use the extracellular pathway and their primary cilia fully extend from the plasma membrane (Molla-Herman et al., 2010; Sorokin, 1962; Sorokin, 1968). The function of these cilia is to sense extracellular fluid flow, and therefore, positioning of the major part of the cilium length on the cell surface seems ideal. In contrast, cells that use the intracellular pathway usually maintain their basal body closer to the nucleus, resulting in a more submerged cilium. Cells that are, for example, strongly involved in Hedgehog signalling like fibroblasts and retinal pigment epithelial cells are found to use this pathway more often (Molla-Herman et al., 2010; Sorokin, 1962). This was illustrated by the study where conversion of submerged cilia into surface cilia promoted the detection of fluid flow but dysregulated Hedgehog signalling (Mazo et al., 2016).

After transition zone formation and cilium docking at the plasma membrane, the cilium must grow to a steady state length. The correct cilium length is essential for its function in signalling pathways, as cilium length deviation is often linked to ciliopathies. The cilium length is directly determined by the axoneme length, and axonemal extension can only occur at the plus ends of the microtubules. The steady state of cilia is also described as a state of dynamic stability or protein turnover, where degradation is balanced by subunit addition. Protein turnover at the ciliary tip of mature cilia was shown by the incorporation of radioactive-labelled proteins at the tip without affecting cilium length (Song and Dentler, 2001). It is challenging to elucidate exactly how cilium length is controlled, because length is a result from complex regulatory pathways. This is illustrated by the recent discovery that axonemal microtubules in primary cilia can have various lengths in a single cilium. Until recently, most of the primary cilium length was believed to consist of microtubule doublets and the only difference between motile and primary cilia was the presence of the central pair. However, studies using serial sectioning and cryo-electron tomography revealed that the presence of doublets only occurs close to the ciliary base (Kiesel et al., 2020; Sun et al., 2019). At the base, microtubule doublets are arranged more to the outside of the cilium but a little more proximal to the base, some doublets can shift more to the center of the axoneme. Additionally, B-tubules stop elongating at variable positions leaving just the single A-tubules and they then also terminate at variable distances from the ciliary tip (Klena and Pigino, 2022). Multiple proteins have been identified to be involved in axonemal length regulation but their separate mechanisms as well as their interplay are poorly understood (Keeling et al., 2016).

Because the cilium is separated from the plasma membrane by the transition zone, most materials required for axoneme elongation and maintenance rely on IFT for ciliary entry and subsequent transport to the ciliary tip. This is one of the reasons IFT molecules have been proposed to be the main regulators of ciliary growth (Keeling et al., 2016). Cilia in embryonic sea urchins get disassembled if anterograde IFT is inhibited, resulting in shorter or missing cilia (Stephens, 1997). Increased activity or accumulation of the anterograde IFT complex in the flagella of *Chlamydomonas reinhardtii* resulted in longer cilia, while decreased mobility of these complexes generated shorter cilia (Marshall et al., 2005; Marshall and Rosenbaum, 2001). Elongated cilia were also observed in mammalian cells, when the mobility of the anterograde IFT complex was increased (Besschetnova et al., 2010). Additionally, depletion of Tctex-1, a component of the IFT-associated dynein also produces longer cilia (Palmer et al., 2011). Although the majority of protein entry into the cilium relies on IFT, there are numerous

proteins that can diffuse in and out of the cilium, and their concentration can also affect cilium length. Tubulin is one of the proteins which can diffuse into the cilium, and it has also been linked to ciliary length control. Overproduction of soluble tubulin leads to longer cilia while overstabilization of cytoplasmic microtubules, thereby limiting the supply of tubulin to the cilium, leads to shorter cilia (Sharma et al., 2011). There are many more proteins, protein families and protein complexes implicated in regulating ciliary length, one of which is the recently identified ciliary tip module (CTM) (Latour et al., 2020). These proteins localize to the ciliary tip, and their depletion is sufficient to shorten ciliary length, leading to impaired Hedgehog signalling (Hh). Dysfunction of most CTM components underlies a ciliopathy called Joubert syndrome (JBTS), a syndrome characterized by malformation of the midbrain-hindbrain junction as well as ataxia, breathing problems or more severe organ malfunctions (Hildebrandt et al., 2011).

The core components of the CTM are ARMC9, CSPP1, CEP104, CCDC66 and TOGARAM1 (Fig. 4) (Conkar and Firat-Karalar, 2021; Latour et al., 2020). ARMC9, armadillo repeat-containing protein 9, was recently identified as a gene modified in individuals presenting with JBTS (Van De Weghe et al., 2017). ARMC9 was found to be colocalizing with γ -tubulin at the basal body and with the daughter centrioles (Van De Weghe et al., 2017). Depletion of ARMC9 resulted in shorter cilia, which also exhibited a lower level of ciliary PTMs (Breslow et al., 2018). Additionally, Hedgehog signalling was impaired by reduced accumulation of Hedgehog signalling components GLI1 and GLI3 at the ciliary tip (Breslow et al., 2018). In wildtype cells, stimulation of Hedgehog signalling led to the relocation of ARMC9 to the ciliary tip suggesting the participation of ARMC9 in trafficking or retention of GLI1 and GLI3 proteins at the ciliary tip (Breslow et al., 2018). Work in *Tetrahymena thermophila* showed that the ortholog of ARMC9, ARMC9A, localizes to unciliated basal bodies, growing cilia tips and near the ends of B-tubules in motile cilia (Louka et al., 2018). Moreover, depletion of

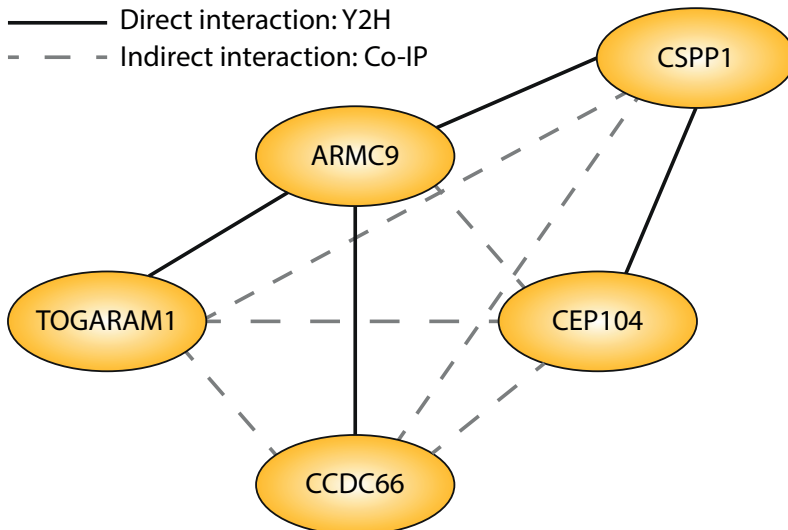


Figure 4: Mapped interactions between the core components of the ciliary tip module (CTM). Direct interactions (continuous lines) confirmed with yeast 2-hybrid (Y2H) assays, and indirect interactions (dashed lines) observed in co-immunoprecipitation assays show that multiple strong interactions exist between the CTM components. Figure adapted from Latour et al., 2020.

ARMC9A changed the geometry of the cilium by an excessive increase in B-tubule length but only induced a slight increase in the total cilium length (Louka et al., 2018). This indicated that ARMC9 functions to shorten the B-tubules. It remains to be determined if this is also the case in primary cilia. ARMC9 contains a N-terminal LisH motif which is considered to contribute to microtubule dynamics, but the protein cannot bind to microtubules on its own (Emes and Ponting, 2001; Latour et al., 2020; Mateja et al., 2006). A study using yeast 2-hybrid (Y2H) screens revealed a direct interaction between ARMC9 and TOGARAM1 and showed that ARMC9 gets recruited to microtubules through this interaction (Latour et al., 2020). Dysfunction of ARMC9 or TOGARAM1 resulted in shorter cilia with reduced post-translationally modified axonemal tubulin, suggesting this interaction is important for ciliary stability (Latour et al., 2020).

TOGARAM1, TOG array regulator of axonemal microtubules 1, contains four conserved TOG domains (TOG1-TOG4) which show similarities to the tubulin-binding domains in ch-TOG and CLASP family proteins (Das et al., 2015). It is a member of the FAM179 protein family, and homologs are found in evolutionarily distant eukaryotes including *Chlamydomonas reinhardtii* (SHF1), *Tetrahymena thermophila* (CHE-12A and CHE-12B), *Caenorhabditis elegans* (CHE-12) and mouse (crescerin1) (Das et al., 2015; Louka et al., 2018; Perlaza et al., 2022). TOGARAM1 localizes at the basal body, along the ciliary axoneme and is enriched at the ciliary tip (Das et al., 2015; Latour et al., 2020). Overexpression of TOGARAM1 showed localization to the lattice of cytoplasmic microtubules but it was never observed at their plus ends (Das et al., 2015). The TOG domains of the mouse homolog of TOGARAM1, crescerin1, were found to have differential tubulin-binding activity, all potentially involved in regulation of microtubule dynamics. In *Caenorhabditis elegans*, the TOGARAM1 homologs bearing mutations in the tubulin-binding regions in all TOG domains still showed ciliary localization but resulted in shorter cilia (Das et al., 2015). This strongly suggests TOGARAM1 contributes to cilia stability by using the TOG array's tubulin-binding activity. Recently, several mutations in the TOG2 and TOG3 domains of TOGARAM1 were linked to JBTS (Latour et al., 2020). Overexpression of wildtype TOGARAM1 resulted in longer cilia, which was also the case for TOG2 disease mutations. Interestingly, overexpression of TOGARAM1 harbouring a disease mutation in TOG3 showed shorter cilia, possibly by having a dominant-negative effect on the polymerization capacity of TOGARAM1 (Latour et al., 2020). TOG2 mutations also disrupted binding to ARMC9, while this was unaffected with the TOG3 mutant. JBTS patient-derived fibroblasts lacking TOGARAM1 lead to shorter cilia, and TOGARAM1 dysfunction resulted in attenuated translocation of Smoothed G protein-coupled receptor upon stimulation of Hedgehog signalling (Latour et al., 2020). In the same study where the homolog of ARMC9 was localized at the tip of the B-tubule in motile cilia of *Tetrahymena thermophila*, the homolog of TOGARAM1, CHE-12, was also found near the ends of B-tubules (Louka et al., 2018). Depletion of CHE-12 resulted in shorter cilia, with the B-tubule being relatively more affected (Louka et al., 2018). Therefore, CHE-12 is suggested to promote elongation of B-tubules (potentially by promoting the addition of tubulin subunits to the ends of microtubules using its TOG domains), in contrast to ARMC9 which potentially promotes shortening of the B-tubules or inhibits their elongation.

Another interaction partner of ARMC9 is CSPP1, as also demonstrated by Y2H screens (Latour et al., 2020). CSPP1, central and spindle pole associated protein 1, has been linked to JBTS, and the more severe Meckel-Gruber syndrome, earlier than ARMC9 and TOGARAM1 (Akizu et al., 2014; Shaheen et al., 2014; Tuz et al., 2014). CSPP1 was first identified in a screen for genes potentially involved in the progression from low-grade to high-grade malignancies (Patzke et al., 2005). There it was found to be associated with centrosomes and microtubules and it plays a role in cell cycle progression and mitosis (Asiedu et al., 2009; Patzke et al., 2005; Patzke et al., 2006). Later, it was found to be localizing to basal bodies, along ciliary

axonemes and at the ciliary tip of motile and primary cilia (Akizu et al., 2014; Frikstad et al., 2019; Patzke et al., 2010; Tuz et al., 2014). CSPP1 also localizes to centriolar satellites where it interacts with CEP290 and PCM1. Additionally, it binds to transition zone protein RPGRIP1L (Frikstad et al., 2019; Patzke et al., 2010). RPGRIP1L is another JBTS-linked gene, also known as NPHP8, and CSPP1 is important for recruitment or retention of RPGRIP1L at the transition zone (Patzke et al., 2010). RPGRIP1L also directly interacts with TOGARAM1, but it is never observed at the ciliary tip and therefore not considered a core component of the CTM (Latour et al., 2020).

Dysfunction of CSPP1, either by depletion or overexpression of JBTS-associated mutations, resulted in shorter cilia, while overexpression of wildtype CSPP1 increased cilia length (Frikstad et al., 2019; Patzke et al., 2010; Tuz et al., 2014). These alterations in axoneme length were shown to be dependent on the direct interaction between CSPP1 and another JBTS-associated protein, CEP104 (Frikstad et al., 2019). CEP104, centrosomal protein of 104 kDa, was first identified as a protein localizing to centrioles and was also found to interact with microtubule plus-end tracking protein EB1 (Jakobsen et al., 2011; Jiang et al., 2012). Further analysis showed that CEP104 interacts with the centriolar capping complex CEP97-CP110 (Jiang et al., 2012). This complex blocks centriolar microtubule outgrowth and needs to be removed to enable cilia formation (Spektor et al., 2007). CEP104 colocalizes with CP110 at the distal end of each centriole in unciliated cells, and depletion of CEP104 results in a decreased ability of cells to form cilia (Jiang et al., 2012; Yamazoe et al., 2020). Additionally, CEP104 was found to be important for cilia elongation (Yamazoe et al., 2020). During formation of primary cilia, CEP104 is found on the daughter centriole but it is not detected on the mother centriole. Instead, CEP104 moves to the growing ciliary tip (Satish Tammana et al., 2013). Homologues of CEP104 in *Chlamydomonas reinhardtii* (FAP256) and *Tetrahymena thermophila* (FAP256A and FAP256B) were also found to localize to the tip of motile cilia (Louka et al., 2018; Satish Tammana et al., 2013). In the latter organism, FAP256A was found to localize to the ends of the central pair and A-tubules and promote their elongation (Louka et al., 2018). Like TOGARAM1, CEP104 is a TOG domain containing protein, and ciliary microtubule elongation might be facilitated by the promotion of tubulin subunit addition via its TOG domain (Al-Jassar et al., 2017; Louka et al., 2018; Rezaabkova et al., 2016). Y2H screens revealed that CEP104 directly interacts with CSPP1, and these proteins were shown to colocalize at the tip of primary cilia (Frikstad et al., 2019). Additionally, the three JBTS-linked mutations in CEP104 were shown to disrupt the interaction with CSPP1 (Frikstad et al., 2019; Srour et al., 2015). Co-depletion of both proteins showed even shorter cilia than single depletions (Frikstad et al., 2019). This suggests that the intra-ciliary interaction between CSPP1 and CEP104 is essential to control axoneme length. Additionally, CSPP1 and CEP104 are both required for functional Hedgehog signalling (Frikstad et al., 2019; Shaheen et al., 2014).

CSPP1 and CEP104 were recently identified to interact with CCDC66, but direct interaction is not yet confirmed (Conkar et al., 2022). CCDC66 was also found to interact with ARMC9, and their direct interaction was confirmed with Y2H (Latour et al., 2020). CCDC66, coiled-coil domain containing protein 66, was first encountered in a screen to identify the mutated gene in dogs suffering from generalized progressive retinal atrophy that exhibits continuous degeneration of photoreceptors (Dekomien et al., 2010). This phenotype was also confirmed in a mouse model used to study retinitis pigmentosa, a retinal disorder (Gerding et al., 2011). Even though CCDC66 mutations cause retinal degeneration, no JBTS-linked mutations are known to date (Conkar et al., 2022; Latour et al., 2020). In human cells, CCDC66 is found to contribute to spindle pole morphology and has been identified as a centriolar satellite protein (Gupta et al., 2015; Sharp et al., 2011). Like CSPP1, CCDC66 colocalizes with centriolar satellite proteins CEP290 and PCM1. Additionally, CCDC66

localizes to the centrosome and relocates to the primary cilium (Conkar et al., 2017). In ciliated cells, CCDC66 localizes along the ciliary axoneme and at the tip (Conkar et al., 2019; Conkar et al., 2017; Conkar et al., 2022). Overexpression of CCDC66 leads to microtubule bundling, alteration of centriolar satellite distribution, and inhibition of ciliogenesis, while depletion of CCDC66 results in fewer and shorter cilia (Conkar et al., 2017; Conkar et al., 2022). This indicates that CCDC66 is required for initiation of ciliogenesis and elongation of the axoneme. Additionally, co-depletion of CCDC66 with CSPP1 or CEP104 resulted in both cases in further reduction in ciliary length (Conkar et al., 2022). Overexpression of CEP104, but not CSPP1, in CCDC66-depleted cells could restore normal ciliary length (Conkar et al., 2022). This suggests that CCDC66 might regulate CEP104-mediated axonemal microtubule polymerization. Like all other CTM proteins, depletion of CCDC66 impaired Hedgehog signalling (Conkar et al., 2022).

In summary, axonemal length control has been demonstrated to depend on JBTS-related components of the CTM. Even though all proteins have been shown to localize to the ciliary tip, they also individually localize to different cellular compartments. It will be interesting to study how their localization is regulated and which cues facilitate ciliary localization. Moreover, each protein has a specific role at the ciliary tip to establish axonemal length control and elucidation of their individual, as well as their collective role and mechanism could advance treatment options for JBTS.

Scope of this thesis

Microtubules are highly dynamic entities which require to be stabilized for various cellular processes. In this thesis, we investigated the components of two different microtubule stabilizing complexes in various systems including cell lines, pancreatic islets, and *in vitro* reconstituted microtubules.

In **Chapter 2**, we focused on the role of CMSC components in pancreatic β -cells. We showed that insulin secretion in pancreatic β -cells is regulated by a combined complex of proteins involved in constitutive exocytosis in migrating cells and proteins facilitating neurotransmitter release at the pre-synaptic active zone in neurons. We found that the first wave of insulin depletion was attenuated by depletion of LL5 β or disassembly of focal adhesions, and that the secretion machinery is not assembled through liquid-liquid phase separation, as could be expected based on previous work from other groups, but by binding and unbinding to low-mobility scaffolds.

In **Chapter 3**, we characterized the microtubule-stabilizing properties of CSPP1, a protein implicated in Joubert syndrome. We found that CSPP1 stabilizes microtubules which grow slowly, undergo growth perturbations, or contain damaged lattices. Stabilization of microtubules is facilitated via two separate domains and cryo-electron tomography and MINFLUX microscopy revealed CSPP1 is a microtubule inner protein.

In **Chapter 4**, we examined the individual and collective behavior of ciliary tip module proteins on dynamic microtubules. We showed that all components can be purified and used in assays with *in vitro* reconstituted microtubules. We found that CEP104 blocked microtubule plus-end growth and this behavior was potentiated by End-Binding proteins, CSPP1 and CCDC66. TOGARAM1 opposed the growth inhibition imposed by CEP104. TOGARAM1 and CEP104 together imparted slow microtubule polymerization, and microtubule growth rate was reduced even further in the presence of ARMC9 and CSPP1. These results provide the foundation for understanding the mechanism behind axonemal length regulation by ciliary tip proteins.

In **Chapter 5**, we discuss our findings in a broader context and provide suggestions for future research directions.

References

- Aher, A., and A. Akhmanova. 2018. Tipping microtubule dynamics, one protofilament at a time. *Curr Opin Cell Biol.* 50:86-93.
- Aher, A., M. Kok, A. Sharma, A. Rai, N. Olieric, R. Rodriguez-Garcia, E.A. Katrukha, T. Weinert, V. Olieric, L.C. Kapitein, M.O. Steinmetz, M. Dogterom, and A. Akhmanova. 2018. CLASP Suppresses Microtubule Catastrophes through a Single TOG Domain. *Dev Cell.* 46:40-58.
- Aher, A., D. Rai, L. Schaedel, J. Gaillard, K. John, Q. Liu, M. Altelaar, L. Blanchoin, M. Thery, and A. Akhmanova. 2020. CLASP Mediates Microtubule Repair by Restricting Lattice Damage and Regulating Tubulin Incorporation. *Curr Biol.* 30:2175-2183.
- Aillaud, C., C. Bosc, L. Peris, A. Bosson, P. Heemeryck, J. Van Dijk, J. Le Friec, B. Boulan, F. Vossier, L.E. Sanman, S. Syed, N. Amara, Y. Couté, L. Lafanechère, E. Denarier, C. Delphin, L. Pelletier, S. Humbert, M. Bogyo, A. Andrieux, K. Rogowski, and M.J. Moutin. 2017. Vasohibins/SVBP are tubulin carboxypeptidases (TCPs) that regulate neuron differentiation. *Science.* 358:1448-1453.
- Akhmanova, A., and C.C. Hoogenraad. 2015. Microtubule Minus-End-Targeting Proteins. *Curr Biol.* 25:R162-R171.
- Akhmanova, A., and L.C. Kapitein. 2022. Mechanisms of microtubule organization in differentiated animal cells. *Nat Rev Mol Cell Biol.* 23:541-558.
- Akhmanova, A., and M.O. Steinmetz. 2015. Control of microtubule organization and dynamics: two ends in the limelight. *Nat Rev Mol Cell Biol.* 16:711-726.
- Akhmanova, A., and M.O. Steinmetz. 2019. Microtubule minus-end regulation at a glance. *J Cell Sci.* 132.
- Akizu, N., J.L. Silhavy, R.O. Rosti, E. Scott, A.G. Fenstermaker, J. Schroth, M.S. Zaki, H. Sanchez, N. Gupta, M. Kabra, M. Kara, T. Ben-Omran, B. Rosti, A. Guemez-Gamboa, E. Spencer, R. Pan, N. Cai, M. Abdellateef, S. Gabriel, J. Halbritter, F. Hildebrandt, H. van Bokhoven, M. Gunel, and J.G. Gleeson. 2014. Mutations in CSPP1 lead to classical Joubert syndrome. *Am J Hum Genet.* 94:80-86.
- Al-Bassam, J., and F. Chang. 2011. Regulation of microtubule dynamics by TOG-domain proteins XMAP215/Dis1 and CLASP. *Trends Cell Biol.* 21:604-614.
- Al-Jassar, C., A. Andreeva, D.D. Barnabas, S.H. McLaughlin, C.M. Johnson, M. Yu, and M. van Breugel. 2017. The Ciliopathy-Associated Cep104 Protein Interacts with Tubulin and Nek1 Kinase. *Structure.* 25:146-156.
- Asiedu, M., D. Wu, F. Matsumura, and Q. Wei. 2009. Centrosome/spindle pole-associated protein regulates cytokinesis via promoting the recruitment of MyoGEF to the central spindle. *Mol Biol Cell.* 20:1428-1440.
- Aumeier, C., L. Schaedel, J. Gaillard, K. John, L. Blanchoin, and M. Thery. 2016. Self-repair promotes microtubule rescue. *Nat Cell Biol.* 18:1054-1064.
- Ayaz, P., X. Ye, P. Huddleston, C.A. Brautigam, and L.M. Rice. 2012. A TOG:alpha-tubulin complex structure reveals conformation-based mechanisms for a microtubule polymerase. *Science.* 337:857-860.
- Baas, P.W., A.N. Rao, A.J. Matamoros, and L. Leo. 2016. Stability properties of neuronal microtubules. *Cytoskeleton (Hoboken).* 73:442-460.
- Bechstedt, S., K. Lu, and G.J. Brouhard. 2014. Doublecortin Recognizes the Longitudinal Curvature of the Microtubule End and Lattice. *Curr Biol.* 24:2366-2375.
- Berbari, N.F., A.K. O'Connor, C.J. Haycraft, and B.K. Yoder. 2009. The primary cilium as a complex signaling center. *Curr Biol.* 19:R526-535.
- Besschetnova, T.Y., E. Kolpakova-Hart, Y. Guan, J. Zhou, B.R. Olsen, and J.V. Shah. 2010. Identification of Signaling Pathways Regulating Primary Cilium Length and Flow-Mediated Adaptation. *Curr Biol.* 20:182-187.
- Bieling, P., I.A. Telley, and T. Surrey. 2010. A minimal midzone protein module controls formation and length of antiparallel microtubule overlaps. *Cell.* 142:420-432.
- Bouchet, B.P., R.E. Gough, Y.C. Ammon, D. van de Willige, H. Post, G. Jacquemet, A.M. Altelaar, A.J. Heck, B.T. Goult, and A. Akhmanova. 2016a. Talin-KANK1 interaction controls the recruitment of cortical microtubule stabilizing complexes to focal adhesions. *eLife.* 5:e18124.
- Bouchet, B.P., I. Noordstra, M. van Amersfoort, E.A. Katrukha, Y.C. Ammon, N.D. Ter Hoeve, L. Hodgson, M. Dogterom, P.W. Derksen, and A. Akhmanova. 2016b. Mesenchymal Cell Invasion Requires Cooperative Regulation of Persistent Microtubule Growth by SLAIN2 and CLASP1. *Dev Cell.* 39:708-723.
- Breslow, D.K., and A.J. Holland. 2019. Mechanism and Regulation of Centriole and Cilium Biogenesis. *Annu Rev Biochem.* 88:691-724.
- Breslow, D.K., S. Hoogendoorn, A.R. Kopp, D.W. Morgens, B.K. Vu, M.C. Kennedy, K. Han, A. Li, G.T. Hess, M.C. Bassik, J.K. Chen, and M.V. Nachury. 2018. A CRISPR-based screen for Hedgehog signaling provides insights into ciliary function and ciliopathies. *Nat Genet.* 50:460-471.
- Brouhard, G.J., and L.M. Rice. 2014. The contribution of alpha-tubulin curvature to microtubule dynamics. *J Cell Biol.* 207:323-334.
- Brouhard, G.J., and L.M. Rice. 2018. Microtubule dynamics: an interplay of biochemistry and mechanics. *Nat Rev Mol Cell Biol.* 19:451-463.
- Byron, A., J.A. Askari, J.D. Humphries, G. Jacquemet, E.J. Koper, S. Warwood, C.K.

- Choi, M.J. Stroud, C.S. Chen, D. Knight, and M.J. Humphries. 2015. A proteomic approach reveals integrin activation state-dependent control of microtubule cortical targeting. *Nat Commun.* 6:6135.
- Chaaban, S., and G.J. Brouhard. 2017. A microtubule bestiary: structural diversity in tubulin polymers. *Mol Biol Cell.* 28:2924-2931.
- Chen, J., E. Kholina, A. Szyk, V.A. Fedorov, I. Kovalenko, N. Gudimchuk, and A. Roll-Mecak. 2021. α -tubulin tail modifications regulate microtubule stability through selective effector recruitment, not changes in intrinsic polymer dynamics. *Dev Cell.* 56:2016-2028.e2014.
- Chu, C.W., F. Hou, J. Zhang, L. Phu, A.V. Loktev, D.S. Kirkpatrick, P.K. Jackson, Y. Zhao, and H. Zou. 2011. A novel acetylation of β -tubulin by San modulates microtubule polymerization via down-regulating tubulin incorporation. *Mol Biol Cell.* 22:448-456.
- Conkar, D., H. Bayraktar, and E.N. Firat-Karalar. 2019. Centrosomal and ciliary targeting of CCDC66 requires cooperative action of centriolar satellites, microtubules and molecular motors. *Sci Rep.* 9:14250.
- Conkar, D., E. Culfa, E. Odabasi, N. Rauniyar, J.R. Yates, and E.N. Firat-Karalar. 2017. The centriolar satellite protein CCDC66 interacts with CEP290 and functions in cilium formation and trafficking. *J Cell Sci.* 130:1450-1462.
- Conkar, D., and E.N. Firat-Karalar. 2021. Microtubule-associated proteins and emerging links to primary cilium structure, assembly, maintenance, and disassembly. *FEBS J.* 288:786-798.
- Conkar, D., E. Odabasi, J. Deretic, U. Batman, K.M. Frikstad, S. Patzke, and E.N. Firat-Karalar. 2022. CCDC66 regulates primary cilium length and signaling competence via multi-site interactions with transition zone and axonemal proteins. *bioRxiv* 2022.04.10.487777
- Coombes, C.E., A. Yamamoto, M.R. Kenzie, D.J. Odde, and M.K. Gardner. 2013. Evolving tip structures can explain age-dependent microtubule catastrophe. *Curr Biol.* 23:1342-1348.
- Cuveillier, C., J. Delaroche, M. Seggio, S. Gory-Faure, C. Bosc, E. Denarier, M. Bacia, G. Schoehn, H. Mohrbach, I. Kulic, A. Andrieux, I. Arnal, and C. Delphin. 2020. MAP6 is an intraluminal protein that induces neuronal microtubules to coil. *Sci Adv.* 6:eaz4344.
- Das, A., D.J. Dickinson, C.C. Wood, B. Goldstein, and K.C. Slep. 2015. Crescerin uses a TOG domain array to regulate microtubules in the primary cilium. *Mol Biol Cell.* 26:4248-4264.
- de Forges, H., A. Pilon, I. Cantaloube, A. Pallandre, A.M. Haghiri-Gosnet, F. Perez, and C. Pous. 2016. Localized Mechanical Stress Promotes Microtubule Rescue. *Curr Biol.* 26:3399-3406.
- Dekomien, G., C. Vollrath, E. Petrasch-Parwez, M.H. Boevé, D.A. Akkad, W.M. Gerding, and J.T. Epplen. 2010. Progressive retinal atrophy in Schapendoes dogs: mutation of the newly identified CCDC66 gene. *Neurogenetics.* 11:163-174.
- Delgehyr, N., J. Sillibourne, and M. Bornens. 2005. Microtubule nucleation and anchoring at the centrosome are independent processes linked by ninein function. *J Cell Sci.* 118:1565-1575.
- Delphin, C., D. Bouvier, M. Seggio, E. Couriol, Y. Saoudi, E. Denarier, C. Bosc, O. Valiron, M. Bisbal, I. Arnal, and A. Andrieux. 2012. MAP6-F is a temperature sensor that directly binds to and protects microtubules from cold-induced depolymerization. *J Biol Chem.* 287:35127-35138.
- Desai, A., and T.J. Mitchison. 1997. Microtubule polymerization dynamics. *Annu Rev Cell Dev Biol.* 13:83-117.
- Dimitrov, A., M. Quesnoit, S. Moutel, I. Cantaloube, C. Pous, and F. Perez. 2008. Detection of GTP-tubulin conformation in vivo reveals a role for GTP remnants in microtubule rescues. *Science.* 322:1353-1356.
- Drechsel, D.N., A.A. Hyman, M.H. Cobb, and M.W. Kirschner. 1992. Modulation of the dynamic instability of tubulin assembly by the microtubule-associated protein tau. *Mol Biol Cell.* 3:1141-1154.
- Emes, R.D., and C.P. Ponting. 2001. A new sequence motif linking lissencephaly, Treacher Collins and oral-facial-digital type 1 syndromes, microtubule dynamics and cell migration. *Hum Mol Genet.* 10:2813-2820.
- Eshun-Wilson, L., R. Zhang, D. Portran, M.V. Nachury, D.B. Toso, T. Lohr, M. Vendruscolo, M. Bonomi, J.S. Fraser, and E. Nogales. 2019. Effects of α -tubulin acetylation on microtubule structure and stability. *Proc Natl Acad Sci U S A.* 116:10366-10371.
- Ezratty, E.J., M.A. Partridge, and G.G. Gundersen. 2005. Microtubule-induced focal adhesion disassembly is mediated by dynamin and focal adhesion kinase. *Nat Cell Biol.* 7:581-590.
- Fan, Y., G.M. Burkart, and R. Dixit. 2018. The Arabidopsis SPIRAL2 Protein Targets and Stabilizes Microtubule Minus Ends. *Curr Biol.* 28:987-994.e983.
- Fréal, A., D. Rai, R.P. Tas, X. Pan, E.A. Katrukha, D. van de Willige, R. Stucchi, A. Aher, C. Yang, A.F.M. Altelaar, K. Vocking, J.A. Post, M. Harterink, L.C. Kaptein, A. Akhmanova, and C.C. Hoogenraad. 2019. Feedback-Driven Assembly of the Axon Initial Segment. *Neuron.* 104:305-321.e308.
- Frikstad, K.M., E. Molinari, M. Thoresen, S.A. Ramsbottom, F. Hughes, S.J.F. Letteboer, S. Gilani, K.O. Schink, T. Stokke, S. Geimer, L.B. Pedersen, R.I.H. Giles, A. Akhmanova, R. Roepman, J.A. Sayer, and S. Patzke. 2019. A CEP104-CSPP1 Complex Is Required for Formation of Primary Cilia Competent in Hedgehog Signaling. *Cell Rep.* 28:1907-1922.e1906.

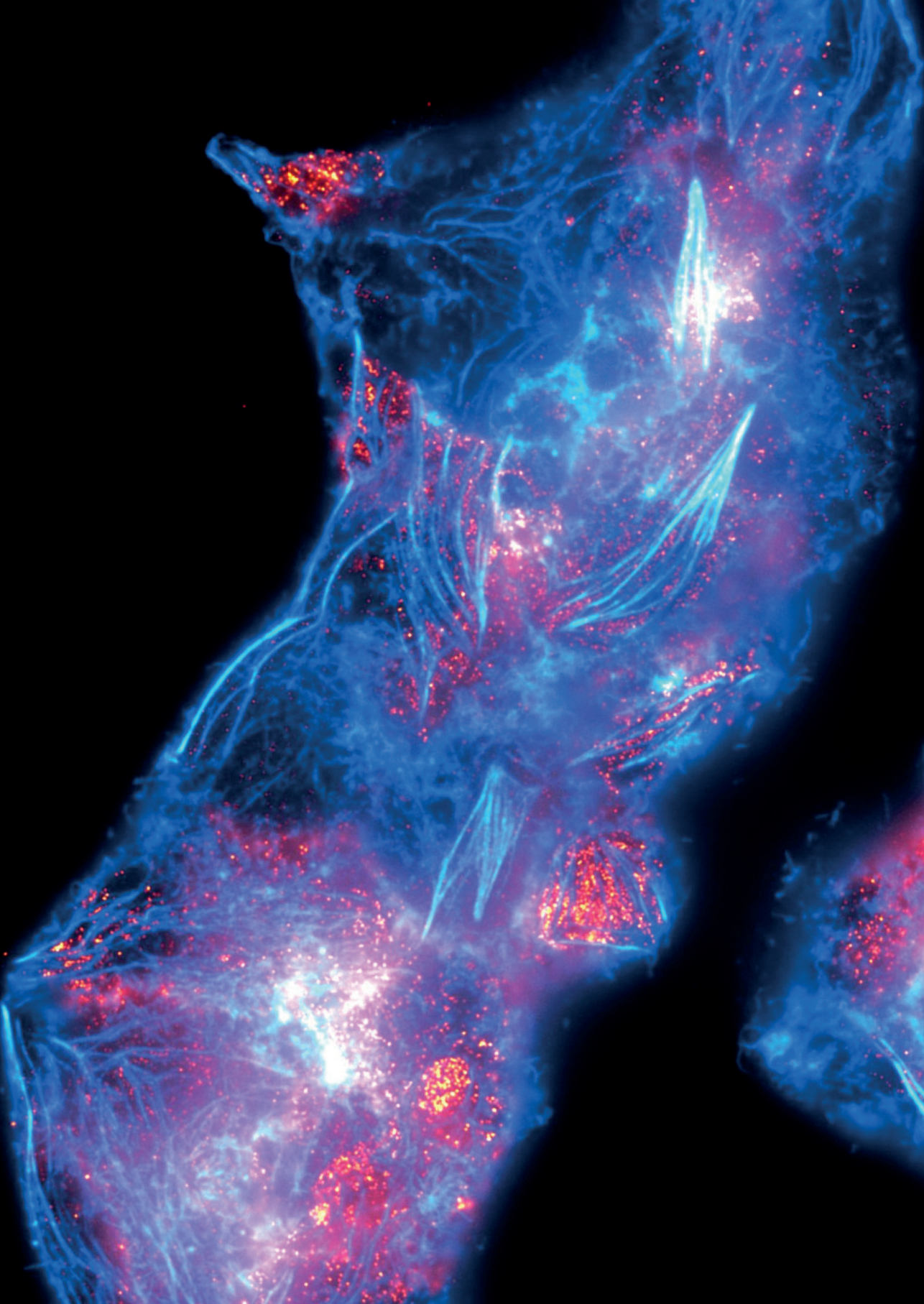
- Gallaud, E., R. Caous, A. Pascal, F. Bazile, J.P. Gagné, S. Huet, G.G. Poirier, D. Chrétien, L. Richard-Parpaillon, and R. Giet. 2014. Enscn5/Map7 promotes microtubule growth and centrosome separation in *Drosophila* neural stem cells. *J Cell Biol.* 204:1111-1121.
- Gamblin, T.C., K. Nachmanoff, S. Halpain, and R.C. Williams, Jr. 1996. Recombinant microtubule-associated protein 2c reduces the dynamic instability of individual microtubules. *Biochemistry.* 35:12576-12586.
- Gerding, W.M., S. Schreiber, T. Schulte-Middelmann, A. de Castro Marques, J. Atorf, D.A. Akkad, G. Dekomien, J. Kremers, R. Dermietzel, A. Gal, T. Rüllicke, S. Ibrahim, J.T. Epplen, and E. Petrasch-Parwez. 2011. *Ccdc66* null mutation causes retinal degeneration and dysfunction. *Hum Mol Genet.* 20:3620-3631.
- Grigoriev, I., D. Splinter, N. Keijzer, P.S. Wulf, J. Demmers, T. Ohtsuka, M. Modesti, I.V. Maly, F. Grosveld, C.C. Hoogenraad, and A. Akhmanova. 2007. Rab6 regulates transport and targeting of exocytotic carriers. *Dev Cell.* 13:305-314.
- Grigoriev, I., K.L. Yu, E. Martinez-Sanchez, A. Serra-Marques, I. Smal, E. Meijering, J. Demmers, J. Peranen, R.J. Pasterkamp, P. van der Sluijs, C.C. Hoogenraad, and A. Akhmanova. 2011. Rab6, Rab8, and MICAL3 Cooperate in Controlling Docking and Fusion of Exocytotic Carriers. *Curr Biol.* 21:967-974.
- Gui, M., H. Farley, P. Anujan, J.R. Anderson, D.W. Maxwell, J.B. Whitchurch, J.J. Botsch, T. Qiu, S. Meleppattu, S.K. Singh, Q. Zhang, J. Thompson, J.S. Lucas, C.D. Bingle, D.P. Norris, S. Roy, and A. Brown. 2021. De novo identification of mammalian ciliary motility proteins using cryo-EM. *Cell.* 184:5791-5806.
- Gundelfinger, E.D., and A. Fejtova. 2012. Molecular organization and plasticity of the cytomatrix at the active zone. *Curr Opin Neurobiol.* 22:423-430.
- Gupta, G.D., E. Coyaud, J. Gonçalves, B.A. Mojarad, Y. Liu, Q. Wu, L. Gheiratmand, D. Comartin, J.M. Tkach, S.W. Cheung, M. Bashkurov, M. Hasegan, J.D. Knight, Z.Y. Lin, M. Schueler, F. Hildebrandt, J. Moffat, A.C. Gingras, B. Raught, and L. Pelletier. 2015. A Dynamic Protein Interaction Landscape of the Human Centrosome-Cilium Interface. *Cell.* 163:1484-1499.
- Halpain, S., and L. Dehmelt. 2006. The MAP1 family of microtubule-associated proteins. *Genome Biol.* 7:224.
- Hendershott, M.C., and R.D. Vale. 2014. Regulation of microtubule minus-end dynamics by CAMSAPs and Patronin. *Proc Natl Acad Sci U S A.* 111:5860-5865.
- Hildebrandt, F., T. Benzing, and N. Katsanis. 2011. Ciliopathies. *N Engl J Med.* 364:1533-1543.
- Holmfeldt, P., G. Brattsand, and M. Gullberg. 2002. MAP4 counteracts microtubule catastrophe promotion but not tubulin-sequestering activity in intact cells. *Curr Biol.* 12:1034-1039.
- Hooikaas, P.J., M. Martin, T. Muhlethaler, G.J. Kuijntjes, C.A.E. Peeters, E.A. Katrukha, L. Ferrari, R. Stucchi, D.G.F. Verhagen, W.E. van Riel, I. Grigoriev, A.F.M. Altelaar, C.C. Hoogenraad, S.G.D. Rudiger, M.O. Steinmetz, L.C. Kapitein, and A. Akhmanova. 2019. MAP7 family proteins regulate kinesin-1 recruitment and activation. *J Cell Biol.* 218:1298-1318.
- Hori, A., C. Ikebe, M. Tada, and T. Toda. 2014. Msd1/SSX2IP-dependent microtubule anchorage ensures spindle orientation and primary cilia formation. *EMBO Rep.* 15:175-184.
- Hotta, A., T. Kawakatsu, T. Nakatani, T. Sato, C. Matsui, T. Sukezane, T. Akagi, T. Hamaji, I. Grigoriev, A. Akhmanova, Y. Takai, and Y. Mimori-Kiyosue. 2010. Laminin-based cell adhesion anchors microtubule plus ends to the epithelial cell basal cortex through LL5alpha/beta. *J Cell Biol.* 189:901-917.
- Iimori, M., K. Ozaki, Y. Chikashige, T. Habu, Y. Hiraoka, T. Maki, I. Hayashi, C. Obuse, and T. Matsumoto. 2012. A mutation of the fission yeast EB1 overcomes negative regulation by phosphorylation and stabilizes microtubules. *Exp Cell Res.* 318:262-275.
- Jakobsen, L., K. Vanselow, M. Skogs, Y. Toyoda, E. Lundberg, I. Poser, L.G. Falkenby, M. Bennetzen, J. Westendorf, E.A. Nigg, M. Uhlen, A.A. Hyman, and J.S. Andersen. 2011. Novel asymmetrically localizing components of human centrosomes identified by complementary proteomics methods. *Embo J.* 30:1520-1535.
- Janke, C., and M.M. Magiera. 2020. The tubulin code and its role in controlling microtubule properties and functions. *Nat Rev Mol Cell Biol.* 21:307-326.
- Jiang, K., S. Hua, R. Mohan, I. Grigoriev, K.W. Yau, Q. Liu, E.A. Katrukha, A.F. Altelaar, A.J. Heck, C.C. Hoogenraad, and A. Akhmanova. 2014. Microtubule minus-end stabilization by polymerization-driven CAMSAP deposition. *Dev Cell.* 28:295-309.
- Jiang, K., G. Toedt, S. Montenegro Gouveia, N.E. Davey, S. Hua, B. van der Vaart, I. Grigoriev, J. Larsen, L.B. Pedersen, K. Bezstarosti, M. Lince-Faria, J. Demmers, M.O. Steinmetz, T.J. Gibson, and A. Akhmanova. 2012. A Proteome-wide screen for mammalian SxIP motif-containing microtubule plus-end tracking proteins. *Curr Biol.* 22:1800-1807.
- Kearns, S., F.M. Mason, W.K. Rathmell, I.Y. Park, C. Walker, K.J. Verhey, and M.A. Cianfrocco. 2021. Molecular determinants for α -tubulin methylation by SETD2. *J Biol Chem.* 297:100898.
- Keeling, J., L. Tsiokas, and D. Maskey. 2016. Cellular Mechanisms of Ciliary Length Control. *Cells.* 5:6.
- Kiesel, P., G. Alvarez Viar, N. Tsoy, R. Maraschini, P. Gorilak, V. Varga, A. Honigsmann, and G. Pigino. 2020. The molecular structure of mammalian primary cilia revealed by cryo-

- electron tomography. *Nat Struct Mol Biol.* 27:1115-1124.
- Klena, N., and G. Pigino. 2022. Structural Biology of Cilia and Intraflagellar Transport. *Annu Rev Cell Dev Biol.*
- Ko, J., M. Na, S. Kim, J.R. Lee, and E. Kim. 2003. Interaction of the ERC family of RIM-binding proteins with the liprin-alpha family of multidomain proteins. *J Biol Chem.* 278:42377-42385.
- Komarova, Y., C.O. De Groot, I. Grigoriev, S.M. Gouveia, E.L. Munteanu, J.M. Schober, S. Honnappa, R.M. Buey, C.C. Hoogenraad, M. Dogterom, G.G. Borisy, M.O. Steinmetz, and A. Akhmanova. 2009. Mammalian end binding proteins control persistent microtubule growth. *J Cell Biol.* 184:691-706.
- Kunishima, S., R. Kobayashi, T.J. Itoh, M. Hamaguchi, and H. Saito. 2009. Mutation of the beta1-tubulin gene associated with congenital macrothrombocytopenia affecting microtubule assembly. *Blood.* 113:458-461.
- Landskron, L., J. Bak, A. Adamopoulos, K. Kaplani, M. Moraiti, L.G. van den Hengel, J.Y. Song, O.B. Bleijerveld, J. Nieuwenhuis, T. Heidebrecht, L. Henneman, M.J. Moutin, M. Barisic, S. Taraviras, A. Perrakis, and T.R. Brummelkamp. 2022. Posttranslational modification of microtubules by the MATCAP detyrosinase. *Science.* 376:eabn6020.
- Lansbergen, G., I. Grigoriev, Y. Mimori-Kiyosue, T. Ohtsuka, S. Higa, I. Kitajima, J. Demmers, N. Galjart, A.B. Houtsmuller, F. Grosveld, and A. Akhmanova. 2006. CLASPs attach microtubule plus ends to the cell cortex through a complex with LL5beta. *Dev Cell.* 11:21-32.
- Latour, B.L., J.C. Van De Weghe, T.D.S. Rusterholz, S.J.F. Letteboer, A. Gomez, R. Shaheen, M. Gesemann, A. Karamzade, M. Asadollahi, M. Barroso-Gil, M. Chitre, M.E. Grout, J. van Reeuwijk, S.E.C. van Beersum, C.V. Miller, J.C. Dempsey, H. Morsy, M.J. Bamshad, D.A. Nickerson, S.C.F. Neuhaus, K. Boldt, M. Ueffing, M. Keramatipour, J.A. Sayer, E.S. Alkuraya, R. Bachmann-Gagescu, R. Roepman, and D. Doherty. 2020. Dysfunction of the ciliary ARMC9/TOGARAM1 protein module causes Joubert syndrome. *J Clin Invest.* 130:4423-4439.
- Leong, S.Y., M. Yamada, N. Yanagisawa, and G. Goshima. 2018. SPIRAL2 Stabilises Endoplasmic Microtubule Minus Ends in the Moss *Physcomitrella patens*. *Cell Struct Funct.* 43:53-60.
- Lin, C.C., T.S. Cheng, C.M. Hsu, C.H. Wu, L.S. Chang, Z.S. Shen, H.M. Yeh, L.K. Chang, S.L. Howng, and Y.R. Hong. 2006. Characterization and functional aspects of human ninein isoforms that regulated by centrosomal targeting signals and evidence for docking sites to direct gamma-tubulin. *Cell Cycle.* 5:2517-2527.
- Louka, P., K.K. Vasudevan, M. Guha, E. Joachimiak, D. Wloga, R.F.-X. Tomasi, C.N. Baroud, P. Dupuis-Williams, D.F. Galati, C.G. Pearson, L.M. Rice, J.J. Moresco, J.R. Yates 3rd, Y. Jiang, K. Lechtreck, W. Dentler, and J. Gaertig. 2018. Proteins that control the geometry of microtubules at the ends of cilia. *J Cell Biol.* 217:4298-4313.
- Ma, M., M. Stoyanova, G. Rademacher, S.K. Dutcher, A. Brown, and R. Zhang. 2019. Structure of the Decorated Ciliary Doublet Microtubule. *Cell.* 179:909-922.
- Mandelkow, E.M., E. Mandelkow, and R.A. Milligan. 1991. Microtubule dynamics and microtubule caps: a time-resolved cryo-electron microscopy study. *J Cell Biol.* 114:977-991.
- Marshall, W.F., H. Qin, M. Rodrigo Brenni, and J.L. Rosenbaum. 2005. Flagellar length control system: testing a simple model based on intraflagellar transport and turnover. *Mol Biol Cell.* 16:270-278.
- Marshall, W.F., and J.L. Rosenbaum. 2001. Intraflagellar transport balances continuous turnover of outer doublet microtubules: implications for flagellar length control. *J Cell Biol.* 155:405-414.
- Mateja, A., T. Cierpicki, M. Paduch, Z.S. Derewenda, and J. Otlewski. 2006. The Dimerization Mechanism of LIS1 and its Implication for Proteins Containing the LisH Motif. *J Mol Biol.* 357:621-631.
- Maurer, S.P., P. Bieling, J. Cope, A. Hoenger, and T. Surrey. 2011. GTPgammaS microtubules mimic the growing microtubule end structure recognised by end-binding proteins (EBs). *Proc Natl Acad Sci U S A.* 109:3988-3993.
- Mazo, G., N. Soplop, W.-J. Wang, K. Uryu, and M.-F.B. Tsou. 2016. Spatial Control of Primary Ciliogenesis by Subdistal Appendages Alters Sensation-Associated Properties of Cilia. *Dev Cell.* 39:424-437.
- McNally, K.P., D. Buster, and F.J. McNally. 2002. Katanin-mediated microtubule severing can be regulated by multiple mechanisms. *Cell Motil Cytoskeleton.* 53:337-349.
- Meunier, S., M. Shvedunova, N. Van Nguyen, L. Avila, I. Vernos, and A. Akhtar. 2015. An epigenetic regulator emerges as microtubule minus-end binding and stabilizing factor in mitosis. *Nat Commun.* 6:7889.
- Mimori-Kiyosue, Y., I. Grigoriev, G. Lansbergen, H. Sasaki, C. Matsui, F. Severin, N. Galjart, F. Grosveld, I. Vorobjev, S. Tsukita, and A. Akhmanova. 2005. CLASP1 and CLASP2 bind to EB1 and regulate microtubule plus-end dynamics at the cell cortex. *J Cell Biol.* 168:141-153.
- Mogessie, B., D. Roth, Z. Rahil, and A. Straube. 2015. A novel isoform of MAP4 organises the paraxial microtubule array required for muscle cell differentiation. *eLife.* 4:e05697.
- Molla-Herman, A., R. Ghossoub, T. Blisnick, A. Meunier, C. Serres, F. Silbermann, C. Emmerson, K. Romeo, P. Bourdoncle, A. Schmitt, S. Saunier, N. Spassky, P. Bastin, and A. Benmerah. 2010. The ciliary pocket: an

- endocytic membrane domain at the base of primary and motile cilia. *J Cell Sci.* 123:1785-1795.
- Monroy, B.Y., D.L. Sawyer, B.E. Ackermann, M.M. Borden, T.C. Tan, and K.M. Ori-McKenney. 2018. Competition between microtubule-associated proteins directs motor transport. *Nat Commun.* 9:1487.
- Moores, C.A., M. Perderiset, F. Francis, J. Chelly, A. Houdusse, and R.A. Milligan. 2004. Mechanism of microtubule stabilization by doublecortin. *Mol Cell.* 14:833-839.
- Nakamura, M., J.J. Lindeboom, M. Saltini, B.M. Mulder, and D.W. Ehrhardt. 2018. SPR2 protects minus ends to promote severing and reorientation of plant cortical microtubule arrays. *J Cell Biol.* 217:915-927.
- Nguyen, H.L., S. Chari, D. Gruber, C.M. Lue, S.J. Chapin, and J.C. Bulinski. 1997. Overexpression of full- or partial-length MAP4 stabilizes microtubules and alters cell growth. *J Cell Sci.* 110:281-294.
- Nguyen, H.L., D. Gruber, T. McGraw, M.P. Sheetz, and J.C. Bulinski. 1998. Stabilization and functional modulation of microtubules by microtubule-associated protein 4. *Biol Bull.* 194:354-357.
- Nieuwenhuis, J., A. Adamopoulos, O.B. Bleijerveld, A. Mazouzi, E. Stickel, P. Celie, M. Altelaar, P. Knipscheer, A. Perrakis, V.A. Blomen, and T.R. Brummelkamp. 2017. Vasohibins encode tubulin detyrosinating activity. *Science.* 358:1453-1456.
- Noiges, R., R. Eichinger, W. Kutschera, I. Fischer, Z. Nemeth, G. Wiche, and F. Propst. 2002. Microtubule-associated protein 1A (MAP1A) and MAP1B: light chains determine distinct functional properties. *J Neurosci.* 22:2106-2114.
- Noordstra, I., and A. Akhmanova. 2017. Linking cortical microtubule attachment and exocytosis. *F1000Res.* 6:469.
- Odde, D.J., L. Cassimeris, and H.M. Buettner. 1995. Kinetics of microtubule catastrophe assessed by probabilistic analysis. *Biophys J.* 69:796-802.
- Palmer, K.J., L. MacCarthy-Morrogh, N. Smyllie, and D.J. Stephens. 2011. A role for Tctex-1 (DYNLT1) in controlling primary cilium length. *Eur J Cell Biol.* 90:865-871.
- Pamula, M.C., S.C. Ti, and T.M. Kapoor. 2016. The structured core of human β tubulin confers isotype-specific polymerization properties. *J Cell Biol.* 213:425-433.
- Paranavitane, V., W.J. Coadwell, A. Eguinoa, P.T. Hawkins, and L. Stephens. 2003. LL5beta is a phosphatidylinositol (3,4,5)-trisphosphate sensor that can bind the cytoskeletal adaptor, gamma-filamin. *J Biol Chem.* 278:1328-1335.
- Patzke, S., H. Hauge, M. Sioud, E.F. Finne, E.A. Sivertsen, J. Delabie, T. Stokke, and H.C. Aasheim. 2005. Identification of a novel centrosome/microtubule-associated coiled-coil protein involved in cell-cycle progression and spindle organization. *Oncogene.* 24:1159-1173.
- Patzke, S., S. Redick, A. Warsame, C.A. Murga-Zamalloa, H. Khanna, S. Doxsey, and T. Stokke. 2010. CSPP is a ciliary protein interacting with Nephrocystin 8 and required for cilia formation. *Mol Biol Cell.* 21:2555-2567.
- Patzke, S., T. Stokke, and H.C. Aasheim. 2006. CSPP and CSPP-L associate with centrosomes and microtubules and differently affect microtubule organization. *J Cell Physiol.* 209:199-210.
- Peris, L., M. Wagenbach, L. Lafanechère, J. Brocard, A.T. Moore, F. Kozielski, D. Job, L. Wordeman, and A. Andrieux. 2009. Motor-dependent microtubule disassembly driven by tubulin tyrosination. *J Cell Biol.* 185:1159-1166.
- Perlaza, K., M. Mirvis, H. Ishikawa, and W. Marshall. 2022. The short flagella 1 (SHF1) gene in *Chlamydomonas* encodes a Crescerin TOG-domain protein required for late stages of flagellar growth. *Mol Biol Cell.* 33:ar12.
- Portran, D., L. Schaedel, Z. Xu, M. Théry, and M.V. Nachury. 2017. Tubulin acetylation protects long-lived microtubules against mechanical ageing. *Nat Cell Biol.* 19:391-398.
- Prota, A.E., M.M. Magiera, M. Kuijpers, K. Bargsten, D. Frey, M. Wieser, R. Jaussi, C.C. Hoogenraad, R.A. Kammerer, C. Janke, and M.O. Steinmetz. 2013. Structural basis of tubulin tyrosination by tubulin tyrosine ligase. *J Cell Biol.* 200:259-270.
- Rai, A., T. Liu, S. Glauser, E.A. Katrukha, J. Estevez-Gallego, R. Rodriguez-Garcia, W.S. Fang, J.F. Diaz, M.O. Steinmetz, K.H. Altmann, L.C. Kapitein, C.A. Moores, and A. Akhmanova. 2020. Taxanes convert regions of perturbed microtubule growth into rescue sites. *Nat Mater.* 19:355-365.
- Ramkumar, A., B.Y. Jong, and K.M. Ori-McKenney. 2018. ReMAPping the microtubule landscape: How phosphorylation dictates the activities of microtubule-associated proteins. *Dev Dyn.* 247:138-155.
- Ren, X.D., W.B. Kiosses, and M.A. Schwartz. 1999. Regulation of the small GTP-binding protein Rho by cell adhesion and the cytoskeleton. *Embo J.* 18:578-585.
- Rezabkova, L., S.H. Kraatz, A. Akhmanova, M.O. Steinmetz, and R.A. Kammerer. 2016. Biophysical and Structural Characterization of the Centriolar Protein Cep104 Interaction Network. *J Biol Chem.* 291:18496-18504.
- Roostalu, J., N.I. Cade, and T. Surrey. 2015. Complementary activities of TPX2 and chTOG constitute an efficient importin-regulated microtubule nucleation module. *Nat Cell Biol.* 17:1422-1434.
- Sackett, D.L., B. Bhattacharyya, and J. Wolff. 1985. Tubulin subunit carboxyl termini determine polymerization efficiency. *J Biol Chem.* 260:43-45.
- Satish Tammana, T.V., D. Tammana, D.R. Diener, and J.L. Rosenbaum. 2013. Centrosomal

- protein CEP104 (Chlamydomonas FAP256) moves to the ciliary tip during ciliary assembly. *J Cell Sci.* 126:5018-5029.
- Schaedel, L., K. John, J. Gaillard, M.V. Nachury, L. Blanchoin, and M. Thery. 2015. Microtubules self-repair in response to mechanical stress. *Nat Mater.* 14:1156-1163.
- Schaedel, L., S. Triclin, D. Chrétien, A. Abrieu, C. Aumeier, J. Gaillard, L. Blanchoin, M. Thery, and K. John. 2019. Lattice defects induce microtubule self-renewal *Nat Physics.* 15:830-838.
- Schweizer, N., and J. Lüders. 2021. From tip to toe - dressing centrioles in γ TuRC. *J Cell Sci.* 134.
- Schwer, H.D., P. Lecine, S. Tiwari, J.E. Italiano, Jr., J.H. Hartwig, and R.A. Shivdasani. 2001. A lineage-restricted and divergent beta-tubulin isoform is essential for the biogenesis, structure and function of blood platelets. *Curr Biol.* 11:579-586.
- Shaheen, R., H.E. Shamseldin, C.M. Loucks, M.Z. Seidahmed, S. Ansari, M. Ibrahim Khalil, N. Al-Yacoub, E.E. Davis, N.A. Mola, K. Szymanska, W. Herridge, A.E. Chudley, B.N. Chodirker, J. Schwartzentruber, J. Majewski, N. Katsanis, C. Poizat, C.A. Johnson, J. Parboosingh, K.M. Boycott, A.M. Innes, and F.S. Alkuraya. 2014. Mutations in CSPP1, encoding a core centrosomal protein, cause a range of ciliopathy phenotypes in humans. *Am J Hum Genet.* 94:73-79.
- Sharma, A., A. Aher, N.J. Dynes, D. Frey, E.A. Katrukha, R. Jaussi, I. Grigoriev, M. Croisier, R.A. Kammerer, A. Akhmanova, P. Gonczy, and M.O. Steinmetz. 2016. Centriolar CPAP/SAS-4 Imparts Slow Processive Microtubule Growth. *Dev Cell.* 37:362-376.
- Sharma, N., Z.A. Kosan, J.E. Stallworth, N.F. Berbari, and B.K. Yoder. 2011. Soluble levels of cytosolic tubulin regulate ciliary length control. *Mol Biol Cell.* 22:806-816.
- Sharp, J.A., J.J. Plant, T.K. Ohsumi, M. Borowsky, and M.D. Blower. 2011. Functional analysis of the microtubule-interacting transcriptome. *Mol Biol Cell.* 22:4312-4323.
- Shida, T., J.G. Cueva, Z. Xu, M.B. Goodman, and M.V. Nachury. 2010. The major alpha-tubulin K40 acetyltransferase alphaTAT1 promotes rapid ciliogenesis and efficient mechanosensation. *Proc Natl Acad Sci U S A.* 107:21517-21522.
- Song, L., and W.L. Dentler. 2001. Flagellar Protein Dynamics in Chlamydomonas. *J Biol Chem.* 276:29754-29763.
- Song, Y., L.L. Kirkpatrick, A.B. Schilling, D.L. Helseth, N. Chabot, J.W. Keillor, G.V. Johnson, and S.T. Brady. 2013. Transglutaminase and polyamination of tubulin: posttranslational modification for stabilizing axonal microtubules. *Neuron.* 78:109-123.
- Sorokin, S.P. 1962. Centrioles and the formation of rudimentary cilia by fibroblasts and smooth muscle cells. *J Cell Biol.* 15:363-377.
- Sorokin, S.P. 1968. Reconstructions of Centriole Formation and Ciliogenesis in Mammalian Lungs. *J Cell Sci.* 3:207-230.
- Spangler, S.A., and C.C. Hoogenraad. 2007. Liprin-alpha proteins: scaffold molecules for synapse maturation. *Biochem Soc Trans.* 35:1278-1282.
- Spektor, A., W.Y. Tsang, D. Khoo, and B.D. Dynlacht. 2007. Cep97 and CP110 suppress a cilia assembly program. *Cell.* 130:678-690.
- Srour, M., F.F. Hamdan, D. McKnight, E. Davis, H. Mandel, J. Schwartzentruber, B. Martin, L. Patry, C. Nassif, A. Dionne-Laporte, L.H. Ospina, E. Lemyre, C. Massicotte, R. Laframboise, B. Maranda, D. Labuda, J.C. Décarie, F. Rypens, D. Goldsher, C. Fallet-Bianco, J.F. Soucy, A.M. Labege, C. Maftei, K. Boycott, B. Brais, R.M. Boucher, G.A. Rouleau, N. Katsanis, J. Majewski, O. Elpeleg, M.K. Kukulich, S. Shalev, and J.L. Michaud. 2015. Joubert Syndrome in French Canadians and Identification of Mutations in CEP104. *Am J Hum Genet.* 97:744-753.
- Stehbens, S., and T. Wittmann. 2012. Targeting and transport: How microtubules control focal adhesion dynamics. *J Cell Biol.* 198:481-489.
- Stehbens, S.J., M. Paszek, H. Pemble, A. Ettinger, S. Gierke, and T. Wittmann. 2014. CLASPs link focal-adhesion-associated microtubule capture to localized exocytosis and adhesion site turnover. *Nat Cell Biol.* 16:561-573.
- Stephens, R.E. 1997. Synthesis and turnover of embryonic sea urchin ciliary proteins during selective inhibition of tubulin synthesis and assembly. *Mol Biol Cell.* 8:2187-2198.
- Subramanian, R., S.C. Ti, L. Tan, S.A. Darst, and T.M. Kapoor. 2013. Marking and measuring single microtubules by PRC1 and kinesin-4. *Cell.* 154:377-390.
- Sudhof, T.C. 2012. The presynaptic active zone. *Neuron.* 75:11-25.
- Sun, S., R.L. Fisher, S.S. Bowser, B.T. Pentecost, and H. Sui. 2019. Three-dimensional architecture of epithelial primary cilia. *Proc Natl Acad Sci U S A.* 116:9370-9379.
- Sun, Z., H.-Y. Tseng, S. Tan, F. Senger, L. Kurzawa, D. Dedden, N. Mizuno, A.A. Wasik, M. Thery, A.R. Dunn, and R. Fässler. 2016. Kank2 activates talin, reduces force transduction across integrins and induces central adhesion formation. *Nat Cell Biol.* 18:941-953.
- Sung, H.H., I.A. Telley, P. Papadaki, A. Ephrussi, T. Surrey, and P. Rørth. 2008. Drosophila ensconsin promotes productive recruitment of Kinesin-1 to microtubules. *Dev Cell.* 15:866-876.
- Szyk, A., A.M. Deaconescu, G. Piszczek, and A. Roll-Mecak. 2011. Tubulin tyrosine ligase structure reveals adaptation of an ancient fold to bind and modify tubulin. *Nat Struct Mol Biol.* 18:1250-1258.
- Tegha-Dunghu, J., E. Bausch, B. Neumann, A. Wuensche, T. Walter, J. Ellenberg, and O.J. Gruss. 2014. MAP1S controls microtubule stability throughout the cell cycle in human cells. *J Cell Sci.* 127:5007-5013.
- Ti, S.C., G.M. Alushin, and T.M. Kapoor. 2018.

- Human β -Tubulin Isoforms Can Regulate Microtubule Protofilament Number and Stability. *Dev Cell*. 47:175-190.e175.
- Tu, H.Q., X.H. Qin, Z.B. Liu, Z.Q. Song, H.B. Hu, Y.C. Zhang, Y. Chang, M. Wu, Y. Huang, Y.F. Bai, G. Wang, Q.Y. Han, A.L. Li, T. Zhou, F. Liu, X.M. Zhang, and H.Y. Li. 2018. Microtubule asters anchored by FSD1 control axoneme assembly and ciliogenesis. *Nat Commun*. 9:5277.
- Tuz, K., R. Bachmann-Gagescu, D.R. O'Day, K. Hua, C.R. Isabella, I.G. Phelps, A.E. Stolarski, B.J. O'Roak, J.C. Dempsey, C. Lourenco, A. Alswaid, C.G. Bonnemann, L. Medne, S. Nampoothiri, Z. Stark, R.J. Leventer, M. Topcu, A. Cansu, S. Jagadeesh, S. Done, G.E. Ishak, I.A. Glass, J. Shendure, S.C. Neuhaus, C.R. Haldeman-Englert, D. Doherty, and R.J. Ferland. 2014. Mutations in CSPP1 cause primary cilia abnormalities and Joubert syndrome with or without Jeune asphyxiating thoracic dystrophy. *Nat Cell Biol*. 94:62-72.
- Tweedie, S., B. Braschi, K. Gray, T.E.M. Jones, R.L. Seal, B. Yates, and E.A. Bruford. 2021. Genenames.org: the HGNC and VGNC resources in 2021. *Nucleic Acids Res*. 49:D939-d946.
- van Beuningen, S.F., L. Will, M. Harterink, A. Chazeau, E.Y. van Battum, C.P. Frias, M.A. Franker, E.A. Katrukha, R. Stucchi, K. Vocking, A.T. Antunes, L. Slenders, S. Doukeridou, P. Sillevius Smitt, A.F. Altelaar, J.A. Post, A. Akhmanova, R.J. Pasterkamp, L.C. Kapitein, E. de Graaff, and C.C. Hoogenraad. 2015. TRIM46 Controls Neuronal Polarity and Axon Specification by Driving the Formation of Parallel Microtubule Arrays. *Neuron*. 88:1208-1226.
- Van De Weghe, J.C., T.D.S. Rusterholz, B. Latour, M.E. Grout, K.A. Aldinger, R. Shaheen, J.C. Dempsey, S. Maddirevula, Y.-H.H. Cheng, I.G. Phelps, M. Gesemann, H. Goel, O.S. Birk, T. Alanzi, R. Rawashdeh, A.O. Khan, M.J. Bamshad, D.A. Nickerson, S.C.F. Neuhaus, W.B. Dobyns, F.S. Alkuraya, R. Roepman, R. Bachmann-Gagescu, and D. Doherty. 2017. Mutations in ARMC9, which Encodes a Basal Body Protein, Cause Joubert Syndrome in Humans and Ciliopathy Phenotypes in Zebrafish. *Nat Cell Biol*. 101:23-36.
- van der Vaart, B., W.E. van Riel, H. Doodhi, J.T. Kevenaar, E.A. Katrukha, L. Gumy, B.P. Bouchet, I. Grigoriev, S.A. Spangler, K.L. Yu, P.S. Wulf, J. Wu, G. Lansbergen, E.Y. van Battum, R.J. Pasterkamp, Y. Mimori-Kiyosue, J. Demmers, N. Olieric, I.V. Maly, C.C. Hoogenraad, and A. Akhmanova. 2013. CFEOM1-associated kinesin KIF21A is a cortical microtubule growth inhibitor. *Dev Cell*. 27:145-160.
- Vineethakumari, C., and J. Lüders. 2022. Microtubule Anchoring: Attaching Dynamic Polymers to Cellular Structures. *Front Cell Dev Biol*. 10:867870.
- Wang, J.T., and T. Stearns. 2017. The ABCs of Centriole Architecture: The Form and Function of Triplet Microtubules. *Cold Spring Harb Symp Quant Biol*. 82:145-155.
- Widlund, P.O., J.H. Stear, A. Pozniakovskiy, M. Zanic, S. Reber, G.J. Brouhard, A.A. Hyman, and J. Howard. 2011. XMAP215 polymerase activity is built by combining multiple tubulin-binding TOG domains and a basic lattice-binding region. *Proc Natl Acad Sci U S A*. 108:2741-2746.
- Wiese, C., and Y. Zheng. 2000. A new function for the gamma-tubulin ring complex as a microtubule minus-end cap. *Nat Cell Biol*. 2:358-364.
- Winograd-Katz, S.E., R. Fässler, B. Geiger, and K.R. Legate. 2014. The integrin adhesome: from genes and proteins to human disease. *Nat Rev Mol Cell Biol*. 15:273-288.
- Wu, J., C. de Heus, Q. Liu, B.P. Bouchet, I. Noordstra, K. Jiang, S. Hua, M. Martin, C. Yang, I. Grigoriev, E.A. Katrukha, A.F.M. Altelaar, C.C. Hoogenraad, R.Z. Qi, J. Klumperman, and A. Akhmanova. 2016. Molecular Pathway of Microtubule Organization at the Golgi Apparatus. *Dev Cell*. 39:44-60.
- Xia, P., Z. Wang, X. Liu, B. Wu, J. Wang, T. Ward, L. Zhang, X. Ding, G. Gibbons, Y. Shi, and X. Yao. 2012. EB1 acetylation by P300/CBP-associated factor (PCAF) ensures accurate kinetochore-microtubule interactions in mitosis. *Proc Natl Acad Sci U S A*. 109:16564-16569.
- Xiao, H., H. Wang, X. Zhang, Z. Tu, C. Bulinski, M. Khrapunovich-Baine, R. Hogue Angeletti, and S.B. Horwitz. 2012. Structural evidence for cooperative microtubule stabilization by Taxol and the endogenous dynamics regulator MAP4. *ACS Chem Biol*. 7:744-752.
- Yamazoe, T., T. Nagai, S. Umeda, Y. Sugaya, and K. Mizuno. 2020. Roles of TOG and jelly-roll domains of centrosomal protein CEP104 in its functions in cilium elongation and Hedgehog signaling. *J Biol Chem*. 295:14723-14736.
- Zanic, M., P.O. Widlund, A.A. Hyman, and J. Howard. 2013. Synergy between XMAP215 and EB1 increases microtubule growth rates to physiological levels. *Nat Cell Biol*. 15:688-693.
- Zhang, R., G.M. Alushin, A. Brown, and E. Nogales. 2015. Mechanistic Origin of Microtubule Dynamic Instability and Its Modulation by EB Proteins. *Cell*. 162:849-859.
- Zhang, R., J. Roostalu, T. Surrey, and E. Nogales. 2017. Structural insight into TPX2-stimulated microtubule assembly. *eLife*. 6.
- Zheng, X., A. Ramani, K. Soni, M. Gottardo, S. Zheng, L. Ming Gooi, W. Li, S. Feng, A. Mariappan, A. Wason, P. Widlund, A. Pozniakovskiy, I. Poser, H. Deng, G. Ou, M. Riparbelli, C. Giuliano, A.A. Hyman, M. Sattler, J. Gopalakrishnan, and H. Li. 2016. Molecular basis for CPAP-tubulin interaction in controlling centriolar and ciliary length. *Nat Commun*. 7:11874.





Organization and dynamics of the cortical complexes controlling insulin secretion in β -cells

Ivar Noordstra¹, Cynthia M. van den Berg¹, Fransje W. J. Boot³, Eugene A. Katrukha¹, Ka Lou Yu¹, Roderick P. Tas¹, Sybren Portegies¹, Bastiaan J. Viergever¹, Esther de Graaff¹, Casper C. Hoogenraad¹, Eelco J. P. de Koning³, Françoise Carlotti³, Lukas C. Kapitein¹, and Anna Akhmanova¹

Journal of Cell Science (2022) 135 (3): jcs259430

* These authors contributed equally

¹Cell Biology, Neurobiology and Biophysics, Department of Biology, Faculty of Science, Utrecht University, Padualaan 8, 3584 CH Utrecht, The Netherlands.

²Division of Cell and Developmental Biology, Institute for Molecular Bioscience, The University of Queensland, St Lucia, QLD 4072, Australia.

³Department of Internal Medicine, Nephrology, Leiden University Medical Center, Albinusdreef 2, 2333 ZA, Leiden, The Netherlands.

Abstract

2 Insulin secretion in pancreatic β -cells is regulated by cortical complexes that are enriched at the sites of adhesion to extracellular matrix facing the vasculature. Many components of these complexes, including bassoon, RIM, ELKS and liprins, are shared with neuronal synapses. Here, we show that insulin secretion sites also contain the non-neuronal proteins LL5 β (also known as PHLDB2) and KANK1, which, in migrating cells, organize exocytotic machinery in the vicinity of integrin-based adhesions. Depletion of LL5 β or focal adhesion disassembly triggered by myosin II inhibition perturbed the clustering of secretory complexes and attenuated the first wave of insulin release. Although previous analyses *in vitro* and in neurons have suggested that secretory machinery might assemble through liquid–liquid phase separation, analysis of endogenously labeled ELKS in pancreatic islets indicated that its dynamics is inconsistent with such a scenario. Instead, fluorescence recovery after photobleaching and single-molecule imaging showed that ELKS turnover is driven by binding and unbinding to low-mobility scaffolds. Both the scaffold movements and ELKS exchange were stimulated by glucose treatment. Our findings help to explain how integrin-based adhesions control spatial organization of glucose-stimulated insulin release.

Introduction

Pancreatic β -cells respond to elevated glucose levels in the bloodstream by the activation of exocytotic machinery and the release of insulin, which subsequently stimulates glucose uptake and conversion in different tissues (Meglasson and Matschinsky, 1986). Defects in insulin secretion lead to diabetes type II, a major worldwide health problem, which affects increasingly large numbers of patients.

Insulin exocytosis is regulated by specialized cortical complexes, which contain bassoon, piccolo, RIM proteins (RIM1 and RIM2), ELKS (also known as ELKS1, ERC1, RAB6-interacting protein 2 and CAST2) and liprins (Gan et al., 2017; Low et al., 2014; Ohara-Imaizumi et al., 2019b; reviewed in Ohara-Imaizumi et al., 2019a). These proteins are also present in neurons, where they form the cytomatrix at the active zone (CAZ), a dense protein meshwork that spatially organizes the coupling of calcium influx to neurotransmitter release (Gundelfinger and Fejtova, 2012; Südhof, 2012). However, unlike in neuronal synapses, the secretion sites in pancreatic β -cells are enriched at the interface with vasculature, where β -cells make contacts with the extracellular matrix (Cottle et al., 2021; Gan et al., 2018, 2017; Low et al., 2014). Interestingly, ELKS and liprins, but not the other CAZ proteins, are also part of the cortical complexes regulating constitutive, Ca^{2+} -independent secretion in non-neuronal cells, such as fibroblasts, keratinocytes, and cancer cells (Grigoriev et al., 2007; Lansbergen et al., 2006; Stehbens et al., 2014; van der Vaart et al., 2013). In such cells, the localization of secretory machinery is controlled by integrin-based cell adhesion, and secretory complexes are concentrated at leading cell edges and around focal adhesions (Fourriere et al., 2019; Grigoriev et al., 2007; Stehbens et al., 2014). Integrin-dependent adhesion, integrin activation and focal adhesion signaling play an important role in insulin secretion (Bosco et al., 2000; Cai et al., 2012; Gan et al., 2018; Kaido et al., 2006; Krishnamurthy et al., 2008; Parnaud et al., 2009, 2006; Riopel et al., 2011, 2013; Rondas et al., 2011, 2012; reviewed in Arous and Halban, 2015; Arous and Wehrle-Haller, 2017; Kalwat and Thurmond, 2013). Specifically, glucose stimulation of β -cells leads to the myosin IIA-dependent remodeling of F-actin and the activation of focal adhesion kinase (FAK; also known as PTK2), paxillin and ERK proteins, ultimately resulting in focal adhesion enlargement (Arous and Halban, 2015; Arous et al., 2013; Gan et al., 2018; Rondas et al., 2011, 2012; Wilson et al., 1999, 2001). Although the importance of focal adhesion remodeling for insulin secretion has been confirmed *in vivo* (Cai et al., 2012), little is known about the relationship between focal adhesions and the proteins organizing insulin exocytosis. Furthermore, a flurry of recent studies have suggested that, in neurons, the CAZ might be formed by liquid–liquid phase separation (LLPS) of the key players, such as liprins, ELKS and RIMs (Emperador-Melero et al., 2021; Liang et al., 2021; McDonald et al., 2020; Sala et al., 2019; Wu et al., 2019, 2021; reviewed in Chen et al., 2020; Hayashi et al., 2021). The idea that the exocytotic machinery in β -cells would form by LLPS is attractive, but it has not been tested.

Here, we explored the connections between the secretory machinery and focal adhesions in β -cells and investigated whether secretory complexes behave like liquid condensates. Previous work has shown that two non-neuronal proteins, LL5 β (also known as PHLDB2) and KANK1, which interact with phosphatidylinositol (3,4,5)-trisphosphate and the integrin adhesion component talin, respectively, play a key role in organizing exocytotic complexes around focal adhesions in different cell types (Bouchet et al., 2016; Grigoriev et al., 2007; Lansbergen et al., 2006; Stehbens et al., 2014; van der Vaart et al., 2013). We previously found that both proteins are part of exocytotic complexes and that LL5 β is required for efficient clustering of secretory complex components in β -cells. We showed that such clustering occurs around focal adhesions and depends on the actomyosin contractility. Importantly, perturbation of the clustering of secretory complexes led to the inhibition of the first, rapid

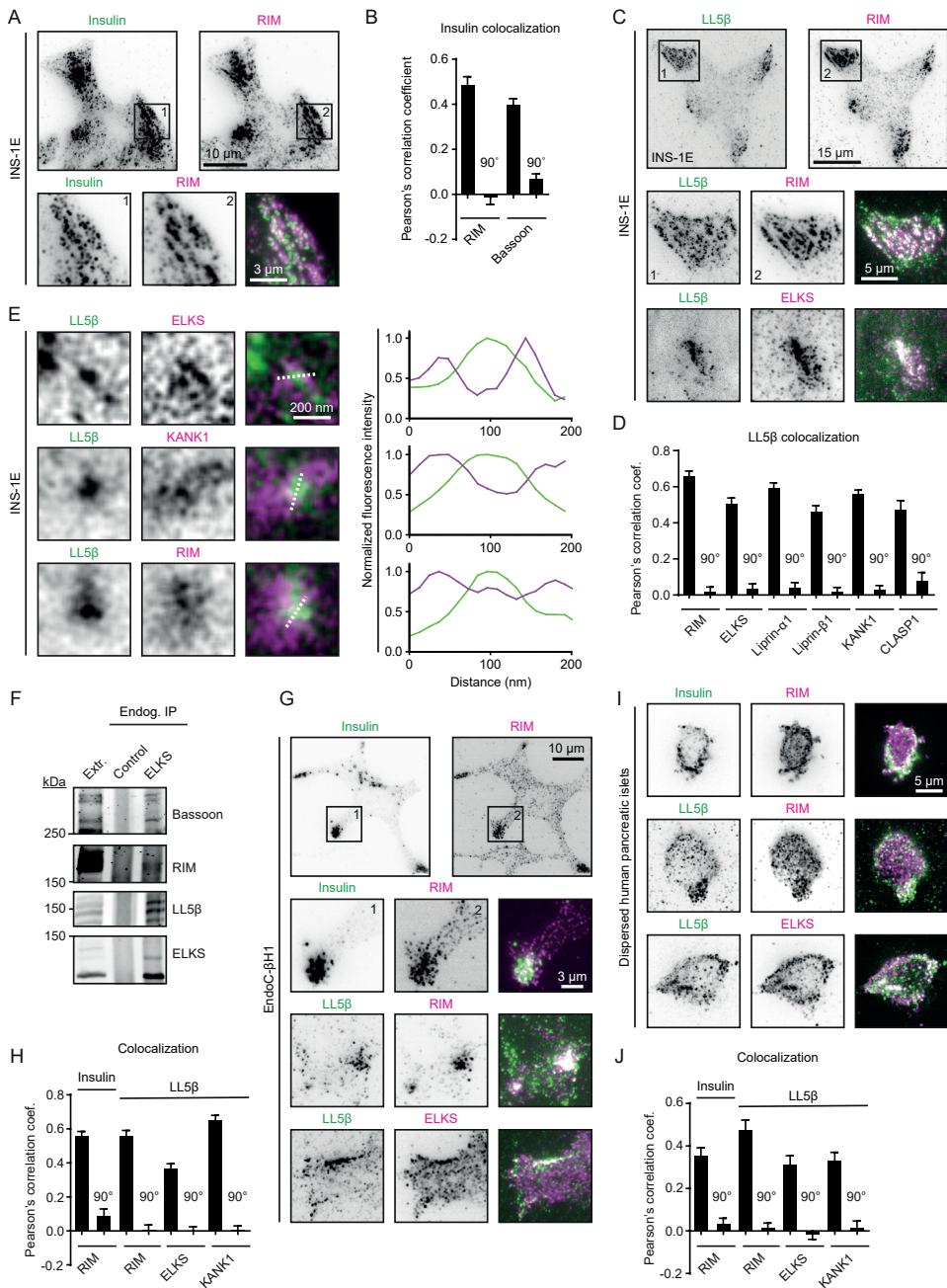


Figure 1: LL5β and KANK1 colocalize with CAZ components and insulin granules in pancreatic β-cell lines and dispersed human pancreatic islets.

(A) Staining for insulin (green) and RIM (RIM1 and RIM2; magenta) in INS-1E cells imaged with total internal reflection fluorescence microscopy (TIRFM). (B) Quantification of colocalization between insulin and indicated proteins in INS-1E cells using Pearson's correlation coefficient between the

two channels. For analysis, intracellular regions of interest (ROIs) of $\sim 25 \mu\text{m}^2$ were used. For RIM, $n=15$ ROIs; for bassoon, $n=21$ ROIs; 90° indicates a 90° rotation of one of the two analyzed channels before analysis; error bars, s.e.m. **(C)** Staining for LL5 β (green) and RIM and ELKS (magenta) in INS-1E cells imaged with TIRFM. **(D)** Quantification of colocalization between LL5 β and indicated proteins in INS-1E cells. Analysis and display as in B. For all conditions, $n=15\text{--}33$ ROIs. **(E)** Stimulated emission depletion (STED) microscopy images of LL5 β (green) and ELKS, KANK1 and RIM (magenta) in INS-1E cells. Intensity profiles along dotted lines are plotted in graphs. Representative images of three experiments are shown. **(F)** Co-immunoprecipitation assay from INS-1E cell extracts using antibodies against endogenous ELKS. Rabbit IgG was used as a control. Extr., cell extract. Representative images of three blots are shown. **(G)** Staining for insulin or LL5 β (green) and RIM and ELKS (magenta) in EndoC- β H1 cells imaged with TIRFM. **(H)** Quantification of colocalization between insulin or LL5 β and indicated proteins in EndoC- β H1 cells using Pearson's correlation coefficient between the two channels. Analysis and display as in B. For all conditions, $n=27\text{--}30$ ROIs. **(I)** Staining for insulin or LL5 β (green) and RIM and ELKS (magenta) in dispersed human pancreatic islets imaged with TIRFM. **(J)** Quantification of colocalization between insulin or LL5 β and indicated proteins in dispersed human pancreatic islets using Pearson's correlation coefficient between the two channels. Analysis and display as in B. For all conditions, $n=14\text{--}22$ ROIs.

phase of insulin secretion, which is known to depend on the release of the pre-docked pool of insulin granules (Rorsman and Renstrom, 2003; Wang and Thurmond, 2009). To test whether the clustering of secretory complexes is driven by LLPS, we focused on the dynamics of ELKS, because ELKS and its homolog ELKS2 (also known as CAST and ERC2) are multivalent proteins that can interact with multiple components of the secretory machinery, including liprin- α isoforms, RIMs, bassoon, LL5 β and voltage-gated Ca^{2+} channels (Kiyonaka et al., 2012; Ko et al., 2003; Lansbergen et al., 2006; Takao-Rikitsu et al., 2004; Wang et al., 2002). Here, we used a newly generated GFP-ELKS mouse knock-in model to investigate in detail the dynamics of endogenously labeled secretory complexes in pancreatic islets. We confirmed the colocalization of neuronal and non-neuronal proteins at the insulin secretion sites in the vicinity of blood vessels in pancreatic islets, characterized the dynamics of ELKS-containing secretory complexes and demonstrated that their turnover is strongly regulated by glucose levels. We found no evidence that would support LLPS as being the basis for formation of ELKS foci, because the majority of them contained only two to four ELKS dimers and showed all hallmarks of protein binding/unbinding to a low-mobility scaffold rather than liquid condensates. Our data support the view that the formation of secretory sites in pancreatic β -cells is driven by protein binding and unbinding to scaffolds clustered around focal adhesions.

Results

LL5 β and KANK1 colocalize with CAZ components in pancreatic β -cells

Using insulin-secreting INS-1E cells as a model system, we confirmed that the regions of cortical accumulation of insulin granules corresponded to the areas where CAZ markers, such as RIM1 or RIM2 (detected here with antibodies recognizing both proteins, termed RIM from now on) and Bassoon, are enriched (Fig. 1A, B; Fig. S1A). Next, we tested whether the localization of LL5 β and KANK1 overlaps with that of RIM, bassoon, liprins and ELKS. Imaging of the cell cortex by total internal reflection fluorescence microscopy (TIRFM) showed that all these proteins displayed punctate staining patterns that were concentrated in the same membrane regions (Fig. 1C, D; Fig. S1B-D). These data confirm previous observations on the colocalization between LL5 β , liprins, ELKS and KANK1 in different cell types (Astro et al., 2014; Bernadzki et al., 2014; Bouchet et al., 2016; Lansbergen et al., 2006; van der Vaart et al., 2013; Yuan et al., 2015) and show that these proteins also colocalize with CAZ

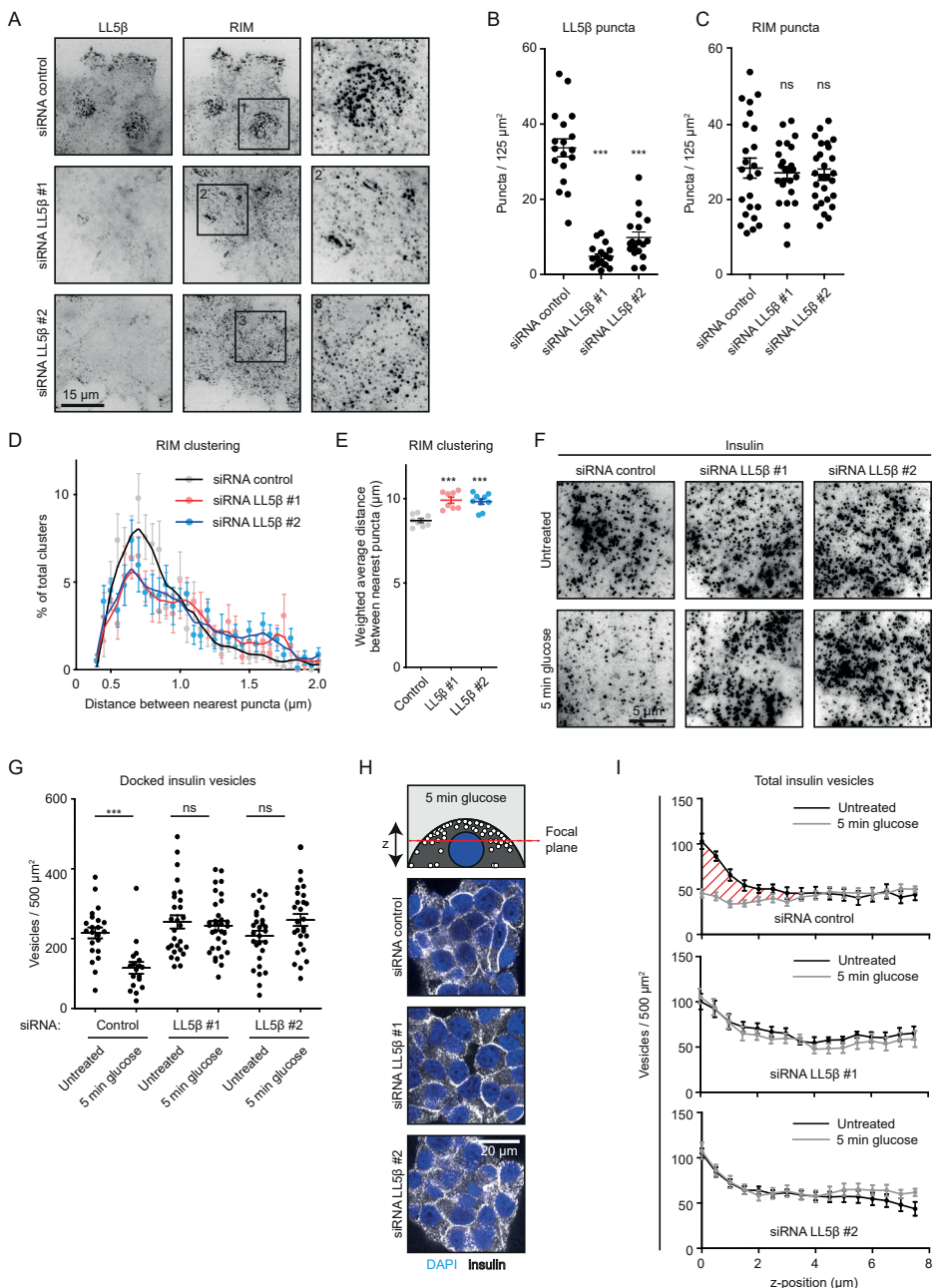


Figure 2: LL5 β is required for clustering of insulin docking complexes and insulin release. (A) Staining for LL5 β and RIM in INS-1E cells transfected with control siRNA or siRNAs against LL5 β imaged with TIRFM. (B) Quantification of number of LL5 β puncta in INS-1E cells treated as in A. For all conditions, $n=18$ ROIs (which represent ~ 1 cell each); *** $P < 0.001$ (one-way ANOVA followed by Dunnett's post-test). Single data points are plotted. Horizontal line, mean; error bars, s.e.m. (C) Quantification of number of RIM puncta in INS-1E cells treated as in A. Analysis and display as in

B. For all conditions, $n=24-27$ ROIs. ns, not significant. **(D)** Quantification of RIM clustering in INS-1E cells treated and stained as in A. Data are plotted as a frequency distribution of distances between nearest puncta. For all conditions, $n=24-27$ ROIs (which represent ~ 1 cell each). Dots represent bin averages; lines represent medium locally weighted scatterplot smoothing (LOWESS) curves; error bars, s.e.m. **(E)** Weighted averages from the RIM clustering quantification shown in D. $***P<0.001$ (one-way ANOVA followed by Dunnett's post-test). **(F)** Staining for insulin and RIM in INS-1E cells treated as in A, stimulated with 25 mM glucose as indicated and imaged with TIRFM. **(G)** Quantification of docked insulin vesicles in INS-1E cells treated and stained as in F. Control, $n=18-22$ ROIs (which represent ~ 4 cells each); LL5 β #1, $n=28-32$; LL5 β #2, $n=28$; $***P<0.001$; ns, not significant (Mann-Whitney U-test). Single data points are plotted. Horizontal line, mean; error bars, s.e.m. **(H)** Staining for insulin (white) and DNA (blue) in INS-1E cells treated as in F and imaged with confocal microscopy. Image focal plane is indicated by red striped line in scheme at top. **(I)** Quantification of total insulin vesicle distribution along the z-axis in INS-1E cells treated and stained as in F. For all conditions, $n=16$ ROIs (which represent ~ 4 cells each). Red shaded area indicates secreted insulin fraction at basal side of the cells. Error bars, s.e.m.

components in insulin-secreting cells. We also observed that the LL5 β -binding microtubule-stabilizing protein CLASP1 was enriched in cell regions containing LL5 β accumulations (**Fig. S1E**; **Fig. 1D**). A higher-resolution analysis using stimulated emission depletion (STED) microscopy showed that the puncta observed with different antibodies were closely apposed but did not coincide (**Fig. 1E**; **Fig. S1F**). The presence of ELKS, bassoon, RIM and LL5 β in the same complexes in INS-1E cells was also confirmed by immunoprecipitation of endogenous proteins with anti-ELKS antibodies (**Fig. 1F**). The spatial distribution and colocalization of the cortical protein complexes and insulin were confirmed in the human β -cell line EndoC- β H1 (**Fig. 1G, H**; **Fig. S1G**) and dispersed human pancreatic islets (**Fig. 1I, J**; **Fig. S1H**). Taken together, these experiments reveal a conserved hybrid protein complex in pancreatic β -cells that consists of both neuronal CAZ components and non-neuronal proteins that regulate cortical microtubule attachment and constitutive secretion in epithelia and fibroblasts.

LL5 β is required for clustering of insulin secretion complexes and efficient insulin release

Our previous work showed that in non-neuronal cells, LL5 β , liprins and KANK1 can independently localize to the plasma membrane, but require each other, as well as ELKS, for the formation of dense cortical clusters at the leading cell edges and around focal adhesions (Bouchet et al., 2016; Lansbergen et al., 2006; van der Vaart et al., 2013). To test whether the same is true for insulin-secreting cells, we depleted LL5 β in INS-1E cells using two different siRNAs, and immunofluorescence showed that LL5 β -positive puncta were almost completely lost in $\sim 30-40\%$ of the cells (**Fig. 2A, B**; **Fig. S2A**). We also observed a $30-40\%$ reduction in the LL5 β signal on western blots (**Fig. S2B, C**). Depletion of LL5 β did not prevent membrane localization of RIM, but its clustering was reduced (**Fig. 2A, C-E**). Next, we examined whether the depletion of LL5 β affected glucose-stimulated insulin secretion. In control cells, the cortex-associated insulin granule pool was strongly reduced due to rapid insulin secretion within the first 5 min after glucose stimulation, and then gradually recovered, as described previously (Curry et al., 1968; Rorsman et al., 2000) (**Fig. S2D, E**). Owing to insufficient compatibility of cell fixation procedures required to detect LL5 β and insulin granules in INS-1E cells, it was not possible to stain them simultaneously. We therefore co-stained INS-1E cells for insulin and RIM, and analyzed the cells with dispersed RIM puncta, as we observed that such cells were strongly depleted of LL5 β (**Fig. 2A, D, E**). In the absence of glucose stimulation, the density of insulin granules in the vicinity of the basal cortex was not affected; however, their release in the vicinity of the basal cortex after 5 min of glucose stimulation was inhibited in LL5 β -depleted cells (**Fig. 2F, G**). Importantly, LL5 β knockdown compromised only the secretion of

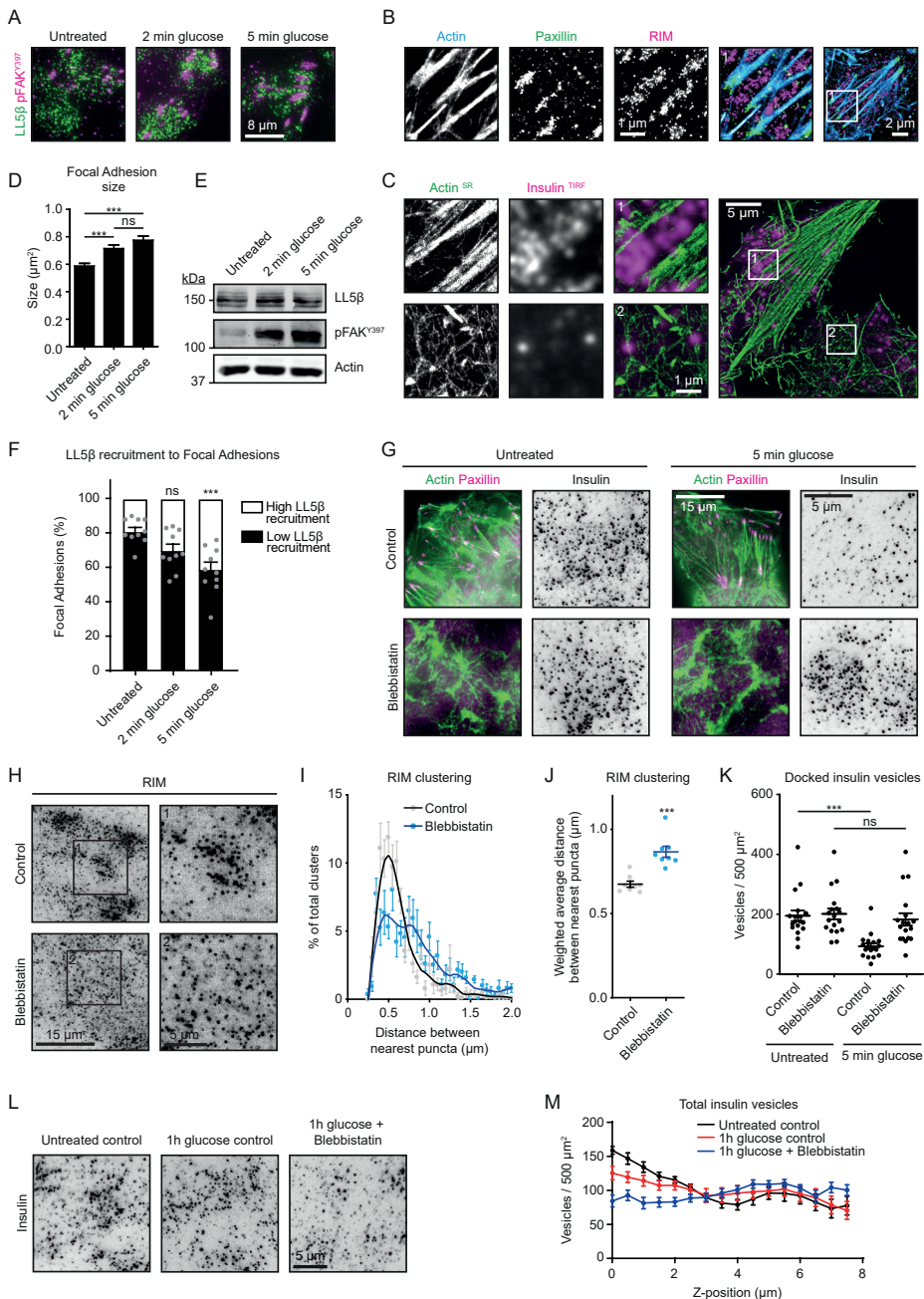


Figure 3: Actomyosin contractility controls the distribution of the cortical insulin docking complexes and insulin release.

(A) Staining for LL5 β (green) and phosphorylated FAK (pFAK^{Y397}, magenta) in INS-1E cells stimulated with 25 mM glucose as indicated and imaged with TIRFM. (B) Single-molecule localization microscopy (SMLM) image of actin (blue), paxillin (green) and RIM (magenta) in untreated INS-1E cells. Actin

was detected using Peptide-PAINT (Points Accumulation for Imaging in Nanoscale Topography) with LifeAct-mNeonGreen, while paxillin and RIM were detected using DNA-PAINT with antibodies against the endogenous proteins. **(C)** SMLM image of actin (green) detected as in B and TIRFM image of insulin (magenta) in INS-1E cells stimulated with 25 mM glucose for 5 min. Representative images of three experiments are shown in B and C. **(D)** Quantification of focal adhesion size in INS-1E cells treated as in A. Untreated, $n=1040$ focal adhesions; 2 min glucose, $n=948$ focal adhesions; 5 min glucose, $n=939$ focal adhesions; $***P<0.001$; ns, not significant (one-way ANOVA followed by Tukey's post-test); error bars, s.e.m. **(E)** Western blot analysis of LL5 β and pFAKY397 in INS-1E cells treated as in A. Representative images of two blots are shown. **(F)** Quantification of LL5 β localization relative to focal adhesions in INS-1E cells treated and stained as in A. LL5 β fluorescence intensity (LL5 β recruitment) was measured in a 1 μ m-broad area around focal adhesions and binned into 'high' LL5 β recruitment (top 75% intensity values) or 'low' LL5 β recruitment (the remaining intensity values). Only data points exceeding $1.5\times$ LL5 β fluorescent background signal were included in plots. Single data points for 'low' LL5 β recruitment are plotted. For all conditions, $n=10$ ROIs with 45–73 focal adhesions per ROI. $***P<0.001$; ns, not significant (one-way ANOVA followed by Dunnett's post-test); error bars, s.e.m. **(G)** Staining for actin (green) and paxillin (magenta), and insulin (gray) imaged with widefield microscopy (actin, paxillin) and TIRFM (insulin) in INS-1E cells treated with 50 μ M blebbistatin for 1 h and subsequently stimulated with glucose as indicated. **(H)** Staining for RIM in INS-1E cells treated with 50 μ M blebbistatin for 1 h and imaged with TIRFM. **(I)** Quantification of RIM clustering in INS-1E cells treated and stained as in H. Analysis and display as in Fig. 2D. For all conditions, $n=24$ ROIs. **(J)** Weighted averages from the RIM clustering quantification shown in I. Analysis and display as in Fig. 2E. **(K)** Quantification of docked insulin vesicles in INS-1E cells treated and stained as in G. Analysis and display as in Fig. 2G. For all conditions, $n=18$ ROIs. **(L)** Staining for insulin in INS-1E cells treated with 50 μ M blebbistatin for 1 h and subsequently stimulated with glucose as indicated and imaged with TIRFM. Representative images of three experiments are shown. **(M)** Quantification of total insulin vesicle distribution along the z-axis in INS-1E cells treated and stained as in L. Analysis and display as in Fig. 2H. For all conditions, $n=16$ ROIs.

the cortex-associated insulin granule pool but did not affect insulin vesicle numbers further away from the basal cortex (Fig. 2H, I). These data suggest that LL5 β -dependent clustering of the components of exocytotic machinery has no effect on the formation and possibly also the docking of insulin granules, but affects their fusion and thus the first, rapid phase of insulin secretion.

Myosin II activity is required for clustering of insulin secretion complexes around focal adhesions and insulin release

In HeLa cells and keratinocytes, LL5 β , liprins, ELKS and KANK1 have been shown to localize around focal adhesions, thereby regulating the CLASP-dependent connection of microtubule plus ends to the cortex (Bouchet et al., 2016; Grigoriev et al., 2007; Lansbergen et al., 2006; Stehbens et al., 2014; van der Vaart et al., 2013). This spatial arrangement allows for the coupling between microtubule-based transport and localized secretion around focal adhesions (Fourriere et al., 2019; Lansbergen et al., 2006; Stehbens et al., 2014; van der Vaart et al., 2013). Immunofluorescence co-staining of α -tubulin and phosphorylated (p)FAKY397 visualized spatial proximity of focal adhesions and microtubules in INS-1E cells (Fig. S3A). In addition, co-staining of LL5 β and focal adhesion markers in INS-1E and EndoC- β H1 cells showed that LL5 β and other cortical proteins localized to the areas adjacent to focal adhesions (Fig. 3A; Fig. S3B–E). These cortical complexes, as well as cortical accumulations of insulin granules, were excluded from the regions with dense actin fibers and were located between actin filaments visualized by single-molecule localization microscopy (SMLM) (Fig. 3B, C).

Work in HeLa cells and fibroblasts previously showed that when focal adhesion formation is suppressed by serum starvation or by inhibition of actomyosin contractility, the clustering of LL5 β , liprins, ELKS and KANK1 at the leading cell edges and around focal adhesions

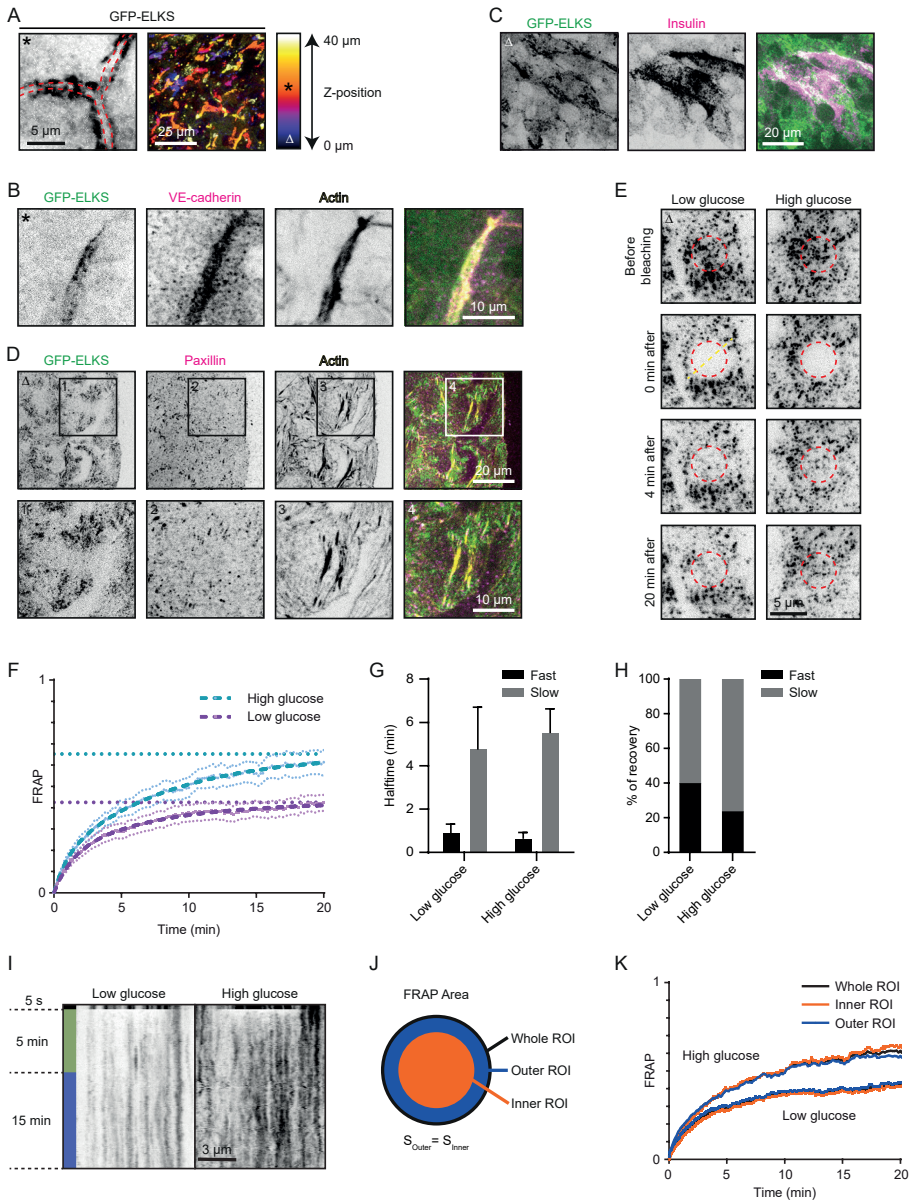


Figure 4: Analysis of the distribution and dynamics of the endogenous cortical insulin secretion complexes in mouse pancreatic islets.

(A) Localization of GFP-ELKS inside a mouse pancreatic islet imaged with confocal microscopy. Left panel, red striped lines indicate extracellular space (presumable blood vessel). Right panel, maximum projection of a z-stack. Image colors indicate z-position (see gradient). Asterisk in top left corner of the shown image corresponds to its position in the z-stack (indicated in gradient). (B) Staining for VE-cadherin (magenta) and actin (yellow) inside a GFP-ELKS (green)-expressing mouse pancreatic islet imaged with confocal microscopy. Z-position of shown images as in A. (C) Staining for insulin (magenta) in the adherent region of a GFP-ELKS (green)-expressing mouse pancreatic

islet imaged with TIRFM. Delta in top left corner of the shown images corresponds to their position in the z-stack (indicated in gradient in A). **(D)** Staining for paxillin (magenta) and actin (yellow) in the adherent region of a GFP-ELKS (green)-expressing mouse pancreatic islet imaged with TIRFM. Z-position of shown images as in C. Representative images of three experiments are shown in A–D. **(E)** FRAP analysis of GFP-ELKS in the adherent region of mouse pancreatic islets stimulated with glucose as indicated and imaged with TIRFM. High glucose (25 mM) was administered 4 h after low glucose (2 mM) starvation 1 h prior to photobleaching. Red dashed circles indicate photobleached regions. Z-position of shown images as in C. **(F)** Average normalized fluorescence intensity recovery and fitted curves (dashed lines) after photobleaching of GFP-ELKS in mouse pancreatic islets treated as in E (low glucose, n=15 FRAP areas; high glucose, n=16 FRAP areas). Error bars represent s.e.m., straight horizontal lines represent recovery plateau derived from the fitting. **(G,H)** Fluorescence recovery halftimes (G) and relative fraction (H) of fast and slow exponential components from the fit shown in F. Error bars represent fitting uncertainty. **(I)** Representative kymographs from three experiments of GFP-ELKS FRAP along the straight line crossing the center of the bleached area (illustrated as dashed yellow line in E). **(J)** Illustration of the original bleaching ROI division into outer and inner areas of equal area for FRAP curves comparison shown in K. **(K)** FRAP curves corresponding to the full bleaching ROI and its outer and inner areas, as shown in J.

is strongly reduced (Bouchet et al., 2016; Lansbergen et al., 2006). It was also established that glucose stimulation of β -cells leads to activation of FAK and remodeling of actin and focal adhesions (Arous and Halban, 2015; Rondas et al., 2011, 2012). We confirmed these observations; even at 2 min after glucose stimulation, a significant enlargement of focal adhesions and an increase in the abundance of the phosphorylated, active form of FAK (pFAKY397) could be detected (**Fig. 3A, D, E**). Interestingly, glucose stimulation also caused an increase in the abundance of LL5 β in the direct vicinity of focal adhesions (**Fig. 3A, F**). In contrast, when we induced loss of stress fibers and focal adhesion disassembly by inhibiting myosin II with blebbistatin (**Fig. 3G**), clustering of the components of exocytotic machinery was reduced (**Fig. 3H–J**), whereas the number of individual puncta was not affected (**Fig. 33F**). Blebbistatin treatment also inhibited glucose-induced loss of insulin granules from the cell cortex during the first, rapid phase of insulin secretion (**Fig. 3G, K**). Interestingly, blebbistatin-treated INS-1E cells stimulated for 1 h with glucose displayed increased loss of insulin vesicles from the cortical area compared to control cells (**Fig. 3L, M**). This could be explained by the observation that the actomyosin cytoskeleton has an inhibitory effect on the sustained, second-phase insulin secretion (Hammar et al., 2009; Kong et al., 2014). We thus conclude that the role of myosin II in insulin secretion is complex; in the first phase (2–5 min), myosin II is required for the activation of focal adhesion signaling and clustering of the secretion machinery. However, on a longer (1 h) time scale, loss of cortical actin structures promotes sustained insulin secretion, possibly due to the elimination of the actin cytoskeleton as a cortical barrier for exocytosis, as proposed previously (Arous and Halban, 2015; Arous and Wehrle-Haller, 2017; Kalwat and Thurmond, 2013).

Visualization of endogenously labeled insulin secretion complexes in mouse pancreatic islets

To confirm that the results obtained in INS-1E cells are valid for endogenous protein complexes, we turned to isolated mouse pancreatic islets. We used islets from wild-type mice as well as mice bearing a GFP knock-in in the gene encoding ELKS. In these mice, the GFP-coding region with an adjacent neomycin-resistance cassette surrounded by two LoxP sites (Lox-Neo-Lox) was inserted directly in front of the first ATG codon in the first coding exon (exon 3) of the *Elks1* gene (**Fig. S4A, B**). This insertion disrupted the *Elks1* gene, leading to embryonic lethality in homozygous animals, consistent with the previous descriptions of *Elks1*-knockout mice (Liu et al., 2014; Wu et al., 2010). When the Lox-Neo-Lox cassette was

removed through Cre-mediated recombination, by crossing these mice to a mouse line in which the Cre gene is under the control of the cytomegalovirus immediate early enhancer-chicken β -actin hybrid promoter and is expressed in oocytes (Sakai and Miyazaki, 1997) (Fig. S4B), the resulting GFP-Elks1 knock-in mice were viable, fertile and displayed no overt defects. Using western blotting, we observed an upward shift of the ELKS-positive bands in different tissues by ~ 30 kDa, as can be expected for GFP fusions (Fig. S4C). These data indicate that the N-terminal fusion to GFP does not perturb the function of the ELKS protein in the mouse, and that the localization of the GFP marker is likely to reflect the endogenous ELKS distribution.

To study ELKS localization and dynamics in mouse β -cells, we isolated pancreatic islets and cultured them on Matrigel-coated coverslips (Fig. S4D). In line with previous publications (Low et al., 2014; Ohara-Imaizumi et al., 2019b, 2005), we observed that the endogenously tagged GFP-ELKS preferentially localized along blood vessels within the islets (Fig. 4A, B). In the parts of the isolated islets that adhered to the coverslips, the accumulation of insulin granules and GFP-ELKS were observed in overlapping cortical areas (Fig. 4C). The same was true for the LL5 β and RIM detected in islets by immunofluorescence staining (Fig. S4E, F), thus showing that the cortical enrichment patterns of these proteins in mouse pancreatic islets were very similar to those observed in INS-1E cells, human EndoC- β H1 and dispersed human pancreatic islets. Similar localization patterns were also found in human pancreatic tissue, where LL5 β and RIM showed colocalization with C-peptide (a by-product of insulin production; Kitabchi, 1977) (Fig. S4G, H).

GFP-ELKS in cultured mouse pancreatic islets displayed a punctate distribution with a characteristic size of an individual spot or a GFP-ELKS cluster being close to the diffraction limit (Fig. 4D). These small clusters were distributed non-homogeneously, often showing local enrichment areas. Such areas often localized around focal adhesions at the base of stress fibers (Fig. 4D; Fig. S4I), supporting the findings described above.

Dynamics of GFP-ELKS in pancreatic islets is consistent with binding and unbinding to a scaffold with low mobility

GFP tagging of endogenous ELKS allowed us to measure its dynamics in order to investigate whether the ELKS-containing cortical complexes behave like liquid droplets and whether their turnover is affected by glucose stimulation. To characterize the dynamics of cortical GFP-ELKS puncta at the ensemble level, we performed fluorescence recovery after photobleaching (FRAP) experiments using TIRFM (Fig. 4E, F). For photobleaching, we chose a round area of 5 μ m diameter, encompassing multiple clusters (Fig. 4E). Comparison of the FRAP curves showed that both in low glucose and after 1 h of glucose stimulation, the fluorescence recovery profile could not be satisfactorily fitted by a one-phase association curve, while a much better fitting was obtained using a two-phase curve (Fig. 4F-H). We found that the recovered (exchangeable) fraction of fluorescence in low-glucose conditions was equal to 42%, while a higher recovery of 65% was observed after glucose stimulation (Fig. 4F). Among the parameters describing recovery curves, this shift in the exchangeable/non-exchangeable fractions was the largest, while changes in halftimes of the fast and slow recovering fractions (Fig. 4G) and their relative contributions were relatively minor (Fig. 4H; Table S1).

The fluorescence recovery of membrane-associated GFP-ELKS clusters can happen due to their lateral mobility or lateral flux of molecules between them, or through the exchange with the pool of cytoplasmic GFP-ELKS molecules (McSwiggen et al., 2019). If lateral mobility is dominating, faster recovery of the peripheral area of the bleached spot would be expected due to the flow of unbleached molecules from the periphery. If the proteins predominantly exchange with the cytoplasmic pool, recovery would be expected to occur homogeneously

throughout the whole bleached area. Kymographs built along the line crossing the center of the bleached round area did not show any noticeable influx of unbleached signal from the periphery (Fig. 4I). To quantify this effect precisely, we divided the bleached spots in two parts of equal areas, a peripheral (outer) ring and central (inner) circle (Fig. 4J). The normalized averaged FRAP curves for both areas showed exactly the same behavior as the whole bleached spot (Fig. 4K), suggesting that the recovery happens homogeneously and is mostly due to the exchange between cortex-bound and cytoplasmic molecules.

To further confirm the prevalence of this mechanism, we imaged and tracked the mobility of individual GFP-ELKS clusters over the course of 15 min (Fig. 5A; Movie 1). The comparison of average mean square displacement (MSD) showed higher cluster mobility upon glucose stimulation (Fig. 5B). In both cases, MSD values demonstrated linear dependence on time delay, suggesting diffusive behavior. Linear fits to the MSD plots produced diffusion coefficients of $5.6 \times 10^{-5} \mu\text{m}^2/\text{s}$ for low and $7.5 \times 10^{-5} \mu\text{m}^2/\text{s}$ for high glucose conditions. Although MSD followed a linear dependence, the values of the calculated diffusion coefficients were extremely low and could not account for the observed fluorescence recovery. For example, even in the case of high glucose conditions, the expected FRAP half-time due to the diffusion would be 4 h (estimated as the area of the bleached spot divided by the diffusion coefficient; Axelrod et al., 1976), which is an order of magnitude higher than the observed values (Fig. 4G). Therefore, for the timescale of less than an hour, the contribution of cluster mobility to ELKS dynamics can be excluded from consideration.

The formation of (relatively) immobile clusters from the molecules present in a cytosolic pool can happen through their binding/unbinding to a scaffold formed by other proteins. Alternatively, as suggested by recent publications (Liang et al., 2021; Sala et al., 2019), ELKS cluster formation could occur spontaneously due to liquid-liquid phase separation. To discern among these two mechanisms, we measured the behavior of GFP-ELKS at the level of individual molecules. We performed a set of recordings on the previously unexposed area of islets with high laser power and high frame rate (Fig. 5C). During the first acquisition, we photobleached all fluorescent signal in the field of view, including bright immobile GFP-ELKS clusters at the cortex. After a short (10–15 s) recovery period, we performed a second high-frame-rate acquisition to record the behavior of single GFP-ELKS molecules (Fig. 5C). Improved contrast after the bleaching of bright immobile spots allowed us to observe the presence of two populations of single molecules – a slow, relatively immobile pool and particles that were rapidly diffusing in and out the field of view (Movie 2). We observed multiple events of transitions between these two populations (Movie 3), confirming the exchange between clusters and cytosolic pool. Substantial photobleaching (caused by the high laser power required for the observation of fast-moving molecules) precluded precise quantification of corresponding rate constants of transitions between these fractions. Therefore, we focused on the characterization of motility of GFP-ELKS molecules. Our first attempt of tracking single molecules led to multiple mistakes at the step of linking detections to trajectories (Fig. S5A; Movie 2, left panels). Automatic linking methods based on the nearest neighbor search generated trajectories that were composed from interspersed fragments of tracks from both populations (Movie 2, left panels). This problem hindered the analysis of trajectories. As can be seen from the MSD density plot (Fig. S5D, left panel), two separate particle populations are present, manifesting themselves as two separate dense areas/shapes, where the higher one corresponds to the fast- and the lower one to the slow-moving population. The average duration of tracks, measured as the length of each area along the x-axis, appeared longer for the fast-moving population. This was in contradiction with the visual inspection of acquired movies, where fast-moving particles rapidly enter and leave the imaging volume, while the slow molecules remain in the field of view for much longer periods. To overcome this analysis problem, we applied a temporal median filter with the sliding window of 15 frames (~0.5 s) to

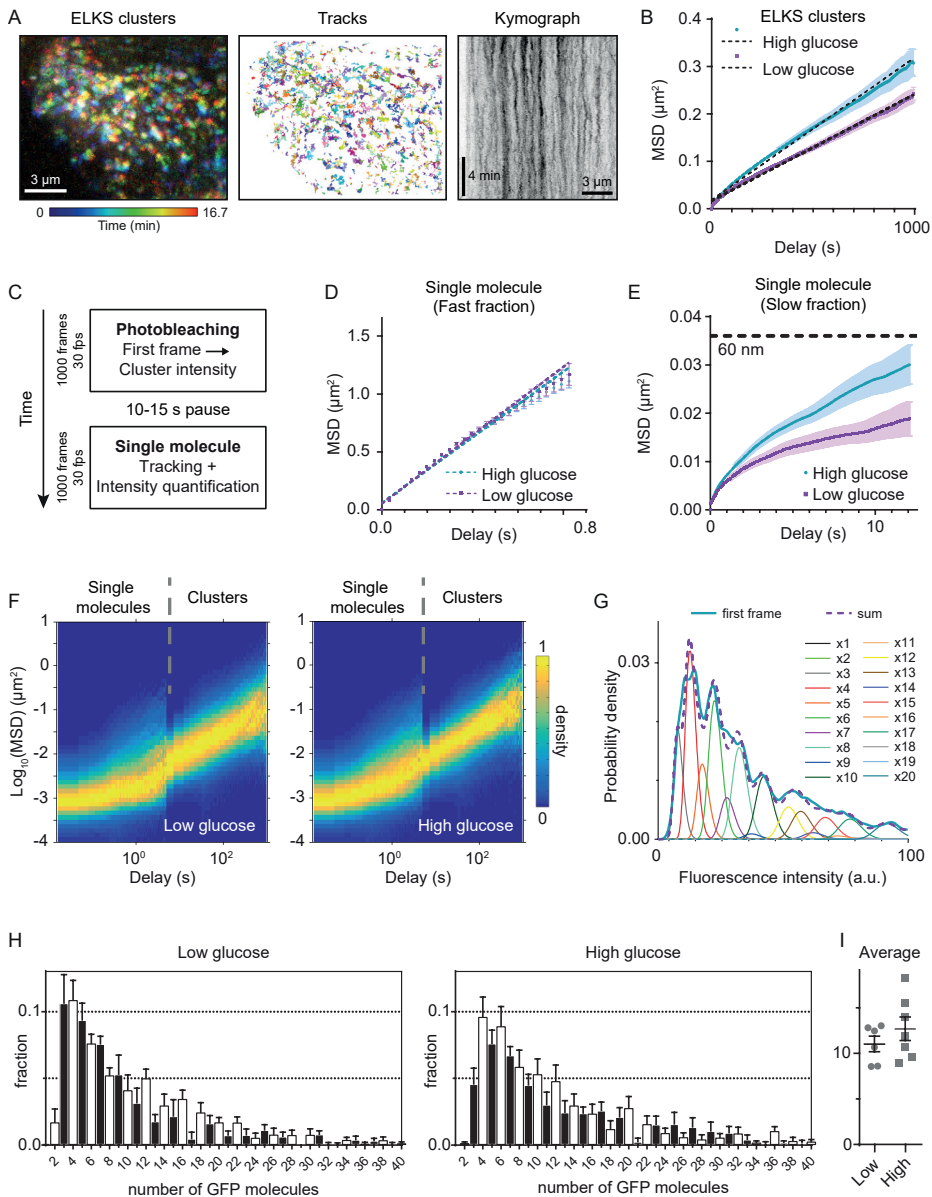


Figure 5: Single-molecule analysis of GFP-ELKS cluster motility and stoichiometry in mouse pancreatic islets.

(A) Representative color-coded maximum intensity projection (200 frames, 5 s per frame) of a time-lapse movie of GFP-ELKS clusters (left panel) and their corresponding trajectories (middle panel). Right panel shows maximum intensity projection of a stack of kymographs built along horizontal lines of the area shown in the left panel. (B) Average MSD of GFP-ELKS clusters trajectories. Low glucose, $n=9658$ tracks; high glucose $n=9586$. Error bars represent s.e.m. Dashed lines show linear fits $\text{MSD}(\tau)=4D\tau+\sigma^2$. Calculated diffusion coefficients are equal to $5.6 \times 10^{-5} \mu\text{m}^2/\text{s}$ for low and $7.5 \times 10^{-5} \mu\text{m}^2/\text{s}$ for high glucose conditions. (C) Schematic representation of experimental design for

observation of single GFP–ELKS molecules. **(D)** Average MSD of the fast fraction of single GFP–ELKS molecule trajectories. Low glucose, $n=3484$ tracks; high glucose, $n=6209$ tracks. Error bars represent s.e.m. Dashed lines show linear fits [$\text{MSD}(\tau)=4D\tau+\sigma^2$]. Calculated diffusion coefficients are equal to $0.37 \mu\text{m}^2/\text{s}$ for low and $0.35 \mu\text{m}^2/\text{s}$ for high glucose conditions. **(E)** Average MSD of slow fraction of single GFP–ELKS molecule trajectories. Low glucose, $n=4449$ tracks; high glucose, $n=7689$ tracks. Error bars represent s.e.m. Dashed line marks squared displacement of 60 nm, i.e. half the length of GFP–ELKS molecule (119 nm; Sala et al., 2019). **(F)** Combined heatmap (3D histogram) of MSD values for the slow fraction of single GFP–ELKS molecules and clusters (separated by gray dashed lines). Same datasets as in B and E. Histogram values are normalized by the maximum value of each column, corresponding to each time delay bin. **(G)** Representative probability density of pre-bleach GFP–ELKS cluster intensities [measured at the first frame, thick blue line, one field of view (FOV), 1095 clusters] fitted to a weighted sum of N-mers of GFP (thick dashed magenta line). The weighted probability densities of individual GFP N-mers intensities are plotted as thin lines. **(H)** Quantification of GFP–ELKS cluster stoichiometry. Averaged histograms of weights of N-mers of GFP determined from the fitting to the GFP–ELKS clusters intensities. Low glucose, $n=6$ FOVs; high glucose, $n=7$ FOVs. Error bars represent s.e.m. Weighted mean values of GFP molecules per cluster for each FOV are shown in the inset (11.0 ± 2.1 for low and 12.7 ± 3.5 for high glucose condition, $\text{mean}\pm\text{s.e.m.}$). **(I)** Average number of GFP–ELKS molecules present in a cluster; error bars represent $\text{mean}\pm\text{s.e.m.}$

each pixel of the original movie (Hoogendoorn et al., 2014; Masucci et al., 2021). As a result, we obtained two movies with clearly separated timescales, where each of the two populations can be tracked independently (Fig. S5B, C; Movie 2). In this case, MSD density plot correctly reflected the shorter duration of fast-moving particle trajectories in comparison to their slow-moving counterparts and demonstrated a two-order difference in the motility between them (Fig. S5D, right).

The average MSD curves of the fast fraction of single GFP–ELKS molecules did not depend on the glucose exposure (Fig. 5D). Linear fits provided similar diffusion coefficient values of $0.37 \mu\text{m}^2/\text{s}$ for low and $0.35 \mu\text{m}^2/\text{s}$ for high glucose conditions. This allowed us to attribute the fast-moving population to the GFP–ELKS molecules freely diffusing in the cytosol. In contrast, the mobility of the slow fraction was dependent on glucose exposure (Fig. 5E) in a similar way to the mobility of clusters (Fig. 5B). More importantly, in this case, the average displacement of GFP–ELKS molecules on timescales of up to 10 s did not exceed 60 nm (Fig. 5E). Given that the size of ELKS dimer determined by EM data is 119 nm (Sala et al., 2019), this means that the individual molecules are essentially immobile within the cluster. To combine the MSD data of single GFP–ELKS molecules and cluster trajectories on different timescales, we generated a ‘stitched’ MSD probability heatmap (Fig. 5F). We observed that the mode (peak) of MSD distribution of single molecules continuously transitioned to the mode of clusters for each glucose concentration (Fig. 5F). Therefore, we conclude that the slow movement of single GFP–ELKS molecules can be explained by movement of clusters as a whole, rather than the diffusion of individual molecules within them. Lack of mobility of individual molecules combined with the slow diffusion of the clusters speaks in favor of the hypothesis that the ELKS molecules are bound to a low-mobility scaffold, being in binding/unbinding equilibrium with cytosolic ELKS molecules. If each cluster would represent a separate liquid phase/droplet, one would expect to observe diffusion of individual molecules within it.

To characterize the size of individual GFP–ELKS clusters, we applied a quantitative fluorescence approach (Fig. 5G, H). By using the single-molecule intensity in the last frame of the tracks, before complete photobleaching, we estimated fluorescence intensity distribution of single GFP fluorophores. Using this distribution, we constructed GFP N-mer distributions corresponding to intensities of oligomers with increasing number N of GFP molecules (Moertelmaier et al., 2005). Initial, unbleached intensity of GFP–ELKS clusters

(at the first frame) was fitted to a sum of these distributions with different weights, which served as fitting parameters (Fig. 5G). We found that oligomers with an even number of GFP molecules were prevalent in the intensity distributions (Fig. 5H), in accordance with a previous report showing that ELKS forms coiled-coil homodimers (Sala et al., 2019). The weighted average number of GFP molecules per cluster did not change significantly and was measured as 11.0 ± 2.1 for low glucose and 12.7 ± 3.5 (mean \pm s.d.) for high glucose condition (Fig. 5I). In both cases the most abundant oligomer fraction contained four GFP molecules (Fig. 5H), corresponding to just two ELKS homodimers. It is highly improbable that a stable molecular assembly with such a low number of molecules could be formed as a result of liquid–liquid phase separation. Therefore, our stoichiometry data analysis strongly favors the idea that GFP-ELKS clusters form by binding to relatively immobile scaffolds.

Our data indicate that at endogenous expression levels, ELKS does not form condensates. We next tested whether previously observed condensate formation (Sala et al., 2019) is a result of elevated protein expression. Since protein overexpression is technically challenging in pancreatic cells, we performed experiments with HeLa cells transiently overexpressing GFP-ELKS. Our previous work in HeLa cells has shown that endogenous ELKS or ELKS overexpressed at low levels is present in relatively immobile cortical complexes around focal adhesions (Grigoriev et al., 2007; Lansbergen et al., 2006; van der Vaart et al., 2013), very similar to what we describe here for β -cells. Indeed, we observed that at low expression levels, GFP-ELKS was exclusively present in cortical foci (Fig. S6A). At higher expression level, we could readily observe formation of cytoplasmic condensates (Fig. S6A–C); these condensates were not visible in the TIRF illumination plane, indicating that they are not bound to the cell cortex and thus cannot participate in targeting vesicles to the plasma membrane. The abundance of the condensates strongly correlated with ELKS expression levels (Fig. S6B, C), and they showed characteristic behaviors such as fusion (Fig. S6D) and fast recovery after photobleaching (Fig. S6E). We conclude that formation of ELKS condensates is a result of protein overexpression.

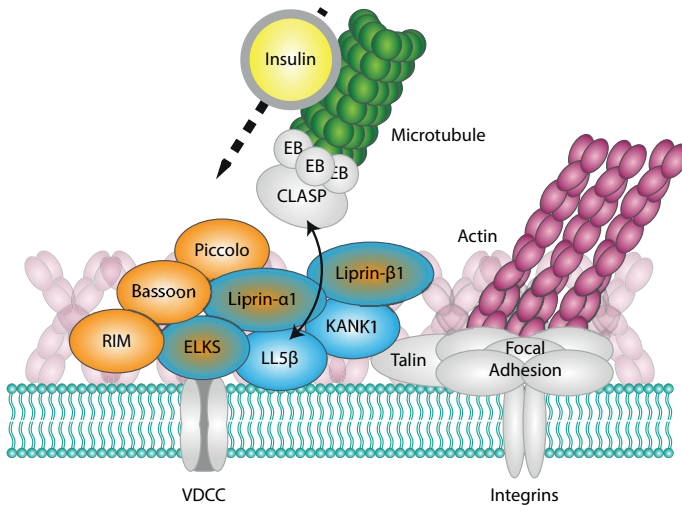


Figure 6: Schematic representation of secretory sites in pancreatic β -cells.

CAZ-specific components are indicated in orange, components that are not present in neurons, in blue, and components shared between neuronal and non-neuronal cells in both colors.

Discussion

In this study, we showed that the sites of insulin secretion in pancreatic β -cells combine molecular components of the neuronal CAZ, controlling the very rapid Ca^{2+} -regulated neurotransmitter secretion (Gundelfinger and Fejtova, 2012; Südhof, 2012), and the cortical platforms responsible for constitutive exocytosis at the leading edges and around focal adhesions in migrating non-neuronal cells (Fig. 6) (Grigoriev et al., 2007; Lansbergen et al., 2006; Stehbens et al., 2014; van der Vaart et al., 2013). The presence of non-neuronal components, such as LL5 β and KANK1, explains the clustering of exocytotic sites in cortical regions where β -cells form integrin-based adhesions to the extracellular matrix, the basement membrane surrounding blood vessels.

Previous work has shown that the depletion of LL5 β perturbs clustering of its cortical partners (Lansbergen et al., 2006; van der Vaart et al., 2013), and we found that the same is true in β -cells. Depletion of LL5 β affected the first rapid phase of insulin release. Enrichment of LL5 β and the microtubule-stabilizing protein CLASP1 at exocytotic sites suggests that these proteins contribute to efficient microtubule connection to the cortex, which could help to balance microtubule-based delivery and withdrawal of insulin granules from secretory platforms, as proposed previously (Bracey et al., 2020; Heaslip et al., 2014; Ho et al., 2020; Tabei et al., 2013; Varadi et al., 2003; Yuan et al., 2015; Zhu et al., 2015). In this way, secretory sites in β -cells are reminiscent of LL5 β - and CLASP-containing podosome-like structures ('synaptic podosomes'), which provide a route for microtubule-based delivery and accumulation of acetylcholine receptors at neuromuscular junctions in skeletal muscle cells (Basu et al., 2015; Kishi et al., 2005; Proszynski et al., 2009; Proszynski and Sanes, 2013; Schmidt et al., 2012). However, although microtubules are in tight contact with the secretion complexes and insulin granules (Müller et al., 2021; Yuan et al., 2015), it is unlikely that the loss of LL5 β perturbs the rapid phase of insulin exocytosis by reducing microtubule density. First, this secretion phase depends on insulin granules that are already docked at the cortex and do not need to be transported along microtubules. Second, recent evidence suggests that dense microtubules at the cortex attenuate rather than promote insulin secretion by controlling vesicle movement away from the plasma membrane (Bracey et al., 2020; Ho et al., 2020; Zhu et al., 2015). Therefore, we favor the idea that LL5 β stimulates insulin secretion by directly enhancing clustering of CAZ components such as RIM, ELKS and liprins, which in turn control, either directly or indirectly, vesicle tethering, connections to the core fusion machinery, such as SNAREs and their regulators, and the activation of voltage-gated calcium channels (reviewed in Gundelfinger and Fejtova, 2012; Ohara-Imaizumi et al., 2019a; Südhof, 2012).

Tight clustering of proteins participating in secretion is a hallmark of neuronal CAZ, and recent work in worms has shown the worm homologues of ELKS and liprin undergo LLPS and then solidify during synapse development (McDonald et al., 2020). Moreover, different mammalian CAZ components can undergo LLPS *in vitro* or when overexpressed in cells (Emperador-Melero et al., 2021; Liang et al., 2021; McDonald et al., 2020; Sala et al., 2019; Wu et al., 2019, 2021). This raised the question of whether LLPS plays a role in organizing secretion machinery in β -cells. Our previous work in non-neuronal cells showed that LL5 β , KANK1 and liprins are recruited to the plasma membrane independently of each other and display their own characteristic turnover, whereas their multivalent interactions with each other and additional membrane-unbound scaffolds such as ELKS promotes their clustering (Bouchet et al., 2016; Lansbergen, 2006; van der Vaart et al., 2013). A similar picture emerges in β -cells – all investigated cortical proteins appear as closely apposed but not fully overlapping membrane-associated foci, which, based on the imaging of endogenously tagged ELKS, contain only a few protein copies that exchange with the cytoplasmic pool and undergo very slow lateral diffusion. The half-time of the slower component of recovery of endogenously tagged ELKS in

pancreatic islets (~5 min) was very similar to that of mildly overexpressed ELKS or liprin- α 1 in HeLa cells (van der Vaart et al., 2013), suggesting that ELKS behaves similarly in other non-neuronal cells. Formation of ELKS condensates in non-neuronal cells (Sala et al., 2019) thus appears to be a consequence of ELKS overexpression, and this is indeed what we have observed when expressing increasing levels of ELKS in HeLa cells. It is still possible that the CAZ in neurons does form by LLPS, for example, because the expression of key players might be higher in neurons than in pancreatic cells, or because more LLPS-prone protein isoforms (e.g. liprin- α 3 rather than liprin- α 1; Emperador-Melero et al., 2021) are expressed. Single-molecule imaging of endogenously tagged mammalian CAZ components in neurons will be needed in order to prove that their complexes indeed represent condensates.

An important distinguishing feature of the secretion sites in β -cells compared to neuronal CAZ is their association with focal adhesions. Integrin activation provides a spatial cue for targeting insulin secretion to blood vessels (Gan et al., 2018; reviewed in Arous and Halban, 2015; Arous and Wehrle-Haller, 2017). Previous work showed that elevated glucose levels lead to enlargement of focal adhesions (Arous and Halban, 2015; Arous and Wehrle-Haller, 2017), and here we found that this is accompanied by enhanced clustering of secretion complexes around adhesions and their increased lateral mobility and turnover. The biochemical basis of this regulation needs to be elucidated and may involve alterations in the state of focal adhesion components, such as conformational changes in talin promoting KANK1 recruitment (Yu et al., 2019), or activation of FAK (Rondas et al., 2011, 2012) and other integrin-linked signaling pathways.

Formation and regulation of focal adhesions critically depends on actomyosin contractility. Here, we showed that inhibition of myosin II, which causes focal adhesion disassembly, had a strong negative effect on the clustering of secretory complexes and the first phase of insulin release from β -cells. This effect represents one of the multiple and complex roles that actin and myosin II play in insulin secretion. Actin filaments in β -cells are seen as tracks for vesicle transport and as a barrier for secretion (Arous and Halban, 2015; Arous and Wehrle-Haller, 2017; Kalwat and Thurmond, 2013). We observed that the exocytotic sites and cortically docked insulin granules form a complementary pattern with the actin filaments, consistent with the idea that a dense cortical actin meshwork might inhibit secretion. On the other hand, myosin II is universally recognized as an important positive regulator of secretion, which acts at different levels, from indirect reorganization of the cortical cytoskeleton to direct contribution to the release of vesicle content during secretion (Arous and Halban, 2015; Gutierrez and Villanueva, 2018; Rouso et al., 2016).

Finally, it is important to note that the interactions between actomyosin, integrin adhesions and secretory machinery are subject to intricate feedback mechanisms. For example, in migrating cells, LL5 β and liprins can regulate integrin activation and focal adhesion turnover (Asperti et al., 2009, 2010; Stehbins et al., 2014). Since integrin-based adhesion to extracellular matrix plays a crucial role in β -cell survival (Bosco et al., 2000; Hammar et al., 2004; Weber et al., 2008), understanding the interplay between secretory machinery, integrin adhesion and the cytoskeleton is important for developing new strategies to treat type 2 diabetes.

Materials and Methods

Cell lines

INS-1E cells (Merglen et al., 2004) (kind gift of Bruno Guigas, Leiden University Medical Center, The Netherlands) were cultured in Roswell Park Memorial Institute (RPMI) medium 1640 (Gibco, Life Technologies) supplemented with 10% fetal calf serum (FCS) (GE Healthcare Life Sciences), 10 mM HEPES pH 7.4, 1 mM sodium pyruvate (Gibco, Life Technologies), 55 μ M β -mercaptoethanol (Gibco, Life Technologies), 11 mM glucose (Sigma-Aldrich) and 1% (v/v) penicillin/streptomycin (Sigma-Aldrich). The human insulinoma cell line EndoC- β H1 cells (Ravassard et al., 2011) obtained from Univercell-Biosolutions, was cultured in complete medium [low glucose DMEM (Gibco, 1 g/l glucose), 2% albumin (Sanquin Bloodbank, The Netherlands), 10 mM nicotinamide (prepared by the Leiden University Medical Center pharmacy), 5.5 g/ml human transferrin (Sigma-Aldrich), 0.5 mg/ml selenite (Sigma-Aldrich), 10 ml penicillin (100 U/ml)/streptomycin (100 g/ml), with fresh β -mercaptoethanol (Sigma-Aldrich) added when culturing (to a final concentration of 0.05 mM)] in a humidified atmosphere with 5% CO₂. HeLa cells were cultured in DMEM (Lonza) supplemented with 10% fetal calf serum (FCS) (GE Healthcare Life Sciences) and 1% (v/v) penicillin/streptomycin. All cells were routinely checked for mycoplasma contamination using the MycoAlert™ Mycoplasma Detection Kit (Lonza).

Mouse pancreatic islets

Both male and female adult 3–6-month-old mice were euthanized by cervical dislocation for the isolation of tissues and primary cultures. All animal experiments were performed in compliance with the institutional guidelines for the welfare of experimental animals approved by the Animal Ethical Review Committee (DEC 2014.I.03.020) of Utrecht University, The Netherlands.

The isolated pancreas was rinsed in PBS, cut into small pieces with surgical blades and incubated in 3 mg/ml collagenase (C9263, Sigma) dissolved in glucose-free RPMI 1640 (Gibco, Life Technologies) in a total volume of 3 ml/pancreas for 20 min at 37°C. During incubation, solution was shaken rigorously. Next, 6 ml of cold RPMI 1640 supplemented with 10% FCS, 10 mM HEPES pH 7.4, 1 mM sodium pyruvate, 55 μ M β -mercaptoethanol and 11 mM glucose was added to the solution, followed by two wash steps using centrifugation (5 min at 200 g and 4°C). After washing, the isolated islets were resuspended in 5 ml RPMI 1640 supplemented as described above, handpicked using a pipette and transferred to new culture dishes until almost no exocrine tissue was left. Finally, the islets were transferred to culture dishes containing Matrigel-coated coverslips. Coverslips were coated with 388 μ g/ml Matrigel (Corning) in phosphate-buffered saline (PBS) for 2 h at 37°C. Isolated islets were cultured in RPMI 1640 supplemented as described for the rat INS-1E cell line until islets were fully attached to coated coverslips.

Human pancreatic islets

Human islet isolations from cadaveric human organ donors were performed in the Good Manufacturing Practice facility of the Leiden University Medical Center according to the method used in the center for the procurement of clinical-grade material (Nijhoff et al., 2016). Islets were isolated from donor pancreas allocated (after anonymization) by Eurotransplant for the clinical islet transplantation program of the Leiden University Medical Center. Islets were used for research only if they could not be used for clinical purposes, and if research consent was obtained according to Dutch national laws.

Islets were cultured in CMRL 1066 medium (Corning, 5.5 mmol/l glucose) containing 10% FCS (Bodinco), 20 mg/ml ciprofloxacin (Fresenius), 50 mg/ml gentamycin (Lonza), 2 mM L-glutamine (Lonza), 10 mM HEPES (pH 7.21, Lonza), and 1.2 mg/ml nicotinamide (prepared by the Leiden University Medical Center pharmacy) in a humidified atmosphere with 5% CO₂. Islets were dispersed into single cells by adding 0.025% trypsin solution containing 10 mg/ml DNase (Pulmozyme, Genentech) at 37°C for 6–8 min.

Immunofluorescence staining of fixed samples

For immunofluorescence staining experiments, cells or pancreatic islets were seeded or attached on coverslips coated with fibronectin (INS-1E, EndoC- β H1), ECM gel (EndoC- β H1, Engelbreth-Holm-Swarm murine sarcoma), Matrigel (mouse pancreatic islets) or poly-L-lysine (dispersed human pancreatic islets). Cells or pancreatic islets were fixed with either 4% paraformaldehyde for 20 min at room temperature (staining for insulin, LL5 β , RIM1/2, bassoon, paxillin, glucagon, VE-cadherin or phalloidin) or -20°C methanol for 10 min (staining for LL5 β , ELKS, liprin- α 1, liprin- β 1, KANK1, RIM, bassoon, CLASP1, pFAKY397 or E-cadherin) followed by permeabilization with 0.15% Triton X-100 for 2 min. Next, samples were blocked with 1% bovine serum albumin (BSA) diluted in PBS

supplemented with 0.05% Tween 20 for 45 min at room temperature and sequentially incubated with primary antibodies (see Table S2) for 1 h at room temperature (pancreatic islets, overnight at 4°C) and fluorescently labeled with secondary antibodies (see Table S2) for 45 min at room temperature (pancreatic islets, 1–3 h). Finally, samples were washed, dried, and mounted in DAPI-containing Vectashield (Vector laboratories).

For human tissue staining experiments, pancreatic tissue biopsies (1 cm×1 cm×1 cm max) were fixed in 4% Formalin (Klinipath) for 24–48 h. After fixation, tissue was placed in 70% ethanol, before moving to dehydration in an ascending series of ethanol (10–100%), followed by xylene and paraffin. Paraffin blocks were cut into 4 μm sections (Leica RM2255 Microtome). Sections were rehydrated and antigen retrieval was performed by heating slides in citrate buffer (pH 6.0) using a pressure cooker. Sections were blocked with 5% normal donkey serum (in 0.3% Triton X-100 in PBS), stained with primary antibodies (LL5β and RIM) overnight at 4°C followed by 1 h incubation with fluorescently labeled secondary antibodies. Subsequently, sections were incubated for 1 h at room temperature with a primary antibody against C-peptide (Abcam), followed by 1 h incubation with corresponding fluorescently labeled secondary antibody. Finally, samples were incubated for 3 min with Hoechst 33258 for nuclear staining and slides were mounted with Prolong gold (ThermoFisher).

For immunofluorescence staining prior to SMLM, cells were extracted and fixed in 0.5% Triton X-100 and 4% PFA in cytoskeleton buffer (10 mM MES pH 6.1, 150 mM NaCl, 5 mM MgCl₂, 5 mM EGTA and 5 mM glucose) for 15 min at room temperature. Next, cells were blocked in 1% BSA diluted in PBS supplemented with 0.05% Tween-20 for 45 min at room temperature and sequentially stained with primary antibodies overnight at 4°C. After three washes in PBS, cells were incubated with either a fluorescently labeled secondary antibody or DNA-sequence-conjugated secondary antibodies (Ultivue) (see Table S2) for 1.5 h at room temperature. Coverslips were mounted in a Ludin chamber.

Co-immunoprecipitation from INS-1E cell extracts

For co-immunoprecipitation, proteins were extracted from INS-1E cells in a Triton X-100 lysis buffer [20 mM Tris-Cl pH 7.5, 150 mM NaCl, 0.5 mM EDTA, 1 mM DTT, 1% Triton X-100, and a protease inhibitor cocktail (Roche)] with gentle rotation for 30 min at 4°C. All further steps were also executed at 4°C. The sample was centrifuged for 20 min at 16,100 g to obtain the supernatant, which was further incubated with Affi-prep Protein A beads (Bio-Rad) for preclearing for 30 min. The sample was centrifuged for 10 min at 16,100 g and the supernatant was further incubated with rabbit control serum or anti-ELKS antibody (Proteintech) for 1 h. After adding Affi-prep Protein A beads, the sample was further incubated for 1 h with rotation. The beads were washed three times before the proteins were eluted by boiling them in an SDS-PAGE sample buffer. The samples were subjected to SDS-PAGE followed by western blotting for analysis.

siRNA and transient DNA transfection

Lipofectamine RNAiMAX (Invitrogen) was used to transfect INS-1E cells with 20 nM siRNAs (see Table S2). Corresponding experiments were performed 72 h after siRNA transfection. FuGene6 (Promega) was used to transiently transfect HeLa cells with DNA. Experiments were performed 28 h after DNA transfection.

Glucose and drug treatment of INS-1E

Before the induction glucose-stimulated insulin secretion, INS-1E cells were glucose starved by culturing the cells for a minimum of 4 h in culture medium as described above supplemented with 2 mM glucose (termed untreated or low glucose). Glucose-stimulated insulin secretion was induced by culturing glucose starved INS-1E cells in the culture medium as described above supplemented with 25 mM glucose (termed high glucose). Cells were treated with 50 μM lebbistatin for 1 h prior to fixation or live-cell imaging.

Generation of GFP–ELKS mouse line

The knockout targeting construct was generated by inserting GFP fused in frame with an N-terminal peptide that can be biotinylated by the biotin ligase BirA (de Boer et al., 2003) and a neomycin resistance cassette flanked by loxP sites in front of the start codon of the mouse *Elks1* gene into exon 3 using a PCR-based strategy. The construct was linearized and electroporated into IB10 embryonic stem cells (ESCs), which were cultured in BRL-cell conditioned medium as described previously (Hoogenraad et al., 2002). Targeted ESCs were further selected with G418 (200 μg/ml; Life Technologies) for neomycin resistance, and individual clones were picked and expanded. Genotyping by PCR was performed to check for the positive clones, which were subsequently injected in blastocysts obtained from C57Bl/6 females. Male chimera mice were mated with C57Bl/6 females to transmit the ELKS knockout allele

to the germline. The generation of the Elks1-knockout mice was performed in compliance with the institutional guidelines and approved by the Animal Ethical Review Committee (DEC) of the Erasmus Medical Center, Rotterdam, The Netherlands.

To obtain GFP-ELKS knock-in mice, heterozygous Elks1 knockout mice were crossed with mice in which the Cre gene is under the control of the cytomegalovirus immediate early enhancer-chicken β -actin hybrid promoter and is expressed in oocytes (Sakai and Miyazaki, 1997). Mice were genotyped by PCR.

Preparation of mouse tissue extracts

Mouse tissues were dissected and placed in ice-cold PBS, pH 7.4. Samples were weighted and homogenized in ice-cold homogenization buffer [150 mM NaCl, 50 mM Tri-HCl pH 8, 0.1% v/v SDS, 0.5% (v/v) NP-40, 1 \times complete protease inhibitor, Roche] with stainless metal beads (Qiagen) using the TissueLyser II (Qiagen) for 30 min. Tissue lysates were then centrifuged at 16,000 g at 4°C for 1 h. Supernatant was used for western blotting.

Fluorescence microscopy

Widefield microscopy

Fixed and stained INS-1E cells were imaged using widefield fluorescence illumination on a Nikon Eclipse 80i upright microscope equipped with a CoolSNAP HQ2 CCD camera (Photometrics), an Intensilight C-HGFI precentered fiber illuminator (Nikon), ET-DAPI, ET-EGFP and ET-mCherry filters (Chroma), controlled by Nikon NIS Br software and using a Plan Apo VC 23 100 \times NA 1.4 oil, Plan Apo VC 60 \times NA 1.4 oil or a Plan Fluor 20 \times MI NA 0.75 oil objective (Nikon). For presentation, images were adjusted for brightness using ImageJ 1.50b.

TIRF microscopy

Fixed and stained INS-1E cells, EndoC- β H1, dispersed human pancreatic islets and live GFP-ELKS-expressing pancreatic islets were imaged using TIRFM performed on an inverted research microscope Nikon Eclipse Ti-E (Nikon) with a perfect focus system (PFS) (Nikon), equipped with a Nikon CFI Apo TIRF 100 \times 1.49 NA oil objective (Nikon), Evolve 512 EMCCD (Photometrics) or Prime BSI camera (Photometrics) or CoolSNAP HQ2 CCD camera (Roper Scientific) and controlled with the MetaMorph 7.7.11.0 software (Molecular Devices). Images were projected onto the chip of an Evolve 512 camera with an intermediate lens 2.5 \times (Nikon C mount adapter 2.5 \times) or onto a CoolSNAP HQ2 or a Prime BSI chip without the lens. In all cases the final magnification was equal to 0.065 μ m/pixel. To keep cells at 37°C a stage top incubator INUBG2E-ZILCS (Tokai Hit) was used. For excitation, 491 nm 100 mW Stradus (Vortran), 561 nm 100 mW Jive (Cobolt) and 642 nm 110 mW Stradus (Vortran) lasers were used. The microscope was equipped with an ET-GFP 49002 filter set (Chroma) for imaging of proteins tagged with GFP, an ET-mCherry 49008 (Chroma) and an ET-405/488/561/647 filter set. For presentation, images were adjusted for brightness using ImageJ 1.50b.

Spinning disc microscopy

Fixed and stained INS-1E cells, dispersed human pancreatic islets and isolated mouse pancreatic islets were imaged using confocal fluorescence illumination on a Nikon Eclipse Ti microscope equipped with a perfect focus system (PFS, Nikon), a spinning-disc-based confocal scanner unit (CSU-X1-A1, Yokogawa), an Evolve 512 EMCCD camera (Photometrics) attached to a 2.0 \times intermediate lens (Edmund Optics), a super-high-pressure mercury lamp (C-SHG1, Nikon), a Roper Scientific set of Stradus 405-nm (100 mW, Vortran), Calypso 491-nm (100 mW, Cobolt) and Jive 561-nm (100 mW, Cobolt) lasers, a set of ET-BFP2, ET-EGFP, ET-mCherry and ET-EGFP-mCherry filters (Chroma) for wide-field fluorescence observation, a set of ET460/50m, ET525/50m or ET535/30m (green), ET630/75m (red) and ET-EGFP/mCherry filters (Chroma) for spinning-disc-based confocal imaging and a motorized stage MS-2000-XYZ with Piezo Top Plate (ASI). The microscope setup was controlled by MetaMorph 7.7.11.0 software. Images were acquired using Plan Fluor 10 \times NA 0.3 air, Plan Fluor 20 \times MI NA 0.75 oil, Apo LWD λ S 40 \times NA 1.15 water, Plan Apochromat λ 60 \times NA 1.4 oil and Plan Apo VC 60 \times NA 1.4 oil objectives. Images are presented as single plane images or maximum projections of 0.5- μ m-step z-scans and adjusted for brightness using ImageJ 1.50b.

Fixed and stained human pancreatic tissue sections were examined using a commercially available DragonFly200 spinning disc system (Andor) on a DMi8 microscope (Leica) with Plan Apo 40 \times NA 1.3 and Plan Apo 63 \times NA 1.4 oil immersion objectives. Microscope setup was controlled by Fusion software (Andor), and images were taken with a Zyla sCMOS camera (Andor).

STED microscopy

Super-resolution imaging of cortical proteins in INS-1E cells was performed using gated STED modality on a Leica TCS SP8 STED 3X SMD confocal microscope, using spectroscopic detection with HyD hybrid detector. For the illumination we used a fully tunable supercontinuum white light laser (WLL; 470 to 670 nm) and 592 nm, 660 nm, and 775 nm STED depletion lasers. Images were acquired using a HC PL APO CS2 100×/1.40 NA oil objective. Alexa-Fluor-488-conjugated antibodies were excited with the 488 nm WLL (80 MHz) and depleted with the CW 592 nm STED depletion laser. Alexa-Fluor-594-conjugated antibodies were excited with the 594 nm super continuum white laser (80 MHz) and depleted with the 775 nm STED pulsed depletion laser. For presentation, images were adjusted for brightness using ImageJ 1.50b.

Single-molecule localization microscopy

Single-molecule localization microscopy (SMLM) of fixed INS-1E cells was performed using a Nikon Ti-E microscope with a 100× Apo TIRF oil immersion objective (NA 1.49) and a Perfect Focus System 3. Excitation was performed through a custom illumination pathway with a Lighthub-6 (Omicron) laser containing a 638 nm laser (BrixX 500 mW multimode, Omicron), a 488 nm laser (Luxx 200 mW, Omicron), and a 405 nm laser (Luxx 60 mW, Omicron) and optics to tune the incident angle for evanescent wave or oblique illumination. Signal was detected with a sCMOS camera (Hamamatsu Flash 4.0v2). For imaging of actin and insulin, first a widefield image of insulin was obtained. Then, a low concentration of LifeAct-mNeonGreen was added such that single molecules could be observed and ~25,000 frames were acquired at 60 ms exposure to reconstruct a super-resolved image (Schätzle et al., 2018; Tas et al., 2018). For co-imaging of paxillin, RIM and actin, first sequential DNA-PAINT was performed with Imager strands I2-560 and I1-650 (Ultivue) to image RIM and paxillin, respectively, with 100 ms exposure time and subsequently LifeAct-mNeonGreen was added to image actin similar to the imaging of actin and insulin described above. Images were reconstructed using 'Detection of Molecules' ImageJ plugin v.1.2.2 (https://github.com/ekatrakha/DoM_Utrecht; Chazeau et al., 2016).

Image analysis

Colocalization analysis

Pearson's correlation coefficients were calculated using the Coloc2 plug-in with TIRFM images acquired as described above. A region of interest was picked in both image channels and Pearson's correlation coefficient was calculated without using a threshold. To rule out non-specific colocalization, the same analysis was done but with one image channel rotated 90° clockwise.

Quantification of focal adhesion complexes

Focal adhesion size was quantified using pFAKY397 TIRFM images acquired as described above. Focal adhesions were detected using 'Automated Moments' thresholding followed by particle detection using particle analysis with a minimal size cut-off of 0.15 μm^2 .

Enrichment of LL5 β or ELKS around focal adhesions was quantified using pFAKY397 or paxillin, and LL5 β or ELKS TIRFM images acquired as described above. Focal adhesions were detected using 'Automated Moments' thresholding followed by particle detection using particle analysis with a minimal size cut-off of 0.15 μm^2 . The total fluorescence intensity of LL5 β or ELKS was measured in 3- μm -broad areas surrounding each focal adhesion, and normalized for surface area. To measure total fluorescence intensity of LL5 β or ELKS outside focal adhesion areas, the opposite of focal adhesion areas was selected by inverting the enlarged focal adhesion areas. Total fluorescence intensity of LL5 β or ELKS outside focal adhesion areas was measured and normalized for surface area. All regions of interests were restricted to areas occupied by cells.

Recruitment of LL5 β to focal adhesions upon glucose-stimulated insulin secretion was quantified using pFAK397 and LL5 β TIRFM images acquired as described above. Focal adhesions were detected using 'Automated Moments' thresholding in ImageJ followed by particle detection using particle analysis with a minimal size cut-off of 0.15 μm^2 . The total fluorescence intensity of LL5 β was measured in 1- μm -broad areas surrounding each focal adhesion and normalized for surface area. Finally, the total fluorescence intensity of LL5 β was measured in the original focal adhesion areas, normalized for surface area and subtracted from normalized total fluorescence intensity of LL5 β in enlarged focal adhesion areas. Only data-points exceeding LL5 β fluorescent background signal by 1.5 times were used for plots. For each ROI, we then generated a distribution of LL5 β recruitment levels per focal adhesion and plotted the values falling into the upper 75% (high recruitment level), whereas the rest were considered as low recruitment.

Quantification of cluster intensity

LL5 β , RIM and GFP-ELKS cluster numbers were quantified using the respective TIRFM images acquired as described above. Images were subjected to Gaussian blur with the radius of 1 pixel and ‘Unsharp’ filtering, followed by ‘Automated Intermodes’ (LL5 β) or ‘Automated Moments’ (RIM, GFP-ELKS) thresholding. Next, a watershed-based segmentation was applied, and clusters were detected using particle analysis with a minimal size cut-off of $0.10 \mu\text{m}^2$.

Docked insulin vesicles were quantified using insulin TIRFM images acquired as described above. Images were subjected to Gaussian blur with the radius of 1 pixel and ‘Unsharp’ filtering, followed by ‘Automated Moments’ thresholding. Next, a watershed-based segmentation was applied, and vesicles were detected using particle analysis with a minimal size cut-off of $0.01 \mu\text{m}^2$.

RIM and GFP-ELKS clustering was quantified using the respective TIRFM images acquired as described above. Images were subjected to Gaussian blur with the radius of 1 pixel and ‘Unsharp’ filtering, followed by ‘Automated Moments’ thresholding. Next, a Watershed-based segmentation was applied, and puncta were detected using particle analysis with a minimal size cut-off of $0.10 \mu\text{m}^2$. The obtained regions of interest were subjected to the ‘Nearest Neighbor Distance Calculation’ ImageJ plugin, and distances were binned in 50 nm bins and plotted as frequency distributions.

Insulin vesicle z-distributions were quantified using insulin confocal images acquired with the setup described above. Z-series images were acquired using a $0.5\text{-}\mu\text{m}$ -step confocal based scan. Images were subjected to Gaussian blur with the radius of 1 pixel and ‘Unsharp’ filtering, followed by ‘Automated Moments’ thresholding. Next, a watershed-based segmentation was applied, and vesicles were detected using particle analysis with a minimal size cut-off of $0.12 \mu\text{m}^2$.

FRAP analysis

FRAP experiments with GFP-ELKS-expressing pancreatic islets were performed using the TIRFM setup described above using CoolSNAP HQ2 camera. FRAP was measured by first acquiring 5 frames every 1 s, followed by bleaching a $5\text{-}\mu\text{m}$ -diameter circle in GFP-ELKS patches followed by 5 min imaging with a frame interval of 5 s and 15 min imaging with a frame interval of 10 s. FRAP acquisitions were corrected for the sample drift using 2D cross-correlation function of ‘Correlescence’ ImageJ plugin (ver.0.0.4, <https://github.com/ekatrakha/Correlescence>). Whole, inner, and outer ROI intensity-time measurements were performed using a custom written ImageJ macro and averaged in MATLAB (available upon request). The recovery curves of intensity were background-subtracted, corrected for the bleaching caused by imaging, and normalized according to Phair et al. (2004). To choose the best fitting to the recovery curves, we performed extra sum-of-squares F test between one-phase and two-phase association exponential recovery equations in GraphPad Prism. In both cases (low and high glucose) two-phase association was the preferred model with $p < 0.0001$. Kymographs of recovery areas were built using KymoResliceWide plugin for ImageJ v.0.3 (<https://github.com/ekatrakha/KymoResliceWide>).

FRAP experiments with GFP-ELKS-expressing HeLa cells were performed using the spinning disc setup. Fluorescence recovery was imaged by first acquiring 5 frames every 200 ms, followed by bleaching an $8 \mu\text{m}^2$ square around GFP-ELKS condensates followed by 1 min imaging with a frame interval of 200 ms.

Analysis of trajectories of GFP-ELKS clusters and single molecules

GFP-ELKS clusters and single molecule dynamics were imaged using the TIRFM setup described above using Prime BSI camera. To record movement of the clusters, we performed timelapse acquisition every 5 s with 50 ms exposure for 200 frames. Movies were corrected for sample drift using 2D cross-correlation function of ‘Correlescence’ ImageJ plugin (ver. 0.0.4, <https://github.com/ekatrakha/Correlescence>). Cluster detection and linking of trajectories were performed using ‘Detection of Molecules’ ImageJ plugin (https://github.com/ekatrakha/DoM_Utrecht) with linking radius of $0.325 \mu\text{m}$ per frame and zero frame gap.

For the single molecule acquisition, we selected previously unexposed area of islets and first performed stream acquisition of 1000 frames with 33 ms exposure with full laser power to ensure complete photobleaching of bright clusters. After a short recovery (10–15 s) with the same laser power we performed a second acquisition of 1000 frames with 33 ms exposure. These paired acquisitions were used both to track single molecules and quantify stoichiometry of clusters (see below). To separate fast movements of the single molecules, we applied a temporal median filter with the sliding window of 15 frames (~ 0.5 s) to each pixel of the second acquisition (Hoogendoorn et al., 2014; Masucci et al., 2021). To retrieve slow movements, we subtracted the generated results of temporal median filter from all pixels/frames of the original movie using Image Calculator function of ImageJ. Tracking of single molecules in these generated movies was performed using the ‘Detection of Molecules’ ImageJ plugin. Average MSD curves were generated using ‘msd_analyzer’ Matlab class (Tarantino et al., 2014)

and imported to GraphPad Prism for linear fitting. Log-log MSD probability density heatmaps were built using a custom written Matlab script.

Analysis of the intensity of GFP–ELKS clusters

To determine the number of GFP–ELKS molecules within clusters, we used the paired set of single molecule acquisitions described in the previous section. Cluster intensity distribution $\rho_{\text{clusters}}(I)$ was measured from detections in the first frame of unexposed first acquisition. We used amplitude of fitted 2D Gaussian (with an offset background) I as a measure of spot intensity. To estimate intensity distribution of single GFP molecules $\rho_1(I)$ we selected intensity in the last detection in the trajectories obtained from the slow component of the second acquisition, before complete photobleaching. Both $\rho_{\text{clusters}}(I)$ and $\rho_1(I)$ were constructed numerically from the individual spot intensity measurements I_1, I_2, \dots, I_M in the following order. First, we calculated optimal intensity sampling step (bin size) δI according to the Freedman-Diaconis rule:

$$\delta I = 2 \frac{\text{IQR}(I)}{\sqrt[3]{M}}$$

From each fitting of the fluorescent spot, apart from the value of 2D Gaussian amplitude, we determined σ , the value of its uncertainty (error). The final $\rho(I)$ were constructed at intensity steps of δI as a sum of normal distributions with means equal to I_1, I_2, \dots, I_M and standard deviations $\sigma_1, \sigma_2, \dots, \sigma_M$.

To build corresponding intensity distributions of N colocalized independent GFP molecules $\rho_N(I)$, we recursively calculated a series of convolution integrals as described previously (Moertelmaier et al., 2005):

$$\rho_N(I) = \int \rho_1(\tilde{I}) \rho_{N-1}(I - \tilde{I}) d\tilde{I}$$

For the numerical implementation, we first approximated discretely sampled $\rho_1(I)$ with B-splines. To calculate $\rho_2(I)$ we convoluted $\rho_1(I)$ with itself using numerical integration with Gauss–Kronrod quadrature formula (Matlab function “quadgk”). After B-spline approximation of $\rho_2(I)$, we calculated its convolution with $\rho_2(I)$ and so on. Overall, for the purpose of fitting, we constructed GFP N -mers basis consisting of oligomers with $N_{\text{max}}=100$ GFP molecules. The cluster intensity distribution $\rho_{\text{clusters}}(I)$ was fitted with a mixture of oligomers $\rho_{\text{fit}}(I)$ using a linear combination of their intensities:

$$\rho_{\text{fit}}(I) = \sum_{N=1}^{N_{\text{max}}} \alpha_N \rho_N(I)$$

where α_N stands for the weights of individual distributions, with $\sum_{N=1}^{N_{\text{max}}} \alpha_N = 1$ representing fractions of the respective GFP N -mers. The fitting was performed using Matlab “fmincon” function using normalization constraint on the weights. As an optimization function, we used maximum likelihood estimation. Practically, at each fitting step, we minimized a sum of negative log-likelihoods for intensity values used to construct $\rho_{\text{clusters}}(I)$ to be sampled from $\rho_{\text{fit}}(I)$ at the current minimizing iteration. The procedure was conducted for each field-of-view acquisition and obtained oligomers weight were averaged to produce final histograms.

Analysis of GFP–ELKS expression in HeLa cells

Mean ELKS intensity per cell was determined by dividing the integrated intensity per cell by total cell area. To determine the condensate area as percentage of total cell area, the maximum pixel intensity where no condensates were formed was measured first. This pixel intensity was subtracted from every pixel intensity in the image. The integrated intensity per cell was measured again and this was plotted as percentage of the earlier measured integrated intensity per cell.

Quantification and statistical analysis

All experiments were conducted at least twice. Statistical analysis was performed using GraphPad Prism 9. Statistical details of each experiment, including the statistical tests used, explanation and value of n and precision measures can be found in the figure legends.

Supplementary movie legends

Movie 1: Dynamics GFP-ELKS clusters in an isolated mouse pancreatic islet.

An example TIRFM acquisition of GFP-ELKS clusters (top) and the corresponding overlay of trajectories (bottom).

Movie 2: Dynamics of single GFP-ELKS molecules in an isolated mouse pancreatic islet.

An example TIRFM acquisition of single GFP-ELKS molecules (top left) and the corresponding overlay of trajectories (bottom left). Right panels illustrate the temporal median filtering method, the splitting of the acquisition into fast (top) and slow (bottom) components.

Movie 3: Transitions of single GFP-ELKS molecules between diffusive and tethered states.

An example TIRFM acquisition of single GFP-ELKS molecules (left) and the corresponding overlay of trajectories (right).

Acknowledgements

We are grateful to M. Jaegle, S. Driegen and B. van der Vaart for technical input in ES cell targeting; J. Kong-a San and A. Maas for blastocyst injection; D. Jaarsma, V. van Dis, E. D. Haasdijk, I. M. Bergen, R. Hendriks, and G. A. Arkesteijn for their help with characterizing Elks1 knockout mice. We thank N. de Graaf for technical support concerning cell culture and J. Sanes and F. Melchior for the gift of antibodies.

Author Contributions

I. N., C. M. vd B. and E. A. K. performed experiments, analyzed data and wrote the paper, F. W. J. B. performed experiments with the human cell line and human pancreatic islets, K. L. Y. generated Elks1 knockout mice, R. P. T. performed super-resolution microscopy experiments, S. P. organized mouse experiments, B. J. V. performed experiments, L. C. K. set up super-resolution microscopy imaging and data analysis and wrote the paper, F. C. and E. J. P. d K. organized human cell line and pancreatic islet experiments and wrote the paper, E. de G. and C. C. H. organized mouse experiments and wrote the paper, A. A. coordinated the project and wrote the paper.

Conflict of Interest

The authors declare no competing interests.

References

- Arous, C., and P.A. Halban. 2015. The skeleton in the closet: actin cytoskeletal remodeling in beta-cell function. *Am J Physiol Endocrinol Metab.* 309:E611-620.
- Arous, C., D. Rondas, and P.A. Halban. 2013. Non-muscle myosin IIA is involved in focal adhesion and actin remodelling controlling glucose-stimulated insulin secretion. *Diabetologia.* 56:792-802.
- Arous, C., and B. Wehrle-Haller. 2017. Role and impact of the extracellular matrix on integrin-mediated pancreatic beta-cell functions. *Biol Cell.* 109:223-237.
- Asperti, C., V. Astro, A. Totaro, S. Paris, and I. de Curtis. 2009. Liprin-alpha1 promotes cell spreading on the extracellular matrix by affecting the distribution of activated integrins. *J Cell Sci.* 122:3225-3232.
- Asperti, C., E. Pettinato, and I. de Curtis. 2010. Liprin-alpha1 affects the distribution of low-affinity beta1 integrins and stabilizes their permanence at the cell surface. *Exp Cell Res.* 316:915-926.
- Astro, V., S. Chiaretti, E. Magistrati, M. Fivaz, and I. de Curtis. 2014. Liprin-alpha1, ERC1 and LL5 define polarized and dynamic structures that are implicated in cell migration. *J Cell Sci.* 127:3862-3876.
- Axelrod, D., D.E. Koppel, J. Schlessinger, E. Elson, and W.W. Webb. 1976. Mobility measurement by analysis of fluorescence photobleaching recovery kinetics. *Biophys J.* 16:1055-1069.
- Basu, S., S. Sladeczek, Y.V.I. Martinez de la Pena, M. Akaaboune, I. Smal, K. Martin, N. Galjart, and H.R. Brenner. 2015. CLASP2-dependent microtubule capture at the neuromuscular junction membrane requires LL5beta and actin for focal delivery of acetylcholine receptor vesicles. *Mol Biol Cell.* 26:938-951.
- Bernadzki, K.M., K.O. Rojek, and T.J. Proszynski. 2014. Podosomes in muscle cells and their role in the remodeling of neuromuscular postsynaptic machinery. *Eur J Cell Biol.* 93:478-485.
- Bosco, D., P. Meda, P.A. Halban, and D.G. Rouiller. 2000. Importance of cell-matrix interactions in rat islet beta-cell secretion in vitro: role of alpha6beta1 integrin. *Diabetes.* 49:233-243.
- Bouchet, B.P., R.E. Gough, Y.C. Ammon, D. van de Willige, H. Post, G. Jacquemet, A.M. Altelaar, A.J. Heck, B.T. Goult, and A. Akhmanova. 2016. Talin-KANK1 interaction controls the recruitment of cortical microtubule stabilizing complexes to focal adhesions. *eLife.* 5:e18124.
- Bracey, K.M., K.H. Ho, D. Yampolsky, G. Gu, I. Kaverina, and W.R. Holmes. 2020. Microtubules Regulate Localization and Availability of Insulin Granules in Pancreatic Beta Cells. *Biophys J.* 118:193-206.
- Cai, E.P., M. Casimir, S.A. Schroer, C.T. Luk, S.Y. Shi, D. Choi, X.Q. Dai, C. Hajmrle, A.F. Spigelman, D. Zhu, H.Y. Gaisano, P.E. MacDonald, and M. Woo. 2012. In vivo role of focal adhesion kinase in regulating pancreatic beta-cell mass and function through insulin signaling, actin dynamics, and granule trafficking. *Diabetes.* 61:1708-1718.
- Chazeau, A., E.A. Katrukha, C.C. Hoogenraad, and L.C. Kapitein. 2016. Studying neuronal microtubule organization and microtubule-associated proteins using single molecule localization microscopy. *Methods Cell Biol.* 131:127-149.
- Chen, X., X. Wu, H. Wu, and M. Zhang. 2020. Phase separation at the synapse. *Nat Neurosci.* 23:301-310.
- Cottle, L., W.J. Gan, I. Gilroy, J.S. Samra, A.J. Gill, T. Loudovaris, H.E. Thomas, W.J. Hawthorne, M.A. Kebede, and P. Thorn. 2021. Structural and functional polarisation of human pancreatic beta cells in islets from organ donors with and without type 2 diabetes. *Diabetologia.* 64:618-629.
- Curry, D.L., L.L. Bennett, and G.M. Grodsky. 1968. Dynamics of insulin secretion by the perfused rat pancreas. *Endocrinology.* 83:572-584.
- de Boer, E., P. Rodriguez, E. Bonte, J. Krijgsveld, E. Katsantoni, A. Heck, F. Grosveld, and J. Strouboulis. 2003. Efficient biotinylation and single-step purification of tagged transcription factors in mammalian cells and transgenic mice. *Proc Natl Acad Sci U S A.* 100:7480-7485.
- Emperador-Melero, J., M.Y. Wong, S.S.H. Wang, G. de Nola, H. Nyitrai, T. Kirchhausen, and P.S. Kaeser. 2021. PKC-phosphorylation of Liprin-alpha3 triggers phase separation and controls presynaptic active zone structure. *Nat Commun.* 12:3057.
- Fourriere, L., A. Kasri, N. Gareil, S. Bardin, H. Bousquet, D. Pereira, F. Perez, B. Goud, G. Boncompain, and S. Miserey-Lenkei. 2019. RAB6 and microtubules restrict protein secretion to focal adhesions. *J Cell Biol.* 218:2215-2231.
- Gan, W.J., O.H. Do, L. Cottle, W. Ma, E. Kosobrodova, J. Cooper-White, M. Bilek, and P. Thorn. 2018. Local Integrin Activation in Pancreatic beta Cells Targets Insulin Secretion to the Vasculature. *Cell Rep.* 24:2819-2826.
- Gan, W.J., M. Zavortink, C. Ludick, R. Templin, R. Webb, W. Ma, P. Poronnik, R.G. Parton, H.Y. Gaisano, A.M. Shewan, and P. Thorn. 2017. Cell polarity defines three distinct domains in pancreatic beta-cells. *J Cell Sci.* 130:143-151.
- Grigoriev, I., D. Splinter, N. Keijzer, P.S. Wulf, J. Demmers, T. Ohtsuka, M. Modesti, I.V. Maly, F. Grosveld, C.C. Hoogenraad, and A. Akhmanova. 2007. Rab6 regulates transport and targeting of exocytotic carriers. *Dev Cell.* 13:305-314.
- Gundelfinger, E.D., and A. Fejtova. 2012. Molecular organization and plasticity of the cytomatrix at the active zone. *Curr Opin Neurobiol.* 22:423-430.

- Gutierrez, L.M., and J. Villanueva. 2018. The role of F-actin in the transport and secretion of chromaffin granules: an historic perspective. *Pflugers Archiv*. 470:181-186.
- Hammar, E., G. Parnaud, D. Bosco, N. Perriraz, K. Maedler, M. Donath, D.G. Rouiller, and P.A. Halban. 2004. Extracellular matrix protects pancreatic beta-cells against apoptosis: role of short- and long-term signaling pathways. *Diabetes*. 53:2034-2041.
- Hammar, E., A. Tomas, D. Bosco, and P.A. Halban. 2009. Role of the Rho-ROCK (Rho-associated kinase) signaling pathway in the regulation of pancreatic beta-cell function. *Endocrinology*. 150:2072-2079.
- Hayashi, Y., L.K. Ford, L. Fioriti, L. McGurk, and M. Zhang. 2021. Liquid-Liquid Phase Separation in Physiology and Pathophysiology of the Nervous System. *J Neurosci*. 41:834-844.
- Heaslip, A.T., S.R. Nelson, A.T. Lombardo, S. Beck Previs, J. Armstrong, and D.M. Warshaw. 2014. Cytoskeletal dependence of insulin granule movement dynamics in INS-1 beta-cells in response to glucose. *PLoS One*. 9:e109082.
- Ho, K.H., X. Yang, A.B. Osipovich, O. Cabrera, M.L. Hayashi, M.A. Magnuson, G. Gu, and I. Kaverina. 2020. Glucose Regulates Microtubule Disassembly and the Dose of Insulin Secretion via Tau Phosphorylation. *Diabetes*. 69:1936-1947.
- Hoogendoorn, E., K.C. Crosby, D. Leyton-Puig, R.M. Breedijk, K. Jalink, T.W. Gadella, and M. Postma. 2014. The fidelity of stochastic single-molecule super-resolution reconstructions critically depends upon robust background estimation. *Sci Rep*. 4:3854.
- Hoogenraad, C.C., B. Koekkoek, A. Akhmanova, H. Krugers, B. Dortland, M. Miedema, A. van Alphen, W.M. Kistler, M. Jaegle, M. Koutsourakis, N. Van Camp, M. Verhoye, A. van der Linden, I. Kaverina, F. Grosveld, C.I. De Zeeuw, and N. Galjart. 2002. Targeted mutation of *Cyln2* in the Williams syndrome critical region links CLIP-115 haploinsufficiency to neurodevelopmental abnormalities in mice. *Nat Genet*. 32:116-127.
- Kaido, T., M. Yebra, V. Cirulli, C. Rhodes, G. Diaferia, and A.M. Montgomery. 2006. Impact of defined matrix interactions on insulin production by cultured human beta-cells: effect on insulin content, secretion, and gene transcription. *Diabetes*. 55:2723-2729.
- Kalwat, M.A., and D.C. Thurmond. 2013. Signaling mechanisms of glucose-induced F-actin remodeling in pancreatic islet beta cells. *Exp Mol Med*. 45:e37.
- Kishi, M., T.T. Kummer, S.J. Eglén, and J.R. Sanes. 2005. LL5beta: a regulator of postsynaptic differentiation identified in a screen for synaptically enriched transcripts at the neuromuscular junction. *J Cell Biol*. 169:355-366.
- Kiyonaka, S., H. Nakajima, Y. Takada, Y. Hida, T. Yoshioka, A. Hagiwara, I. Kitajima, Y. Mori, and T. Ohtsuka. 2012. Physical and functional interaction of the active zone protein CAST/ERC2 and the beta-subunit of the voltage-dependent Ca(2+) channel. *J Biochem*. 152:149-159.
- Ko, J., M. Na, S. Kim, J.R. Lee, and E. Kim. 2003. Interaction of the ERC family of RIM-binding proteins with the liprin-alpha family of multidomain proteins. *J Biol Chem*. 278:42377-42385.
- Kong, X., D. Yan, J. Sun, X. Wu, H. Mulder, X. Hua, and X. Ma. 2014. Glucagon-like peptide 1 stimulates insulin secretion via inhibiting RhoA/ROCK signaling and disassembling glucotoxicity-induced stress fibers. *Endocrinology*. 155:4676-4685.
- Krishnamurthy, M., J. Li, M. Al-Masri, and R. Wang. 2008. Expression and function of alphabeta1 integrins in pancreatic beta (INS-1) cells. *J Cell Commun Signal*. 2:67-79.
- Lansbergen, G., and A. Akhmanova. 2006. Microtubule plus end: a hub of cellular activities. *Traffic*. 7:499-507.
- Lansbergen, G., I. Grigoriev, Y. Mimori-Kiyosue, T. Ohtsuka, S. Higa, I. Kitajima, J. Demmers, N. Galjart, A.B. Houtsmuller, F. Grosveld, and A. Akhmanova. 2006. CLASPs attach microtubule plus ends to the cell cortex through a complex with LL5beta. *Dev Cell*. 11:21-32.
- Liang, M., G. Jin, X. Xie, W. Zhang, K. Li, F. Niu, C. Yu, and Z. Wei. 2021. Oligomerized liprin-alpha promotes phase separation of ELKS for compartmentalization of presynaptic active zone proteins. *Cell Rep*. 34:108901.
- Liu, C., L.S. Bickford, R.G. Held, H. Nyitrai, T.C. Sudhof, and P.S. Kaeser. 2014. The active zone protein family ELKS supports Ca²⁺ influx at nerve terminals of inhibitory hippocampal neurons. *J Neurosci*. 34:12289-12303.
- Low, J.T., M. Zavortink, J.M. Mitchell, W.J. Gan, O.H. Do, C.J. Schwiening, H.Y. Gaisano, and P. Thorn. 2014. Insulin secretion from beta cells in intact mouse islets is targeted towards the vasculature. *Diabetologia*. 57:1655-1663.
- Masucci, E.M., P.K. Relich, E.M. Ostap, E.L.F. Holzbaur, and M. Lakadamyali. 2021. Cega: a single particle segmentation algorithm to identify moving particles in a noisy system. *Mol Biol Cell*. 32:931-941.
- McDonald, N.A., R.D. Fetter, and K. Shen. 2020. Assembly of synaptic active zones requires phase separation of scaffold molecules. *Nature*. 588:454-458.
- McSwiggen, D.T., M. Mir, X. Darzacq, and R. Tjian. 2019. Evaluating phase separation in live cells: diagnosis, caveats, and functional consequences. *Genes Dev*. 33:1619-1634.
- Meglasson, M.D., and F.M. Matschinsky. 1986. Pancreatic islet glucose metabolism and regulation of insulin secretion. *Diabetes Metab Rev*. 2:163-214.
- Merglen, A., S. Theander, B. Rubi, G. Chaffard,

- C.B. Wollheim, and P. Maechler. 2004. Glucose sensitivity and metabolism-secretion coupling studied during two-year continuous culture in INS-1E insulinoma cells. *Endocrinology*. 145:667-678.
- Moertelmaier, M., M. Brameshuber, M. Linimeier, and G.J. Schütza. 2005. Thinning out clusters while conserving stoichiometry of labeling. *Appl. Phys. Lett.* 87:263903.
- Muller, A., D. Schmidt, C.S. Xu, S. Pang, J.V. D'Costa, S. Kretschmar, C. Munster, T. Kurth, F. Jug, M. Weigert, H.F. Hess, and M. Solimena. 2021. 3D FIB-SEM reconstruction of microtubule-organelle interaction in whole primary mouse beta cells. *J Cell Biol.* 220:e202010039.
- Nijhoff, M.F., M.A. Engelse, J. Dubbeld, A.E. Braat, J. Ringers, D.L. Roelen, A.R. van Erkel, H.S. Spijker, H. Bouwsma, P.J. van der Boog, J.W. de Fijter, T.J. Rabelink, and E.J. de Koning. 2016. Glycemic Stability Through Islet-After-Kidney Transplantation Using an Alemtuzumab-Based Induction Regimen and Long-Term Triple-Maintenance Immunosuppression. *Am J Transplant.* 16:246-253.
- Ohara-Imaizumi, M., K. Aoyagi, and T. Ohtsuka. 2019a. Role of the active zone protein, ELKS, in insulin secretion from pancreatic beta-cells. *Mol Metab.* 27S:S81-S91.
- Ohara-Imaizumi, M., K. Aoyagi, H. Yamauchi, M. Yoshida, M.X. Mori, Y. Hida, H.N. Tran, M. Ohkura, M. Abe, Y. Akimoto, Y. Nakamichi, C. Nishiwaki, H. Kawakami, K. Hara, K. Sakimura, S. Nagamatsu, Y. Mori, J. Nakai, M. Kakei, and T. Ohtsuka. 2019b. ELKS/Voltage-Dependent Ca(2+) Channel-beta Subunit Module Regulates Polarized Ca(2+) Influx in Pancreatic beta Cells. *Cell Rep.* 26:1213-1226.
- Ohara-Imaizumi, M., T. Ohtsuka, S. Matsushima, Y. Akimoto, C. Nishiwaki, Y. Nakamichi, T. Kikuta, S. Nagai, H. Kawakami, T. Watanabe, and S. Nagamatsu. 2005. ELKS, a protein structurally related to the active zone-associated protein CAST, is expressed in pancreatic beta cells and functions in insulin exocytosis: interaction of ELKS with exocytotic machinery analyzed by total internal reflection fluorescence microscopy. *Mol Biol Cell.* 16:3289-3300.
- Parnaud, G., E. Hammar, P. Ribaux, M.Y. Donath, T. Berney, and P.A. Halban. 2009. Signaling pathways implicated in the stimulation of beta-cell proliferation by extracellular matrix. *Mol Endocrinol.* 23:1264-1271.
- Parnaud, G., E. Hammar, D.G. Rouiller, M. Armanet, P.A. Halban, and D. Bosco. 2006. Blockade of beta1 integrin-laminin-5 interaction affects spreading and insulin secretion of rat beta-cells attached on extracellular matrix. *Diabetes.* 55:1413-1420.
- Phair, R.D., S.A. Gorski, and T. Misteli. 2004. Measurement of dynamic protein binding to chromatin in vivo, using photobleaching microscopy. *Methods Enzymol.* 375:393-414.
- Proszynski, T.J., J. Gingras, G. Valdez, K. Krzewski, and J.R. Sanes. 2009. Podosomes are present in a postsynaptic apparatus and participate in its maturation. *Proc Natl Acad Sci U S A.* 106:18373-18378.
- Proszynski, T.J., and J.R. Sanes. 2013. Amotl2 interacts with LL5beta, localizes to podosomes and regulates postsynaptic differentiation in muscle. *J Cell Sci.* 126:2225-2235.
- Ravassard, P., Y. Hazhouz, S. Pechberly, E. Bricout-Neveu, M. Armanet, P. Czernichow, and R. Scharfmann. 2011. A genetically engineered human pancreatic beta cell line exhibiting glucose-inducible insulin secretion. *J Clin Invest.* 121:3589-3597.
- Riopel, M., M. Krishnamurthy, J. Li, S. Liu, A. Leask, and R. Wang. 2011. Conditional beta1-integrin-deficient mice display impaired pancreatic beta cell function. *J Pathol.* 224:45-55.
- Riopel, M.M., J. Li, S. Liu, A. Leask, and R. Wang. 2013. beta1 integrin-extracellular matrix interactions are essential for maintaining exocrine pancreas architecture and function. *Lab Invest.* 93:31-40.
- Rondas, D., A. Tomas, and P.A. Halban. 2011. Focal adhesion remodeling is crucial for glucose-stimulated insulin secretion and involves activation of focal adhesion kinase and paxillin. *Diabetes.* 60:1146-1157.
- Rorsman, P., L. Eliasson, E. Renstrom, J. Gromada, S. Barg, and S. Gopel. 2000. The Cell Physiology of Biphasic Insulin Secretion. *News Physiol Sci.* 15:72-77.
- Rorsman, P., and E. Renstrom. 2003. Insulin granule dynamics in pancreatic beta cells. *Diabetologia.* 46:1029-1045.
- Rouso, T., E.D. Schejter, and B.Z. Shilo. 2016. Orchestrated content release from Drosophila glue-protein vesicles by a contractile actomyosin network. *Nat Cell Biol.* 18:181-190.
- Sakai, K., and J. Miyazaki. 1997. A transgenic mouse line that retains Cre recombinase activity in mature oocytes irrespective of the cre transgene transmission. *Biochem Biophys Res Commun.* 237:318-324.
- Sala, K., A. Corbetta, C. Minici, D. Tonoli, D.H. Murray, E. Cammarota, L. Ribolla, M. Ramella, R. Fesce, D. Mazza, M. Degano, and I. de Curtis. 2019. The ERC1 scaffold protein implicated in cell motility drives the assembly of a liquid phase. *Sci Rep.* 9:13530.
- Schatzle, P., M. Esteves da Silva, R.P. Tas, E.A. Katrukha, H.Y. Hu, C.J. Wierenga, L.C. Kapitein, and C.C. Hoogenraad. 2018. Activity-Dependent Actin Remodeling at the Base of Dendritic Spines Promotes Microtubule Entry. *Curr Biol.* 28:2081-2093.
- Schmidt, N., S. Basu, S. Sladecsek, S. Gatti, J. van Haren, S. Treves, J. Pielage, N. Galjart, and H.R. Brenner. 2012. Agrin regulates CLASP2-mediated capture of microtubules at the neuromuscular junction synaptic membrane. *J Cell Biol.* 198:421-437.

- Stehbens, S.J., M. Paszek, H. Pemble, A. Ettinger, S. Gierke, and T. Wittmann. 2014. CLASPs link focal-adhesion-associated microtubule capture to localized exocytosis and adhesion site turnover. *Nat Cell Biol.* 16:561-573.
- Sudhof, T.C. 2012. The presynaptic active zone. *Neuron.* 75:11-25.
- Tabei, S.M., S. Burov, H.Y. Kim, A. Kuznetsov, T. Huynh, J. Jureller, L.H. Philipson, A.R. Dinner, and N.F. Scherer. 2013. Intracellular transport of insulin granules is a subordinated random walk. *Proc Natl Acad Sci U S A.* 110:4911-4916.
- Takao-Rikitsu, E., S. Mochida, E. Inoue, M. Deguchi-Tawarada, M. Inoue, T. Ohtsuka, and Y. Takai. 2004. Physical and functional interaction of the active zone proteins, CAST, RIM1, and Bassoon, in neurotransmitter release. *J Cell Biol.* 164:301-311.
- Tarantino, N., J.Y. Tinevez, E.F. Crowell, B. Boisson, R. Henriques, M. Mhlanga, F. Agou, A. Israel, and E. Laplantine. 2014. TNF and IL-1 exhibit distinct ubiquitin requirements for inducing NEMO-IKK supramolecular structures. *J Cell Biol.* 204:231-245.
- Tas, R.P., T. Bos, and L.C. Kapitein. 2018. Purification and Application of a Small Actin Probe for Single-Molecule Localization Microscopy. *Methods Mol Biol.* 1665:155-171.
- van der Vaart, B., W.E. van Riel, H. Doodhi, J.T. Kevenaar, E.A. Katrukha, L. Gumy, B.P. Bouchet, I. Grigoriev, S.A. Spangler, K.L. Yu, P.S. Wulf, J. Wu, G. Lansbergen, E.Y. van Battum, R.J. Pasterkamp, Y. Mimori-Kiyosue, J. Demmers, N. Olieric, I.V. Maly, C.C. Hoogenraad, and A. Akhmanova. 2013. CFEOM1-associated kinesin KIF21A is a cortical microtubule growth inhibitor. *Dev Cell.* 27:145-160.
- Varadi, A., T. Tsuboi, L.I. Johnson-Cadwell, V.J. Allan, and G.A. Rutter. 2003. Kinesin I and cytoplasmic dynein orchestrate glucose-stimulated insulin-containing vesicle movements in clonal MIN6 beta-cells. *Biochem Biophys Res Commun.* 311:272-282.
- Wang, Y., X. Liu, T. Biederer, and T.C. Sudhof. 2002. A family of RIM-binding proteins regulated by alternative splicing: Implications for the genesis of synaptic active zones. *Proc Natl Acad Sci U S A.* 99:14464-14469.
- Wang, Z., and D.C. Thurmond. 2009. Mechanisms of biphasic insulin-granule exocytosis - roles of the cytoskeleton, small GTPases and SNARE proteins. *J Cell Sci.* 122:893-903.
- Weber, L.M., K.N. Hayda, and K.S. Anseth. 2008. Cell-matrix interactions improve beta-cell survival and insulin secretion in three-dimensional culture. *Tissue Eng Part A.* 14:1959-1968.
- Wilson, J.R., T.J. Biden, and R.I. Ludowyke. 1999. Increases in phosphorylation of the myosin II heavy chain, but not regulatory light chains, correlate with insulin secretion in rat pancreatic islets and RINm5F cells. *Diabetes.* 48:2383-2389.
- Wilson, J.R., R.I. Ludowyke, and T.J. Biden. 2001. A redistribution of actin and myosin IIA accompanies Ca^{2+} -dependent insulin secretion. *FEBS Lett.* 492:101-106.
- Wu, X., Q. Cai, Z. Shen, X. Chen, M. Zeng, S. Du, and M. Zhang. 2019. RIM and RIM- β P Form Presynaptic Active-Zone-like Condensates via Phase Separation. *Mol Cell.* 73:971-984.
- Wu, X., M. Ganzella, J. Zhou, S. Zhu, R. Jahn, and M. Zhang. 2021. Vesicle Tethering on the Surface of Phase-Separated Active Zone Condensates. *Mol Cell.* 81:13-24.
- Wu, Z.H., E.T. Wong, Y. Shi, J. Niu, Z. Chen, S. Miyamoto, and V. Tergaonkar. 2010. ATM- and NEMO-dependent ELKS ubiquitination coordinates TAK1-mediated IKK activation in response to genotoxic stress. *Mol Cell.* 40:75-86.
- Yu, M., S. Le, Y.C. Ammon, B.T. Goult, A. Akhmanova, and J. Yan. 2019. Force-Dependent Regulation of Talin-KANK1 Complex at Focal Adhesions. *Nano Lett.* 19:5982-5990.
- Yuan, T., L. Liu, Y. Zhang, L. Wei, S. Zhao, X. Zheng, X. Huang, J. Boulanger, C. Gueudry, J. Lu, L. Xie, W. Du, W. Zong, L. Yang, J. Salamero, Y. Liu, and L. Chen. 2015. Diacylglycerol Guides the Hopping of Clathrin-Coated Pits along Microtubules for Exo-Endocytosis Coupling. *Dev Cell.* 35:120-130.
- Zhu, X., R. Hu, M. Brissova, R.W. Stein, A.C. Powers, G. Gu, and I. Kaverina. 2015. Microtubules Negatively Regulate Insulin Secretion in Pancreatic beta Cells. *Dev Cell.* 34:656-668.

Supplementary figures

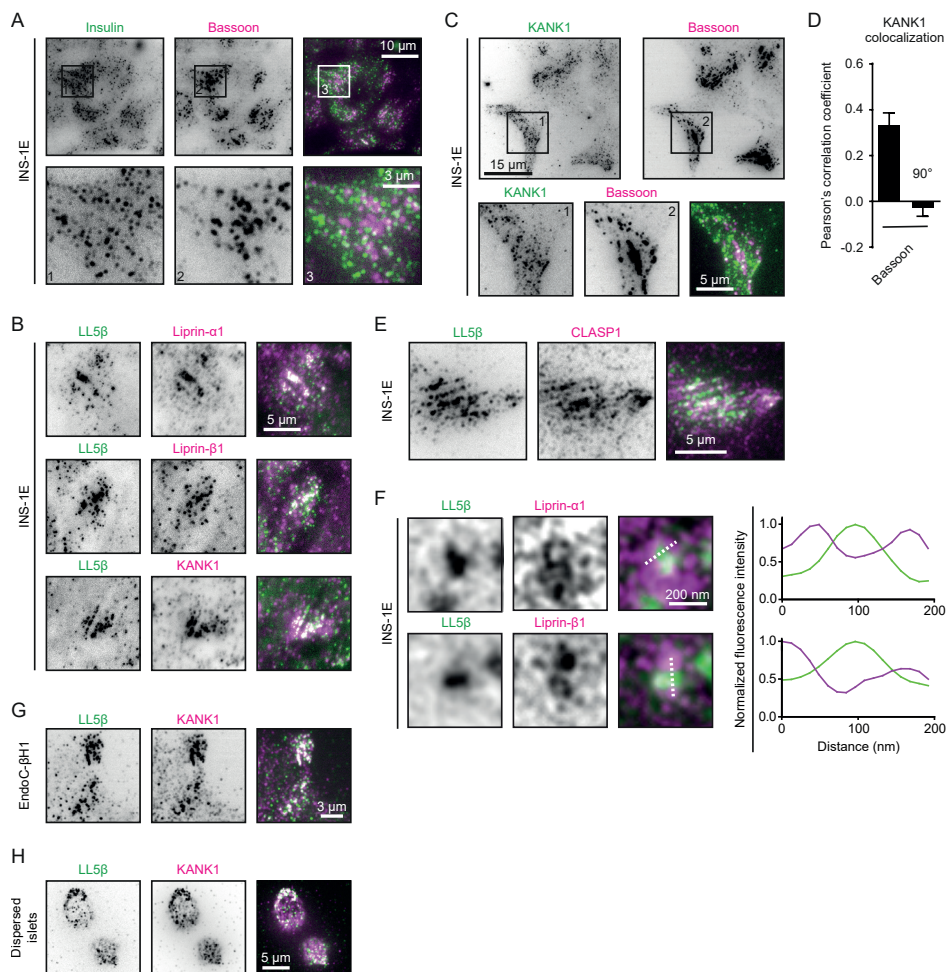


Figure S1: Organization of the insulin secretion sites in INS-1E cells.

(A) Staining for insulin (green) and Bassoon (magenta) in INS-1E cells imaged with TIRFM. (B) Staining for LL5 β (green) and liprin- α 1, liprin- β 1 and KANK1 (magenta) in INS-1E cells imaged with TIRFM. (C) Staining for KANK1 (green) and Bassoon (magenta) in INS-1E cells imaged with TIRFM. (D) Quantification of colocalization between KANK1 and Bassoon in INS-1E cells. Analysis and display as in Fig. 1B. $n=12$ ROIs. (E) Staining for LL5 β (green) and CLASP1 (magenta) in INS-1E cells imaged with TIRFM. (F) Stimulated Emission Depletion (STED) microscopy images of LL5 β (green) and liprin- α 1 and liprin- β 1 (magenta) in INS-1E cells. Intensity profiles along dotted lines are plotted in graphs. (G) Staining for LL5 β (green) and KANK1 (magenta) in EndoC- β H1 cells imaged with TIRFM. (H) Staining for LL5 β (green) and KANK1 (magenta) in dispersed human pancreatic islets imaged with TIRFM.

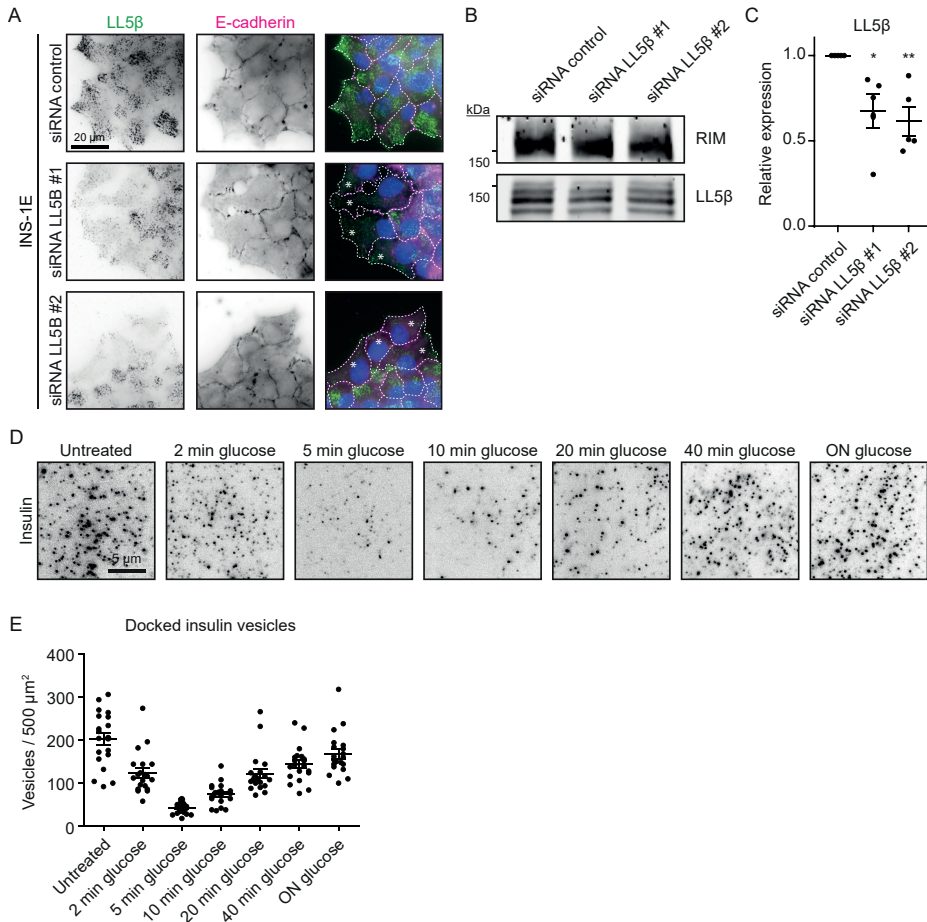


Figure S2: LL5 β knock-down and glucose stimulated insulin secretion in INS-1E cells.

(A) Staining for LL5 β (green), E-cadherin (magenta) and DNA (blue) in INS-1E cells transfected with control siRNA or siRNAs against LL5 β imaged with widefield microscopy. White asterisks indicate cells with LL5 β knock-down. (B) Western blot analysis of RIM and LL5 β expression in INS-1E cells treated with siRNAs as indicated. (C) Quantification of LL5 β expression based on Western blot analysis as shown in A. * $p < 0.1$; ** $p < 0.01$; one-way ANOVA followed by Dunnett's post-test. Single data points are plotted. Horizontal line, mean; error bars, s.e.m. For all conditions, $n = 5$ ROIs. (D) Staining for insulin in INS-1E cells starved with 2 mM glucose for 4 hours followed by 25 mM glucose stimulation for indicated times and imaged with TIRFM. (E) Quantification of docked insulin vesicles in INS-1E cells treated and stained as in C. Analysis and display as in Fig. 2F. For all conditions, $n = 20$ ROIs.

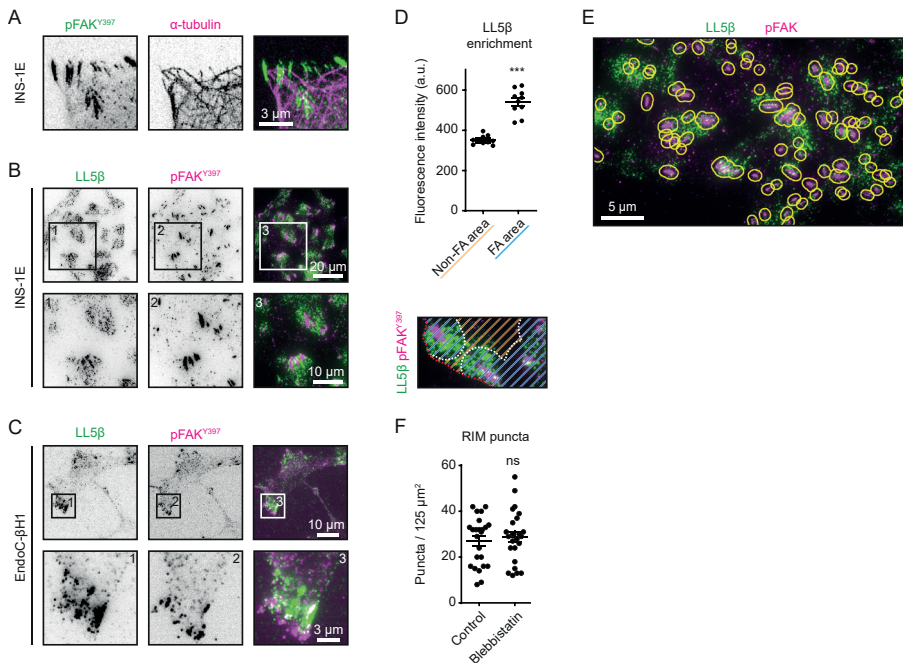


Figure S3: Analysis of the distribution of cortical secretion complexes.

(A) Stimulated Emission Depletion (STED) microscopy images of phosphorylated FAK (pFAKY397, green) and α -tubulin (magenta) in INS-1E cells. (B) Staining for LL5 β (green) and phosphorylated FAK (pFAKY397, magenta) in INS-1E cells imaged with TIRFM. (C) Staining for LL5 β (green) and phosphorylated FAK (pFAKY397, magenta) in EndoC- β H1 cells imaged with TIRFM. (D) Quantification of LL5 β localization relative to focal adhesions in INS-1E cells. Definition of analyzed cell areas are indicated in scheme. Non-focal adhesion area (orange stripes); focal adhesion area (blue stripes); cell boundary (red dotted line). Single data points are plotted. For both conditions, $n=10$ focal adhesions; *** $p<0.001$; Mann-Whitney U-test; error bars, s.e.m. (E) Analysis example of LL5 β (green) localization relative to focal adhesions (pFAKY397, magenta) in INS-1E cells. Yellow lines indicate areas in which LL5 β fluorescence signal was quantified in Fig. 3F. (F) Quantification of the numbers of RIM puncta in INS-1E cells treated and stained as in Fig. 3H. Analysis and display as in Fig. 2C. For both conditions, $n=24$ ROIs.

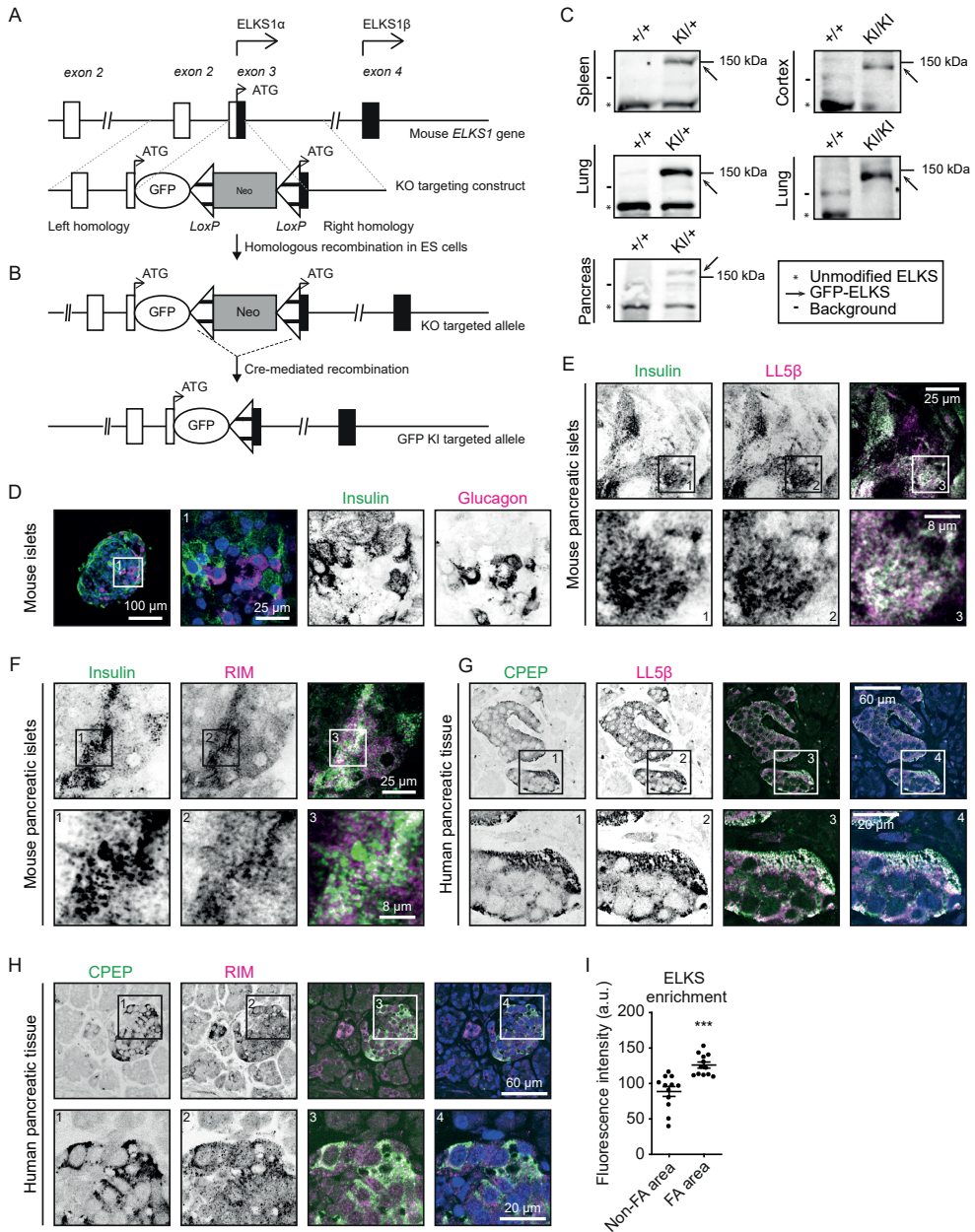


Figure S4: Generation and characterization of GFP-ELKS knock-in mouse line.

(A) Schematic representation of the ELKS knockout (KO) targeting construct. The top line represents the first four exons of ELKS1 gene on mouse chromosome 6. The bottom line represents the ELKS knockout targeting construct containing GFP, the neomycin resistance cassette (NEO) and two LoxP sites (represented by triangles) flanking both sides of NEO. The KO targeting construct has been inserted into exon 3. (B) Schematic representation of the ELKS KO allele and the generation of GFP-ELKS knock-in (KI) targeted allele. The top line shows the ELKS KO targeted allele; after

Cre-mediated recombination, the GFP-ELKS KI targeted allele is generated (bottom). **(C)** Western blot analysis of the indicated mouse tissues with ELKS antibodies. The bands corresponding to unmodified ELKS are indicated by asterisks, GFP-ELKS by arrows, and background bands by lines. +/+, wild-type; KI/+, heterozygous GFP-ELKS knock-in; KI/KI homozygous GFP-ELKS knock-in. **(D)** Staining for insulin (green), glucagon (magenta) and DNA (blue) in a wild-type mouse pancreatic islet imaged by confocal microscopy. **(E)** Staining for insulin (green) and LL5 β (magenta) in an adherent region of a mouse pancreatic islet imaged by confocal microscopy. **(F)** Staining for insulin (green) and RIM (magenta) in an adherent region of a mouse pancreatic islet imaged by confocal microscopy. **(G)** Staining for C-peptide (CPEP, green) and LL5 β (magenta) and DNA (blue) in human pancreatic tissue imaged by confocal microscopy. **(H)** Staining for C-peptide (CPEP, green) and RIM (magenta) and DNA (blue) in human pancreatic tissue imaged by confocal microscopy. **(I)** Quantification of ELKS localization relative to focal adhesions in INS-1E cells. Analysis and display as in Fig. S3D. For all conditions, n=12 focal adhesions.

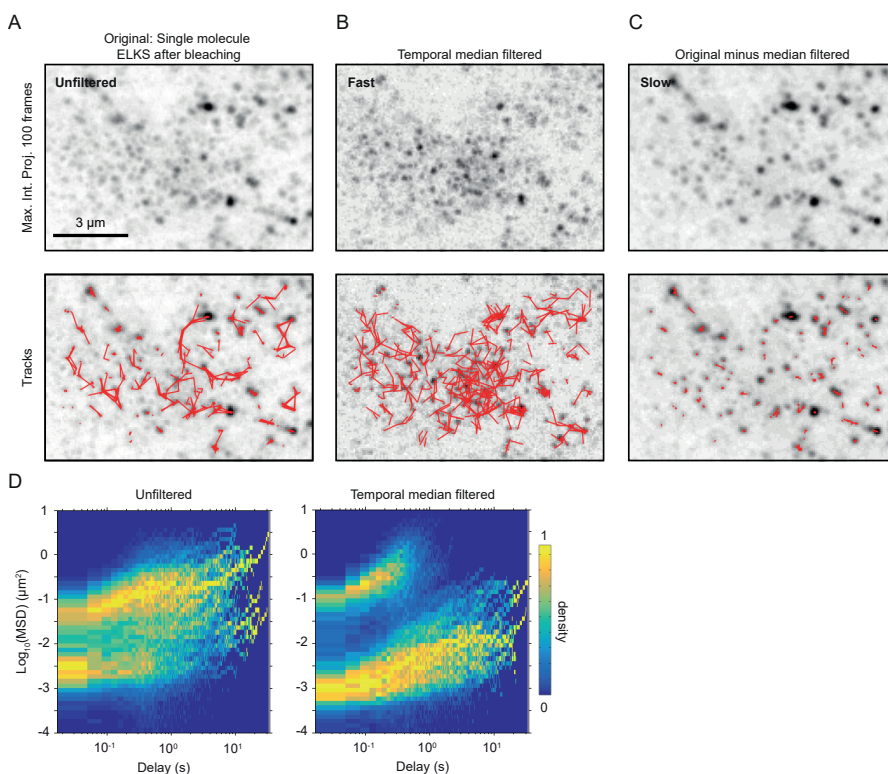


Figure S5: Single molecule analysis of GFP-ELKS in mouse pancreatic islets.

(A) Representative maximum intensity projection of single GFP-ELKS molecules dynamics (100 frames, 33 ms per frame, top) and the corresponding trajectories (bottom). **(B)** Maximum intensity projection of the movie shown in A after application of temporal median filtering with the window size of 15 frames (top) and the corresponding trajectories (bottom). Fast-moving fraction of single molecules is highlighted as a result. **(C)** Maximum intensity projection of the result of frame-by-frame and per pixel subtraction of movie shown in B from the movie shown in A (top) and corresponding trajectories (bottom). Slow-moving fraction of single molecules is highlighted as a result. **(D)** Heatmap (3D histogram) of MSD values for the trajectories of single GFP-ELKS molecules, tracked with and without temporal median filtering. Histogram values are normalized by the maximum value of each column, corresponding to each time delay bin.

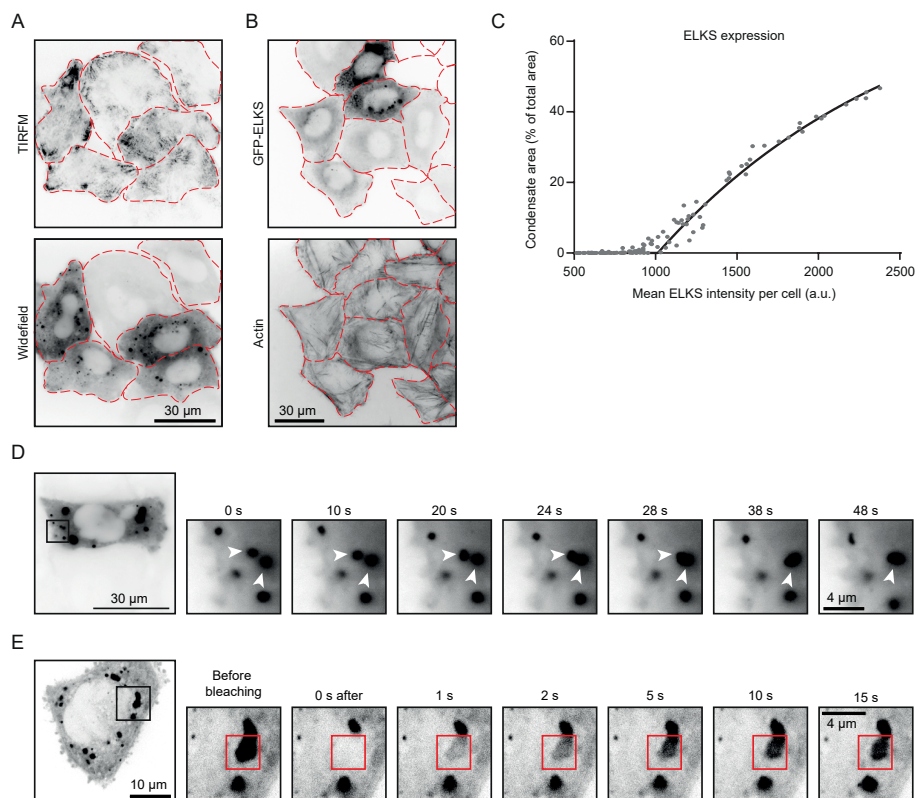


Figure S6: Analysis of condensates in HeLa cells overexpressing GFP-ELKS.

(A) Live HeLa cells with transient overexpression of GFP-ELKS imaged by TIRFM (top) and widefield microscopy (bottom). Red dotted lines indicate cell borders. (B) Staining for actin (bottom) in HeLa cells transiently overexpressing GFP-ELKS imaged by widefield microscopy. Red dotted lines indicate cell borders. (C) Quantification of GFP-ELKS expression in HeLa cells treated and stained as in B. Data are plotted as percentage of cell area occupied by condensates against the mean GFP-ELKS intensity per cell. Dots represent single data points; line shows non-linear fit; $n=115$ cells. (D) Live HeLa cells with transient overexpression of GFP-ELKS imaged by widefield microscopy. White arrowheads indicate fusion of condensates. (E) FRAP in HeLa cells transiently overexpressing GFP-ELKS imaged by confocal microscopy. Red squares indicate the photobleached region.

Supplementary tables

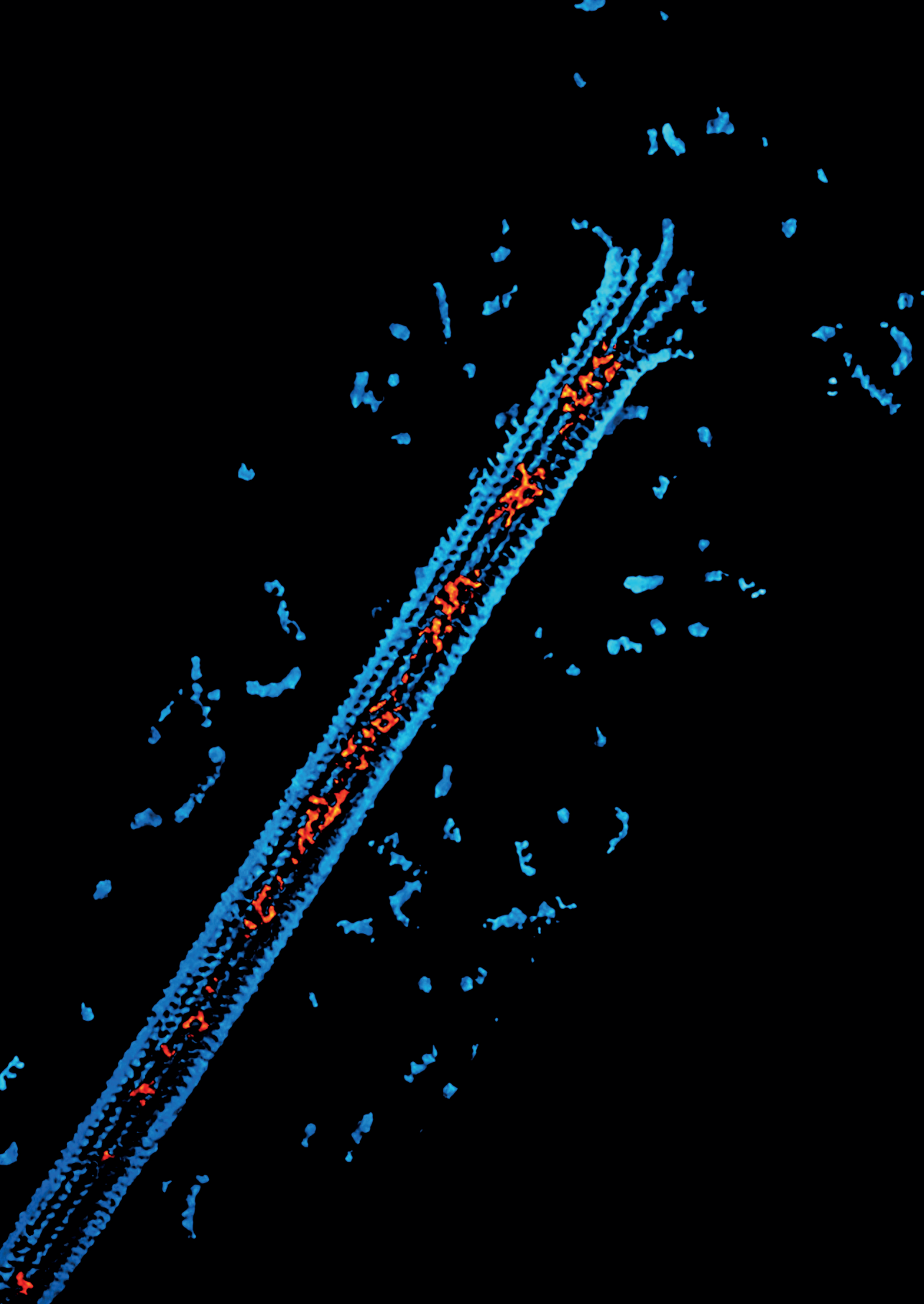
Table S1: Average FRAP curves fitting parameters

Fitted value \pm error of fit / Condition	Plateau (exchangeable fraction)	Fast halftime (min)	Slow halftime (min)	Percent fast
Low glucose	0.42 ± 0.02	0.93 ± 0.37	4.8 ± 1.9	40 ± 16
High glucose	0.65 ± 0.03	0.67 ± 0.26	5.5 ± 1.1	24 ± 6

Table S2: Key resources table

REAGENT or RESOURCE	SOURCE	IDENTIFIER	ANTIBODY DILUTION IF
Antibodies			
Mouse anti-LL5 β	Dr. J. Sanes ; (Kishi et al., 2005)	N/A	1:200
Mouse anti-Bassoon (SAP7F407)	Enzo Life Sciences	Cat#ADI-VAMPS003; RRID: AB_10618753	1:200
Mouse anti-paxillin (Clone 165)	BD Biosciences	Cat# 610619; RRID: AB_397951	1:100
Mouse anti-glucagon (Clone K79bB10)	Abcam	Cat# ab10988; RRID:AB_297642	1:100
Rabbit anti-LL5 β	(Lansbergen et al., 2006)	N/A	1:200
Rabbit anti-ERC1	Proteintech Group	Cat# 22211-1-AP; RRID:AB_11232409	1:200
Rabbit anti-ERC1 c-terminus	Dr. F. Melchior; (Grigoriev et al., 2011)	N/A	1:200
Rabbit anti-liprin- α 1	(Spangler et al., 2011)	N/A	1:100
Rabbit anti-liprin- β 1	(van der Vaart et al., 2013)	N/A	1:50
Rabbit anti-KANK1	Sigma-Aldrich	Cat# HPA005539; RRID:AB_1078164	1:400
Rabbit anti-RIM1/2	Synaptic Systems	Cat# 140 203; RRID:AB_887775	1:500
Rabbit anti-CLASP1	(Mimori-Kiyosue et al., 2005)	N/A	1:400
Rabbit anti-PhosphoFAK (Tyr397) (pFAK) (31H5L17)	Thermo Fisher Scientific	Cat# 700255; RRID:AB_2532307	1:300
Rabbit anti-E-cadherin	Gift from A. Yap	N/A	1:1000
Rat Anti-Mouse CD144 (VE-cadherin)	BD Biosciences	Cat# 555289; RRID:AB_395707	1:100
Rat anti-tyrosinated α -tubulin (Clone YL1/2)	Abcam	Cat# ab6160; RRID:AB_305328	1:300
Guinea pig anti-insulin	Dako	Cat# A0564; RRID:AB_10013624	1:500
Guinea pig anti C-peptide	Abcam	Cat# ab30477, RRID:AB_726924	1:100
Alexa Fluor 488 Phalloidin	Thermo Fisher Scientific	Cat# A12379; RRID:AB_2315147	1:200
Alexa Fluor 594 Phalloidin	Thermo Fisher Scientific	Cat# A12381; RRID:AB_2315633	1:200
Alexa Fluor 647 Phalloidin	Thermo Fisher Scientific	Cat# A22287; RRID:AB_2620155	1:100
Alexa488 Goat anti-Mouse IgG, highly cross-adsorbed	Thermo Fisher Scientific	Cat# A-11001; RRID:AB_2534069	1:300
Alexa594 Goat anti-Mouse IgG, highly cross-adsorbed	Thermo Fisher Scientific	Cat# R37121; RRID:AB_2556549	1:300
Alexa488 Goat anti-rabbit IgG, highly cross-adsorbed	Thermo Fisher Scientific	Cat# A-11034; RRID:AB_2576217	1:300
Alexa594 Goat anti-rabbit IgG, highly cross-adsorbed	Thermo Fisher Scientific	Cat# R37117; RRID:AB_2556545	1:300
Alexa488 Goat anti-rat IgG, highly cross-adsorbed	Thermo Fisher Scientific	Cat# A-11006; RRID:AB_2534074	1:300

Alexa594 Goat anti-rat IgG, highly cross-adsorbed	Thermo Fisher Scientific	Cat# A-11007; RRID:AB_10561522	1:300
Alexa488 Goat anti-guinea pig IgG, highly cross-adsorbed	Thermo Fisher Scientific	Cat# A-11073; RRID:AB_2534117	1:300
Alexa594 Goat anti-guinea pig IgG, highly cross-adsorbed	Thermo Fisher Scientific	Cat# A-11076; RRID:AB_2534120	1:300
IRDye 800CW Goat anti-Mouse IgG	Li-cor Biosciences	Cat# 925-32210; RRID:AB_2687825	1:15000
IRDye 800CW Goat anti-Rabbit IgG	Li-cor Biosciences	Cat# 925-32211; RRID:AB_2651127	1:15000
IRDye 680LT Goat anti-Mouse IgG	Li-cor Biosciences	Cat# 925-68020; RRID:AB_2687826	1:15000
IRDye 680LT Goat anti-Rabbit IgG	Li-cor Biosciences	Cat# 925-68021; RRID:AB_2713919	1:15000
Anti-mouse-D1	Ultivue	N/A	1:100
Anti-rabbit-D2	Ultivue	N/A	1:100
Chemicals, Peptides, and Recombinant Proteins			
Blebbistatin	Enzo Life Sciences	Cat# BML-EI315-0025	
LifeAct-mNeonGreen	(Tas et al., 2018)	N/A	
Experimental Models: Cell Lines			
Rat: INS-1E line	(Asfari et al., 1992)	RRID:CVCL_0351	
Human: EndoC- β H1 line	(Ravassard et al., 2011)	RRID:CVCL_L909	
Human: HeLa cell line	JCRB9004	RRID:CVCL_0030	
Experimental Models: Organisms/Strains			
Mouse: C57BL/6	Charles River	C57Bl6/NCrI	
Mouse: GFP-ELKS KI/KI	This paper	NCBI Gene: 111173	
Oligonucleotides			
siRNA targeting sequence LL5 β #1: GGAGATTCTAGATCATCTA	(Lansbergen et al., 2006)	N/A	
siRNA targeting sequence LL5 β #2: GGATCTACCTCACAGCCTA	This paper	N/A	
siRNA control targeting luciferase: CGTACGCGGAATACTTCGA	(Bouchet et al., 2016b)	N/A	
Imager strand I2-560	Ultivue	N/A	
Imager strand I1-650	Ultivue	N/A	
Software and Algorithms			
GraphPad Prism 9	GraphPad Software		
Metamorph Version 7.8	Molecular Devices		
ImageJ 1.50b			
MATLAB R2011b	MathWorks		





CSPP1 stabilizes growing microtubule ends and damaged lattices from the luminal side

Cyntha M. van den Berg¹, Vladimir A. Volkov^{1,2}, Sebastian Schnorrenberg³, Ziqiang Huang³, Kelly E. Stecker⁴, Ilya Grigoriev¹, Sebastian Patzke⁵, Timo Zimmermann³, Marileen Dogterom², and Anna Akhmanova¹

Manuscript under review

bioRxiv; <https://doi.org/10.1101/2022.06.23.497320>

¹Cell Biology, Neurobiology and Biophysics, Department of Biology, Faculty of Science, Utrecht University, Padualaan 8, Utrecht 3584 CH, the Netherlands.

²Department of Bionanoscience, Kavli Institute of Nanoscience, Delft University of Technology, van der Maasweg 9, 2629 HZ, Delft, the Netherlands.

³EMBL Imaging Centre, EMBL-Heidelberg, Meyerhofstraße 1, 69117 Heidelberg, Germany.

⁴Biomolecular Mass Spectrometry and Proteomics, Bijvoet Center for Biomolecular Research and Utrecht Institute for Pharmaceutical Sciences, Utrecht University, Padualaan 8, 3584 CH Utrecht, the Netherlands.

⁵Department of Radiation Biology, Institute for Cancer Research, Norwegian Radium Hospital, Oslo University Hospital, 0310 Oslo, Norway.

Abstract

Microtubules are dynamic cytoskeletal polymers, and their organization and stability are tightly regulated by numerous cellular factors. While regulatory proteins controlling formation of interphase microtubule arrays and mitotic spindles have been extensively studied, the biochemical mechanisms responsible for generating stable microtubule cores of centrioles and cilia are poorly understood. Here, we used *in vitro* reconstitution assays to investigate microtubule-stabilizing properties of CSPP1, a centrosome and cilia-associated protein mutated in the neurodevelopmental ciliopathy Joubert syndrome. We found that CSPP1 preferentially binds to polymerizing microtubule ends that grow slowly or undergo growth perturbations and, in this way, resembles microtubule-stabilizing compounds such as taxanes. Fluorescence microscopy and cryo-electron tomography showed that CSPP1 is deposited in the microtubule lumen and inhibits microtubule growth and shortening through two separate domains. CSPP1 also specifically recognizes and stabilizes damaged microtubule lattices. These data help to explain how CSPP1 regulates elongation and stability of ciliary axonemes and other microtubule-based structures.

Introduction

Microtubules are dynamic cytoskeletal polymers that serve as tracks for intracellular transport and drive chromosome separation during cell division. The majority of cellular microtubules turn over rapidly because microtubules frequently switch between phases of growth and shortening (Desai and Mitchison, 1997). Proteins controlling microtubule dynamics in interphase and mitosis have been studied in great detail by a combination of genetic, cell-biological, biochemical, and biophysical experiments (Akhmanova and Steinmetz, 2015; Gudimchuk and McIntosh, 2021). In particular, *in vitro* reconstitution studies with purified components have been instrumental for understanding the mechanisms underlying the activity of these proteins (Bieling et al., 2007; Gell et al., 2010). However, cells also form stable microtubule-based structures, such as centrioles and cilia. Multiple molecular players responsible for biogenesis of centrioles and cilia have been identified through genetic and cell-biological approaches, but their biochemical properties and their effects on microtubule dynamics are very poorly understood, because most of them have never been investigated using purified proteins.

Here, we focused on the centrosome/spindle pole associated protein 1 (CSPP1) (Patzke et al., 2005; Patzke et al., 2006). Previous work established that CSPP1 binds to spindle poles and the central spindle during mitosis and to ciliary axonemes, centrosomes and centriolar satellites in interphase (Asiedu et al., 2009; Frikstad et al., 2019; Patzke et al., 2005; Patzke et al., 2010; Patzke et al., 2006). CSPP1 accumulates at ciliary tips, interacts with several other ciliary tip proteins, contributes to ciliogenesis and controls axoneme length. Loss of CSPP1 leads to the formation of shortened cilia and impaired Hedgehog signaling, which depends on ciliary function (Frikstad et al., 2019; Latour et al., 2020; Patzke et al., 2010). Mutations in genes encoding CSPP1 and its ciliary binding partners lead to defects in ciliogenesis and result in a range of ciliopathies, such as the neurodevelopmental disorder known as Joubert syndrome, or the more severe Meckel-Gruber syndrome with multiple developmental abnormalities (Akizu et al., 2014; Latour et al., 2020; Shaheen et al., 2014; Tuz et al., 2014).

While the tissue and cellular phenotypes associated with CSPP1 defects have been analyzed in some detail, very little is known about its mechanism of action. To close this knowledge gap, we have performed *in vitro* reconstitution experiments to investigate the impact of full-length CSPP1 and its individual domains on microtubule dynamics. We found that CSPP1 specifically associates with growing microtubule ends when they undergo a growth perturbation and enter a pre-catastrophe state. CSPP1 stabilizes such ends and induces microtubule pausing followed by growth, thus effectively preventing microtubule depolymerization. This effect of CSPP1 on microtubule behavior strikingly resembles that of microtubule-stabilizing compounds, taxanes and epothilones, which also preferentially accumulate at growing microtubule ends in pre-catastrophe state, causing their stabilization and pausing followed by polymerization (Rai et al., 2020). Since taxanes bind to microtubules from the luminal side, we hypothesized that the same would be true for CSPP1. We investigated CSPP1 localization using cryo-electron tomography (cryoET) and MINFLUX microscopy and found that CSPP1 is a microtubule inner protein (MIP). In line with this finding, we observed that in addition to localizing at growing microtubule ends, CSPP1 also efficiently binds to sites where microtubule lattices are damaged. Furthermore, deletion mapping showed that CSPP1 contains separate domains responsible for microtubule rescue and stabilization and for growth inhibition. Altogether, our findings reveal how microtubule dynamics can be controlled from the luminal side. These data have important implications for understanding how highly stable microtubule populations, such as those in ciliary axonemes, are generated and maintained.

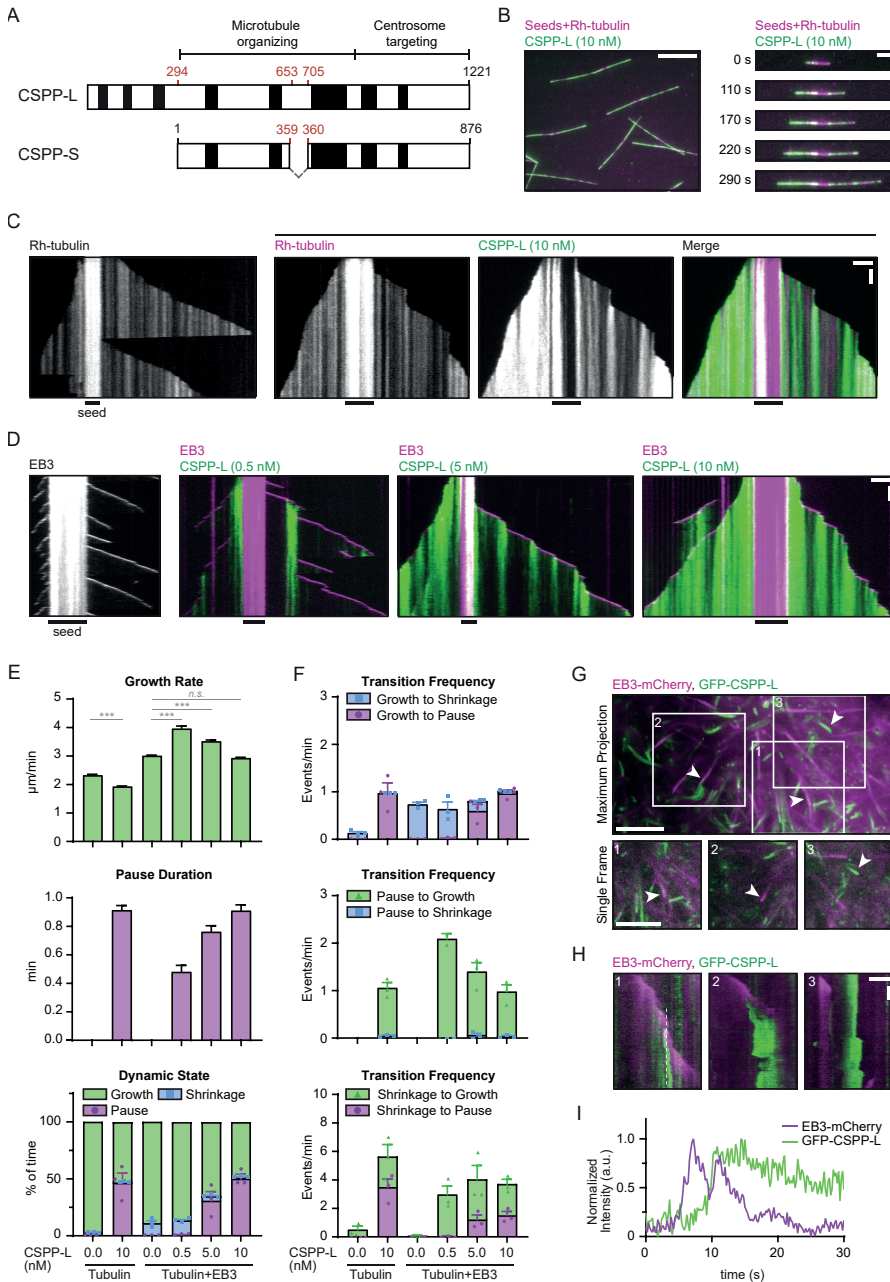


Figure 1: CSPP1 suppresses catastrophes by binding to polymerizing ends where it induces pausing

(A) Schematic representation of the two isoforms expressed by the CSPP1 gene in mammals. Black boxes represent α -helical domains larger than 20 amino acids predicted by AlphaFold. (B) Field of view (left, scale bar 10 μm) and time-lapse images (right, scale bar 3 μm) illustrating microtubule growth from GMPCPP stabilized microtubule seeds in the presence of 15 μM tubulin supplemented with

3% rhodamine-labelled tubulin and 10 nM GFP-CSPP-L. **(C,D)** Kymographs illustrating microtubule growth either with rhodamine-tubulin (C) or mCherry-EB3 (D), supplemented, where indicated, with the indicated concentrations of GFP-CSPP-L. Scale bars, 2 μm (horizontal) and 60 s (vertical). **(E,F)** Parameters of microtubule plus end dynamics in the presence of rhodamine-tubulin alone or together with 20 nM mCherry-EB3 in combination with the indicated GFP-CSPP-L concentrations (from kymographs as shown in C,D). Events were classified as pauses when the pause duration was longer than 20 s. Number of growth events, pauses and microtubules analyzed (E); tubulin alone, n= 394, 0, 110; tubulin with 10 nM CSPP-L, n= 596, 481, 78; EB3 alone, n= 514, 0, 53; EB3 with 0.5 nM CSPP-L, n=476, 10, 44; EB3 with 5 nM CSPP-L, n=564, 241, 47; EB3 with 10 nM CSPP-L, n=731, 518, 89. Number of transition events analyzed (F): tubulin alone, n= 194, 0, 0, 0, 15, 0; tubulin with 10 nM CSPP-L, n= 0, 443, 410, 25, 7, 17; EB3 alone, n= 461, 0, 0, 0, 4, 0; EB3 with 0.5 nM CSPP-L, n=309, 8, 10, 0, 216, 2; EB3 with 5 nM CSPP-L, n=75, 209, 224, 9, 57, 27; EB3 with 10 nM CSPP-L, n=24, 465, 455, 22, 25, 21. Single data points represent averages of three independent experiments. Error bars represent s.e.m. ***, $p < 0.001$; n.s., not significant; Kruskal-Wallis test followed by Dunn's post-test. **(G)** Maximum projection (top) and enlarged single frame images (bottom) of a COS-7 cell overexpressing GFP-CSPP-L and EB3-mCherry, imaged by TIRF microscopy. Scale bars, 5 μm . **(H)** Kymographs of the events indicated with arrowheads in G. Scale bars, 2 μm (horizontal) and 4 s (vertical). **(I)** Normalized intensity graphs of EB3-mCherry and GFP-CSPP-L along the white dashed line in H. See also Figure S1 and Videos S1 and S2.

Results

CSPP1 suppresses catastrophes by binding to polymerizing ends where it induces pausing

CSPP1 contains several predicted helical domains interspersed with regions of unknown structure and is represented by two isoforms, the long isoform CSPP-L and a shorter isoform (termed here CSPP-S), which lacks 294 amino acids at N-terminus and contains an internal deletion of 52 amino acids (Fig. 1A, (Frikstad et al., 2019; Patzke et al., 2006)). In our initial analysis, we focused on the CSPP-L isoform. To get insight into the autonomous effects of CSPP-L on microtubule dynamics, we have purified it from HEK293 cells (Fig. S1A). Mass spectrometry-based analysis demonstrated that CSPP-L preparations contained no other known regulators of microtubule dynamics (Fig. S1B). We used purified GFP-CSPP-L to perform *in vitro* assays where microtubules grown from GMPCPP-stabilized seeds were observed by Total Internal Reflection Fluorescence microscopy (TIRFM) (Fig. S1C) (Aher et al., 2018; Bieling et al., 2007). In the presence of tubulin alone, microtubules regularly switched from growth to shortening that proceeded all the way back to the seed. However, the addition of 10 nM CSPP-L suppressed shrinkage and led to frequent pausing of microtubule plus ends, while their growth rate was slightly reduced (Fig. 1B, C, E, F; Fig. S1D, E; Video S1). A similar effect was observed when we included in the assay mCherry-EB3, a marker of growing microtubule ends, which by itself increases microtubule growth rate and promotes catastrophes (Fig. 1D-F; Fig. S1E) (Komarova et al., 2009). In our *in vitro* assays, CSPP-L also bound to growing microtubule minus ends and strongly accumulated along the lattice formed by minus-end polymerization (Fig. 1B-D; Fig. S1E). However, in cells, this protein normally acts at the distal tip of the cilium which contains microtubule plus ends, and therefore we have not investigated the effects of CSPP-L on microtubule minus-end dynamics. CSPP-L binding was always initiated close to the growing microtubule end, and after binding, CSPP-L showed little lateral diffusion along microtubules, so that CSPP-L binding zones remained well-confined (Fig. 1C, D). The low lateral mobility of CSPP1 was confirmed by spiking experiments where 0.5 nM GFP-CSPP-L was combined with 9.5 nM mCherry-CSPP-L (Fig. S1F). When CSPP-L concentration was increased, the zones of CSPP-L accumulation coincided with longer and more frequent microtubule pausing events (Fig. 1D-F). CSPP-L-induced

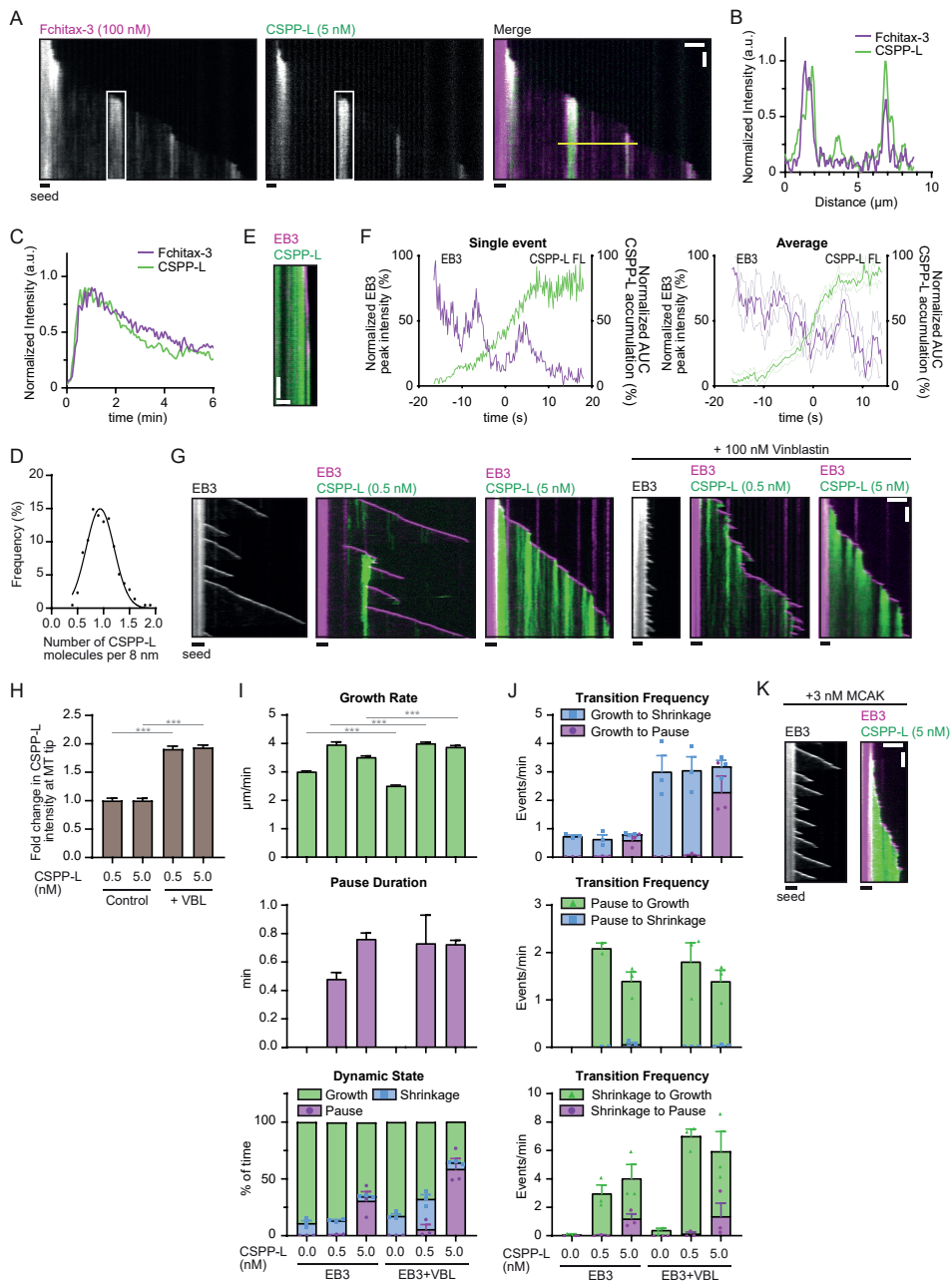


Figure 2: CSPP1 binds to pre-catastrophe microtubule ends, resembling taxane behavior. (A) Kymographs of microtubule growth with 100 nM Fchitax-3 together with 5 nM mCherry-CSPP-L in presence of 20 nM dark EB3. Scale bars, 2 μm (horizontal) and 60 s (vertical). (B) Normalized intensity graph of Fchitax-3 and GFP-CSPP-L along the yellow line in A. (C) Normalized intensity graph of Fchitax-3 and GFP-CSPP-L within the white box in A. (D) Quantification of the number of GFP-CSPP-L molecules per 8 nm microtubules. The integrated intensity of one GFP-CSPP-L

accumulation in an *in vitro* assay was divided by the average intensity of single GFP monomers in a separate chamber on the same coverslip and subsequently normalized to 8 nm accumulation length. Number of GFP-CSPP-L accumulations $n=215$. **(E)** Kymograph illustrating microtubule growth in the presence of 20 nM mCherry-EB3 together with 10 nM GFP-CSPP-L. Scale bars, 2 μm (horizontal) and 5 s (vertical). **(F)** Time plot of the normalized maximum intensity profile of a single mCherry-EB3 comet and the normalized area under the curve (AUC) of a single GFP-CSPP-L accumulation (left) and averaged EB3 and GFP-CSPP-L profiles, normalized and aligned using half-maximum effective intensity values from Hill equation fits as reference points (right) (from kymographs as shown in E. Dashed lines represent SEM. Number of events analyzed, $n=12$ from two independent experiments. **(G)** Kymographs of microtubule growth with mCherry-EB3 alone or together with indicated concentrations of GFP-CSPP-L in presence or absence of 100 nM vinblastine (VBL). Scale bars, 2 μm (horizontal) and 60 s (vertical). **(H)** Quantification of the mean GFP-CSPP-L intensity at the microtubule tip per growth event. The average mean intensity of GFP-CSPP-L in presence of 100 nM vinblastine was normalized to the average mean intensity in absence of vinblastine. Number of growth events analyzed; 0.5 nM GFP-CSPP-L control, $n=474$; 5 nM GFP-CSPP-L control, $n=598$; 0.5 nM GFP-CSPP-L with VBL, $n=1363$; 5 nM GFP-CSPP-L with VBL, $n=897$. **(I, J)** Parameters of microtubule plus end dynamics in the presence of 20 nM mCherry-EB3 together with the indicated GFP-CSPP-L concentrations (from kymographs as shown in G). Events were classified as pauses when the pause duration was longer than 20 s. Number of growth events, pauses and microtubules analyzed (I); EB3 alone, $n=514$, 0, 53; EB3 with 0.5 nM CSPP-L, $n=476$, 10, 44; EB3 with 5 nM CSPP-L, $n=564$, 241, 47; EB3 with VBL, $n=915$, 0, 54; EB3 with 0.5 nM CSPP-L and VBL $n=1204$, 33, 40; EB3 with 5 nM CSPP-L and VBL, $n=632$, 408, 47. Number of transition events analyzed (J): EB3 alone, $n=461$, 0, 0, 0, 4, 0; EB3 with 0.5 nM CSPP-L, $n=309$, 8, 10, 0, 216, 2; EB3 with 5 nM CSPP-L, $n=75$, 209, 224, 9, 57, 27; EB3 with VBL, $n=162$, 0, 0, 0, 33, 0; EB3 with 0.5 nM CSPP-L and VBL, $n=1079$, 19, 31, 0, 1002, 14; EB3 with 5 nM CSPP-L and VBL, $n=147$, 372, 386, 7, 127, 27. Single data points represent averages of three independent experiments. Data for conditions without vinblastine is the same as in Fig. 1E, F. **(K)** Kymographs illustrating microtubule growth with mCherry-EB3 alone or together with 5 nM GFP-CSPP-L in presence of 3 nM MCAK. Scale bars, 2 μm (horizontal) and 60 s (vertical). For all plots. Error bars represent s.e.m. ***, $p < 0.001$; n.s., Kruskal-Wallis test followed by Dunn's post-test.

pausing was almost always (in ~95% of the cases) followed by growth and not by shrinkage, and at CSPP-L concentrations exceeding 5 nM, very little microtubule depolymerization was observed (Fig. 1B-F; Fig. S1E). At low, 0.5 nM concentration of CSPP-L, long microtubule depolymerization episodes were still present, but zones of CSPP-L accumulation triggered microtubule rescues (Fig. 1D, F).

Next, we investigated the behavior of GFP-CSPP-L in COS-7 cells. Endogenous CSPP1 in these cells is only localized to centrioles and centriolar satellites but not to cytoplasmic microtubules (Fig. S1G). Similar to what we observed *in vitro*, overexpressed GFP-CSPP-L formed accumulations along microtubules (Fig. 1G; Fig. S1H; Video S2). Elevated levels of CSPP-L led to an increase in microtubule acetylation (Fig. S1H, I), a hallmark of microtubule stabilization (Magiera et al., 2018). Moreover, the number of microtubule plus ends labeled with EB1, a marker of growing microtubule ends (Mimori-Kiyosue et al., 2000), was strongly reduced (Fig. S1H, J), indicating that microtubule dynamics was suppressed. Live cell imaging in COS-7 cells co-expressing GFP-CSPP-L and EB3-mCherry showed that CSPP-L bound to growing, EB3-positive microtubule ends upon EB3 signal reduction, and CSPP-L accumulation led to microtubule pausing (Fig. 1G-I). Microtubules could regrow from CSPP-L accumulations (Fig. 1G, H, box 1) or stay paused for longer periods of time (Fig. 1G, H, box 2), and many pausing microtubule ends strongly labeled with CSPP-L were observed throughout the cell (Fig. 1G, H, box 3; Video S2). We conclude that CSPP-L binds to growing microtubule ends, prevents their shrinkage and induces pausing both *in vitro* and in cells.

CSPP1 binds to pre-catastrophe microtubule ends, resembling taxane behavior

Formation of confined accumulation zones that initiate at growing microtubule ends and

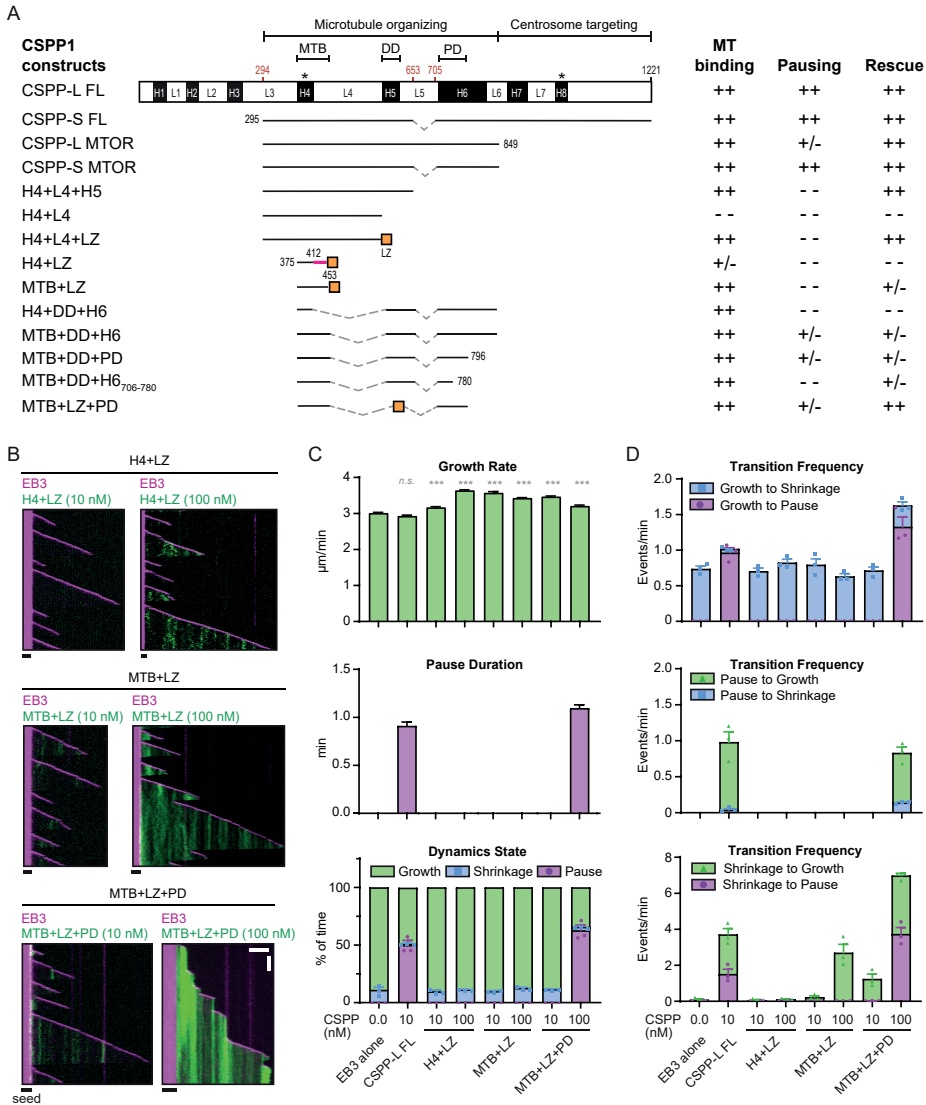


Figure 3: Separate CSPP1 domains control the balance between microtubule polymerization and depolymerization

(A) Schematic representation of the different CSPP1 constructs used and a summary of their binding to microtubules and their effects on microtubule dynamics. Black boxes represent α -helical domains larger than 20 amino acids predicted by AlphaFold; asterisks indicate previously unidentified helices. ++: frequently observed at protein below 40 nM; +/-: occasionally observed at protein concentrations below 40 nM and/or frequently observed at protein concentrations up to 100 nM; --: observed infrequently or not observed at all even at protein concentrations higher than 100 nM. (B) Kymographs illustrating microtubule growth with 20 nM mCherry-EB3 alone or together with 10 or 100 nM of the indicated GFP-CSPP1 constructs. Scale bars, 2 μ m (horizontal) and 60 s (vertical). (C,D) Parameters of microtubule plus end dynamics in the presence of 20 nM mCherry-EB3 together with 10 or 100 nM of the indicated GFP-CSPP1 constructs (from kymographs as shown in B). Events were classified as pauses when the pause duration was longer than 20 s. Number of growth events,

pauses and microtubules analyzed (C); EB3 alone, n= 514, 0, 53; EB3 with 10 nM CSPP-L, n=731, 518, 89; EB3 with 10 nM H4+LZ, n=855, 0, 87; EB3 with 100 nM H4+LZ, n=987, 0, 103; EB3 with 10 nM MTB+LZ, n=1006, 0, 109; EB3 with 100 nM MTB+LZ, n=1206, 0, 139; EB3 with 10 nM MTB+LZ+PD, n=934, 0, 104; EB3 with 100 nM MTB+LZ+PD, n=776, 707, 123. Number of transition events analyzed (D); EB3 alone, n= 461, 0, 0, 0, 4, 0; EB3 with 10 nM CSPP-L, n=24, 465, 455, 22, 25, 21; EB3 with 10 nM H4+LZ, n=751, 0, 0, 0, 3, 0; EB3 with 100 nM H4+LZ, n=889, 0, 0, 0, 15, 0; EB3 with 10 nM MTB+LZ, n= 902, 0, 0, 0, 26, 0; EB3 with 100 nM MTB+LZ, n= 1035, 0, 0, 0, 582; EB3 with 10 nM MTB+LZ+PD, n=797, 0, 0, 0, 191, 0; EB3 with 100 nM MTB+LZ+PD, n=126, 545, 520, 105, 107, 121. Single data points represent averages of three independent experiments. Error bars represent SEM. ***, p< 0.001; n.s., not significant; Kruskal-Wallis test followed by Dunn's post-test. Data for EB3 alone and EB3 with 10 nM CSPP-L is the same as in Fig. 1E, F. See also Figure S2.

prevent microtubule shrinkage makes the dynamic behavior of CSPP-L strikingly similar to that we have recently described for taxanes (Rai et al., 2020). To determine if CSPP-L and taxanes recognize the same features of microtubules, we have tested whether fluorescently labelled taxane Fchitax-3 colocalized with CSPP-L and found that this was indeed the case (Fig. 2A, B). Over time, the intensity of both Fchitax-3 and CSPP-L first increased and then decreased in a similar way (Fig. 2A, C). Measurements of fluorescence intensity of 10 nM CSPP-L within accumulation zones, performed as described previously (Rai et al., 2020), indicated that on average, one CSPP-L molecule was bound per 8 nm of microtubule length (corresponding to the length of one layer of α/β -tubulin dimers) (Fig. 2D), indicating that the binding sites are likely not saturated in these conditions.

Since our previous work has demonstrated that binding of Fchitax-3 is triggered by perturbed microtubule growth and occurs when microtubules enter a pre-catastrophe state manifested by the loss of GTP cap and reduced EB3 binding (Rai et al., 2020), we tested whether the same is true for CSPP-L. Indeed, periods of strong CSPP-L accumulation always initiated a few seconds after EB3 signal started to diminish (Fig. 2E, F), and a similar CSPP-L accumulation pattern was observed in cells (Fig. 1G-I). To support our interpretation that perturbed microtubule growth triggers CSPP-L binding, we supplemented the assay with 100 nM vinblastine, which promotes frequent catastrophes at low concentrations in the presence of EB3 (Mohan et al., 2013). Catastrophes indeed became much more frequent, and this resulted in the increased number of CSPP-L accumulation zones, leading to a higher overall binding of the protein along microtubules (Fig. 2G, H, J). Similar to the conditions without vinblastine, 0.5 nM CSPP-L did not block depolymerization completely but induced formation of rescue sites, whereas 5 nM CSPP-L induced more frequent pausing episodes followed by re-growth (Fig. 2G, I, J). In the presence of the kinesin-13 MCAK, which also triggers frequent catastrophes in the presence of EB3 (Montenegro Gouveia et al., 2010), enhancement of CSPP-L accumulation along microtubules was observed as well (Fig. 2K). We conclude that similar to taxanes, CSPP-L strongly accumulates at microtubule ends that undergo a growth perturbation, inhibits both their growth and shortening and gradually dissociates when microtubule growth resumes.

Separate CSPP1 domains control the balance between microtubule polymerization and depolymerization

Next, we examined which CSPP1 domains are responsible for its effects on microtubule dynamics. As a starting point for deletion mapping of CSPP1, we used structure predictions made by a recently developed neural network AlphaFold (Jumper et al., 2021; Varadi et al., 2022). As mentioned previously, CSPP-L contains several putative α -helical domains (H1-8) interspersed with regions of unknown structure (L1-L7) (Fig. 3A). Compared to the previously performed analyses of CSPP1 sequence, this prediction suggested presence of two additional

α -helical regions, H4 and H8, in the middle and C-terminal part of the protein. Based on the predicted domains, we generated various GFP-tagged fragments of CSPP1 (Fig. 3A) and tested them in the *in vitro* assays. The short isoform of CSPP1, CSPP-S, behaved similarly to CSPP-L, though at 10 nM it was less efficient at preventing microtubule depolymerization and could also occasionally block microtubule outgrowth from the seed, whereas we have never observed this effect with CSPP-L (Fig. 3A; Fig. S2A). Next, we focused on the middle part of CSPP1, because previous work has identified it as the microtubule-organizing region (Frikstad et al., 2019; Patzke et al., 2006) (MTOR, Fig. 3A; Fig. S2B, C). The MTOR region derived from the CSPP-L isoform displayed local accumulations along microtubules and prevented catastrophes at 10 nM, but did not cause long pauses, even at 40 nM concentration (Fig. S2B). The MTOR version with the internal deletion present in CSPP-S showed little microtubule binding at 10 nM, but the binding became visible at 40 nM and was accompanied by frequent pauses, followed by either growth or shrinkage (Fig. 3A; Fig. S2C). Further deletion mapping at the C-terminus of the MTOR domain (the construct H4+L4+H5) showed that the helical domain H6 with the preceding linker L5 was not essential for microtubule binding or rescue activity but was needed to trigger pausing (Fig. 3A; Fig. S2D). An even shorter truncation mutant, which also lacked helical domain H5 (H4+L4) displayed only a very weak binding to microtubules (Fig. 3A; Fig. S2E). However, the affinity of this fragment for microtubules was increased by linking it to the leucine zipper dimerization domain of GCN4 (H4+L4+LZ) (Fig. 3A, Fig. S2F). Therefore, from this point onwards we termed helical domain H5 the dimerization domain (DD). Linking the newly identified short α -helical domain H4 directly to the leucine zipper through a short flexible linker yielded again a construct that weakly bound to microtubules but did not induce rescues, even at concentrations up to 300 nM (H4+LZ; Fig. 3A-D; Fig. S2G). Extension of H4 with a part of linker L4 (amino acids 375-453; a protein fragment we termed MTB, for “microtubule-binding”), fused to the leucine zipper, resulted in a construct which was sufficient for microtubule binding and rescue induction (MTB+LZ; Fig. 3A-D; Fig. S2H). Microtubule binding of CSPP1 thus depends on a short region, which is predicted to be α -helical, and is augmented by dimerization and additional regions distributed throughout the CSPP1 molecule, including the region missing in the CSPP-S isoform.

Importantly, all CSPP1 fragments lacking the domain H6 did not cause microtubule pausing, suggesting that H6 could be responsible for pause induction. To test this idea, we first directly fused the DD and H6 domains to H4 (H4+DD+H6). Already at 40 nM concentration, this construct strongly inhibited microtubule outgrowth from the seed and induced catastrophes (Fig. 3A; Fig. S2I). Attaching the DD and H6 domains to MTB (MTB+DD+H6) resulted in a construct that could induce microtubule pausing and inhibit depolymerization at 100 nM, whereas at lower concentrations (40 nM), it showed occasional rescues but no pauses (Fig. 3A; Fig. S2J). To determine which part of H6 is responsible for inhibiting microtubule growth, we truncated it at the C-terminus and found that MTB+DD+H6₇₀₆₋₇₉₆ but not a shorter version, MTB+DD+H6₇₀₆₋₇₈₀, still triggered pausing and inhibited microtubule shrinkage when fused to MTB and H5 (Fig. 3A, Fig. S2K, L). We therefore termed H6₇₀₆₋₇₉₆ the pausing domain (PD). Swapping DD within this construct for the leucine zipper (MTB+LZ+PD) yielded a construct with similar properties (Fig. 3A-D; Fig. S2M), confirming that DD primarily acts as a dimerization domain.

Next, we compared the impact of truncated CSPP1 constructs with that of GFP-CSPP-L on microtubules in COS-7 cells. GFP-MTB+LZ+PD, GFP-MTB+LZ and GFP-H4+LZ localized to microtubules in interphase cells. However, compared to CSPP-L, the shorter constructs were less potent in inducing microtubule acetylation and reducing the number of EB1 comets, indicating that they are less efficient in stabilizing microtubules (Fig. S2N-Q; control in Fig. S1H-J). Altogether, we conclude that CSPP1 has multiple regions

contributing to microtubule binding, but the minimal construct that reproduces the major effects of CSPP-L on microtubule dynamics is MTB+LZ+PD. These effects appear to depend on the interplay between two separate activities, residing in two predicted helical regions: microtubule binding and stabilization by the MTB and the growth-inhibiting activity of the truncated α -helical domain H6, the PD.

CSPP1 binds to microtubule lumen

As described above, the behavior and effect of CSPP1 on dynamic microtubules resembles that of taxanes. Taxanes are known to bind to the microtubule lumen (reviewed in (Steinmetz and Prota, 2018)), and therefore, we set up cryoET experiments to investigate whether CSPP1 is a MIP. Using a previously established experimental design (Ogunmolu et al., 2021), we polymerized dynamic microtubules from GMPCPP-stabilized seeds in presence or absence of 10 nM CSPP-L, with or without 250 nM vinblastine and vitrified them on EM grids. To increase the signal-to-noise ratio in the reconstructed tomograms, we used the cryoCARE denoising method (Buchholz et al., 2019). Microtubules polymerized in presence of CSPP-L frequently contained luminal densities, which were absent in CSPP-L-free samples (Fig. 4A, B; Fig. S3A). Presence of vinblastine resulted in higher percentage of microtubules containing MIP particles: $68\% \pm 22\%$ (mean \pm SD), compared to $35\% \pm 11\%$ in absence of vinblastine ($p < 10^{-4}$, Fig. 4A, B). We did not observe CSPP-L densities outside of microtubule lumen.

We further used automated segmentation of denoised tomograms (Chen et al., 2017) to get a better understanding of the intraluminal particles. CSPP-L particles appeared quite disordered, and could either block the microtubule lumen completely, or only partially (Fig. 4C, Video S3). They were occupying variable length of the microtubule lumen, preventing further analysis of their structure. Some CSPP-L particles were bound close to the terminal flare of tubulin protofilaments, but we never observed them binding to tapered microtubule ends or other incomplete microtubule lattices.

Next, we aimed to confirm that the densities inside microtubules we observed with Cryo-ET indeed represent CSPP-L and determine the localization of shorter CSPP1 fragments. Since the latter would be difficult to achieve by cryo-ET due to the small protein size, we turned to MINFLUX microscopy, which allows localization of individual fluorophores with very high spatial resolution, as was demonstrated by the separation of e.g. two fluorophores as close as 6 nm from each other (Balzarotti et al., 2017; Gwosch et al., 2020). The localization resolution of MINFLUX would allow us to determine whether the CSPP1 fragments localize inside or outside 25-nm-wide microtubule filaments.

For 2D MINFLUX measurements, we used fixed microtubules that were grown *in vitro* in the presence of SNAP-tagged CSPP1 or one of its fragments. We first performed measurements for CSPP-L, the same protein we used for cryo-ET. We determined the Full-Width-Half-Maximum (FWHM) values of the measured localizations and found the diameter CSPP-L signal was 15.87 ± 7.47 nm (mean \pm SD) (Fig. 4D, F; Fig. S3B), clearly indicating it is inside microtubule lumen. This is supported by the determined localization precision in x and y of the MINFLUX measurements, as these values are 3.7 and 3.2 nm, respectively (Fig. S3C). The smallest CSPP1 fragment binding to microtubules, H4+LZ, gave too much background signal to allow meaningful measurements. However, the smallest CSPP1 construct affecting microtubule dynamics *in vitro*, MTB+LZ (Fig. 3A-C) gave a signal diameter of 16.35 ± 6.80 nm (mean \pm SD), also indicating that it is located inside the microtubule lumen (Fig. 4E, F; Fig. S3B). To validate that the signal width is due to the protein being inside the microtubule lumen, we performed the same assays with GFP-labeled N-terminal, microtubule-binding part of MAP7, a protein known to bind to microtubule exterior (Ferro et al., 2022), which was also added during microtubule polymerization. Dual color 2D MINFLUX measurements

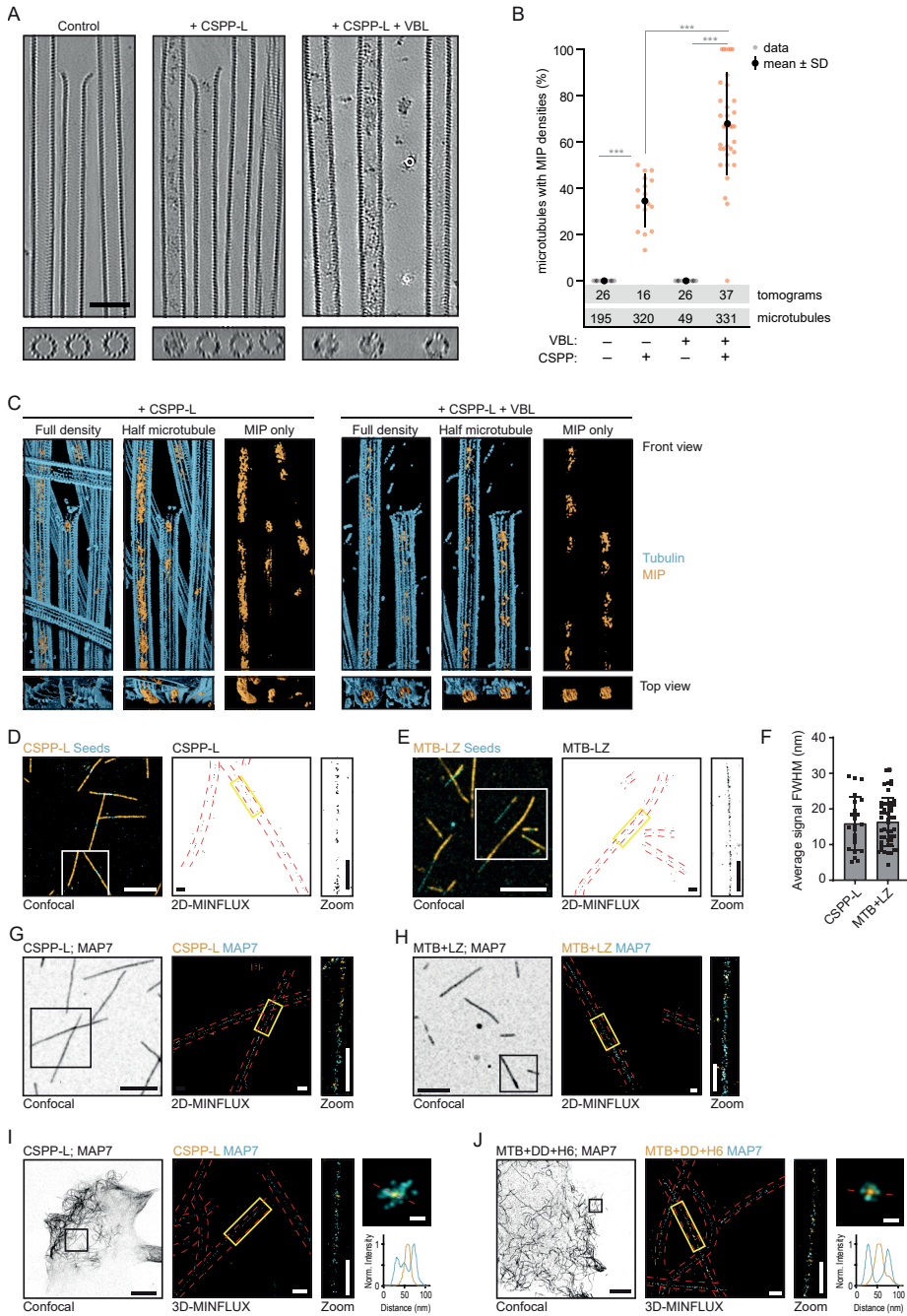


Figure 4: CSPP1 binds to microtubule lumen.

(A) Denoised tomograms of dynamic microtubules polymerized from GMPCPP-stabilized seeds in the presence or absence of 10 nM GFP-CSPP-L, with or without 250 nM vinblastine vitrified on EM grids. Scale bar, 50 nm. (B) Quantification of the percentage of microtubules containing

luminal densities from total microtubules (from tomograms as shown in A). Orange and grey dots (single data points, tomograms), black circle (mean), SD (error bars). Number of microtubules and tomograms are displayed in the graph. ***, $p < 0.001$, Mann-Whitney test. Analysis from two experiments. **(C)** Reconstituted images from automated segmentation of denoised tomograms as in A. **(D,E)** Single color 2D-MINFLUX measurements of *in vitro* reconstituted microtubules polymerized in the presence of SNAP-CSPP-L (D) or SNAP-MTB-LZ (E). Images were rendered with 1 nm voxel size for visualization. White boxes in confocal image indicate the region shown in the rendered 2D-MINFLUX image, yellow boxes in the 2D-MINFLUX image indicate the region of the zoom, red dashed lines represent the microtubule outline from the confocal image. Scale bars; 5 μm (Confocal image), 500 nm (2D-MINFLUX image and Zoom). **(F)** Quantification of the fitted, Full-Width-Half-Maximum values per microtubule (from 2D-MINFLUX images as shown in D and E). Single data points are shown. SD (error bars). Number of measured microtubules; CSPP-L, $n = 23$; MTB+LZ, $n = 49$. Analysis from three experiments. **(G,H)** Dual color 2D MINFLUX measurements of *in vitro* reconstituted microtubules polymerized in the presence of GFP-MAP7 N-terminus together with SNAP-CSPP-L (G) or SNAP-MTB-LZ (H). Images were rendered with 4 nm voxel size for visualization. Panel representation as in (D,E). **(I,J)** Dual color 3D-MINFLUX measurements of COS-7 cells overexpressing GFP-MAP7 plus SNAP-CSPP-L (I) or SNAP-MTB-DD-H6 (J). Images were rendered with 4 nm voxel size for visualization. Black boxes in confocal image indicate the region shown in the rendered 3D-MINFLUX image, yellow boxes in the 3D-MINFLUX image indicate the region of the zoom, red dashed lines represent the microtubule outline from the confocal image. Top right image shows a maximum intensity projection of the cross section of the microtubule over 400 nm (CSPP-L) or 800 nm (MTB+DD+H6). The red dashed line there indicates the line scan related to the bottom right graph. Scale bars; 10 μm (Confocal image), 500 nm (2D-MINFLUX image and Zoom), 50 nm (maximum intensity projection image). See also Figure S3 and Videos S3 and S4.

showed that both CSPP-L and MTB+LZ were surrounded by the MAP7 signal (**Fig. 4G, H; Fig. S3B**). The distinct localization of CSPP1 and MAP7, a label for the outer microtubule surface, together with the FWHM analysis indicate that CSPP-L and its short microtubule-binding fragment indeed localize to the lumen of *in vitro* reconstituted microtubules.

Next, we tested whether CSPP1 fragments localize inside microtubules in mammalian cells. We overexpressed SNAP-CSPP-L and GFP-MAP7 in COS-7 cells, fixed them and stained them for SNAP and GFP. Even though the labeling density of CSPP-L was very sparse, the maximum intensity projection over the cross section of the microtubule showed a ring of MAP7 signal surrounding CSPP-L (**Fig. 4I; Fig. S3D**). This was even more striking when we overexpressed the smaller SNAP-MTB+DD+H6 fragment together with GFP-MAP7 (**Fig. 4J, Fig. S3D, E; Video S4**). Acquisition of MINFLUX images for even shorter CSPP1 fragments were impeded by the high cytosolic background due to the presence of a significant pool of microtubule-unbound proteins. Taken together, the data obtained *in vitro* and in cells support the intraluminal localization of CSPP1 and indicate that the short MTB domain is sufficient for this localization.

CSPP1 efficiently binds to sites where microtubule lattices are damaged

Since CSPP1 is a MIP, we next examined whether it can bind to sites of lattice damage, which would provide access to microtubule lumen. First, we compared the binding of CSPP1 to Taxol-stabilized microtubules, which are known to acquire extensive lattice defects when incubated without soluble tubulin (Aher et al., 2020; Arnal and Wade, 1995), to more stable GMPCPP-bound microtubules. In the absence of soluble tubulin, CSPP-L gradually accumulated at discrete sites on both types of microtubules, but the binding to Taxol-stabilized microtubules was stronger and faster (**Fig. 5A, B**). Next, we induced local damage of GMPCPP-stabilized microtubules using illumination with a pulsed 532 nm laser, as described previously (Aher et al., 2020). We chose microtubule regions where no prior

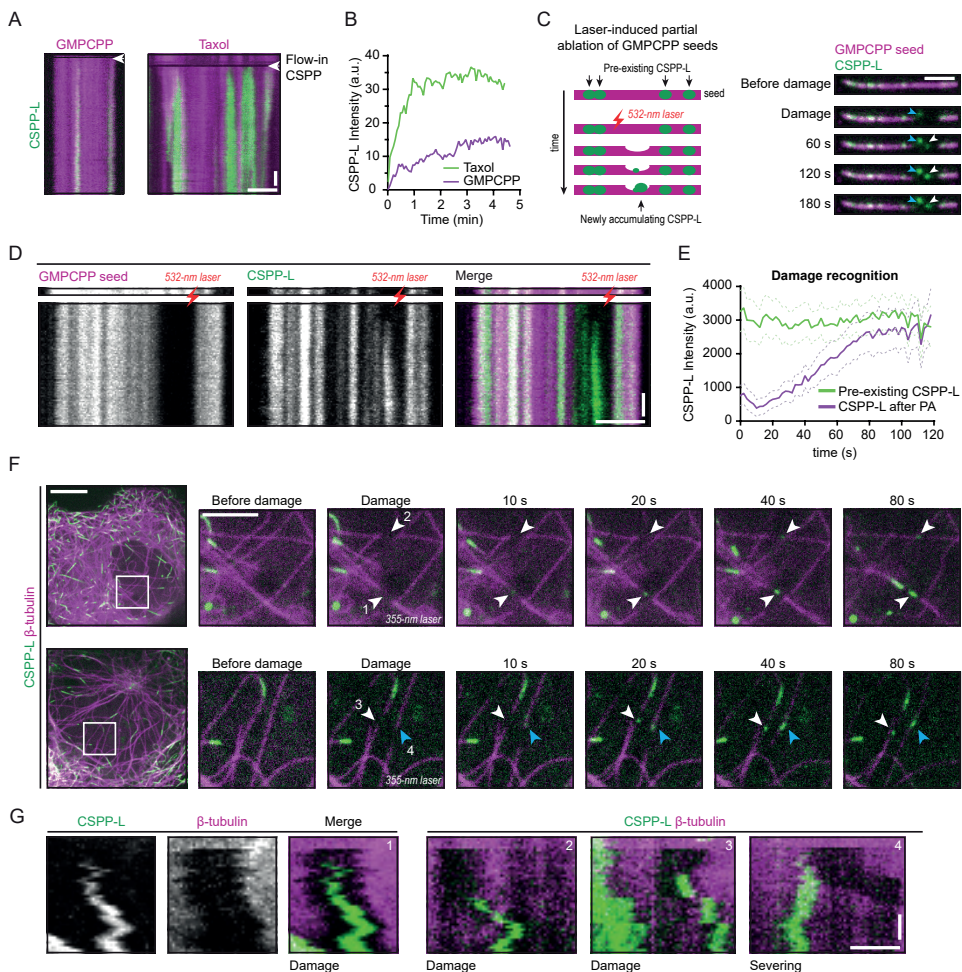


Figure 5: CSPP1 binds to sites where microtubule lattices are damaged.

(A) Kymographs of GMPCPP- (left) and Taxol-stabilized (right) microtubule seeds. 5 nM GFP-CSPP-L was flushed in during acquisition, in absence of free Taxol or tubulin. Scale bars, 2 μm (horizontal) and 30 s (vertical). (B) GFP-CSPP-L intensity profile of developing accumulation after flow-in of experiments done in A. (C) Schematic representation (left) and time lapse images (right) of laser damage of a GMPCPP-stabilized microtubule seed at regions with no prior GFP-CSPP-L accumulation. The microtubule region illuminated with the 532 nm pulsed laser is highlighted by a white arrowhead. The blue arrowhead indicates the damage inflicted on the coverslip. Scale bar 2 μm . (D) Kymograph corresponding to time lapse images shown in C. The laser illuminated microtubule region is highlighted by a red lightning bolt. Scale bars, 2 μm (horizontal) and 30 s (vertical). (E) Averaged GFP-CSPP-L intensity profiles of after photodamage (from kymographs as shown in D). Plots were aligned using half-maximum effective intensity values from nonlinear regression fits as reference points. Dashed lines represent s.e.m. Number of events analyzed, $n = 15$ from three independent experiments. (F) Time lapse images of photodamage experiments in COS-7 cells overexpressing GFP-CSPP-L and β -tubulin-mCherry. Arrowheads indicate the events where microtubules were damaged (white) or severed (blue). Imaging was performed using spinning disk microscopy and photodamage was induced with a 355 nm laser. Scale bars 10 μm (left) and 4 μm (zoom). (G) Kymographs of the events shown in F. Scale bars, 1 μm (horizontal) and 20 s (vertical). See also Video S5.

CSPP-L signal was present and selected for analysis only the microtubules that were not fully severed during laser illumination. We observed strong accumulation of CSPP-L at the illuminated sites, whereas the CSPP-L signal was relatively stable within the same time period at the sites that were not damaged with the laser (Fig. 5C-E).

Finally, we examined whether CSPP-L can recognize sites of microtubule damage in cells by performing laser microsurgery in COS-7 cells co-expressing GFP-CSPP-L and β -tubulin-mCherry. We damaged single microtubules in the z-plane just below the nucleus by local illumination with a 355 nm laser and observed CSPP-L accumulations forming at the illuminated positions (Fig. 5F, G; Video S5). It was more difficult to introduce local microtubule damage by laser microsurgery in cells than *in vitro* because the intensity of the laser beam varied with microtubule positions in the z-plane, so the degree of the photodamage was difficult to predict. For the analysis, we only considered events where new CSPP-L signal appeared at the position where the microtubule intensity was reduced after laser illumination. To distinguish partial damage from complete severing, we focused on the events where the illuminated microtubule was visible on both sides of the newly formed CSPP-L accumulation and where both microtubule parts moved synchronously with the photobleached region (Fig. 5F, G). The average time between laser illumination and the appearance of CSPP-L signal was 21 ± 13 s and the size of the CSPP-L accumulation 564 ± 157 nm (mean \pm SD, $n = 83$). Thus, CSPP1 can bind to damaged microtubule lattices *in vitro* and in cells.

CSPP1 stabilizes damaged microtubules and promotes lattice integrity

To determine whether CSPP1 can stabilize damaged microtubules, we again used Taxol-stabilized microtubules. Binding of CSPP-L to Taxol-stabilized microtubules was suppressed by the presence of free Taxol, which can prevent microtubule disassembly and erosion (Fig. 6A, B; Fig. S4A). In the absence of Taxol in solution, Taxol-stabilized microtubules gradually depolymerized (Fig. 6A). To quantify the effects of Taxol, CSPP-L, and free tubulin on microtubule stability, we determined the percentage of Taxol-stabilized seeds surviving after 5 min (Fig. 6C). CSPP-L could slow down though not block microtubule depolymerization in a concentration-dependent manner (Fig. 6A, C). The addition of free Taxol to these assays stabilized the microtubules completely, but when CSPP-L was also present, stabilization was slightly reduced, suggesting a potential competition between Taxol and CSPP1 for microtubule binding. The addition of low concentrations of free tubulin (2-5 μ M) in the absence of free Taxol had a very mild stabilizing effect in these assays, but in the presence of CSPP-L, complete microtubule stabilization was observed already at 2 μ M tubulin (Fig. 6A, C). At 5 μ M tubulin, CSPP-L even facilitated new microtubule lattice outgrowth (Fig. 6A), indicating that it might lower the tubulin concentration threshold for templated microtubule polymerization, as previously observed with some other microtubule regulators (Aher et al., 2018; Wiczorek et al., 2015). To confirm this conclusion, we repeated the assays with GMPCPP-stabilized microtubule seeds and found that CSPP-L strongly increased the frequency of microtubule outgrowth from seeds at 5 μ M tubulin (Fig. 6D; Fig. S4B). Interestingly, CSPP-L intensity along the newly formed microtubule lattice was much higher when microtubules were grown in 5 μ M tubulin compared to 15 μ M tubulin (Fig. 6E, F). This suggests that CSPP-L binds to microtubules more efficiently when they grow slowly, either due to a slow on-rate or because slowly growing microtubule ends have a different, possibly more pre-catastrophe-like structure. Thus, CSPP-L stabilizes microtubule polymerization intermediates at microtubule tips or damage sites when tubulin addition occurs slowly.

To better understand the mechanism underlying the activity of CSPP1, we again turned to cryo-ET. We stabilized microtubules by the addition of Taxol, and then resuspended them in a buffer containing CSPP-L with or without free Taxol, and no free tubulin. Absence of free Taxol increased CSPP-L binding: on average $26\% \pm 23\%$ of microtubules contained MIP

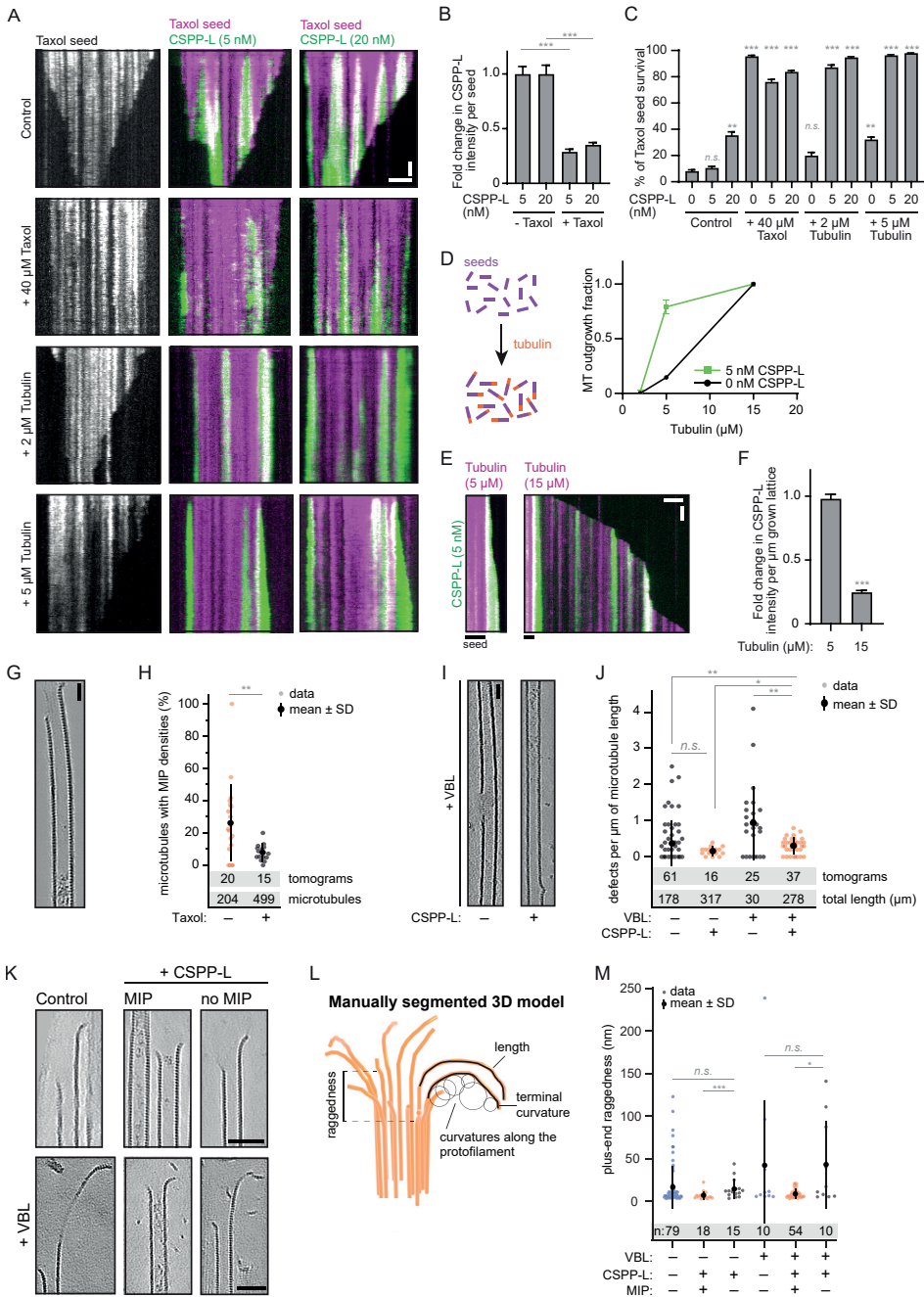


Figure 6: CSPP1 stabilizes microtubules by promoting lattice repair.

(A) Kymographs of Taxol-stabilized microtubule seeds in absence or presence of the indicated Taxol, tubulin, and GFP-CSPP-L concentrations. Scale bars, 2 μ m (horizontal) and 60 s (vertical). (B) GFP-CSPP-L intensity quantification per microtubule seed (from kymographs as shown in A). Mean

GFP-CSPP-L intensity was measured along the complete seed 2 min after flowing in the protein. The average mean intensity of GFP-CSPP-L in presence of 40 μM Taxol was normalized to the average mean intensity in absence of free Taxol. Number of Taxol-stabilized microtubule seeds analyzed: 5 nM CSPP-L alone, n=102; 20 nM CSPP-L alone, n=108; 40 μM Taxol, n=99; 40 μM Taxol together with 5 nM CSPP-L, n=84; 40 μM Taxol together with 20 nM CSPP-L, n=114. Error bars represent s.e.m. ***, $p < 0.001$; n.s., not significant; Kruskal-Wallis test followed by Dunn's post-test. Data quantified from two experiments. (C) Quantification of the percentage of microtubule seeds which survived 5 min after flow-in of the reaction mix (from kymographs as shown in A). Number of Taxol-stabilized microtubule seeds analyzed: control: n=95; 5 nM CSPP-L alone, n=120; 20 nM CSPP-L alone, n=110; 40 μM Taxol, n=99; 40 μM Taxol together with 5 nM CSPP-L, n=84; 40 μM Taxol together with 20 nM CSPP-L, n=120; 2 μM tubulin alone, n=115; 2 μM tubulin together with 5 nM CSPP-L, n=124; 2 μM tubulin together with 20 nM CSPP-L, n=112; 5 μM tubulin alone, n=122; 5 μM tubulin together with 5 nM CSPP-L, n=106; 5 μM tubulin together with 20 nM CSPP-L, n=128. Error bars represent s.e.m. ***, $p < 0.001$; **, $p < 0.01$; n.s., not significant; Kruskal-Wallis test followed by Dunn's post-test. In "control", conditions with 5 and 20 nM CSPP-L are compared to 0 nM CSPP-L, and for all other bars, comparisons were made to the same CSPP-L concentration in the control condition. Data quantified from two experiments. (D) Quantification of the fraction of the total GMPCPP seeds that showed microtubule outgrowth within 10 min at indicated tubulin concentrations, with tubulin alone or together with 5 nM GFP-CSPP-L. Number of GMPCPP seeds analyzed: 2 μM tubulin alone, n=74; 5 μM tubulin alone, n=75; 15 μM alone, n=69; 2 μM tubulin together with 5 nM CSPP-L, n=70; 5 μM tubulin together with 5 nM CSPP-L, n=66; 15 μM tubulin together with 5 nM CSPP-L FL, n=71. Error bars represent s.e.m. Data quantified from two experiments. (E) Kymographs of GMPCPP-stabilized microtubule seeds in the presence of 5 nM GFP-CSPP-L and the indicated tubulin concentrations. Scale bars, 2 μm (horizontal) and 60 s (vertical). (F) GFP-CSPP-L intensity quantification per μm newly grown microtubule lattice (from kymographs as shown in E). GFP-CSPP-L integrated intensity was measured on newly grown lattice 5 min after flow-in of the reaction mix. Integrated intensity was normalized to newly grown microtubule lattice length, and the average mean intensity of GFP-CSPP-L in presence of 15 μM tubulin was normalized to the average mean intensity in presence of 5 μM tubulin. Number of growth episodes analyzed: 5 μM tubulin, n=105; 15 μM tubulin, n=104. Error bars represent s.e.m. ***, $p < 0.001$, Mann-Whitney test. Data quantified from two experiments. (G) Denoised tomograms of dynamic microtubules polymerized in the presence of 250 μM Taxol, resuspended in buffer containing only 20 nM GFP-CSPP-L with or without free 40 μM Taxol, vitrified on EM grids. Scale bar, 25 nm. (H) Quantification of the percentage of microtubules containing luminal densities from total microtubules (from tomograms as shown in G). Orange and grey dots (single data points, tomograms), black circle (mean), SD (error bars). **, $p < 0.01$, Mann-Whitney test. Analysis from two experiments. (I) Denoised tomograms of dynamic microtubules polymerized in the presence or absence of 250 nM vinblastine with or without 20 nM GFP-CSPP-L, vitrified on EM grids. Scale bar, 25 nm. (J) Quantification of the number of defects per μm microtubule (from tomograms as shown in I). Orange and grey dots (single data points, tomograms), black circles (mean), SD (error bars). *, $p < 0.1$, **, $p < 0.01$, n.s., not significant, Mann-Whitney test. Analysis from two experiments. (K) Denoised tomograms of microtubule ends in presence or absence of 250 nM vinblastine with or without 20 nM GFP-CSPP-L, vitrified on EM grids. Scale bars, 50 nm. (L) Parameters extracted from manual segmentations of terminal protofilaments. (M) Quantification of plus-end raggedness (from tomograms as shown in K). Blue, orange, and grey dots (single data points, tomograms), black circle (mean), SD (error bars). *, $p < 0.1$, ***, $p < 0.001$, n.s., not significant, Mann-Whitney test. Analysis from two experiments. See also Figure S4.

densities, compared to only $8\% \pm 5\%$ in presence of Taxol ($p < 0.01$, Fig. 6G, H). Despite the fact that samples with disassembling Taxol-stabilized microtubules contained many incomplete lattices and tubulin sheets, we only observed MIP densities inside fully closed tubes (Fig. 6G). Moreover, CSPP-L accumulation zones did not bind CAMSAP3 in *in vitro* assays and thus did not contain lattice apertures (Fig. S4C), unlike previous observations with Fchitax-3 (Rai et al., 2020). Presence of vinblastine during microtubule growth led to the presence of more numerous defects in the microtubule lattices (Fig. 6L, J). However, presence of both vinblastine and CSPP-L during microtubule growth led to a significant reduction of

the number of lattice defects, comparing to vinblastine alone (0.3 ± 0.2 vs 1 ± 1 defects/ μm , $p = 0.005$). These observations, in combination with increased number of MIP-containing microtubules in presence of vinblastine (Fig. 4A, B), support our hypothesis that CSPP1 can enter microtubules through lattice openings, and then promote their repair.

In order to explain how CSPP1 stabilizes microtubules, we analyzed the shapes of terminal tubulin flares in our cryo-ET samples. We used manual segmentation to extract parameters of protofilament shape and length in 3D, as well as raggedness, or tapering (Fig. 6K, L). Comparing microtubule ends with MIPs to MIP-free microtubules in the same sample, we did not observe any significant differences in protofilament length or curvature (Fig. S4D). However, we did observe reduced raggedness of MIP-containing microtubule ends comparing MIP-positive and MIP-negative microtubules in presence of both CSPP-L and vinblastine (Fig. 6M). This might indicate CSPP1 does not act at terminal protofilament flares but stabilizes microtubules by holding protofilaments together within the tube, thus preventing microtubule disassembly and allowing them to resume growth. In a similar way, CSPP1 could potentially bind to damaged lattices and hold protofilaments together, to enable lattice repair by tubulin incorporation.

Discussion

While a lot of information exists about the control of microtubule dynamics by proteins associated with the outer microtubule surface, the regulatory effects of factors binding to microtubule lumen are understood much less well. Here, we show that the ciliary tip regulator CSPP1 is a MIP and dissect its behavior and molecular function. We show that CSPP1 displays some striking parallels to microtubule-stabilizing compounds, such as taxanes and epothilones, which also bind to microtubule lumen (reviewed in (Steinmetz and Prota, 2018)). Similar to these compounds, CSPP1 binds to polymerizing microtubule ends in the pre-catastrophe state, when the GTP cap is diminished, prevents catastrophe, and induces microtubule pausing followed by growth; at low concentration, CSPP1 triggers formation of sites of stabilized microtubule lattice that cause repeated rescues (“stable rescue sites” (Rai et al., 2020)). Preferential accumulation of CSPP1 at growing microtubule ends can be explained by the better accessibility of intraluminal binding sites, which become available when tubulin dimers are added to microtubule ends. Theory predicts that intraluminal diffusion of a protein with affinity for the inner microtubule surface would be very slow (Odde, 1998). Furthermore, unlike small molecules, CSPP1 would be too large to penetrate into the microtubule lumen through the regular lattice fenestrations, although it does bind to sites where the lattice has been damaged. Additionally, for CSPP1 to be able to accumulate inside the microtubule, this damage needs to be sufficiently large as accumulations are only observed in Taxol-stabilized microtubules with large defects but not in GMPCPP-stabilized microtubules which have smaller defects. The selectivity of CSPP1 for pre-catastrophe microtubule ends could be explained by their specific conformation (such as presence of tubulin sheets or tapers, or the loss of GTP-tubulin) or simply by their slow growth. The observation that CSPP1 binds to growing microtubule ends better when tubulin concentration is low and that it strongly accumulates inside microtubules lattices polymerized from the minus end is in agreement with its preference for slowly polymerizing microtubule ends. The striking overlap between the binding profiles of CSPP1 and the fluorescent taxane Fchitax-3, combined with our previous data demonstrating cooperative Fchitax-3 binding to microtubule ends (Rai et al., 2020), suggests that also CSPP1 can cooperatively bind to microtubule tips that undergo a growth perturbation. This would explain how CSPP1 forms regions of high enrichment when present at low concentrations. After binding, CSPP1 exerts a microtubule-stabilizing effect by preventing shrinkage; it could do so by supporting individual protofilaments and/

or by promoting lateral interactions between protofilaments, and both mechanisms would be consistent with the action of microtubule-stabilizing agents ((Elie-Caille et al., 2007; Prota et al., 2013; reviewed in Steinmetz and Prota, 2018). Spanning lateral protofilament contacts could potentially explain how CSPP1 reduces tip raggedness and why it is not found at protofilament flares.

Another interesting property of CSPP1 is its ability to induce pausing. While this property also resembles the effect of low concentrations of taxanes, in CSPP1, the lumen binding and growth-inhibiting functions depend on two separate protein domains. Presence of two activities, an activity that inhibits polymerization and an activity that prevents microtubule shrinkage, seems to be a common property of microtubule growth inhibitors, such as the kinesin-4 KIF21B (van Riel et al., 2017) or the centriolar protein CPAP (Sharma et al., 2016). In CSPP1, both regulatory domains are predicted to be helical and are quite short, less than a hundred amino acids. Presence of α -helices seems to be a common property of ciliary MIPs, including many linearly arranged proteins that form the regularly spaced inner sheath within ciliary doublets (Gui et al., 2021; Ichikawa and Bui, 2018; Ma et al., 2019). Identification of a minimal lumen-binding domain of CSPP1 (termed here the MTB) can be potentially useful for directing different protein activities to the microtubule lumen. It is possible that the binding site of the CSPP1 MTB domain overlaps with that of Taxol because we found some evidence of competition between Taxol and CSPP1 in microtubule stabilization assays.

Importantly, there is also a notable difference between the effects microtubule-stabilizing drugs and CSPP1: taxanes induce structural defects (holes) in microtubule lattices because they promote switching in protofilament number (Rai et al., 2021). In contrast, CSPP1 seems to promote lattice integrity. Although CSPP1 can specifically bind to the sites of lattice damage, CSPP1 densities are predominantly found within complete tubes; moreover, CSPP1 reduces the number of vinblastine-induced lattice defects and stabilizes eroding microtubule seeds. CSPP1 likely acts in part by stabilizing protofilament ends close to the damage sites and possibly by promoting tubulin incorporation to form complete tubes. Whether CSPP1 participates in repair of microtubule defects in cells, either on cytoplasmic or axonemal microtubules, remains to be determined. There are indications that cellular microtubules can be damaged by interaction with other microtubules, severing enzymes or motor proteins that use microtubules as rails (Aumeier et al., 2016; Gazzola et al., 2022; Triclin et al., 2021; Vemu et al., 2018). The ability of CSPP1 to specifically bind to incomplete microtubules can be harnessed for studying microtubule damage and repair. It should be noted that another protein, SSNA1, was also reported to bind to microtubule defects, albeit it appears much less potent than CSPP1 in stabilizing microtubules, because 0.5-5 μ M SSNA1 was needed to affect microtubule growth *in vitro* (Lawrence et al., 2021), whereas CSPP1 displays strong effects already at 5-10 nM concentration. It would be interesting to examine whether SSNA1 is also a MIP, as it was reported to stabilize partial microtubule structures (Basnet et al., 2018).

CSPP1 also shows some similarities to another intraluminal protein that has been analyzed *in vitro*, MAP6 (Cuveillier et al., 2020). While MAP6 shows some strikingly distinct features, such as the induction of microtubule coiling and lattice apertures (Cuveillier et al., 2020), both MAP6 and CSPP1 are microtubule stabilizers, which reduce overall microtubule shrinkage and promote rescues. Furthermore, both proteins contain a short domain that can perturb processive growth. In the case of MAP6, this domain is also required for the formation of intraluminal particles, and without it, the protein seems to function on the outer microtubule surface. In contrast, our cryoET and MINFLUX data support the idea that CSPP1 binds only to the inner surface of the microtubule. It is however still possible that some parts of CSPP1 extend out of the tube. For example, the site of action of the growth-inhibiting part of CSPP1 is currently unclear, as the shape and curvature of the protofilament flares in the presence of CSPP1 looked very similar to that of control microtubules and thus provided

no clues on the nature of this activity. Furthermore, CSPP1 is part of a multiprotein module associated with ciliary tips (Latour et al., 2020), and two other members of the same module, TOGARAM1 and CEP104, are likely to bind to the outer microtubule surface, because they contain canonical tubulin-binding TOG domains; moreover, CEP104 binds to EBs, which decorate microtubules from the outside (Al-Jassar et al., 2017; Das et al., 2015; Jiang et al., 2012; Rezabkova et al., 2016).

CSPP1 participates in controlling the elongation and stability of ciliary axonemes, and when CSPP1 or its binding partners are absent, ciliogenesis is impaired and cilia are shorter (Frikstad et al., 2019; Latour et al., 2020; Patzke et al., 2010). Our findings help to explain the microtubule-stabilizing activity of CSPP1 and suggest that ciliary tips are kept in shape by protein complexes that span both the inner and the outer microtubule surface. This arrangement might be important for controlling different signaling pathways such as Hedgehog signaling, which strongly relies on the state of axoneme tip and is dysregulated by ciliopathies (Andreu-Cervera et al., 2021; Hildebrandt et al., 2011; Reiter and Leroux, 2017). Furthermore, the similarity between the activities of CSPP1 and microtubule-stabilizing agents raise an interesting possibility that the absence of CSPP1 or its binding partners might be compensated by such compounds, suggesting potential avenues for pharmacological intervention in ciliopathies.

Materials and Methods

DNA constructs, cell lines and cell culture

CSPP1 truncations expressed in mammalian cells were made from the full-length constructs described previously (Patzke et al., 2005; Patzke et al., 2006) in modified pEGFP-C1 or pmCherry-C1 vectors with a StrepII tag. HEK293T cells and COS-7 cells (ATCC) were cultured in DMEM medium (Lonza) supplemented with 10% fetal calf serum (FCS) (GE Healthcare Life Sciences) and 1% (v/v) penicillin/streptomycin. All cells were routinely checked for mycoplasma contamination using the MycoAlert™ Mycoplasma Detection Kit (Lonza). For overexpression of CSPP1 constructs, COS-7 cells were transiently transfected with FuGENE6 (Promega) with different StrepII-GFP-CSPP1 constructs for 24 h. Single transfections were used for immunofluorescence experiments and co-transfections with EB3-mCherry (Stepanova et al., 2003), β IVb-tubulin-mCherry (Bouchet et al., 2016) or StrepII-GFP-MAP7 FL (Hooikaas et al., 2019) were used for live-cell imaging or MINFLUX microscopy.

Protein purification from HEK293T cells for in vitro reconstitution assays

For the purification of CSPP1 constructs, HEK293T cells were transiently transfected with polyethyleneimine (Polysciences) with different StrepII-GFP-CSPP1 constructs. The cells were harvested 28 h after transfection. Cells from a 15 cm dish were lysed in 500 μ l lysis buffer (50 mM HEPES, 300 mM NaCl, 1 mM MgCl₂, 1 mM DTT, 0.5% Triton X-100, pH 7.4) supplemented with protease inhibitors (Roche) on ice for 15 min. The lysate was cleared from debris by centrifugation and the supernatant was incubated with 20 μ l StrepTactin beads (GE Healthcare) for 45 min. Beads were washed five times with a 300 mM salt wash buffer (50 mM HEPES, 300 mM NaCl, 1 mM MgCl₂, 1 mM EGTA, 1 mM DTT, 0.05% Triton X-100, pH 7.4) and three times with a 150 mM salt wash buffer (similar to the 300 mM salt buffer but with 150 mM NaCl). The protein was eluted in elution buffer (similar to the 150 mM salt wash but supplemented with 2.5 mM d-Desthiobiotin (Sigma-Aldrich)) where the volume depended on the expression levels before harvesting. Purified proteins were snap-frozen and stored at -80°C.

Mass spectrometry

To confirm we purified GFP-CSPP-L without any interactors that could affect its effect on microtubule dynamics, the purified protein sample was digested using S-TRAP microfilters (ProtiFi) according to the manufacturer's protocol. In short, 7 μ g of protein sample was denatured in 5% SDS buffer and reduced and alkylated using DTT (20 mM, 10 min, 95°C) and iodoacetamide (IAA; 40 mM, 30 min). After acidification, the proteins were precipitated using a methanol triethylammonium bicarbonate buffer (TEAB) after which they were loaded on the S-TRAP column. The trapped proteins were washed four times with the methanol TEAB buffer and then digested using 1 μ g Trypsin (Promega) overnight at 37°C. Digested peptides were eluted and dried in a vacuum centrifuge before liquid chromatography-mass spectrometry (LC-MS) analysis.

The sample was analyzed by reversed-phase nLC-MS/MS using an Ultimate 3000 UHPLC coupled to an Orbitrap Q Exactive HF-X mass spectrometer (Thermo Scientific). Digested peptides were separated using a 50 cm reversed-phase column packed in-house (Agilent Poroshell EC-C18, 2.7 μ m, 50 cm x 75 μ m). The peptides were eluted from the column at a flow rate of 300 nl/min using a linear gradient with buffer A (0.1% formic acid (FA)) and buffer B (80% acetonitrile (ACN), 0.1% FA) ranging from 13-44% B over 38 min. This procedure was followed by a column wash and re-equilibration step resulting in a total data acquisition time of 55 min. Mass spectrometry data were acquired using a data-dependent acquisition (DDA) method with the following MS1 scan parameters: maximum injection time of 20 msec, automatic gain control (AGC) target equal to 3E6, 60,000 resolution, the scan range of 375-1600 m/z, acquired in profile mode. The MS2 method was set at 15,000 resolution, an automatic maximum injection time, with an AGC target set to standard and an isolation window of 1.4 m/z. Scans were acquired using a fixed first mass of 120 m/z and a mass range of 200-2000, and a normalized collision energy (NCE) of 28. Precursor ions were selected for fragmentation using a 1-second scan cycle, a dynamic exclusion time set to 10 sec, and a precursor charge selection filter for ions possessing +2 to +6 charges.

Raw files were processed using Proteome Discoverer (PD) (version 2.4, Thermo Scientific). MSMS fragment spectra were searched using Sequest HT against a human database (UniProt, year 2020) that was modified to contain the exact protein sequence from SII-GFP-CSPP-L and a common contaminants database. The search parameters were set using a fragment mass tolerance of 0.06 Da and a precursor mass tolerance of 20 ppm and. The maximum amount of missed cleavages for trypsin digestion was set to two. Methionine oxidation and protein N-term acetylation were set as variable modifications and carbamidomethylation was set as a fixed modification. Percolator was used to assign a 1% false discovery

rate (FDR) for peptide spectral matches, and a 1% FDR was applied to protein and peptide assemblies. For peptide-spectrum match (PSM) inclusion, an additional filter was set to require a minimum Sequest score of 2.0. The Precursor Ion Quantifier node was used for MS1 based quantification; default were settings applied. Precursor ion feature matching was enabled using the Feature Mapper node. Proteins that matched the common contaminant database were filtered out from the results table.

In vitro reconstitution assays

Microtubule seed preparation

Double-cycled GMPCPP-stabilized microtubule seeds or Taxol-stabilized microtubule seeds were used as templates for microtubule nucleation or to test protein binding in *in vitro* assays. GMPCPP-stabilized microtubule seeds were prepared as described before (Mohan et al., 2013). Briefly, a tubulin mix consisting of 70% unlabeled porcine brain tubulin, 18% biotin-labeled porcine tubulin and 12% rhodamine-labeled porcine tubulin (all from Cytoskeleton) was incubated with 1 mM GMPCPP (Jena Biosciences) at 37°C for 30 min. Polymerized microtubules were pelleted by centrifugation in an Airfuge for 5 min at 119,000g and then depolymerized on ice for 20 min. Next, microtubules were let to polymerize again at 37°C with newly added 1 mM GMPCPP. Polymerized microtubule seeds were then pelleted as above and diluted tenfold in MRB80 buffer containing 10% glycerol. Last, microtubule seeds were frozen and stored at -80°C. Taxol-stabilized microtubule seeds were prepared as described before with some modifications (Aher et al., 2020). Briefly, a tubulin mix consisting of 28 μ M porcine brain tubulin, 10% biotin-labeled porcine tubulin and 4.5% rhodamine-labeled porcine tubulin was incubated with 2 mM GTP (Sigma-Aldrich) and 20 μ M Taxol at 37°C for 35 min. Then, 20 μ M Taxol was added to the tubulin mix and polymerized microtubules were pelleted by centrifugation for 15 min at 16,200g at room temperature. The microtubule pellet was resuspended in warm 20 μ M Taxol solution in MRB80 buffer and stored at room temperature in the dark for a maximum of one day.

In vitro reconstitution assays

In vitro assays with dynamic or stabilized microtubules were performed as described before (Rai et al., 2020). In short, plasma-cleaned glass coverslips (square or rectangular) were attached on microscopic slides by two strips of double-sided tape. The coverslips were functionalized by sequential incubation with 0.2 mg/ml PLL-PEG-biotin (Susos AG, Switzerland) and 1 mg/ml neutravidin (Invitrogen) in MRB80 buffer (80 mM piperazine-N, N[prime]-bis (2-ethane sulfonic acid), pH 6.8, supplemented with 4 mM MgCl₂, and 1 mM EGTA). Then, GMPCPP- or Taxol-stabilized microtubule seeds were attached to the coverslips through biotin-neutravidin interactions. During the subsequent blocking step with 1 mg/ml κ -casein, the reaction mix containing the different concentrations of purified proteins and drugs was spun down in an Airfuge for 5 min at 119,000g. For dynamic microtubules, the reaction mix consisted of MRB80 buffer supplemented with 15 μ M porcine brain tubulin (100% dark porcine brain tubulin when 20 nM GFP-EB3 or mCherry-EB3 was added, or 97% dark porcine brain tubulin with 3% rhodamine- or HiLyte488-labeled porcine tubulin), 50 mM KCl, 1 mM GTP, 0.2 mg/ml κ -casein, 0.1% methylcellulose and oxygen scavenger mix [50 mM glucose, 400 μ g/ml glucose oxidase, 200 μ g/ml catalase and 4 mM DTT]. For stabilized microtubules, porcine tubulin, GTP and EB3 were omitted from the reaction mix. After spinning, the reaction mix was added to the flow chamber and the flow chamber was most often sealed with vacuum grease or left open (for flow-in assays during acquisition or for MINFLUX sample preparation). Microtubules were imaged immediately at 30°C using a total internal reflection fluorescence (TIRF) microscope. All tubulin products were from Cytoskeleton Inc.

To estimate the number of GFP-CSPP-L molecules per 8 nm microtubule, two parallel flow chambers were made on the same coverslip. In one chamber, regular microtubule dynamic assay in the presence of GMPCPP-stabilized microtubule seeds with tubulin, EB3-mCherry and 5 nM GFP-CSPP-L was performed. The other chamber was incubated with strongly diluted GFP protein so that single molecules were detectable. Microtubules were let to polymerize for 5-10 min. Then, for both the chamber with single GFP molecules and the chamber with dynamic microtubule and GFP-CSPP-L, 20 images of unexposed coverslip areas were acquired at 100-ms exposure time using high laser intensity.

In vitro assays for Cryo-ET sample preparation

Sample preparation for imaging *in vitro* microtubules with cryo-ET is a slightly modified version of the method described above. All steps occur in a tube instead of a flow chamber. After centrifugation of the reaction mix for dynamic microtubules, GMPCPP-stabilized seeds and 5 nm gold particles were added, and microtubules were let to polymerize for 20-30 min at 37°C. Then, 3.5 μ l was transferred to a recently glow-discharged, lacey carbon grid suspended in the chamber of Leica EM GP2 plunge freezer, equilibrated at 37°C and 98% relative humidity. The grid was immediately blotted for 4 s and plunge-frozen in liquid ethane.

In vitro assays for MINFLUX sample preparation

Sample preparation for imaging *in vitro* microtubules with MINFLUX microscopy is a slightly modified version of the method described above. For flow-chambers, round plasma-cleaned coverslips were attached to big, rectangular coverslips via two stripes of glue (Twinsil®). The reaction mix contained the same components as for dynamic microtubules, supplemented with an CF680-GFP-Nanobody and SNAP-Abberior FLUX-640. After addition of the reaction mix, the chamber was left open and was incubated in a 30°C incubator for 15 min. To remove background signal, the flow chamber was washed with a second reaction mix containing 25 µM tubulin before fixing with 1% glutaraldehyde (Electron Microscopy Sciences) for 5 min at room temperature. After washing with MRB80, the round glass coverslip was demounted and stored in MRB80 at 4°C or incubated with gold nanoparticles (Nanopartz) for 5 min. Then, the coverslips were mounted in GLOX buffer (50 mM Tris/HCl pH 8, 10 mM NaCl, 10% (w/v) d-glucose, 500 µg/ml glucose oxidase, 40 µg/ml glucose catalase) supplemented with 56 mM 2-Mercaptoethylamin (MEA) and sealed with glue (Picodent Twinsil®).

Immunofluorescence staining of fixed cells

Sample preparation for widefield fluorescence imaging

For immunofluorescence staining experiments, COS-7 cells were seeded on coverslips one day before transfection. Cells were fixed after 24 h with either -20°C MeOH for 10 min (staining for acetylated tubulin, α -tubulin, PCM1 and CSPP1) or -20°C MeOH for 10 min followed by 4% paraformaldehyde for 15 min at room temperature (staining for α -tubulin and EB1). This was followed by permeabilization with 0.15% Triton X-100 for 2 min. Next, samples were blocked with 1% bovine serum albumin (BSA) diluted in phosphate buffered saline (PBS) supplemented with 0.05% Tween-20 for 45 min at room temperature and sequentially incubated with primary antibodies for 1 h at room temperature and fluorescently labeled with secondary antibodies for 45 min at room temperature. Finally, samples were washed, dried, and mounted in Vectashield (Vector laboratories).

Sample preparation for MINFLUX microscopy imaging

For immunofluorescence staining experiments, COS-7 cells were seeded on coverslips one day before transfection. 24 h after transfection, the cells were incubated with warm extraction buffer (0.2% glutaraldehyde, 0.35% Triton X-100 in MRB80) for 2 min before incubation with fixation buffer (0.1% glutaraldehyde, 4% paraformaldehyde and 4% sucrose (w/v)) for 10 min at room temperature (staining for α -tubulin and EB1) followed by permeabilization with 0.5% Triton X-100 for 10 min. Next, samples were quenched with 100 mM NaBH₄ before blocking with Image-iT Signal Enhancer (Thermo Fisher Scientific) for 30 min at room temperature and sequentially incubated with 1 µM Alexa647-SNAP-dye (NEB) and 1 mM DTT in PBS for 1 h at room temperature. Next, samples were blocked with 1% bovine serum albumin (BSA) diluted in phosphate buffered saline (PBS) for 50 min at room temperature and sequentially incubated with CF680-GFP-Nanobody for 1 h at room temperature or overnight at 4°C. Coverslips were incubated with gold nanoparticles (Nanopartz) for 5 min. Then, the coverslips were mounted in GLOX buffer supplemented with 56 mM MEA and sealed with glue (Picodent Twinsil®).

Microscopy

Widefield microscopy

Fixed and stained COS-7 cells were imaged using widefield fluorescence illumination on a Nikon Eclipse Ni upright microscope equipped with a Nikon DS-Qi2 camera (Nikon), an Intensilight C-HGFI precentered fiber illuminator (Nikon), ET-DAPI, ET-EGFP and ET-mCherry filters (Chroma), controlled by Nikon NIS Br software and using a Plan Apo Lambda 60x NA 1.4 oil objective (Nikon). For presentation, images were adjusted for brightness using ImageJ 1.50b.

TIRF microscopy

In vitro reconstitution assays and live COS-7 cells overexpressing GFP-CSPP-L and mCherry-EB3 were imaged on previously described (iLas2) TIRF microscope setups (Aher et al., 2020). In brief, we used an inverted research microscope Nikon Eclipse Ti-E (Nikon) with the perfect focus system (Nikon), equipped with Nikon CFI Apo TIRF 100x 1.49 N.A. oil objective (Nikon) and controlled with MetaMorph 7.10.2.240 software (Molecular Devices). The microscope was equipped with TIRF-E motorized TIRF illuminator modified by Gataca Systems (France). To keep the *in vitro* samples at 30°C, a stage top incubator model INUBG2E-ZILCS (Tokai Hit) was used. For excitation, 490 nm 150 mW Vortran Stradus 488 laser (Vortran) and 561 nm 100 mW Cobolt Jive (Cobolt) lasers were used. We used ET-GFP 49002 filter set (Chroma) for imaging of proteins tagged with GFP or tubulin labeled with Hylite488 or ET-mCherry 49008 filter set (Chroma) for imaging of proteins tagged with mCherry

or tubulin labeled with rhodamine. Fluorescence was detected using a Prime BSI camera (Teledyne Photometrics) with the intermediate lens 2.5X (Nikon C mount adaptor 2.5X) or an EMCCD Evolve 512 camera (Roper Scientific) without an additional lens. The final resolution using Prime BSI camera was 0.068 $\mu\text{m}/\text{pixel}$, using EMCCD camera it was 0.063 $\mu\text{m}/\text{pixel}$.

The iLas3 system (Gataca Systems (France)) is a dual laser illuminator for azimuthal spinning TIRF (or Hilo) illumination and targeted photomanipulation option. This system was installed on Nikon Ti microscope (with the perfect focus system, Nikon), equipped with 489 nm 150 mW Vortran Stradus 488 laser (Vortran) and 100 mW 561 nm OBIS laser (Coherent), 49002 and 49008 Chroma filter sets, EMCCD Evolve DELTA 512 camera (Teledyne Photometrics) with the intermediate lens 2.5X (Nikon C mount adaptor 2.5X), CCD camera CoolSNAP MYO (Teledyne Photometrics) and controlled with MetaMorph 7.10.2.240 software (Molecular Device). To keep the *in vitro* samples at 30°C or the live cells at 37°C, a stage top incubator model INUBG2E-ZILCS (Tokai Hit) was used. The final resolution using EMCCD camera was 0.064 $\mu\text{m}/\text{pixel}$, using CCD camera it was 0.045 $\mu\text{m}/\text{pixel}$. This microscope was also used for photoablation. The 532 nm Q-switched pulsed laser (Teem Photonics) as part of iLas3 system was used for photoablation by targeting the laser on the TIRF microscope very close but not directly at the microtubule lattice to induce damage. For photodamage, a circle with a diameter of 7 pixels was used for 50 ms illumination at 20%–25% laser power of the 532 nm pulsed laser.

Spinning disk microscopy

Photodamage assays in cells were performed using spinning disk microscopy. COS-7 cells overexpressing GFP-CSPP-L and β -tubulin-mCherry were imaged using confocal spinning disc fluorescence microscopy on an inverted research microscope Nikon Eclipse Ti-E (Nikon), equipped with the perfect focus system (Nikon), Nikon Plan Apo VC 100x N.A. 1.40 oil objective (Nikon) and a spinning disk-based confocal scanner unit (CSU-X1-A1, Yokogawa). The system was also equipped with ASI motorized stage with the piezo plate MS-2000-XYZ (ASI), Photometrics PRIME BSI sCMOS camera (Teledyne Photometrics) and controlled by the MetaMorph 7.10.2.240 software (Molecular Devices). For imaging we used 487 nm 150 mW Vortran Stradus 488 (Vortran) and 100 mW 561 nm OBIS (Coherent) lasers, the ET-EGFP/mCherry filter (Chroma) for spinning-disc-based confocal imaging. The final resolution using PRIME BSI camera was 0.063 $\mu\text{m}/\text{pixel}$. To keep the live cells at 37°C, a stage top incubator model INUBG2E-ZILCS (Tokai Hit) was used. The 355 nm laser (Teem Photonics) of the iLAS pulse system was used to induce photodamage by targeting the laser on the spinning disk microscope in a 1-pixel-thick line across microtubules in the z-plane under the nucleus at 9%–11% laser power to induce damage.

MINFLUX microscopy

MINFLUX imaging was performed on an Abberior MINFLUX microscope (Abberior) equipped with a 1.4 NA 100 \times Oil objective lens as previously described (Schmidt et al., 2021). Two color images were recorded using ratiometric detection on two avalanche photodiodes. The fluorescence signal of two far-red fluorophores was split at 685 nm into two detection channels (Ch1: 650–685 nm and Ch2: 685–750 nm), the ratio between both detector channels allowed to assign the individual single molecule events to the respective fluorophores. Images were acquired in 2D or 3D MINFLUX imaging mode using a 642 nm excitation laser (17.4 $\mu\text{W}/\text{cm}^2$). Laser powers were measured at the position of the objective back focal plane using a Thorlabs PM100D power meter equipped with a S120C sensor head.

Cryo-ET microscopy

Images were recorded on a JEM3200FSC microscope (JEOL) equipped with an in-column energy filter operated in zero-loss imaging mode with a 30 eV slit. Movies consisting of 8–10 frames were recorded using a K2 Summit direct electron detector (Gatan), with a target total electron dose of 80 $e^-/\text{\AA}^2$. Images were recorded at 300 kV with a nominal magnification of 10000, resulting in a pixel size of 3.668 \AA at the specimen level. Imaging was performed using SerialEM software (Mastroradar, 2005), recording bidirectional tilt series starting from 0° \pm 60°; tilt increment 2°; target defocus -4 μm .

Image analysis

Analysis of microtubule plus end dynamics *in vitro*

Movies of dynamic microtubules, acquired as describe above, were corrected for drift, and kymographs were generated using the ImageJ plugin KymoResliceWide v.0.4 (<https://github.com/ekatrakha/KymoResliceWide>). The microtubule tips were traced with lines and measured lengths and angles were used to calculate the microtubule dynamics parameters such as growth rate, pause duration, event duration and all transition events. All events with growth rates faster than 0.24 $\mu\text{m}/\text{s}$

min were categorized as growth events and all events with shrinkage rates faster than $0.24 \mu\text{m}/\text{min}$ were categorized as shrinkage events. The events with slower growth rates or faster shrinkage rates than the before mentioned rates were categorized as pause events. Only growth events longer than $0.40 \mu\text{m}$ and pause events longer than 20 s were included in the analysis. Transition frequency was calculated by dividing the sum of the transition events per experiment by the total time this event could have occurred.

Quantification of EB1 comets

Images of COS-7 cells overexpressing GFP-CSPP1 constructs and stained for α -tubulin and EB1 were acquired on a widefield microscope as described above. The background was subtracted using the Rollin Ball Background Subtraction plugin in ImageJ. This plugin uses the rolling-ball algorithm where we set the radius to 10 pixels. EB1 comets were detected by “MaxEntropy” thresholding and subsequent particle analysis with a minimal size cut-off of $0.10 \mu\text{m}^2$ and the total number of EB1 comets per cell was normalized to $100 \mu\text{m}^2$.

3D volume reconstruction and analysis

Reconstruction, denoising, and analysis of tomographic volumes were performed as described previously (Ogunmolu et al., 2021). In brief, direct electron detector movie frames were aligned using MotionCor2 (Zheng et al., 2017) and then split into even and odd stacks used further for denoising. Tilt series alignment and tomographic reconstructions were performed with IMOD 4.11 (Kremer et al., 1996). Final tomographic volumes were binned by two, corrected for contrast transfer function, and the densities of gold beads were erased in IMOD. CryoCARE denoising was performed on tomograms reconstructed from the same tilt-series using even and odd movie frames (Buchholz et al., 2019). Tubulin lattice defects were identified upon visual inspection of denoised tomograms in 3dmod as interruptions of regular microtubule lattice that could not be attributed to missing wedge artifacts. Microtubules were sometimes damaged at microtubule-carbon or microtubule-microtubule contacts followed by blotting; these instances were not included in the quantification of defects.

Automated segmentation of denoised tomograms into tubulin and MIP densities was performed using the tomoseg module of EMAN2.2 (Chen et al., 2017). To do this, we trained three separate neural networks: ‘microtubules’, ‘tubulin’ and ‘MIP’. The resulting segmentations were used to mask the denoised tomographic densities using UCSF Chimera (Pettersen et al., 2004). This resulted in volume maximum projections of ‘microtubules’- and ‘tubulin’-masked densities in cyan, and ‘MIP’-masked densities in yellow. Final visualization and rendering were performed in Blender using 3D scenes imported from UCSF Chimera. Manual segmentation to obtain protofilament shapes at microtubule ends was performed as described previously (McIntosh et al., 2018; Ogunmolu et al., 2021) using 3dmod (Kremer et al., 1996). Protofilament coordinates were further analyzed using Matlab scripts available at <https://github.com/ngudimchuk/Process-PFs>.

MINFLUX data analysis

Images of microtubule were rendered from MINFLUX data as density map as described in (Schmidt et al., 2021). For the two-channel data, the channels were separated by applying cut-off on the “dcr” (detector channel ratio) attribute of the MINFLUX data. The cut-off values were decided by fitting of linear mixture of two Gaussian distributions over the “dcr” values. Data point with “dcr” value in the range between 0 and $\mu + 0.5\sigma$ of the first Gaussian component was considered as belonging to the 1st channel. And data point with “dcr” value in the range between $\mu - 0.5\sigma$ of the second Gaussian component and 1.0 was considered as belonging to the second channel. The rendered MINFLUX data were exported as TIFF images and used for subsequent analysis in Fiji.

To determine whether the fluorescence signal originated from protein binding on the outside or on the luminal side of the microtubules, we measured the lateral width of the microtubule filaments in the rendered MINFLUX images. To do that, we applied a custom analysis workflow implemented in Fiji. Briefly, for a given microtubule filament, we first extracted the central line along its longitudinal axis. The signal intensities of the nearby regions were then plotted against its distance to the central line and summed along the length of the filament. Thus, we generated the “profile plot”, similar to ImageJ’s intensity profile plot, for each microtubule filament. We then extracted the Full-Width at Half-Maximum (FWHM) of the intensity profile plot, as the estimation of the width of the given filament. A first Fiji script was created to automatically generate the central line segments from the rendered MINFLUX images. In short, it applies line and curvilinear filter to the images to generate first a microtubule segmentation, and then extracts the skeleton of each segmented microtubule filaments as the central line segments. Some manual correction can be applied here to remove the bad segmentation or line segments results, but in most cases, it was not necessary. A second Fiji script was then applied to measure the FWHM of

the intensity profile of each of the filaments. It reports the FWHM, as well as the length of each filament, and summarize the results of all filaments, to facilitate further statistical analysis.

Statistical analysis

All experiments were conducted at least twice. Statistical analysis was performed using GraphPad Prism 9. Statistical details of each experiment, including the statistical tests used, explanation and number of measurement and precision measures can be found in the figure legends.

Data availability

All cryo-ET data shown in the paper were deposited in EMDDB. Accession numbers are:
 Fig. 4A: control - EMD-15236; + CSPP-L - EMD-15237; + CSPP-L + VBL - EMD-15238
 Fig 4C: + CSPP-L - EMD-15237; + CSPP-L + VBL - EMD-15239.
 Fig 6G: taxol MTs + CSPP-L, no taxol added - EMD-15245.
 Fig 6I: + VBL - EMD-15246; + VBL + CSPP-L - EMD-15247.
 Fig 6K: control - EMD-15249; + CSPP-L + MIP - EMD-15237; + CSPP-L - EMD-15237;
 + VBL - EMD-15248; + VBL + CSPP-L + MIP - EMD-15250; + VBL + CSPP-L - EMD-15251.

Supplementary movie legends

Video S1: Dynamics of microtubules growing *in vitro* in the presence CSPP-L.

An example of TIRF microscopy imaging of microtubules growing from GMPCPP-stabilized microtubule seeds, in presence of 15 μM tubulin (supplemented with 3% rhodamine-tubulin) and 10 nM GFP-CSPP-L.

Video S2: Dynamics of microtubules labeled with CSPP-L and EB3 in COS-7 cells.

An example of TIRF microscopy imaging of microtubules in COS-7 cells overexpressing GFP-CSPP-L and EB3-mCherry. Full field of view (top) and three enlarged areas of interest are shown (bottom, indicated by white boxes). Arrowheads point to events of interest.

Video S3: 3D view of microtubules in the presence of CSPP-L.

Rendering of a tomogram acquired with Cryo-ET of microtubules grown *in vitro* in the presence of GFP-CSPP-L. The denoised densities were segmented into tubulin and microtubules (blue) and all other densities (orange) as described in Methods.

Video S4: 3D view of a microtubule showing MAP7 as an outside ring with CSPP1 construct MTB+DD+H6 inside.

An example of dual-color 3D-MINFLUX acquisition in COS-7 cells overexpressing SNAP-MTB+DD+H6 and GFP-MAP7.

Video S5: Photodamage of microtubules in COS-7 cells overexpressing GFP-CSPP-L and β -tubulin-mCherry.

An example of spinning disk confocal imaging of a photodamage experiment in COS-7 cells overexpressing GFP-CSPP-L and β -tubulin-mCherry. Arrowheads point to damage events.

Acknowledgements

We thank A. Jakobi (TU Delft) for providing access to a GPU computational cluster. V.A.V. acknowledges support from the QMUL Startup grant (SBC8VOL2). This work was supported by the European Research Council Synergy grant 609822 to M.D. and A.A. and the ZonMW TOP 91216006 program. We acknowledge the access and services provided by the Imaging Centre at the European Molecular Biology Laboratory (EMBL IC), generously supported by the Boehringer Ingelheim Foundation. The MINFLUX image acquisition of *in vitro* microtubules was facilitated by the Christian Boulin Fellowship awarded to C.M. vdB.

Author Contributions

C.M. vdB designed and performed protein purifications, *in vitro* reconstitution

experiments and cellular experiments, analyzed data and wrote the paper; V.A.V. designed and performed cryo-ET experiments, analyzed data and wrote the paper, S.S., Z.H. and T.Z. facilitated and performed MINFLUX imaging and analysis, K.E.S. performed and analyzed mass spectrometry experiments, I.G. performed and analyzed live cell imaging experiments using TIRF microscopy, S.P. provided reagents, insights into data analysis and contributed to writing, M.D. coordinated the project, A.A. coordinated the project and wrote the paper.

Competing financial interests

The authors declare no competing financial interests.

References

- Aher, A., M. Kok, A. Sharma, A. Rai, N. Olieric, R. Rodriguez-Garcia, E.A. Katrukha, T. Weinert, V. Olieric, L.C. Kapitein, M.O. Steinmetz, M. Dogterom, and A. Akhmanova. 2018. CLASP Suppresses Microtubule Catastrophes through a Single TOG Domain. *Dev Cell.* 46:40-58.
- Aher, A., D. Rai, L. Schaedel, J. Gaillard, K. John, Q. Liu, M. Altelaar, L. Blanchoin, M. Thery, and A. Akhmanova. 2020. CLASP Mediates Microtubule Repair by Restricting Lattice Damage and Regulating Tubulin Incorporation. *Curr Biol.* 30:2175-2183.
- Akhmanova, A., and M.O. Steinmetz. 2015. Control of microtubule organization and dynamics: two ends in the limelight. *Nat Rev Mol Cell Biol.* 16:711-726.
- Akizu, N., J.L. Silhavy, R.O. Rosti, E. Scott, A.G. Fenstermaker, J. Schroth, M.S. Zaki, H. Sanchez, N. Gupta, M. Kabra, M. Kara, T. Ben-Omran, B. Rosti, A. Guemez-Gamboa, E. Spencer, R. Pan, N. Cai, M. Abdellateef, S. Gabriel, J. Halbritter, F. Hildebrandt, H. van Bokhoven, M. Gunel, and J.G. Gleeson. 2014. Mutations in CSPP1 lead to classical Joubert syndrome. *Am J Hum Genet.* 94:80-86.
- Al-Jassar, C., A. Andreeva, D.D. Barnabas, S.H. McLaughlin, C.M. Johnson, M. Yu, and M. van Breugel. 2017. The Cilopathy-Associated Cep104 Protein Interacts with Tubulin and Nek1 Kinase. *Structure.* 25:146-156.
- Andreu-Cervera, A., M. Catala, and S. Schneider-Maunoury. 2021. Cilia, ciliopathies and hedgehog-related forebrain developmental disorders. *Neurobiol Dis.* 150:105236.
- Arnal, I., and R.H. Wade. 1995. How does taxol stabilize microtubules? *Curr Biol.* 5:900-908.
- Asiedu, M., D. Wu, F. Matsumura, and Q. Wei. 2009. Centrosome/spindle pole-associated protein regulates cytokinesis via promoting the recruitment of MyoGEF to the central spindle. *Mol Biol Cell.* 20:1428-1440.
- Aumeier, C., L. Schaedel, J. Gaillard, K. John, L. Blanchoin, and M. Thery. 2016. Self-repair promotes microtubule rescue. *Nat Cell Biol.* 18:1054-1064.
- Balzarotti, F., Y. Eilers, K.C. Gwosch, A.H. Gynna, V. Westphal, F.D. Stefani, J. Elf, and S.W. Hell. 2017. Nanometer resolution imaging and tracking of fluorescent molecules with minimal photon fluxes. *Science.* 355:606-612.
- Basnet, N., H. Nedozralova, A.H. Crevenna, S. Bodakuntla, T. Schlichthaerle, M. Taschner, G. Cardone, C. Janke, R. Jungmann, M.M. Magiera, C. Biertumpfel, and N. Mizuno. 2018. Direct induction of microtubule branching by microtubule nucleation factor SSNA1. *Nat Cell Biol.* 20:1172-1180.
- Bieling, P., L. Laan, H. Schek, E.L. Munteanu, L. Sandblad, M. Dogterom, D. Brunner, and T. Surrey. 2007. Reconstitution of a microtubule plus-end tracking system in vitro. *Nature.* 450:1100-1105.
- Bouchet, B.P., I. Noordstra, M. van Amersfoort, E.A. Katrukha, Y.C. Ammon, N.D. Ter Hoeve, L. Hodgson, M. Dogterom, P.W. Derksen, and A. Akhmanova. 2016. Mesenchymal Cell Invasion Requires Cooperative Regulation of Persistent Microtubule Growth by SLAIN2 and CLASP1. *Dev Cell.* 39:708-723.
- Buchholz, T.O., A. Krull, R. Shahidi, G. Pigino, G. Jekely, and F. Jug. 2019. Content-aware image restoration for electron microscopy. *Methods Cell Biol.* 152:277-289.
- Chen, M., W. Dai, S.Y. Sun, D. Jonasch, C.Y. He, M.F. Schmid, W. Chiu, and S.J. Ludtke. 2017. Convolutional neural networks for automated annotation of cellular cryo-electron tomograms. *Nat Methods.* 14:983-985.
- Cuveillier, C., J. Delarochette, M. Seggio, S. Gory-Faure, C. Bosc, E. Denarier, M. Bacia, G. Schoehn, H. Mohrbach, I. Kulic, A. Andrieux, I. Arnal, and C. Delphin. 2020. MAP6 is an intraluminal protein that induces neuronal microtubules to coil. *Sci Adv.* 6:eaa4344.
- Das, A., D.J. Dickinson, C.C. Wood, B. Goldstein, and K.C. Slep. 2015. Crescerin uses a TOG domain array to regulate microtubules in the primary cilium. *Mol Biol Cell.* 26:4248-4264.
- Desai, A., and T.J. Mitchison. 1997. Microtubule polymerization dynamics. *Annu Rev Cell Dev Biol.* 13:83-117.
- Diaz, J.F., R. Strobe, Y. Engelborghs, A.A. Souto, and J.M. Andreu. 2000. Molecular recognition of taxol by microtubules. Kinetics and thermodynamics of binding of fluorescent taxol derivatives to an exposed site. *J Biol Chem.* 275:26265-26276.
- Elie-Caille, C., F. Severin, J. Helenius, J. Howard, D.J. Muller, and A.A. Hyman. 2007. Straight GDP-tubulin protofilaments form in the presence of taxol. *Curr Biol.* 17:1765-1770.
- Ferro, L.S., Q. Fang, L. Eshun-Golson, J. Fernandes, A. Jack, D.P. Farrell, M. Wilcuk, T. Huijben, K. Costa, M. Gur, F. DiMaio, E. Nogales, and A. Yildiz. 2022. Structural and functional insight into regulation of kinesin-1 by microtubule-associated protein MAP7. *Science.* 375:326-331.
- Frikstad, K.M., E. Molinari, M. Thoresen, S.A. Ramsbottom, F. Hughes, S.J.F. Letteboer, S. Gilani, K.O. Schink, T. Stokke, S. Geimer, L.B. Pedersen, R.H. Giles, A. Akhmanova, R. Roepman, J.A. Sayer, and S. Patzke. 2019. A CEP104-CSPP1 Complex Is Required for Formation of Primary Cilia Competent in Hedgehog Signaling. *Cell Rep.* 28:1907-1922.
- Gazzola, M., A. Schaeffer, B. Vianay, J. Gaillard, L. Blanchoin, and M. Thery. 2022. Microtubules self-repair in living cells. *bioRxiv.* 2022.03.31.486545.
- Gell, C., V. Bormuth, G.J. Brouhard, D.N. Cohen, S. Diez, C.T. Friel, J. Helenius, B. Nitzsche, H. Petzold, J. Ribbe, E. Schaffer, J.H. Stear, A. Trushko, V. Varga, P.O. Widlund, M. Zanic, and J. Howard. 2010. Microtubule dynamics reconstituted in vitro and imaged by single-molecule fluorescence microscopy. *Methods*

- Cell Biol.* 95:221-245.
- Gudimchuk, N.B., and J.R. McIntosh. 2021. Regulation of microtubule dynamics, mechanics and function through the growing tip. *Nat Rev Mol Cell Biol.* 22:777-795.
- Gui, M., H. Farley, P. Anujan, J.R. Anderson, D.W. Maxwell, J.B. Whitchurch, J.J. Botsch, T. Qiu, S. Meleppattu, S.K. Singh, Q. Zhang, J. Thompson, J.S. Lucas, C.D. Bingle, D.P. Norris, S. Roy, and A. Brown. 2021. De novo identification of mammalian ciliary motility proteins using cryo-EM. *Cell.* 184:5791-5806.
- Gwosch, K.C., J.K. Pape, F. Balzarotti, P. Hoess, J. Ellenberg, J. Ries, and S.W. Hell. 2020. MINIFLUX nanoscopy delivers 3D multicolor nanometer resolution in cells. *Nat Methods.* 17:217-224.
- Hildebrandt, F., T. Benzing, and N. Katsanis. 2011. Ciliopathies. *N Engl J Med.* 364:1533-1543.
- Hooikaas, P.J., M. Martin, T. Muhlethaler, G.J. Kuijntjes, C.A.E. Peeters, E.A. Katrukha, L. Ferrari, R. Stucchi, D.G.F. Verhagen, W.E. van Riel, I. Grigoriev, A.F.M. Altelaar, C.C. Hoogenraad, S.G.D. Rudiger, M.O. Steinmetz, L.C. Kapitein, and A. Akhmanova. 2019. MAP7 family proteins regulate kinesin-1 recruitment and activation. *J Cell Biol.* 218:1298-1318.
- Ichikawa, M., and K.H. Bui. 2018. Microtubule Inner Proteins: A Meshwork of Luminal Proteins Stabilizing the Doublet Microtubule. *Bioessays.* 40:1700209.
- Jiang, K., G. Toedt, S. Montenegro Gouveia, N.E. Davey, S. Hua, B. van der Vaart, I. Grigoriev, J. Larsen, L.B. Pedersen, K. Bezstarosti, M. Lince-Faria, J. Demmers, M.O. Steinmetz, T.J. Gibson, and A. Akhmanova. 2012. A Proteome-wide screen for mammalian SxIP motif-containing microtubule plus-end tracking proteins. *Curr Biol.* 22:1800-1807.
- Jumper, J., R. Evans, A. Pritzel, T. Green, M. Figurnov, O. Ronneberger, K. Tunyasuvunakool, R. Bates, A. Židek, A. Potapenko, A. Bridgland, C. Meyer, S.A.A. Kohl, A.J. Ballard, A. Cowie, B. Romera-Paredes, S. Nikolov, R. Jain, J. Adler, T. Back, S. Petersen, D. Reiman, E. Clancy, M. Zielinski, M. Steinegger, M. Pacholska, T. Berghammer, S. Bodenstein, D. Silver, O. Vinyals, A.W. Senior, K. Kavukcuoglu, P. Kohli, and D. Hassabis. 2021. Highly accurate protein structure prediction with AlphaFold. *Nature.* 596:583-589.
- Komarova, Y., C.O. De Groot, I. Grigoriev, S.M. Gouveia, E.L. Munteanu, J.M. Schober, S. Honnappa, R.M. Buey, C.C. Hoogenraad, M. Dogterom, G.G. Borisov, M.O. Steinmetz, and A. Akhmanova. 2009. Mammalian end binding proteins control persistent microtubule growth. *J Cell Biol.* 184:691-706.
- Kremer, J.R., D.N. Mastronarde, and J.R. McIntosh. 1996. Computer visualization of three-dimensional image data using IMOD. *J Struct Biol.* 116:71-76.
- Latour, B.L., J.C. Van De Weghe, T.D. Rusterholz, S.J. Letteboer, A. Gomez, R. Shaheen, M. Gesemann, A. Karamzade, M. Asadollahi, M. Barroso-Gil, M. Chitre, M.E. Grout, J. van Reeuwijk, S.E. van Beersum, C.V. Miller, J.C. Dempsey, H. Morsy, G. University of Washington Center for Mendelian, M.J. Bamshad, C. Genomics England Research, D.A. Nickerson, S.C. Neuhaus, K. Boldt, M. Ueffing, M. Keramatipour, J.A. Sayer, F.S. Alkuraya, R. Bachmann-Gagescu, R. Roepman, and D. Doherty. 2020. Dysfunction of the ciliary ARMC9/TOGARAM1 protein module causes Joubert syndrome. *J Clin Invest.* 130:4423-4439.
- Lawrence, E.J., G. Arpag, C. Arnaiz, and M. Zanic. 2021. SSNA1 stabilizes dynamic microtubules and detects microtubule damage. *Elife.* 10:e67282.
- Ma, M., M. Stoyanova, G. Rademacher, S.K. Dutcher, A. Brown, and R. Zhang. 2019. Structure of the Decorated Ciliary Doublet Microtubule. *Cell.* 179:909-922.
- Magiera, M.M., P. Singh, S. Gadadhar, and C. Janke. 2018. Tubulin Posttranslational Modifications and Emerging Links to Human Disease. *Cell.* 173:1323-1327.
- Mastronarde, D.N. 2005. Automated electron microscope tomography using robust prediction of specimen movements. *J Struct Biol.* 152:36-51.
- McIntosh, J.R., E. O'Toole, G. Morgan, J. Austin, E. Ulyanov, F. Ataulakhanov, and N. Gudimchuk. 2018. Microtubules grow by the addition of bent guanosine triphosphate tubulin to the tips of curved protofilaments. *J Cell Biol.* 217:2691-2708.
- Mimori-Kiyosue, Y., N. Shiina, and S. Tsukita. 2000. The dynamic behavior of the APC-binding protein EB1 on the distal ends of microtubules. *Curr Biol.* 10:865-868.
- Mohan, R., E.A. Katrukha, H. Doodhi, I. Smal, E. Meijering, L.C. Kapitein, M.O. Steinmetz, and A. Akhmanova. 2013. End-binding proteins sensitize microtubules to the action of microtubule-targeting agents. *Proc Natl Acad Sci U S A.* 110:8900-8905.
- Montenegro Gouveia, S., K. Leslie, L.C. Kapitein, R.M. Buey, I. Grigoriev, M. Wagenbach, I. Smal, E. Meijering, C.C. Hoogenraad, L. Wordeman, M.O. Steinmetz, and A. Akhmanova. 2010. In vitro reconstitution of the functional interplay between MCAK and EB3 at microtubule plus ends. *Curr Biol.* 20:1717-1722.
- Odde, D. 1998. Diffusion inside microtubules. *Eur Biophys J.* 27:514-520.
- Ogunmolu, F.E., S. Moradi, V.A. Volkov, C. van Hoorn, J. Wu, N. Andrea, S. Hua, K. Jiang, I. Vakonakis, M. Potočnjak, F. Herzog, B. Gigant, N. Gudimchuk, K.E. Stecker, M. Dogterom, M.O. Steinmetz, and A. Akhmanova. 2021. Microtubule plus-end regulation by centriolar cap proteins. *bioRxiv.* 2021.12.29.474442.
- Patzke, S., H. Hauge, M. Sioud, E.F. Finne, E.A. Sivertsen, J. Delabie, T. Stokke, and H.C. Aasheim. 2005. Identification of a novel centrosome/microtubule-associated coiled-coil protein involved in cell-cycle progression and spindle organization. *Oncogene.* 24:1159-

- 1173.
- Patzke, S., S. Redick, A. Warsame, C.A. Murga-Zamalloa, H. Khanna, S. Doxsey, and T. Stokke. 2010. CSPP is a ciliary protein interacting with Nephrocystin 8 and required for cilia formation. *Mol Biol Cell*. 21:2555-2567.
- Patzke, S., T. Stokke, and H.C. Aasheim. 2006. CSPP and CSPP-L associate with centrosomes and microtubules and differently affect microtubule organization. *J Cell Physiol*. 209:199-210.
- Pettersen, E.F., T.D. Goddard, C.C. Huang, G.S. Couch, D.M. Greenblatt, E.C. Meng, and T.E. Ferrin. 2004. UCSF Chimera—a visualization system for exploratory research and analysis. *J Comput Chem*. 25:1605-1612.
- Prota, A.E., K. Bargsten, D. Zurwerra, J.J. Field, J.F. Diaz, K.H. Altmann, and M.O. Steinmetz. 2013. Molecular mechanism of action of microtubule-stabilizing anticancer agents. *Science*. 339:587-590.
- Rai, A., T. Liu, S. Glauser, E.A. Katrukha, J. Estevez-Gallego, R. Rodriguez-Garcia, W.S. Fang, J.F. Diaz, M.O. Steinmetz, K.H. Altmann, L.C. Kapitein, C.A. Moores, and A. Akhmanova. 2020. Taxanes convert regions of perturbed microtubule growth into rescue sites. *Nat Mater*. 19:355-365.
- Rai, A., T. Liu, E.A. Katrukha, J. Estevez-Gallego, S.W. Manka, I. Paterson, J.F. Diaz, L.C. Kapitein, C.A. Moores, and A. Akhmanova. 2021. Lattice defects induced by microtubule-stabilizing agents exert a long-range effect on microtubule growth by promoting catastrophes. *Proc Natl Acad Sci U S A*. 118:e2112261118.
- Reiter, J.F., and M.R. Leroux. 2017. Genes and molecular pathways underpinning ciliopathies. *Nat Rev Mol Cell Biol*. 18:533-547.
- Rezabkova, L., S.H. Kraatz, A. Akhmanova, M.O. Steinmetz, and R.A. Kammerer. 2016. Biophysical and Structural Characterization of the Centriolar Protein Cep104 Interaction Network. *J Biol Chem*. 291:18496-18504.
- Schmidt, R., T. Weihs, C.A. Wurm, I. Jansen, J. Rehman, S.J. Sahl, and S.W. Hell. 2021. MINFLUX nanometer-scale 3D imaging and microsecond-range tracking on a common fluorescence microscope. *Nat Commun*. 12:1478.
- Shaheen, R., H.E. Shamseldin, C.M. Loucks, M.Z. Seidahmed, S. Ansari, M. Ibrahim Khalil, N. Al-Yacoub, E.E. Davis, N.A. Mola, K. Szymanska, W. Herridge, A.E. Chudley, B.N. Chodirker, J. Schwartzentruber, J. Majewski, N. Katsanis, C. Poizat, C.A. Johnson, J. Parboosingh, K.M. Boycott, A.M. Innes, and F.S. Alkuraya. 2014. Mutations in CSPP1, encoding a core centrosomal protein, cause a range of ciliopathy phenotypes in humans. *Am J Hum Genet*. 94:73-79.
- Sharma, A., A. Aher, N.J. Dynes, D. Frey, E.A. Katrukha, R. Jaussi, I. Grigoriev, M. Croisier, R.A. Kammerer, A. Akhmanova, P. Gonczy, and M.O. Steinmetz. 2016. Centriolar CPAP/SAS-4 Imparts Slow Processive Microtubule Growth. *Dev Cell*. 37:362-376.
- Steinmetz, M.O., and A.E. Prota. 2018. Microtubule-Targeting Agents: Strategies To Hijack the Cytoskeleton. *Trends Cell Biol*. 28:776-792.
- Stepanova, T., J. Slemmer, C.C. Hoogenraad, G. Lansbergen, B. Dortmund, C.I. De Zeeuw, F. Grosveld, G. van Cappellen, A. Akhmanova, and N. Galjart. 2003. Visualization of microtubule growth in cultured neurons via the use of EB3-GFP (end-binding protein 3-green fluorescent protein). *J Neurosci*. 23:2655-2664.
- Triclin, S., D. Inoue, J. Gaillard, Z.M. Htet, M.E. DeSantis, D. Portran, E. Derivery, C. Aumeier, L. Schaedel, K. John, C. Letierrier, S.L. Reck-Peterson, L. Blanchoin, and M. Thery. 2021. Self-repair protects microtubules from destruction by molecular motors. *Nat Mater*. 20:883-891.
- Tuz, K., R. Bachmann-Gagescu, D.R. O'Day, K. Hua, C.R. Isabella, I.G. Phelps, A.E. Stolarski, B.J. O'Roak, J.C. Dempsey, C. Lourenco, A. Alswaid, C.G. Bonnemann, L. Medne, S. Nampoothiri, Z. Stark, R.J. Leventer, M. Topcu, A. Cansu, S. Jagadeesh, S. Done, G.E. Ishak, I.A. Glass, J. Shendure, S.C. Neuhaus, C.R. Haldeaman-Englert, D. Doherty, and R.J. Ferland. 2014. Mutations in CSPP1 cause primary cilia abnormalities and Joubert syndrome with or without Jeune asphyxiating thoracic dystrophy. *Am J Hum Genet*. 94:62-72.
- van Riel, W.E., A. Rai, S. Bianchi, E.A. Katrukha, Q. Liu, A.J. Heck, C.C. Hoogenraad, M.O. Steinmetz, L.C. Kapitein, and A. Akhmanova. 2017. Kinesin-4 KIF21B is a potent microtubule pausing factor. *Elife*. 6:e24746.
- Varadi, M., S. Anyango, M. Deshpande, S. Nair, C. Natassa, G. Yordanova, D. Yuan, O. Stroe, G. Wood, A. Laydon, A. Zidek, T. Green, K. Tunyasuvunakool, S. Petersen, J. Jumper, E. Clancy, R. Green, A. Vora, M. Lutfi, M. Figurnov, A. Cowie, N. Hobbs, P. Kohli, G. Kleywegt, E. Birney, D. Hassabis, and S. Velankar. 2022. AlphaFold Protein Structure Database: massively expanding the structural coverage of protein-sequence space with high-accuracy models. *Nucleic Acids Res*. 50:D439-D444.
- Vemu, A., E. Szczesna, E.A. Zehr, J.O. Spector, N. Grigorieff, A.M. Deaconescu, and A. Roll-Mecak. 2018. Severing enzymes amplify microtubule arrays through lattice GTP-tubulin incorporation. *Science*. 361:eaau1504.
- Wieczorek, M., S. Bechstedt, S. Chaaban, and G.J. Brouhard. 2015. Microtubule-associated proteins control the kinetics of microtubule nucleation. *Nat Cell Biol*. 17:907-916.
- Zheng, S.Q., E. Palovcak, J.P. Armache, K.A. Verba, Y. Cheng, and D.A. Agard. 2017. MotionCor2: anisotropic correction of beam-induced motion for improved cryo-electron microscopy. *Nat Methods*. 14:331-332.

Supplementary figures

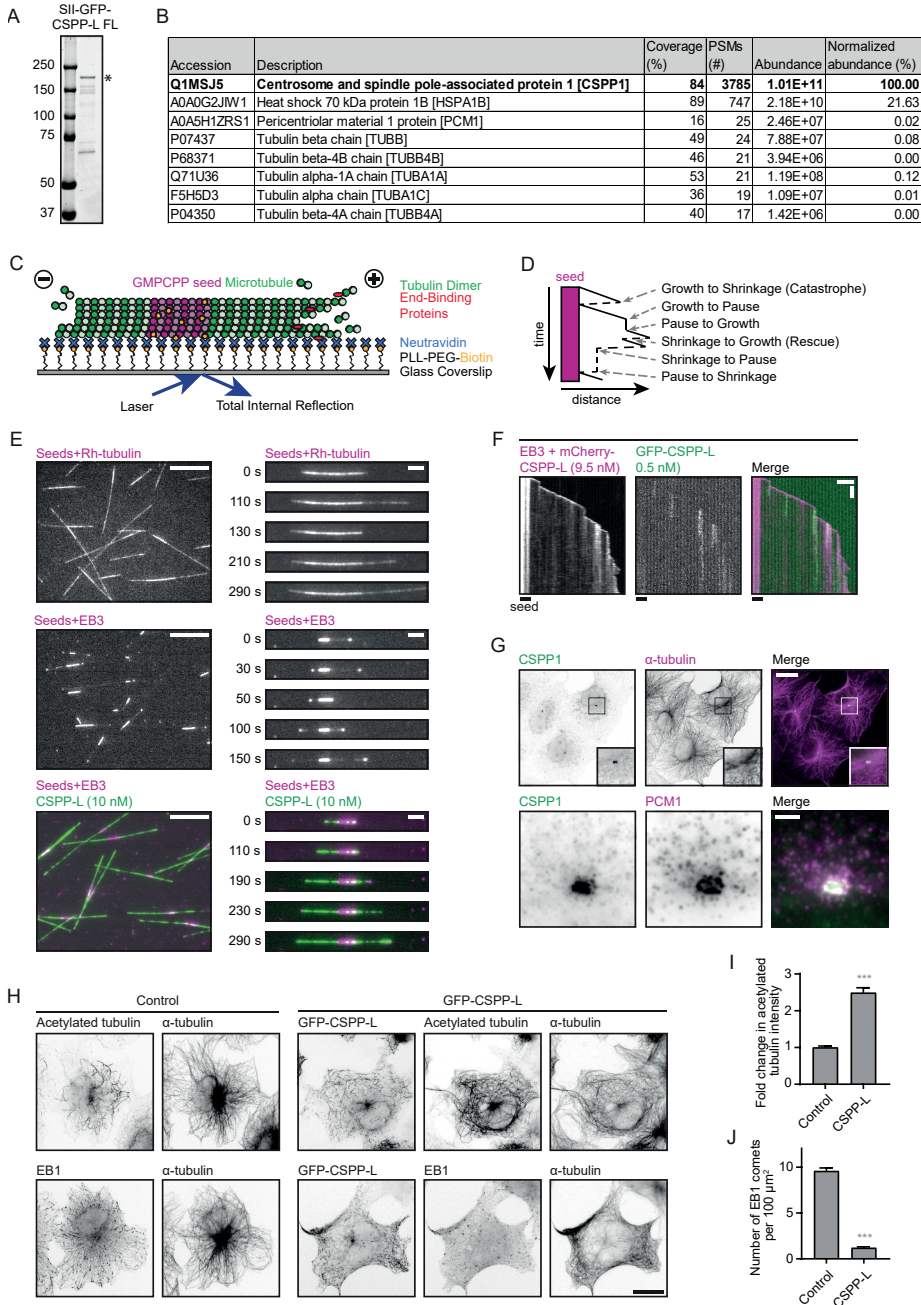


Figure S1, related to Figure 1: Characterization of GFP-CSPP-L in vitro and in COS-7 cells. (A) Analysis of purified GFP-CSPP-L by SDS-PAGE. Asterisk indicates the full-length protein band. Protein concentrations were determined from BSA standard. (B) Mass spectrometry analysis

of purified GFP-CSPP-L. **(C)** Schematic representation of the *in vitro* reconstitution assays with dynamic microtubules for imaging with TIRF microscopy. GMPCPP-stabilized microtubule seeds containing fluorescent tubulin, such as rhodamine tubulin (for visualization) and biotinylated tubulin (for surface attachment via NeutrAvidin), are immobilized on a plasma-cleaned coverslip coated with biotinylated poly(L-lysine)-[g]-poly(ethylene glycol) (PLL-PEG-biotin), which is coupled to NeutrAvidin. Microtubule growth from GMPCPP-stabilized seeds is initiated and visualized by the addition of tubulin supplemented with fluorescently-labeled tubulin, or by the addition of unlabeled tubulin combined with fluorescently-tagged EB3. Microtubule plus- and minus ends are indicated. **(D)** Schematic representation of a kymograph visualizing the various transition events observed and quantified in this paper. **(E)** Field of view (left, scale bar 10 μm) and time-lapse images (right, scale bar 2 μm) illustrating microtubule growth from GMPCPP stabilized microtubule seeds in the presence of 15 μM tubulin supplemented with 3% rhodamine-labelled tubulin, or with 20 nM mCherry-EB3 in presence or absence of 10 nM GFP-CSPP-L. See also Fig. 1B. **(F)** Kymographs illustrating microtubule growth with 20 nM GFP-EB3 together with 9.5 nM mCherry-CSPP-L and 0.5 nM GFP-CSPP-L. Scale bars, 2 μm (horizontal) and 60 s (vertical). **(G)** Widefield fluorescence image of COS-7 cells stained for CSPP1 and α -tubulin or PCM1. Top scale bar, 25 μm ; bottom scale bar, 2 μm . **(H)** Widefield fluorescence images of COS-7 cells overexpressing GFP-CSPP-L and stained for α -tubulin and acetylated tubulin or EB1. Scale bar, 20 μm . **(I)** Quantification of mean acetylated tubulin intensity per COS-7 cell (from images as in H). The average mean intensity of cells overexpressing GFP-CSPP-L was normalized to the average mean intensity in control cells. Number of cells analyzed: control cells, n=137; cells overexpressing GFP-CSPP-L, n=77. Data quantified from two experiments. **(J)** Quantification of the number of EB1 comets per 100 μm^2 in COS-7 cells (from images as in H). Number of cells analyzed: control cells, n=111; cells overexpressing GFP-CSPP-L, n=75. Data quantified from two experiments. For all plots. Error bars represent s.e.m. Data quantified from two experiments. ***, $p < 0.001$; Mann-Whitney test.

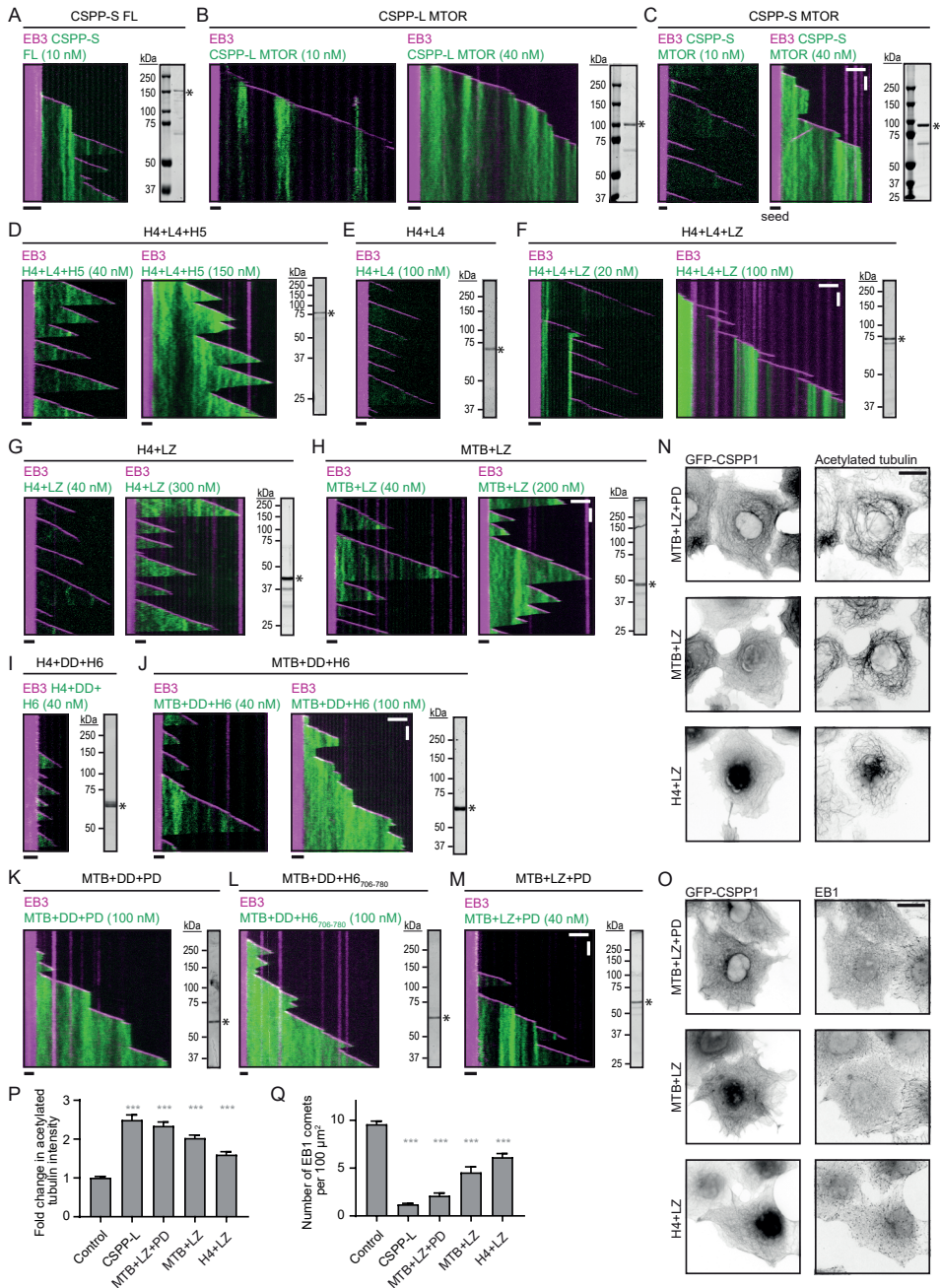


Figure S2, related to Figure 3: Shorter CSPP1 constructs are less potent in stabilizing microtubules in cells

(A-M) Kymographs of microtubule growth with 20 nM mCherry-EB3 together with the indicated GFP-CSPP1 constructs at the indicated concentrations. Scale bars, 2 μm (horizontal) and 60 s (vertical). Images of SDS-PAGE gels with purified proteins are included for each construct. Asterisk

indicates full-length protein band. **(N,O)** Widefield fluorescence images of COS-7 cells overexpressing GFP-CSPP-L and stained for α -tubulin and acetylated tubulin (N) or EB1 (O). Scale bar, 20 μm . **(P,Q)** Quantification of mean acetylated tubulin intensity (P) or quantification of number of EB1 comets per 100 μm^2 (Q) per COS-7 cell (from images as in N and O). Quantification and statistics as in S11. Number of cells analyzed acetylated tubulin, EB1: control cells, n=137, n=111; cells overexpressing GFP-CSPP-L, n=77, n=75; cells overexpressing GFP-MTB+LZ+PD, n=83, n=72; cells overexpressing GFP-MTB+LZ, n=70, n=61; cells overexpressing GFP-H4+LZ, n=50, n=75; Data for control and GFP-CSPP-L is the same as in Fig. S11. Data quantified from two experiments.

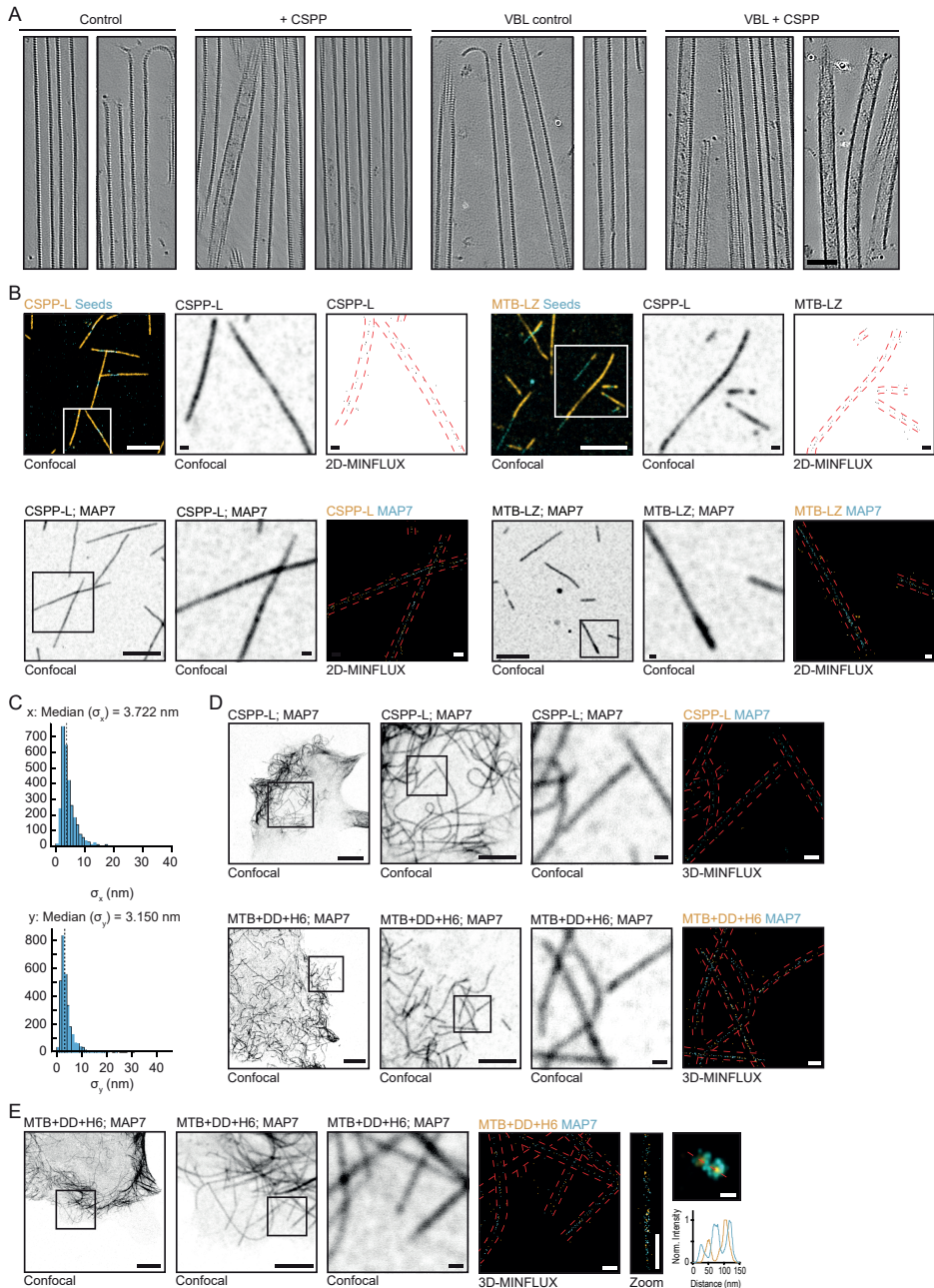
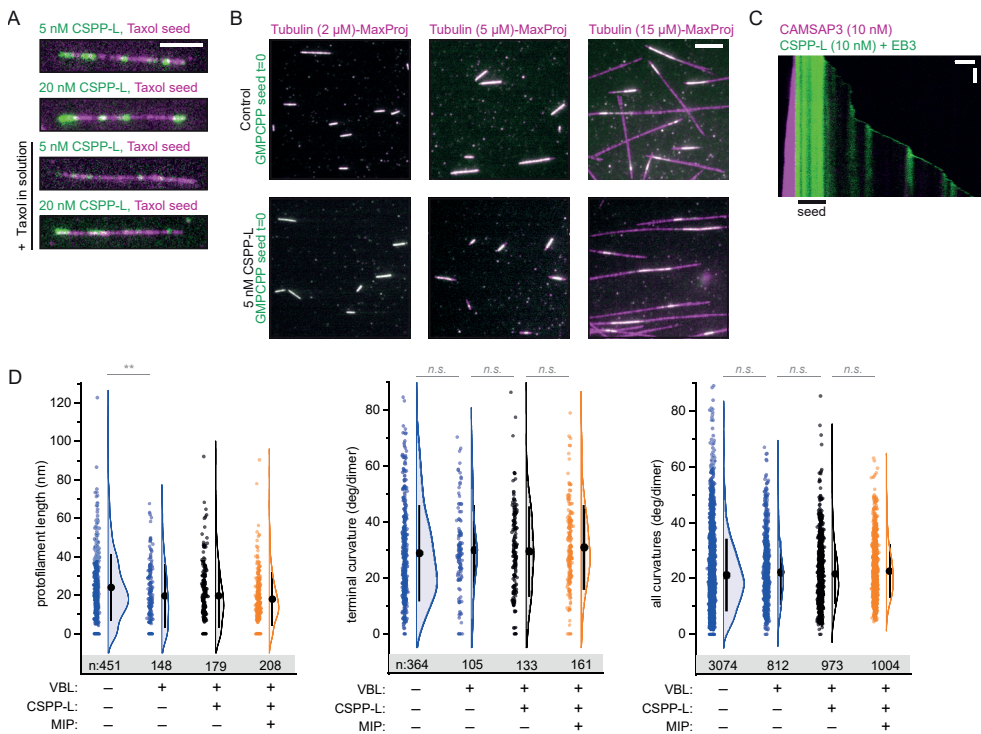


Figure S3, related to Figure 4: Characterization of CSPP1 inside the microtubule lumen. (A) Additional tomograms of dynamic microtubules polymerized from GMPCPP-stabilized seeds in the presence or absence of 10 nM GFP-CSPP-L, with or without 250 nM vinblastine vitrified on EM grids. Scale bar, 50 nm. See also Fig. 4A. (B) Additional zooms of confocal images of *in vitro* MINFLUX regions shown in Fig. 4D-E, G-H. Large confocal field of view (FOV) and 2D-MINFLUX images are identical to the images in Fig. 4D-E, G-H. Panel representation as in (Fig. 4D-E). Scale bars;

5 μm (Large FOV confocal image), 500 nm (Zoom FOV confocal image and 2D-MINFLUX image). **(C)** Standard deviation histograms (x and y-axis) of groups of ≥ 4 successive localizations from the same fluorophore depicting the localization precision of one example of a single color 2D-MINFLUX measurement of *in vitro* microtubules polymerized in presence of SNAP-CSPP-L. The localization precision of all single color 2D-MINFLUX measurements used for the FWHM analysis were in the range of 3.0 and 4.3 nm. **(D)** Additional zooms of confocal images of cellular MINFLUX regions shown in Fig. 4I-J. Large confocal field of view (FOV) and 3D-MINFLUX images are identical to the images in Fig. 4I-J. Panel representation as in (Fig. 4I-J). Scale bars; 10 μm (Large FOV confocal image), 5 μm (Medium FOV confocal image), 500 nm (Small FOV confocal image and 3D-MINFLUX image). **(E)** Dual color 3D-MINFLUX measurements of COS-7 cells overexpressing GFP-MAP7 together with SNAP-MTB-DD-H6. Panel representation as in Fig. 4I. Scale bars; 10 μm (Large FOV confocal image), 5 μm (Medium FOV confocal image), 500 nm (Small FOV confocal image, 3D-MINFLUX image and Zoom), 50 nm (maximum intensity projection image).



Supplementary Figure S4, related to Figure 6: CSPP1 stabilized microtubules but there is no change in protofilament length or curvature.

(A) Still images from assays with Taxol-stabilized microtubule seeds in the absence or presence 40 μM Taxol and the indicated GFP-CSPP-L concentrations. Scale bar, 5 μm . See also Fig. 6A. **(B)** Microtubule outgrowth from GMPCPP stabilized microtubule seeds five minutes after flowing in 5 nM GFP-CSPP-L at the indicated tubulin concentrations. The first frame of the acquisition (green) is overlaid with the maximum projections of 5 min acquisition (magenta) illustrating the newly grown microtubule lattice. Scale bar 5 μm . **(C)** Kymograph illustrating microtubule growth in the presence of 20 nM mCherry-EB3 together with 10 nM mCherry-CSPP-L and 10 nM GFP-CAMSAP3. Scale bars, 2 μm (horizontal) and 60 s (vertical). **(D)** Quantification of protofilament length, terminal curvature, and total curvature (from tomograms as shown in 1K). Blue, orange, and grey dots (single data points, tomograms), black circle (mean), SD (error bars). **, $p < 0.01$, n.s., not significant, Mann-Whitney test. Analysis from two experiments.

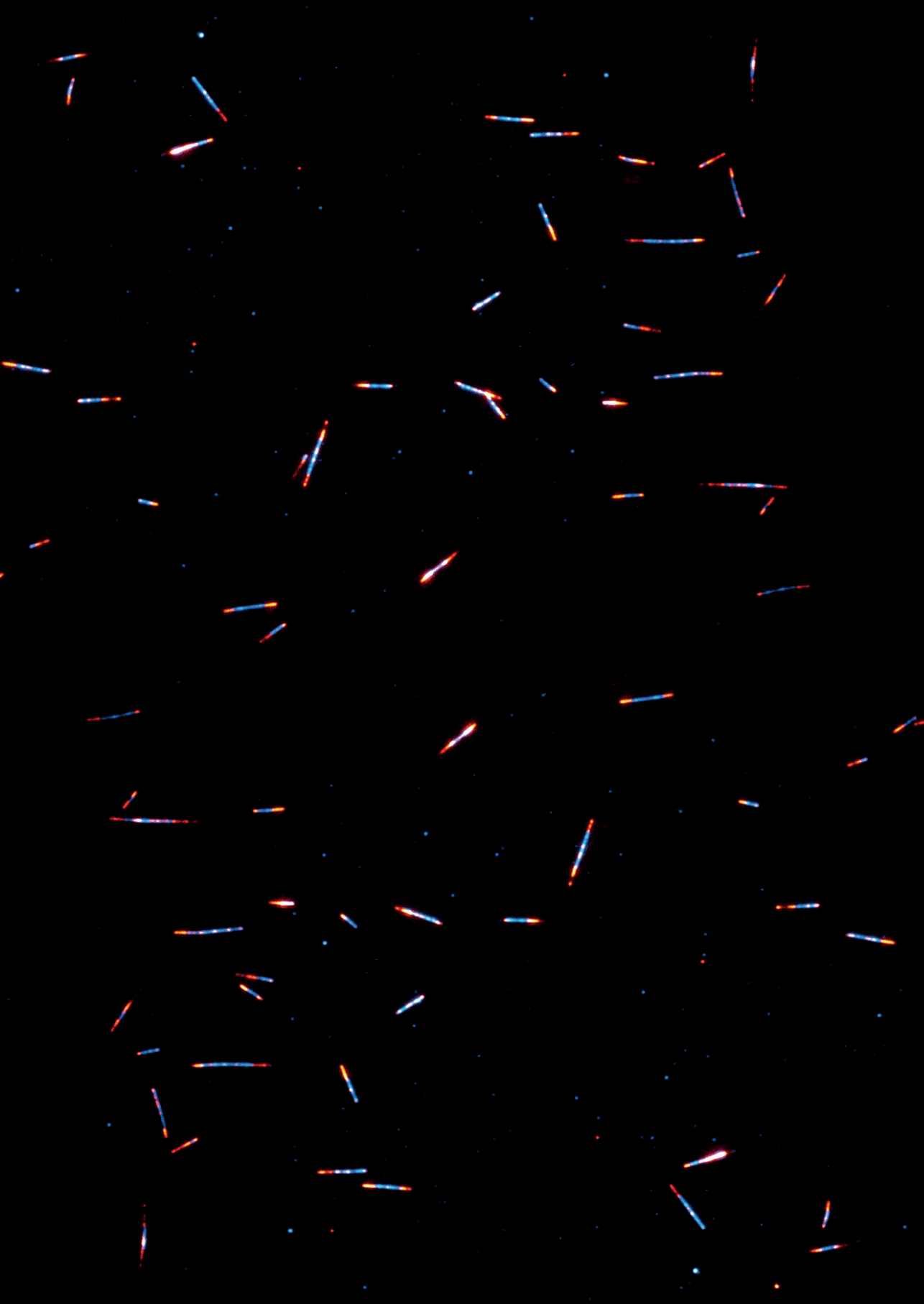
Supplementary table

Table S1: Key resources table

REAGENT or RESOURCE	SOURCE	IDENTIFIER
Antibodies		
Mouse anti-acetylated tubulin	Sigma-Aldrich	Cat# T7451
Purified Mouse Anti-EB1 (Clone 5/EB1)	BD Biosciences	Cat# 610535
Rat anti-tyrosinated α -tubulin (Clone YL1/2)	Abcam	Cat# ab6160
Rabbit anti-CSPP1	Proteintech	Cat# 11931-1-AP
Goat anti-PCMI antibody (G-6)	Santa Cruz Biotechnology	Cat# sc-398365
Goat anti-Mouse IgG (H+L), Highly Cross-Adsorbed, Alexa Fluor 594	Thermo Fisher Scientific	Cat# A-11032
Goat anti-Rabbit IgG (H+L), Highly Cross-Adsorbed, Alexa Fluor 488	Thermo Fisher Scientific	Cat# A-11034
Goat Anti-Rat IgG H&L (Alexa Fluor® 405) preadsorbed	Abcam	Cat# ab175673
Donkey anti-Goat IgG (H+L), Cross-Absorbed, Alexa Fluor 568	Thermo Fisher Scientific	Cat# A-11057
Donkey anti-Rabbit IgG (H+L), Highly Cross-Absorbed, Alexa Fluor 488	Thermo Fisher Scientific	Cat# A-21206
Manually conjugated CF680-GFP-Nanobody	Biotium (CF680-dye) + NanoTag (FluoTag®-X4 anti-GFP)	Cat# 92029 + Cat# N0304
FluoTag®-X4 anti-GFP-Alexa 647	NanoTag	Cat# N0304-AF647-L
Chemicals, Peptides, and Recombinant Proteins		
StrepTactin Sepharose High Performance	GE Healthcare	Cat# 28-9355-99
Polyethyleneimine	Polysciences	Cat# 24765-2
cOmplete™, EDTA-free Protease Inhibitor Cocktail	Roche	Cat# 4693116001
Tubulin protein: porcine brain	Cytoskeleton	Cat# T240
Tubulin protein (fluorescent HiLyte 488): porcine brain	Cytoskeleton	Cat# TL488M
Tubulin protein (rhodamine): porcine brain	Cytoskeleton	Cat# TL590M
Tubulin protein (biotin labeled): porcine brain	Cytoskeleton	Cat# T333P
PLL-PEG-biotin	Susos AG, Switzerland	PLL(20)-g[3.5]-PEG(2)/PEG(3.4)-biotin(50%)
Methyl cellulose, 4000 cp	Sigma-Aldrich	Cat# M0512
GMPCPP	Jena Biosciences	Cat# NU-405L
GTP	Sigma-Aldrich	Cat# G8877
Glucose oxidase	Sigma-Aldrich	Cat# G7141
Catalase	Sigma-Aldrich	Cat# C9322
DTT	Sigma-Aldrich	Cat# R0861
k-casein	Sigma-Aldrich	Cat# C0406
Neutravidin	Invitrogen	Cat# A-2666
d-Desthiobiotin	Sigma-Aldrich	Cat# D1411
Taxol	Sigma-Aldrich	Cat# T7402
Vinblastine sulfate salt	Sigma-Aldrich	Cat# V1377
Fchitax-3	(Diaz et al., 2000)	N/A
Glucose Oxidase (GLOX-buffer)	Sigma-Aldrich	Cat# G2133
Catalase (GLOX-buffer)	Sigma-Aldrich	Cat# C40
MEA	Sigma-Aldrich	Cat# M9768
StrepII-GFP-CSPP-L full length (CSPP-L FL)	This study	N/A

StrepII-GFP-CSPP-L 295-653 [^] 705-1221 (CSPP-S FL)	This study	N/A
StrepII-GFP-CSPP-L 295-849 (CSPP-L MTOR)	This study	N/A
StrepII-GFP-CSPP-L 295-653 [^] 705-849 (CSPP-S MTOR)	This study	N/A
StrepII-GFP-CSPP-L 295-653 (H4+L4+H5)	This study	N/A
StrepII-GFP-CSPP-L 295-594 (H4+L4)	This study	N/A
StrepII-GFP-CSPP-L 295-594+LZ (H4+L4+LZ)	This study	N/A
StrepII-GFP-CSPP-L 375-412+(G ₄ S) ₂ +LZ (H4+LZ)	This study	N/A
StrepII-GFP-CSPP-L 375-453+LZ (MTB+LZ)	This study	N/A
StrepII-GFP-CSPP-L 375-422 [^] 583-653 [^] 705-849 (H4+DD+H6)	This study	N/A
StrepII-GFP-CSPP-L 375-453 [^] 583-653 [^] 705-849 (MTB+DD+H ₆₇₀₆₋₇₈₀)	This study	N/A
StrepII-GFP-CSPP-L 375-453 [^] 583-653 [^] 705-796 (MTB+DD+PD)	This study	N/A
StrepII-GFP-CSPP-L 375-453 [^] 583-653 [^] 705-780 (MTB+DD+H ₆₇₀₆₋₇₈₀)	This study	N/A
StrepII-GFP-CSPP-L 375-453+LZ+705-796 (MTB+LZ+PD)	This study	N/A
StrepII-GFP-MCAK	(Aher et al., 2018)	
mCherry-EB3 full length	(Montenegro Gouveia et al., 2010)	N/A
GFP-EB3 full length	(Montenegro Gouveia et al., 2010)	N/A
StrepII-GFP-MAP7 N-terminus	(Hooikaas et al., 2019)	N/A
FuGENE6	Promega	Cat# E2691
SNAP-Surface® Alexa Fluor® 647	NEB	Cat# S9136S
SNAP-Abberior FLUX 680	Abberior	FX680
Glutaraldehyde	Electron Microscopy Sciences	Cat# #16110
Lacey EM grids	SPI supplies	Cat# 3840G
5 nm gold particles	Sigma-Aldrich	Cat# 808628
Spherical Gold Nanoparticles (200 nm)	Nanopartz	Cat# A11-200-CIT-DIH-1-10
Experimental Models: Cell Lines		
Human: HEK293T	ATCC	CRL-11268
Monkey: COS-7	ATCC	CRL-1651
Recombinant DNA		
Human EB3-mCherry	(Stepanova et al., 2003)	N/A
Human βIVb-tubulin-mCherry	(Bouchet et al., 2016)	N/A
Human StrepII-GFP-MAP7	(Hooikaas et al., 2019)	N/A
StrepII-GFP-CSPP-L full length (CSPP-L FL)	This study	N/A
StrepII-GFP-CSPP-L 375-453+LZ+705-796 (MTB+LZ+PD)	This study	N/A
StrepII-GFP-CSPP-L 375-453+LZ (MTB+LZ)	This study	N/A
StrepII-GFP-CSPP-L 375-412+(G ₄ S) ₂ +LZ (H4+LZ)	This study	N/A

Software and Algorithms		
ImageJ	NIH	https://imagej.nih.gov/ij/
Metamorph Version 7.8	Molecular Devices	https://www.moleculardevices.com/products/cellular-imaging-systems/acquisition-and-analysis-software/metamorph-microscopy
GraphPad Prism 9	GraphPad Software	https://www.graphpad.com/scientific-software/prism/
KymoResliceWide plugin	Eugene Katrukha	https://github.com/ekatrukha/KymoResliceWide
DoM Utrecht plugin	Eugene Katrukha	https://github.com/ekatrukha/DoM_Utrecht
MATLAB	MathWorks	https://www.mathworks.com/
MATLAB code for max intensity fit of EB3 comet and AUC of fitted CSPP-L signal	(Rai et al., 2020)	N/A
IMOD v. 4.11	(Kremer et al., 1996)	https://bio3d.colorado.edu/imod/
EMAN 2, tomoseg	(Chen et al., 2017)	https://cryoem.bcm.edu/cryoem/downloads/view_eman2_versions
Python scripts for cryoCARE denoising	(Buchholz et al., 2019; Ogunmolu et al., 2021)	https://github.com/NemoAndrea/cryoCARE-hpc04
MATLAB scripts for analysis of protofilament shapes	This study	https://github.com/ngudimhuk/Process-PFs
UCSF Chimera	(Pettersen et al., 2004)	https://www.cgl.ucsf.edu/chimera/download.html
MATLAB and Fiji Groovy scripts for MINFLUX Analysis	This study	https://github.com/EMBL-ICLM/microtubule_width_measurement_MINFLUX



4

Slow and steady: combined action of ciliary tip module proteins with opposing activities imparts slow microtubule growth

Cyntha M. van den Berg¹, Harriet A. J. Saunders¹, Kelly E. Stecker², and Anna Akhmanova¹

Manuscript in preparation

¹Cell Biology, Neurobiology and Biophysics, Department of Biology, Faculty of Science, Utrecht University, Padualaan 8, Utrecht 3584 CH, the Netherlands.

²Biomolecular Mass Spectrometry and Proteomics, Bijvoet Center for Biomolecular Research and Utrecht Institute for Pharmaceutical Sciences, Utrecht University, Padualaan 8, 3584 CH Utrecht, the Netherlands.

Abstract

Cilia are essential microtubule-based organelles found on the surface of most cells. In order for cilia to function properly, their length needs to be carefully controlled. Unlike cytoplasmic microtubules, ciliary microtubules exhibit much slower growth dynamics. Furthermore, defects in the structure and dynamics of ciliary microtubules can cause severe developmental diseases. However, very little is known about the biochemical mechanisms controlling ciliary microtubule growth. Here, we explored the individual and collective effects of the recently identified ciliary tip module proteins ARMC9, TOGARAM1, CSPP1, CEP104 and CCDC66. These proteins are known to interact with microtubules and with each other, and mutations in the first four proteins have been identified in patients suffering from the ciliopathy Joubert syndrome. Depletion of any of these proteins results in shorter cilia, however, their impact on microtubule dynamics has not yet been studied. Here, we used *in vitro* reconstitution assays to investigate the individual and collective effects of the ciliary tip module components on dynamic microtubules. We found that each protein differently affected microtubule dynamics. Two of the five module proteins have evolutionary conserved tubulin-binding TOG domains. Surprisingly, they showed very different effects on dynamic microtubules. Unlike any other characterised TOG domain protein, we found that CEP104 blocked microtubule plus-end growth. This behaviour was potentiated by End-Binding proteins, pausing factor CSPP1 and microtubule lattice binder CCDC66. In contrast, the other TOG domain protein, TOGARAM1, acted as a rescue factor and opposed the growth inhibition imposed by CEP104. Together, they imparted very slow microtubule polymerization, and microtubule growth was reduced even further in the presence of a scaffolding protein ARMC9 and CSPP1. These data increase our understanding of the mechanisms of ciliary microtubule regulation and provide insight into how the dysfunction of these proteins causes Joubert syndrome.

Introduction

Cilia are organelles present on the surface of almost every cell. The core of the extracellular part, called the axoneme, is a microtubule-based structure consisting of nine microtubule doublets. This microtubule scaffold provides structure and stability which is required for ciliary function. Motile cilia generate movement for processes such as driving fluid flow over apical surfaces in mammalian trachea cells, while primary cilia function as signalling hubs with fundamental roles in organism development (Berbari et al., 2009; Klena and Pigino, 2022). Ciliary dysfunction is associated with numerous diseases, collectively called ciliopathies, which affect multiple organs and tissues resulting in developmental abnormalities, ataxia, and intellectual disabilities (Hildebrandt et al., 2011; Klena and Pigino, 2022). Mutations linked to ciliopathies often directly or indirectly affect cilia formation, stability and structure, and thus disrupt cilia function. Patient-derived cells typically contain cilia with deviating axoneme lengths, indicating that ciliary length is essential for cilia to function properly. Ciliary length is directly determined by the length of axonemal microtubules. A recent study elegantly showed that singlet microtubules in a primary cilium can terminate at variable distances from the ciliary tip, however, how these microtubule tips are regulated is not known (Kiesel et al., 2020). Multiple proteins and pathways responsible for regulating axoneme structure have been identified through genetic screens and *in vivo* cell biology studies, yet the molecular mechanisms that regulate axoneme microtubules remain elusive (Keeling et al., 2016).

Here, we focus on the recently identified ciliary tip module (Latour et al., 2020). The core components of this module, ARMC9, TOGARAM1, CSPP1, CEP104 and CCDC66, localize to the ciliary tip. Depletion of any of these proteins results in shorter cilia and identified mutations in most of the ciliary tip module components underly a ciliopathy called Joubert syndrome (Akizu et al., 2014; Latour et al., 2020; Shaheen et al., 2014; Srouf et al., 2015; Tuz et al., 2014; Van De Weghe et al., 2017). Joubert syndrome is characterized by malformation of the midbrain-hindbrain junction, and patients additionally suffer from breathing problems or more severe developmental disorders (Hildebrandt et al., 2011). The five proteins that comprise the ciliary tip module have been shown to interact with each other and are important for ciliary signalling (Conkar et al., 2022; Frikstad et al., 2019; Latour et al., 2020; Van De Weghe et al., 2017). Two of the five members, TOGARAM1 and CEP104, have evolutionary conserved TOG tubulin-binding domains. TOGARAM1 contains four TOG domains and is a microtubule polymerase (Das et al., 2015). Multiple studies have found that deletion or loss of function mutations in TOGARAM1 result in short cilia in mammalian cells and other model organisms (Bacaj et al., 2008; Das et al., 2015; Latour et al., 2020; Louka et al., 2018; Perlaza et al., 2022). CEP104 has only one TOG domain which binds tubulin (Al-Jassar et al., 2017; Rezabkova et al., 2016). Light scattering experiments suggest that CEP104 also has microtubule polymerase activity, and similar to TOGARAM1, loss of CEP104 results in short cilia (Frikstad et al., 2019; Satish Tamma et al., 2013; Yamazoe et al., 2020). In addition to these two members which directly bind tubulin, we recently showed that CSPP1 influences microtubule stability by binding inside the microtubule lumen and promoting pauses (van den Berg et al., 2022). CSPP1 stabilizes damaged and poorly growing microtubules, and loss of CSPP1 results in short cilia with impaired signalling capabilities (Frikstad et al., 2019; van den Berg et al., 2022). The final two members, ARMC9 and CCDC66, do not have known domains that regulate microtubule dynamics and stability, but they likely regulate the functions of the other three module members. To this end, it was shown that ARMC9 on its own cannot bind to microtubules, but it has been identified as a scaffold to recruit the other microtubule-binding ciliary tip module components to form a complex (Latour et al., 2020). ARMC9, together with TOGARAM1, is involved in the regulation of microtubule dynamics. These two proteins have been localized to the B-tubule in motile cilia (Das et al.,

2015; Louka et al., 2018), where they were found to have opposite functions in regulating B-tubule length (Louka et al., 2018). It remains to be determined if this is also the case in primary cilia. Finally, CSPP1 and CEP104 were recently found to interact with CCDC66, and co-depletion of CCDC66 with either CSPP1 or CEP104 resulted in further reduction of ciliary length compared to removal of either CSPP1 or CEP104 alone (Conkar et al., 2022).

So far, the ciliary tip module proteins have mostly been studied in a cellular context with methods using overexpression or depletion in cultured cells or by using patient-derived materials. Unfortunately, these methods do not provide mechanistic details of protein contribution to microtubule regulation. To close this knowledge gap, we performed *in vitro* reconstitution assays using full length proteins to investigate their individual and collective effects on dynamic microtubules. We found that they differently affect microtubule dynamics. We found that ARMC9 and CCDC66 on their own did not affect microtubule dynamics but enhanced the activities of the other three module members. Excitingly, we found that CEP104 specifically blocked microtubule plus-end elongation. Such behaviour has not been described before for a TOG domain protein. This activity was potentiated by EB3, CSPP1 and CCDC66. TOGARAM1, the other TOG domain protein in the complex, acted as a rescue factor and opposed blocking of microtubule growth by CEP104, and together, they imparted slow microtubule polymerization. ARMC9 could not bind to microtubules on its own but was able to enhance pausing induced by CSPP1. The combination of ARMC9, CSPP1, TOGARAM1 and CEP104 resulted in very slow, but processive microtubule plus-end growth. Microtubule growth rate in these conditions was in the same range as initial elongation rates of regenerating flagella of single-celled organisms (Rosenbaum and Child, 1967; Rosenbaum et al., 1969; Witman, 1975). Altogether, our findings show that each ciliary tip module protein has its specific role in the complex to collectively control microtubule extension.

Results

Individual ciliary tip module proteins differently affect microtubule dynamics *in vitro*

The domain organization of the ciliary tip module proteins is very varied, implicating different functions and mechanisms of action for each protein (Fig. 1A). However, some domains are present in multiple proteins, such as evolutionary conserved TOG tubulin-binding domains in both TOGARAM1 and CEP104 and coiled-coil domains in every member except for TOGARAM1. Previous studies showed that CSPP1 directly interacts with CEP104, and ARMC9 directly binds to CSPP1, TOGARAM1 and CCDC66 (Fig. 1B) (Frikstad et al., 2019; Latour et al., 2020). Additionally, all proteins except for ARMC9 were shown to bind to microtubules upon overexpression (Conkar et al., 2017; Das et al., 2015; Jiang et al., 2012; Patzke et al., 2006; Van De Weghe et al., 2017). We confirmed these findings by overexpressing GFP-tagged constructs in COS-7 cells (Fig. 1C). We experienced difficulties with cloning and expression of human TOGARAM1 but were successful with its mouse homolog Crescerin1 (from now on termed mCrescerin1). mCrescerin1 has the same domain structure and more than 85% sequence similarity with human TOGARAM1. CCDC66, mCrescerin1 and CSPP1 decorated stretches of microtubule lattice and caused some microtubule bundling when expression levels were high. CEP104, a microtubule plus-end tracking protein containing an SxIP motif (x for any amino acid) that mediates binding to members of the End Binding (EB) protein family (Fig. 1A) (Jiang et al., 2012), formed comet-like structures at growing microtubule ends (Fig. 1C).

Next, we overexpressed the ciliary tip module components tagged with mCherry or GFP in HEK293 cells for purification. Mass spectrometry-based analysis demonstrated that the preparations contained no other known regulators of microtubule dynamics except for

minor contamination with CSPP1 in some cases (Fig. S1A-D). Mass spectrometry analysis of purified CSPP1 protein has been reported previously (van den Berg et al., 2022). We performed *in vitro* reconstitution assays with microtubules grown from GMPCPP-stabilized seeds in presence of individual ciliary tip module proteins or their combinations and observed their behavior and impact on microtubule dynamics by Total Internal Reflection Fluorescence microscopy (Fig. S1E) (Bieling et al., 2007; van den Berg et al., 2022). In the initial set of assays, growing microtubule ends were marked by fluorescently labeled End-Binding protein 3 (mCherry-EB3 or GFP-EB3). In these assays, microtubules grew at a rate of $\sim 3 \mu\text{m}/\text{min}$ and regularly underwent a switch from growth to shrinkage (termed catastrophe), which proceeded all the way back to the seed (Fig. 1D, J, K; Fig. S1F). This behavior did not change in the presence of ARMC9, even when it was added at a concentration as high as 300 nM, and no binding to microtubules was observed, confirming previous results (Fig. 1C, E) (Latour et al., 2020). CCDC66 bound along the microtubule lattice and slightly increased the microtubule growth rate, but it did not affect the transition frequency from growth to shortening (Fig. 1F, J, K; Fig. S1F).

The TOG domain protein mCrescerin1 also bound to the microtubule lattice and showed no specific accumulation at the microtubule ends (Fig. 1G). Instead, it bound to regions on the microtubule lattice that were already polymerized for some time and diffused upon binding. Microtubule lattices formed by plus-end polymerization are longer-lived, potentially explaining why stronger signal was observed on these lattices. In the presence of mCrescerin1, microtubules grew slightly slower, and the number of transitions from growth to shrinkage was reduced, while the frequency of transitions from shrinkage to growth (called rescues) was increased (Fig. 1G, J, K; Fig. S1F). These effects seemed to be plus-end specific, but this need to be confirmed. A decrease in microtubule growth rate was unexpected, as most proteins containing TOG domains have been shown to be canonical polymerases which increase microtubule growth rate (Al-Bassam et al., 2006; Brouhard et al., 2008; Zanic et al., 2013). Additionally, certain mCrescerin1 TOG domains were previously shown to increase tubulin polymerization rates *in vitro* (Das et al., 2015).

Like we have shown previously, CSPP1 displayed sites of increased accumulation which initiated at growing plus- and minus ends and prevented microtubules from shrinking at both ends (Fig. 1H) (van den Berg et al., 2022). At the plus end, it prevented depolymerization by inducing pauses and facilitating transitions from a paused state to a growing state but pause induction events were less clear at the minus ends due to their overall slower dynamics (Fig. 1H, J, K; Fig. S1F) (van den Berg et al., 2022).

CEP104 did not bind to microtubule lattice but displayed association with growing, EB3-positive plus- end minus ends and occasionally also tracked depolymerizing ends (Fig. 1I). A low concentration of CEP104 (2 nM) did not affect microtubule dynamics, but a higher concentration (10 nM) resulted in microtubules that were blocked at one end of the GMPCPP-stabilized seeds (Fig. 1I). Blocking typically occurred after a few growth episodes, and this could be due to accumulation of CEP104 tracking the shrinking microtubule end and then preventing a new outgrowth episode. Once microtubule growth was arrested, no regrowth would be detected for the remainder of the experiment. To determine which end of the microtubule seeds was blocked, we introduced a constitutively active fragment of the plus-end directed kinesin motor kinesin-1 KIF5B (KIF5B-560) into the assay. Analysis of the tracks of the motor protein revealed that CEP104 specifically blocks the plus end of the stabilized microtubule seeds (Fig. 1I). Altogether, we show that all the full-length members of the ciliary tip module can be purified and used in assays with *in vitro* reconstituted microtubules, where they display different effects on microtubule dynamics.

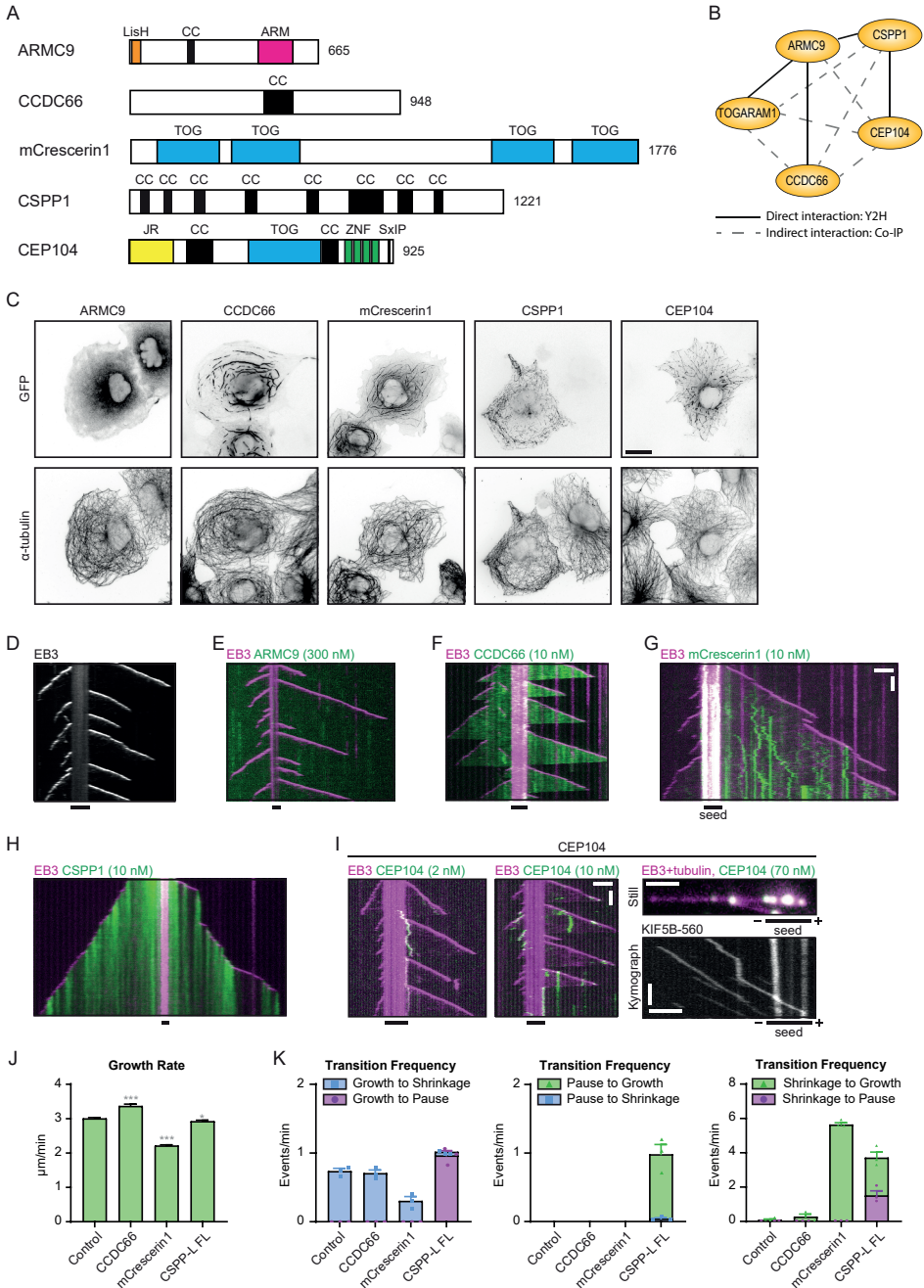


Figure 1: Individual ciliary tip module proteins differently affect microtubule dynamics in vitro.

(A) Schematic representation of the individual ciliary tip module components. All proteins are human, except for m(mouse)Crescerin1. CC, coiled-coil domain; ARM, Armadillo repeats; JR, jelly-roll domain; ZNF, Zinc Finger domain. (B) Interaction scheme of the ciliary tip module components.

Direct interactions are confirmed with Y2H (continuous lines), and indirect interactions are observed in co-immunoprecipitation assays (dashed lines). Figure adapted from Latour et al., 2020. **(C)** Widefield fluorescence images of COS-7 cells overexpressing the indicated GFP-proteins and stained for α -tubulin. Scale bar, 20 μ m. **(D)** Representative kymograph showing microtubule dynamics in the presence of 20 nM mCherry-EB3. Scale bars, 2 μ m (horizontal) and 60 s (vertical). **(E-H)** Representative kymographs showing microtubule dynamics in the presence of 20 nM mCherry-EB3 or GFP-EB3 supplemented with the indicated concentrations of SII-mCherry-ARMC9 (E), SII-GFP-CCDC66 (F), SII-GFP-mCrescerin1 (G) or SII-GFP-CSPP1 (H). Scale bars, 2 μ m (horizontal) and 60 s (vertical). **(I)** Representative kymographs showing microtubule dynamics in the presence of 20 nM GFP-EB3 supplemented with the indicated concentrations of SII-mCherry-CEP104 (left, middle). Still image displaying grown microtubule from the seed in presence of 70 nM CEP104, which completely blocks microtubule outgrowth from one end (right, top). Kymograph displaying tracks of KIF5B-560 proteins moving on the microtubule shown in the still above (right, bottom). The direction of motor protein KIF5B-560 was used to determine which microtubule end was blocked by CEP104 (indicated on both ends of the seed). Scale bars, 2 μ m (horizontal) and 60 s (vertical, CEP104) or 4 s (vertical, KIF5B-560). **(J)** Growth rate of microtubule plus ends in the presence of 20 nM mCherry-EB3 alone or in combination with 10 nM of the indicated proteins (from kymographs as shown in D-H). Growth rates faster than 0.24 μ m/min were used for analysis. Number of growth events: EB3 alone, n= 514; EB3 with CCDC66, n= 559; EB3 with mCrescerin1, n= 509; EB3 with CSPP1, n= 731. **(K)** Transition frequencies of microtubule plus ends in the presence of 20 nM mCherry-EB3 alone or in combination with 10 nM of the indicated proteins (from kymographs as shown in D-H). Events were classified as pauses when the pause duration was longer than 20 s. Number of transition events: EB3 alone, n= 461, 0, 0, 0, 4, 0; EB3 with CCDC66, n= 0, 484, 0, 0, 34, 0; EB3 with mCrescerin1, n= 0, 352, 0, 0, 339, 0; EB3 with CSPP1, n= 465, 24, 455, 22, 25, 21. Single data points represent averages of three independent experiments.

For all plots. Error bars represent s.e.m. ***, $p < 0.001$; n.s., not significant; Kruskal-Wallis test followed by Dunn's post-test. Data from three independent experiments. Dataset in panel J and K for EB3 with CSPP1 is the same as used in van den Berg et al, 2022.

See also Figure S1.

The plus-end blocking behavior of CEP104 is potentiated by EB3, CCDC66 and CSPP1, and opposed by mCrescerin1

Next, we wanted to examine the unique microtubule plus-end blocking behavior of CEP104 in more detail because it contradicts previous findings where CEP104 was shown to be involved in cilia elongation, and its TOG domain was found to enhance microtubule polymerization (Conkar et al., 2022; Friksstad et al., 2019; Yamazoe et al., 2020). First, we wondered whether CEP104-imposed microtubule plus-end growth inhibition was dependent on EB3 and, therefore, performed *in vitro* assays without EB3. As described previously (Komarova et al., 2009), in the absence of EB3, microtubules grew slower and underwent fewer catastrophes (Fig. 2A). We found that CEP104 could still specifically block microtubule plus ends, whereas the minus ends remained dynamic, although a much higher CEP104 concentration (200 nM) was required compared to when EB3 was present (Fig. 1I; Fig. 2B, J; Fig. S2A). In these conditions, CEP104 slowly accumulated along the whole microtubule lattice and was not present at the growing microtubule minus ends, in line with the view that the end-binding behavior of CEP104 is EB-dependent. This indicates that EB3 does not determine the plus-end specificity of CEP104 growth-inhibiting activity but potentiates it by recruiting CEP104 to microtubules.

We next set out to investigate the effect of other module components on the microtubule-blocking behavior of CEP104. A recent study suggested a functional interplay between CCDC66 and CEP104 in axonemal microtubule polymerization because overexpression of CEP104, which on its own elongated axonemes, compensated for the ciliary length defects caused by CCDC66 depletion (Conkar et al., 2022). We found that CEP104 and CCDC66 colocalized in COS-7 cells when overexpressed (Fig. S2B), and next tested the combination

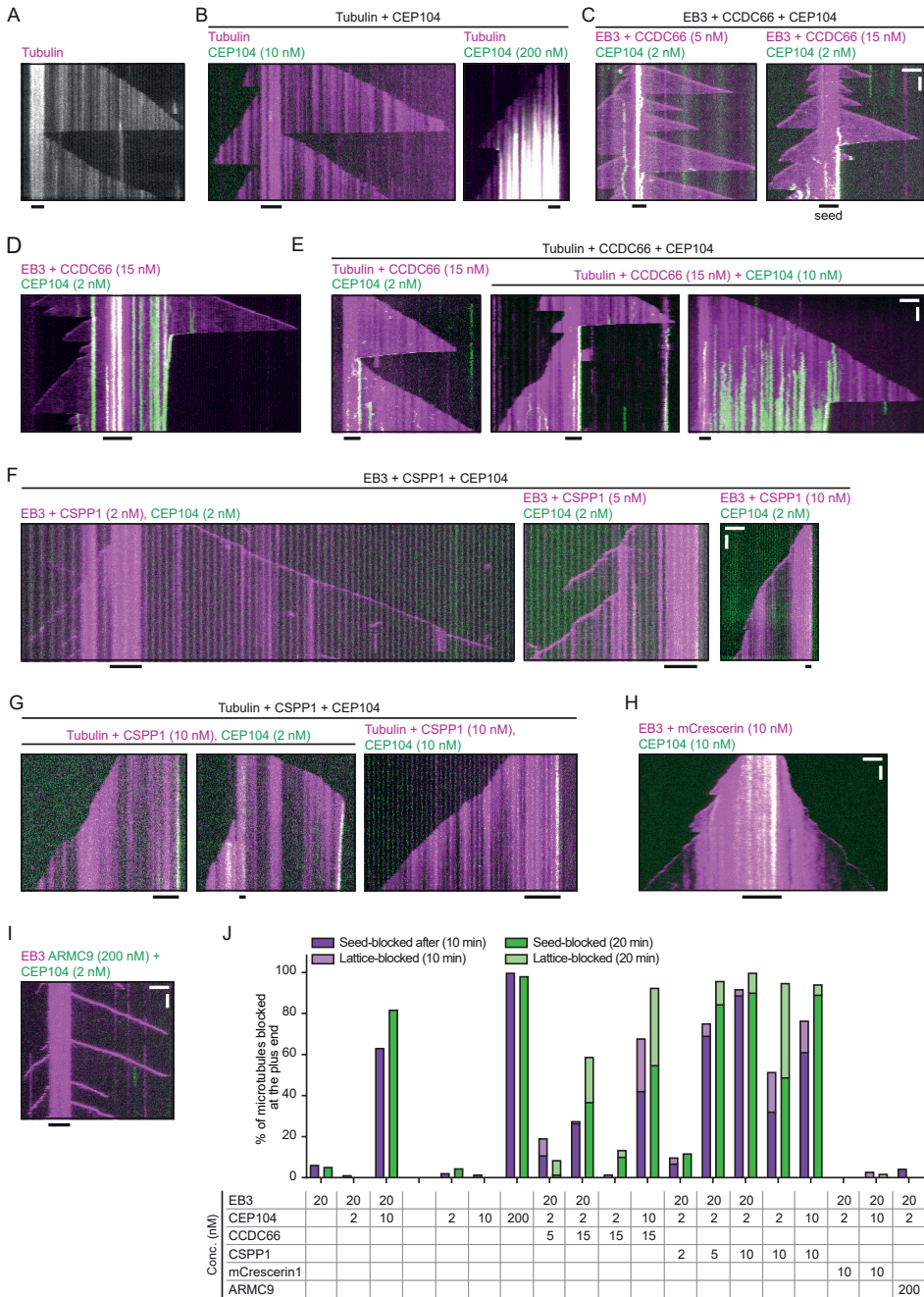


Figure 2: The plus-end blocking behavior of CEP104 is potentiated by EB3, CDC66 and CSPP1, and opposed by mCrescerin1.

(A) Representative kymograph showing microtubule dynamics in the presence of Hilyte488-labeled tubulin. (B) Representative kymographs showing microtubule dynamics in the presence of

Hilyte488-labeled tubulin supplemented with the indicated concentrations of SII-mCherry-CEP104. (C-D) Representative kymographs of 0-10 minutes (C) or 10-20 minutes (D) of reaction incubation showing microtubule dynamics in the presence of 20 nM mCherry-EB3 supplemented with the indicated concentrations of SII-mCherry-CCDC66 and 2 nM SII-GFP-CEP104. (E) Representative kymographs showing microtubule dynamics in the presence of rhodamine-labeled tubulin supplemented with the indicated concentrations of SII-mCherry-CCDC66 and 2 nM SII-GFP-CEP104. (F) Representative kymographs showing microtubule dynamics in the presence of 20 nM GFP-EB3 supplemented with the indicated concentrations of SII-GFP-CSPP1 and 2 nM SII-mCherry-CEP104. (G) Representative kymographs showing microtubule dynamics in the presence of Hilyte488-labeled tubulin supplemented with 10 nM SII-GFP-CSPP1 and the indicated concentrations of SII-mCherry-CEP104. (H) Representative kymograph showing microtubule dynamics in the presence of 20 nM GFP-EB3 supplemented with 10 nM SII-GFP-mCrescerin1 2nM SII-mCherry-CEP104. (I) Representative kymograph showing microtubule dynamics in the presence of 20 nM GFP-EB3 supplemented with 200 nM SII-mCherry-ARMC9 and 2 nM SII-mCherry-CEP104. (J) Quantification of the percentage of microtubules that was blocked at the plus end of the seed (Seed-blocked; dark bar) or at the plus-end lattice (Lattice-blocked; light bar), 10 minutes (magenta) or 20 minutes (green) after reaction incubation (from kymographs as shown in Fig. 1D, I; Fig. 2A-I). Data from 2 or 3 independent experiments. All scale bars, 2 μm (horizontal) and 60 s (vertical). See also Figure S2.

of these two proteins *in vitro*. We observed that, while in the presence of EB3, 2 nM CEP104 was insufficient to block plus-end growth, it could inhibit polymerization of a larger fraction of the total microtubule pool if increasing CCDC66 concentrations were added to the assay (Fig. 2C, J). Interestingly, in the presence of 15 nM CCDC66, when the reaction mix was incubated for a longer time, we found that 22% of the microtubule plus ends were blocked within the dynamic part of the microtubule lattice rather than at the plus end of the GMPCPP-stabilized microtubule seed (Fig. 2D, J). Such blocking resulted from arrested depolymerization events: CEP104 particles back-tracking of on shrinking microtubule ends could trigger a transition from fast to extremely slow depolymerization (Fig. 2D). CCDC66 could also potentiate microtubule plus-end blocking by CEP104 in the absence of EB3, but then a higher concentration of CEP104 (10 nM) was needed to observe similar effects (Fig. 2E, J). Also here, the microtubule lattice could be blocked during depolymerization, and such events became more frequent when 10 nM CEP104 was present. Since CCDC66 is a microtubule-binding protein, it likely potentiates CEP104 by recruiting it to microtubules, similar to EB3. Importantly, although CCDC66 by itself cannot inhibit microtubule shrinkage, the combination of CCDC66 and CEP104 not only inhibits tubulin addition but also prevents rapid microtubule depolymerization, indicating that CEP104 in this protein combination has microtubule-stabilizing properties.

The interaction between CSPP1 and CEP104 was previously shown to be required for normal cilia length, and they were shown to colocalize upon overexpression in cells (Frikstad et al., 2019). We confirmed their colocalization in cells (Fig. S2B), and we also tested the effect of CSPP1 on the growth-inhibiting activity of CEP104 *in vitro*. Similar to CCDC66, increasing concentrations of CSPP1 combined with 2 nM CEP104, in presence of EB3, were able to block microtubule plus-end outgrowth from the seeds (Fig. 2F, J). In the absence of EB3, 2 nM CEP104 and 10 nM CSPP1 resulted in a mix of microtubules blocked at the seeds, and microtubules blocked within the dynamic lattice (Fig. 2G, J). In contrast to CCDC66, the “lattice-block” did not occur during depolymerization but during polymerization or CSPP1-induced pausing, as depolymerization was rarely observed in presence of CSPP1 (Fig. 2F, G). This suggests that there is sufficient accumulation of CEP104 at growing or paused microtubule plus ends in the presence of CSPP1. Similar to CCDC66, we observed very slow depolymerization when microtubules were blocked at a site within their dynamic lattice (Fig. 2D, E, G). At a higher concentration of CEP104 (10 nM) in presence of CSPP1, most

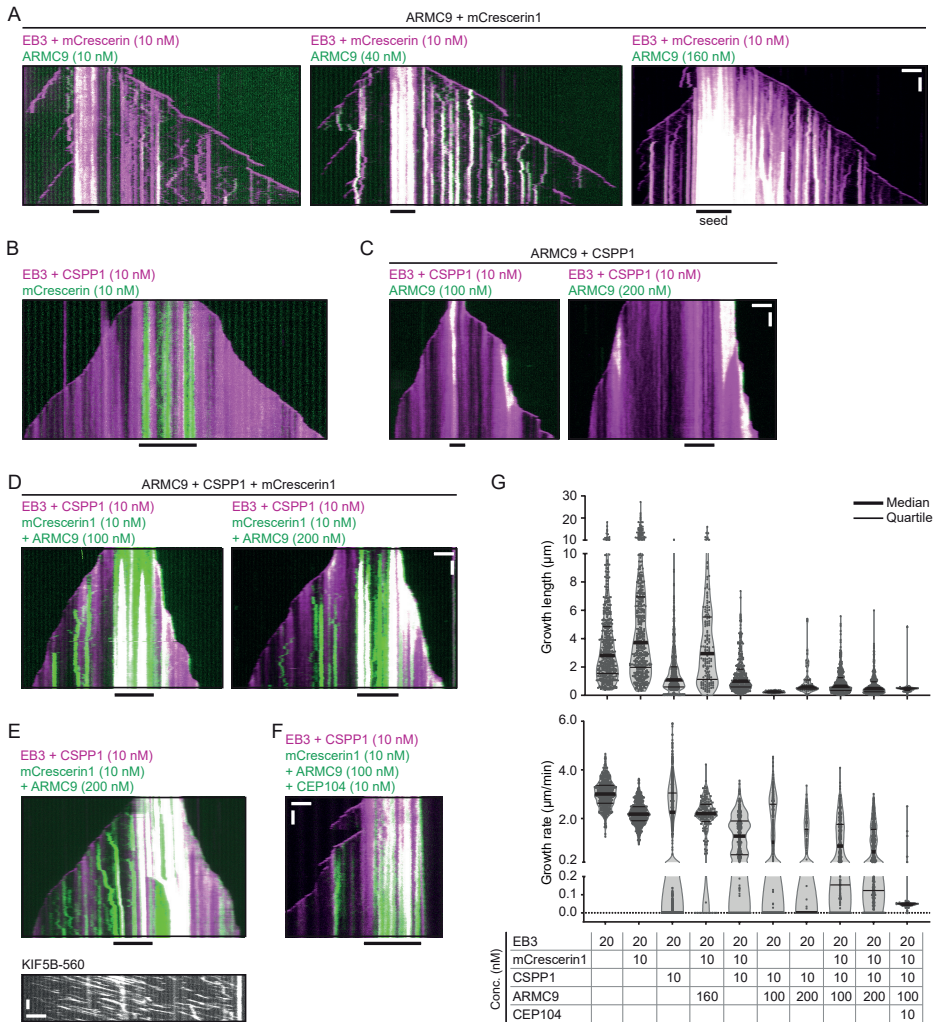


Figure 3: Collective action of ciliary tip module proteins leads to very slow but processive microtubule polymerization.

(A) Representative kymograph showing microtubule dynamics in the presence of 10 nM SII-GFP-mCrescerin1 and the indicated concentrations of SII-mCherry-ARMC9. (B,C) Representative kymographs showing microtubule dynamics in the presence of 10 nM SII-GFP-CSPP1 with SII-mCherry-mCrescerin1 (B) or with the indicated concentrations of SII-mCherry-ARMC9 (C). (D) Representative kymographs showing microtubule dynamics in conditions as in C, supplemented with 10 nM SII-mCherry-mCrescerin1. (E) Representative kymograph showing microtubule dynamics in conditions as in D (top), in presence of KIF5B-560 (bottom). Scale bar KIF5B-560, 2 μ m (horizontal) and 4 s (vertical). (F) Representative kymographs showing microtubule dynamics in conditions as in D (left), in presence of 2 nM SII-mCherry-CEP104. (G) Violin plots representing the frequency distribution of growth rates and growth lengths (from kymographs shown in Fig. 1D, G, H; Fig. 3A-F). Number of growth events; EB3 alone, $n = 1015$; mCrescerin1, $n = 510$; CSPP1, $n = 825$; 160 nM ARMC9 + mCrescerin1, $n = 242$; mCrescerin1 + CSPP1, $n = 323$; 100 nM ARMC9 + CSPP1, $n = 214$; 200 nM ARMC9 + CSPP1, $n = 61$; 100 nM ARMC9 + CSPP1, $n = 214$; 100 nM ARMC9 + mCrescerin1 + CSPP1, $n = 349$; 200 nM ARMC9 + mCrescerin1 + CSPP1, $n = 380$; 100 nM ARMC9 + mCrescerin1 + CSPP1 +

CEP104, n= 44. Data points represent single growth events from 1 or 3 independent experiments. All assays were performed in the presence of 20 nM GFP-EB3. All scale bars, 2 μm (horizontal) and 60 s (vertical). See also Figure S2.

microtubules were blocked at the seed from the beginning of the assay (Fig. 2G, J). CSPP1 thus can also recruit CEP104 to microtubules and potentiate plus-end growth inhibition imposed by this protein.

Because CEP104 was previously shown to be involved in cilia elongation and microtubule polymerization, as mentioned earlier, we hypothesized that there must be a factor which can overcome CEP104-mediated plus-end blocking to facilitate ciliary outgrowth. mCrescerin1 was previously shown to promote tubulin polymerization *in vitro* (Das et al., 2015), and we showed that it reduced the catastrophe frequency and increased the rescue frequency (Fig. 1G), so we reasoned mCrescerin1 could be involved in counteracting the activity of CEP104. CEP104 colocalizes with mCrescerin1 *in vitro* as well as in COS-7 cells, but this colocalization is less pronounced than that with other ciliary tip module proteins (Fig. 2H; Fig. S2B, C). In presence of EB3, a low concentration of CEP104 (2 nM) combined with mCrescerin1 did not result in plus-end growth inhibition (Fig. 2J; Fig. S2C). It also did not affect microtubule plus-end dynamics compared to mCrescerin1 alone, but more rescues were observed at the minus end (Fig. 1G; Fig. S2C). At 10 nM, CEP104 still could not block plus-end elongation, but caused reduction in growth rate and induced occasional pausing at the microtubule plus end while minus-end dynamics were similar to that with 2 nM (Fig. 1G; Fig. 2H, J; Fig. S2C). This suggests a combined action of the plus-end blocking behavior of CEP104 and the polymerization and rescue activity of mCrescerin1, validating our hypothesis.

To complete the analysis, we combined ARMC9 with CEP104, but did not observe colocalization in cells or *in vitro*, and microtubule dynamics were not affected (Fig. 2I, J; Fig. S2D). This was expected because no direct interaction between ARMC9 and CEP104 has previously been shown (Latour et al., 2020). Altogether, CEP104 is able to block microtubule seeds at the plus ends, and this behavior is potentiated by EB3, CCDC66 and CSPP1. Once CEP104 accumulates at the seed plus ends, microtubule outgrowth is fully blocked. In absence of EB3, but in presence of CCDC66 or CSPP1 we observed recruitment of CEP104 to the dynamic microtubule lattice where it could induce a polymerization block accompanied by very slow depolymerization. In presence of mCrescerin1, plus-end growth arrest was not observed, but together, mCrescerin1 and CEP104 reduced microtubule growth rate and induced occasional pausing.

Collective action of ciliary tip module proteins leads to very slow but processive microtubule polymerization

The next step in our analysis was to test more complex combinations of the ciliary tip module proteins. TOGARAM1 was previously shown to recruit ARMC9 to microtubules (Latour et al., 2020), so we first confirmed in COS-7 cells that mCrescerin1 and ARMC9 colocalize on microtubules (Fig. S2D). Next, we combined them in *in vitro* assays and found that increasing concentrations of ARMC9 did not affect microtubule growth dynamics (Fig. 3A, G). We also combined mCrescerin1 with CSPP1, and despite not seeing colocalization between these two proteins in COS-7 cells (Fig. S2E), when they were combined in the *in vitro* assay, we observed a decrease in the number and duration of microtubule pauses when compared to CSPP1 alone (Fig 1G, H; Fig. 3B), an effect that would need to be confirmed by quantification. Furthermore, we also observed a decrease in the microtubule plus-end growth rate when compared to mCrescerin1 alone (Fig 1G, H; Fig. 3B, G). The ability of mCrescerin1 to reduce the number and duration of pauses induced by CSPP1 seems similar to its capability

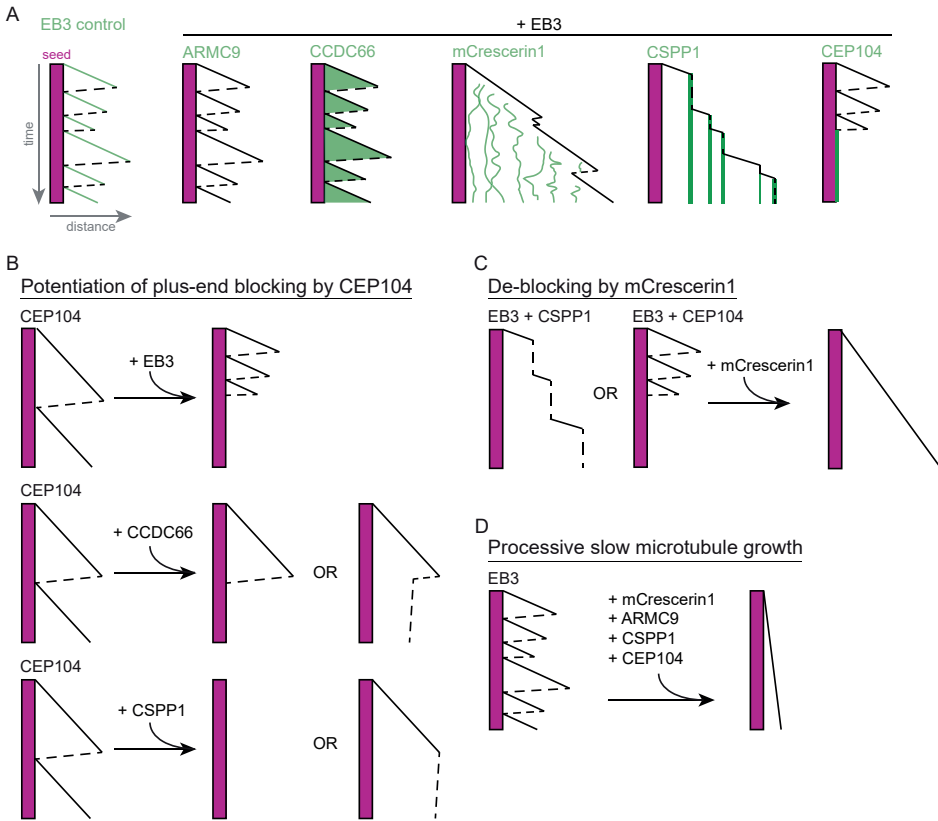


Figure 4: Schematic representation of the effect of ciliary tip protein combinations on microtubule plus ends.

Effects of ciliary tip module proteins on microtubule plus-end dynamics are presented in schematic kymographs (GMPCPP-stabilized seed, magenta; polymerization: uninterrupted lines; depolymerization or pause: dashed line; see also Fig. S1F). **(A)** Microtubule plus-end dynamics in presence of EB3 and single ciliary tip module proteins. Specific localization of each protein is illustrated in green. **(B)** Potentiation of microtubule CEP104-mediated plus-end blocking by its binding partners. **(C)** Attenuation of microtubule growth inhibition imposed by CEP104 and CSPP1 in the presence of mCrescerin1. **(D)** Processive slow microtubule plus-end growth imparted by the combined action of ciliary tip module proteins.

to attenuate the plus-end blocking behavior of CEP104. In both cases, mCrescerin1 releases the block or pause at microtubule ends resulting in microtubules that can grow, albeit at a slower rate.

CSPP1 was previously shown to directly bind to ARMC9 in a yeast 2-hybrid experiment, but their interaction has not been further investigated (Fig. 1B) (Latour et al., 2020). We overexpressed both proteins in COS-7 cells, but there was no apparent colocalization between them (Fig. S2D). *In vitro*, ARMC9 occasionally colocalized with CSPP1 (Fig. 3C). At these spots, ARMC9 increased the duration of CSPP1-induced pauses at microtubule plus ends in a concentration dependent manner (Fig. 3C). Together, ARMC9 and CSPP1 shifted the growth rate distribution of microtubules to slower values, and this decrease was further amplified

upon the addition of mCrescerin1 (Fig. 3C, D, G). Until this point, we could determine the polarity of the microtubules by using the clear differences in growth rate to identify the plus end as the fast-growing end and the minus end as the slow-growing end, or CSPP1-induced pauses at the plus end. However, in the assays with ARMC9, CSPP1 and mCrescerin1, there was no clear distinction anymore. Therefore, we turned again to the addition of KIF5B-560. This revealed that the slowest growing microtubule end was now actually the plus end (Fig. 3E, G). To find out if we could generate even slower growing microtubule plus ends, we combined full length EB3, CSPP1, mCrescerin1, ARMC9 and CEP104 in a single *in vitro* assay. Indeed, this resulted in even slower but processive polymerization of microtubule plus ends (Fig. 3F, G). In absence of CEP104, plus-end growth rates were quite broadly distributed while the distribution was quite narrow around the very slow growth rate in presence of CEP104 (Fig. 3D, F, G). We conclude that the collective action of four ciliary tip module proteins leads to slowly growing microtubules that do not undergo catastrophes.

Discussion

Ciliopathies are a group of diseases which are characterized by dysfunctional cilia. In many cases, the length of these cilia is altered suggesting that correct ciliary length is required for their function. So far, proteins and protein complexes involved in ciliary length control have been studied in a cellular context or in model organisms. Here, we wanted to investigate their exact molecular mechanism of action using *in vitro* reconstituted dynamic microtubules. We studied the individual and collective effects of the components of the ciliary tip module. We found that ARMC9 and CCDC66 by themselves do not majorly affect microtubule dynamics (Fig. 4A), but function as recruiters or scaffolds for the other components. Previous studies determined direct interactions between ARMC9 and TOGARAM1, CSPP1 and CCDC66 (Latour et al., 2020). We confirmed the interactions between ARMC9 and mCrescerin1, the mouse homolog of human TOGARAM1, and ARMC9 and CSPP1 on *in vitro* reconstituted microtubules. However, we did not observe an interaction between ARMC9 and CCDC66 in either our cellular or *in vitro* assays. Previous work on CEP104 showed its importance for cilia elongation, and the presence of the isolated TOG domain of CEP104 enhanced microtubule polymerization *in vitro* (Yamazoe et al., 2020). Surprisingly, our data demonstrated that full-length CEP104 blocks rather than stimulates growth of microtubule plus ends, and this effect was potentiated by EB3, CCDC66 and CSPP1 (Fig. 4A, B). The growth-inhibiting activity of CEP104 was counteracted by mCrescerin1, which on its own slightly decreased the microtubule growth rate and induced rescues (Fig. 4A, C). mCrescerin1 also reduced the number and duration of CSPP1-induced pauses (Fig. 4A, C). Four of the ciliary tip module proteins together, in absence of CCDC66 but in the presence of EB3, imparted slow and processive microtubule growth (Fig. 4D).

In our previous study, as well as this one, we have shown that CSPP1 contributes to microtubule stabilization by inducing pauses (van den Berg et al., 2022). Here, we found that CSPP1 directly interacted with CEP104 to potentiate the microtubule-blocking behavior of CEP104. This microtubule-blocking behavior of CEP104 is quite counterintuitive for several reasons. Firstly, because knockdown of CEP104 resulted in shorter cilia, and CSPP1 and CEP104 together were shown to be essential in the regulation of ciliary length (Frikstad et al., 2019; Jiang et al., 2012). Secondly, CEP104 contains a single TOG-domain which resembles the yeast Stu2 TOG1 domain and was therefore expected to be a microtubule polymerase. The best characterized microtubule polymerases are the members of the XMAP215/Stu2/ch-TOG family. Canonical microtubule polymerases are proteins which bind to soluble tubulin dimers and promote their addition to the microtubule plus end resulting in faster microtubule growth (Al-Bassam et al., 2006). Binding to free tubulin dimers is mediated by one or more TOG

domains within the polymerase, and dimer delivery to the microtubule plus end is facilitated by lattice binding through a basic linker (Widlund et al., 2011). Microtubule polymerases exhibit plus-end specificity because only at these ends the basic region of the polymerases is able to bind to the microtubule lattice while their TOG domains simultaneously bind to a soluble tubulin dimer in the right orientation for addition (Ayaz et al., 2012). The domain organization of CEP104 is slightly different because no basic region has been identified, but the isolated TOG domain of CEP104 was previously shown to promote tubulin polymerization (Yamazoe et al., 2020). We have not yet tested the effects of the TOG domain alone in our *in vitro* reconstitutions, however, we observed strong microtubule growth inhibition using the full-length protein. It is therefore possible that the presence of additional CEP104 domains could be regulating microtubule polymerization by positioning the TOG domain in a certain way.

We showed that the blocking behavior of CEP104 is potentiated by EB3, CSPP1 and CCDC66. These proteins all bind to the microtubule lattice, suggesting they recruit CEP104 to microtubules to execute its function. Interestingly, these proteins can bind to both ends of growing microtubules while plus-end blocking by CEP104 is only observed at the plus end. Additionally, we observed lattice-blocks in the absence of EB3, but in the presence of CSPP1 or CCDC66. These lattice-blocks specifically occurred at the microtubule plus end. Moreover, in these conditions we also observed gradual microtubule depolymerization. In presence of CCDC66, CEP104 induced slow microtubule depolymerization after rapid shortening. This indicates that CEP104 could stabilize shortening microtubules which might explain its overall positive effect on ciliary length. Slow depolymerization in presence of CSPP1 or CCDC66 and CEP104 could be achieved by CEP104 removing tubulin dimers from existing microtubules, either actively or by stabilizing an intermediate state of soluble tubulin dimers at the microtubule plus-end, like has been shown for canonical polymerase XMAP215 (Brouhard et al., 2008). Microtubule depolymerization was observed *in vitro* in presence of 100 nM XMAP215 in absence of soluble tubulin, while we have performed these experiments in the presence of soluble tubulin. This could explain why we did not observe depolymerization of GMPCPP-stabilized seeds in our assays. Similar to how microtubule polymerases only act on the plus ends of microtubules, CEP104 probably needs to be positioned in a specific way to be able to block tubulin addition or remove tubulin dimers from the microtubule plus end. Structural studies alongside more extensive reconstitution assays will be critical in furthering our understanding of how CEP104 specifically blocks microtubule plus ends and induces slow depolymerization.

As mentioned above, the plus-end blocking behavior of CEP104 is potentiated by EBs. In primary cilia, EBs have been localized to the outer surface of axonemal microtubules (Kiesel et al., 2020). This, in combination with the hypothesis that TOG domain proteins bind to the outer microtubule surface, as suggested by modelling studies (Byrnes and Slep, 2017), indicates that CEP104 may also bind to the outside of microtubules. However, we have previously shown that its interaction partner in cilia, CSPP1, is located at the microtubule lumen (van den Berg et al., 2022). So far, the binding site of CCDC66 on microtubules is unknown so there are no clues how CEP104 and CCDC66 are interacting. It will be interesting to study the geometry of all ciliary tip module proteins at the ciliary tip and find out if they form one big complex. If so, it will be exciting to figure out how protein-protein interactions are facilitated and regulated especially if they are on opposite sides of the tubulin wall. Future studies will hopefully reveal structural details of the ciliary tip module components at the ciliary tip.

The other TOG domain protein of the ciliary tip module, TOGARAM1/mCrescerin1, also showed surprising behavior by reducing microtubule growth rate instead of increasing it because we expected mCrescerin1 to be a microtubule polymerase for several reasons. First, unlike CEP104, mCrescerin1 contains central basic linker which is required for microtubule

lattice association, and it contains multiple TOG domains (Das et al., 2015). Second, the TOG2 domain of mCrescerin1 resembles the yeast Stu2 TOG1 domain, and CEP104 TOG domain, which has been shown to promote microtubule polymerization. Third, the isolated TOG2 and TOG4 domains of mCrescerin1 were found to promote microtubule polymerization *in vitro* (Das et al., 2015). In addition to the unexpected decrease in the microtubule plus-end growth rate, mCrescerin1 also induced rescues. Interestingly, we observed that mCrescerin1 could oppose the plus-end blocking effect of CEP104, and the pauses induced by CSPP1, to promote tubulin addition. This suggests that mCrescerin1 makes microtubule plus-end growth more robust in the presence of blocking or pausing factors, by allowing tubulin addition when the GTP cap is small or absent. Thus, it seems that the TOG domains of mCrescerin1 can promote microtubule growth but possibly by utilizing a different molecular mechanism to the canonical TOG domain polymerases. Whether the effect of mCrescerin1 is plus-end specific, requires further investigation.

It is fascinating that the combination of just a few proteins, scaffolding protein ARMC9, catastrophe-inducing factor EB3, microtubule growth inhibitor CEP104, pause-inducing factor CSPP1, and rescue factor TOGARAM1 resulted in processive slow growing microtubules. Typically, in the absence of MAPs, microtubule plus ends that grow slowly undergo more frequent catastrophes (Drechsel et al., 1992). Slower microtubule polymerization results in a smaller GTP cap, which can be measured by the comet size of EBs (Roostalu et al., 2020). A smaller GTP cap is also linked to an increase in the number of catastrophes, thus slow growing microtubules undergo more catastrophes. However, the combination of proteins in our study generated extremely slowly growing microtubules that did not undergo catastrophes. mCrescerin1 on its own, in presence of EB3, already reduced microtubule growth rate and catastrophe frequency, and increased the number of rescues. This suggests that mCrescerin1 can potentiate polymerization when the GTP cap is small or absent. Addition of either CEP104 or CSPP1 resulted in further reduction of the microtubule growth rate and reduced the length of depolymerization events. This was even more pronounced when mCrescerin1, EB3, CEP104, CSPP1 and ARMC9 were combined. Thus, these proteins combined can stabilize the GDP-lattice to prevent shrinkage and facilitate GTP-tubulin addition to generate processive slowly growing microtubules. This makes sense in the context of primary cilia assembly, because axonemal microtubules elongate quite slowly without undergoing long depolymerization events. It is not possible to compare our measured growth rate with the elongation rates of primary cilia, because they have not been measured. However, elongation rates of regenerating flagella (a type of motile cilia) from single-celled organisms such as *Chlamydomonas reinhardtii* have been determined. When full length flagella were amputated using shear force or a pH shock, or resorbed by cold treatment, two phases of cilia elongation were observed during regeneration (Marshall et al., 2005; Rosenbaum and Child, 1967; Rosenbaum et al., 1969; Witman, 1975). The initial elongation rates were in the range of 0.08-0.40 $\mu\text{m}/\text{min}$ and these rates decelerated when the flagella started to reach their normal length. The flagellar elongation rates of the second phase varied widely depending on the specific organism, but for *Chlamydomonas reinhardtii* this has been measured to be 0.15-0.20 $\mu\text{m}/\text{h}$ (Rosenbaum and Child, 1967; Rosenbaum et al., 1969; Witman, 1975). The latter is also similar to the elongation rate of flagellar outgrowth after mitosis (Madey and Melkonian, 1990; Rosenbaum et al., 1969). Our measured growth rate of 0.17 $\mu\text{m}/\text{min}$ falls nicely within the range of the measured initial elongation rates of regenerating flagella. However, it remains to be determined if our measured microtubule growth rate will be within the range of elongating primary cilia.

Materials and Methods

DNA constructs, cell lines and cell culture

All proteins were expressed in mammalian cells in modified pEGFP-C1 or pmCherry-C1 vectors with a StrepII tag. COS-7 cells and HEK293T cells (ATCC) were cultured in DMEM medium (Lonza) supplemented with 10% fetal calf serum (FCS) (GE Healthcare Life Sciences) and 1% (v/v) penicillin/streptomycin. All cells were routinely checked for mycoplasma contamination using the MycoAlert™ Mycoplasma Detection Kit (Lonza). For immunofluorescence experiments with overexpression of constructs, COS-7 cells were transiently transfected with FuGENE6 (Promega) for 24 h.

Protein purification from HEK293T cells for in vitro reconstitution assays

HEK293T cells were transiently transfected with a mix consisting of polyethyleneimine (Polysciences) and a DNA construct for one of the ciliary tip module proteins. Protein purification was performed as described before (van den Berg et al., 2022). Briefly, the cells were harvested 28 h after transfection in lysis buffer (50 mM HEPES, 300 mM NaCl, 1 mM MgCl₂, 1 mM DTT, 0.5% Triton X-100, pH 7.4) supplemented with protease inhibitors (Roche) and kept on ice for 15 min. After clearance of the debris by centrifugation, the supernatant was incubated with 20 μl StrepTactin beads (GE Healthcare) for 45 min. After several washing steps, five times with a 300 mM salt wash buffer (50 mM HEPES, 300 mM NaCl, 1 mM MgCl₂, 1 mM EGTA, 1 mM DTT, 0.05% Triton X-100, pH 7.4) and three times with a 150 mM salt wash buffer (similar to the 300 mM salt buffer but with 150 mM NaCl), the protein was eluted in elution buffer (similar to the 150 mM salt wash but supplemented with 2.5 mM d-Desthiobiotin (Sigma-Aldrich)). Purified proteins were snap-frozen and stored at -80°C.

Mass spectrometry

To confirm each protein was purified, and the eluted protein did not contain any contaminants or known interactors that could affect microtubule dynamics, we performed mass spectrometry analysis. Mass spectrometry measurements were performed as described previously (van den Berg et al., 2022). In short, the purified protein sample was digested using S-TRAP microfilters (ProtiFi) according to the manufacturer's protocol. Digested peptides were eluted and dried in a vacuum centrifuge before liquid chromatography-mass spectrometry (LC-MS) analysis. The samples were analyzed by reversed-phase nLC-MS/MS using an Ultimate 3000 UHPLC coupled to an Orbitrap Q Exactive HF-X mass spectrometer (Thermo Scientific). Digested peptides were separated using a 50 cm reversed-phase column packed in-house (Agilent Poroshell EC-C18, 2.7 μm, 50 cm x 75 μm) and eluted from the column at a flow rate of 300 nl/min. Mass spectrometry data were acquired using a data-dependent acquisition (DDA) method. MS/MS fragment spectra were searched using Sequest HT against a human database (UniProt, year 2020) that was modified to contain the exact protein sequence from each ciliary tip module protein and a common contaminants database. Peptides that matched the common contaminant database were filtered out from the results table.

In vitro reconstitution assays

Microtubule seed preparation

Double-cycled GMPCPP-stabilized microtubule seeds were used as templates for microtubule nucleation in vitro assays. GMPCPP-stabilized microtubule seeds were prepared as described before (van den Berg et al., 2022). Briefly, a tubulin mix consisting of 70% unlabeled porcine brain tubulin, 18% biotin-labeled porcine tubulin and 12% rhodamine-labeled porcine tubulin (all from Cytoskeleton) was incubated with 1 mM GMPCPP (Jena Biosciences) at 37°C for 30 min. Centrifugation in an Airfuge for 5 min at 199,000 x g spun down polymerized microtubules, which were subsequently depolymerized on ice for 20 min. Next, 1 mM GMPCPP was added, and microtubules were let to polymerize again at 37°C. Polymerized microtubules were again pelleted and diluted tenfold in MRB80 buffer containing 10% glycerol prior to snap-freezing to store them at -80°C.

In vitro reconstitution assays

In vitro assays with dynamic microtubules were performed as described before (van den Berg et al., 2022). In short, microscopic slides were prepared by adding two strips of double-sided tape to mount plasma-cleaned glass coverslips. The coverslips were functionalized by sequential incubation with 0.2 mg/ml PLL-PEG-biotin (Susos AG, Switzerland) and 1 mg/ml neutravidin (Invitrogen) in MRB80 buffer (80 mM piperazine-N, N[prime]-bis (2-ethane sulfonic acid), pH 6.8, supplemented with 4 mM MgCl₂, and 1 mM EGTA). Then, GMPCPP-stabilized microtubule seeds were attached to the coverslips

through biotin-neutravidin interactions. The coverslip was blocked with 1 mg/ml κ -casein before the reaction mix was flushed in. The reaction mix consisted of different concentrations and combinations of fluorescently labeled purified proteins in MRB80 buffer supplemented with 15 μ M porcine brain tubulin (100% dark porcine brain tubulin when 20 nM GFP-EB3 or mCherry-EB3 was added, or 97% dark porcine brain tubulin with 3% rhodamine- or HiLyte488-labeled porcine tubulin), 0.1% methylcellulose, 1 mM GTP, 50 mM KCl, 0.2 mg/ml κ -casein, and oxygen scavenger mix [50 mM glucose, 400 μ g/ml glucose oxidase, 200 μ g/ml catalase and 4 mM DTT]. This mix was spun down in an Airfuge for 5 min at 119,000 x g before addition to the flow chamber and the flow chamber was sealed with vacuum grease. Microtubules were imaged immediately at 30°C using a total internal reflection fluorescence (TIRF) microscope.

Immunofluorescence staining of fixed cells

For immunofluorescence staining experiments, COS-7 cells were seeded on coverslips one day before transfection. Cells were fixed after 24 h with -20°C MeOH for 10 min. This was followed by a blocking step with 1% bovine serum albumin (BSA) diluted in phosphate buffered saline (PBS) supplemented with 0.05% Tween-20 for 45 min at room temperature. Then, coverslips were incubated with primary antibodies for 1 h at room temperature and fluorescently labeled with secondary antibodies for 45 min at room temperature. Finally, samples were washed, dried, and mounted in Vectashield (Vector laboratories).

Microscopy

Widefield microscopy

Fixed and stained COS-7 cells were imaged on a Nikon Eclipse Ni upright microscope for widefield fluorescence illumination. This microscope is equipped with a Nikon DS-Qi2 camera (Nikon), an Intensilight C-HGFI precentered fiber illuminator (Nikon), ET-DAPI, ET-EGFP and ET-mCherry filters (Chroma) and a Plan Apo Lambda 60x NA 1.4 oil objective (Nikon). The set-up is controlled by Nikon NIS Br software. For presentation, images were adjusted for brightness using ImageJ 1.50b.

TIRF microscopy

In vitro reconstitution assays imaged on a previously described (iLas2) TIRF microscope setup (van den Berg et al., 2022). In brief, we used the iLas3 system (Gataca Systems (France)) which is a dual laser illuminator for azimuthal spinning TIRF (or Hilo) illumination. This system was installed on Nikon Ti microscope (with the perfect focus system, Nikon), equipped with 489 nm 150 mW Vortran Stradus 488 laser (Vortran) and 100 mW 561 nm OBIS laser (Coherent), 49002 and 49008 Chroma filter sets. Additionally, a CCD camera CoolSNAP MYO (Teledyne Photometrics) was installed and the set up was controlled with MetaMorph 7.10.2.240 software (Molecular Device). To keep the in vitro samples at 30 $^{\circ}\text{C}$, a stage top incubator model INUBG2E-ZILCS (Tokai Hit) was used. The final resolution using CCD camera was 0.045 $\mu\text{m}/\text{pixel}$.

Analysis of microtubule plus-end dynamics in vitro

Analysis of microtubule plus-end dynamics was performed as described before (van den Berg et al., 2022). In short, movies of dynamic microtubules, were corrected for drift, and kymographs were generated using the plugin KymoResliceWide v.0.4 in ImageJ (<https://github.com/ekatrakha/KymoResliceWide>). The microtubule tips were traced with lines and measured lengths and angles were used to calculate the microtubule dynamics parameters such as growth rate and transition events. Transition frequency was calculated by dividing the sum of the transition events per experiment by the total time this event could have occurred. For transition events related to pausing, only transitions from and to a paused state that was longer than 20 s were included in the analysis.

Statistical analysis

Statistical analysis was performed using GraphPad Prism 9. Figure legends contain statistical details of each experiment, including the statistical tests used, the number of measurements and the number of experiments.

Acknowledgements

We thank Kevin Slep and Ronald Roepman for providing plasmids containing cDNA of full-length proteins. This work was supported by the European Research Council Synergy grant 609822.

Author Contributions

C. M. vdB. performed experiments, analyzed data, and wrote the paper, H.A.J.S. performed experiments and analyzed data, K.E.S. performed and analyzed mass spectrometry experiments, A.A. coordinated the project and wrote the paper.

Competing financial interests

The authors declare no competing financial interests.

References

- Akizu, N., J.L. Silhavy, R.O. Rosti, E. Scott, A.G. Fenstermaker, J. Schroth, M.S. Zaki, H. Sanchez, N. Gupta, M. Kabra, M. Kara, T. Ben-Omran, B. Rosti, A. Guemez-Gamboa, E. Spencer, R. Pan, N. Cai, M. Abdellateef, S. Gabriel, J. Halbritter, F. Hildebrandt, H. van Bokhoven, M. Gunel, and J.G. Gleeson. 2014. Mutations in CSPP1 lead to classical Joubert syndrome. *Am J Hum Genet.* 94:80-86.
- Al-Bassam, J., M. van Breugel, S.C. Harrison, and A. Hyman. 2006. Stu2p binds tubulin and undergoes an open-to-closed conformational change. *J Cell Biol.* 172:1009-1022.
- Al-Jassar, C., A. Andreeva, D.D. Barnabas, S.H. McLaughlin, C.M. Johnson, M. Yu, and M. van Breugel. 2017. The Ciliopathy-Associated Cep104 Protein Interacts with Tubulin and Nek1 Kinase. *Structure.* 25:146-156.
- Ayaz, P., X. Ye, P. Huddleston, C.A. Brautigam, and L.M. Rice. 2012. A TOG:alpha-tubulin complex structure reveals conformation-based mechanisms for a microtubule polymerase. *Science.* 337:857-860.
- Bacaj, T., Y. Lu, and S. Shaham. 2008. The conserved proteins CHE-12 and DYF-11 are required for sensory cilium function in *Caenorhabditis elegans*. *Genetics.* 178:989-1002.
- Berbari, N.F., A.K. O'Connor, C.J. Haycraft, and B.K. Yoder. 2009. The primary cilium as a complex signaling center. *Curr Biol.* 19:R526-535.
- Bieling, P., L. Laan, H. Schek, E.L. Munteanu, L. Sandblad, M. Dogterom, D. Brunner, and T. Surrey. 2007. Reconstitution of a microtubule plus-end tracking system in vitro. *Nature.* 450:1100-1105.
- Brouhard, G.J., J.H. Stear, T.L. Noetzel, J. Al-Bassam, K. Kinoshita, S.C. Harrison, J. Howard, and A.A. Hyman. 2008. XMAP215 is a processive microtubule polymerase. *Cell.* 132:79-88.
- Byrnes, A.E., and K.C. Slep. 2017. TOG-tubulin binding specificity promotes microtubule dynamics and mitotic spindle formation. *J Cell Biol.* 216:1641-1657.
- Conkar, D., E. Culfa, E. Odabasi, N. Rauniyar, J.R. Yates, and E.N. Firat-Karalar. 2017. The centriolar satellite protein CCDC66 interacts with CEP290 and functions in cilium formation and trafficking. *J Cell Sci.* 130:1450-1462.
- Conkar, D., E. Odabasi, J. Deretic, U. Batman, K.M. Frikstad, S. Patzke, and E.N. Firat-Karalar. 2022. CCDC66 regulates primary cilium length and signaling competence via multi-site interactions with transition zone and axonemal proteins. *bioRxiv.* 2022.04.10.487777.
- Das, A., D.J. Dickinson, C.C. Wood, B. Goldstein, and K.C. Slep. 2015. Crescerin uses a TOG domain array to regulate microtubules in the primary cilium. *Mol Biol Cell.* 26:4248-4264.
- Drechsel, D.N., A.A. Hyman, M.H. Cobb, and M.W. Kirschner. 1992. Modulation of the dynamic instability of tubulin assembly by the microtubule-associated protein tau. *Mol Biol Cell.* 3:1141-1154.
- Frikstad, K.M., E. Molinari, M. Thoresen, S.A. Ramsbottom, F. Hughes, S.J.F. Letteboer, S. Gilani, K.O. Schink, T. Stokke, S. Geimer, L.B. Pedersen, R.I.H. Giles, A. Akhmanova, R. Roepman, J.A. Sayer, and S. Patzke. 2019. A CEP104-CSPP1 Complex Is Required for Formation of Primary Cilia Competent in Hedgehog Signaling. *Cell Rep.* 28:1907-1922. e1906.
- Hildebrandt, F., T. Benzing, and N. Katsanis. 2011. Ciliopathies. *N Engl J Med.* 364:1533-1543.
- Jiang, K., G. Toedt, S. Montenegro Gouveia, N.E. Davey, S. Hua, B. van der Vaart, I. Grigoriev, J. Larsen, L.B. Pedersen, K. Bezstarosti, M. Lince-Faria, J. Demmers, M.O. Steinmetz, T.J. Gibson, and A. Akhmanova. 2012. A Proteome-wide screen for mammalian SxIP motif-containing microtubule plus-end tracking proteins. *Curr Biol.* 22:1800-1807.
- Keeling, J., L. Tsiokas, and D. Maskey. 2016. Cellular Mechanisms of Ciliary Length Control. *Cells.* 5:6.
- Kiesel, P., G. Alvarez Viar, N. Tsoy, R. Maraschini, P. Gorilak, V. Varga, A. Honigsmann, and G. Pigino. 2020. The molecular structure of mammalian primary cilia revealed by cryo-electron tomography. *Nat Struct Mol Biol.* 27:1115-1124.
- Klena, N., and G. Pigino. 2022. Structural Biology of Cilia and Intraflagellar Transport. *Annu Rev Cell Dev Biol.*
- Komarova, Y., C.O. De Groot, I. Grigoriev, S.M. Gouveia, E.L. Munteanu, J.M. Schober, S. Honnappa, R.M. Buey, C.C. Hoogenraad, M. Dogterom, G.G. Borisy, M.O. Steinmetz, and A. Akhmanova. 2009. Mammalian end binding proteins control persistent microtubule growth. *J Cell Biol.* 184:691-706.
- Latour, B.L., J.C. Van De Weghe, T.D.S. Rusterholz, S.J.F. Letteboer, A. Gomez, R. Shaheen, M. Gesemann, A. Karamzade, M. Asadollahi, M. Barroso-Gil, M. Chitre, M.E. GROUT, J. van Reeuwijk, S.E.C. van Beersum, C.V. Miller, J.C. Dempsey, H. Morsy, M.J. Bamshad, D.A. Nickerson, S.C.F. Neuhaus, K. Boldt, M. Ueffing, M. Keramatipour, J.A. Sayer, F.S. Alkuraya, R. Bachmann-Gagescu, R. Roepman, and D. Doherty. 2020. Dysfunction of the ciliary ARMC9/TOGARAM1 protein module causes Joubert syndrome. *J Clin Invest.* 130:4423-4439.
- Louka, P., K.K. Vasudevan, M. Guha, E. Joachimiak, D. Wloga, R.F.-X. Tomasi, C.N. Baroud, P. Dupuis-Williams, D.F. Galati, C.G. Pearson, L.M. Rice, J.J. Moresco, J.R. Yates 3rd, Y. Jiang, K. Lechtreck, W. Dentler, and J. Gaertig. 2018. Proteins that control the geometry of microtubules at the ends of cilia. *J Cell Biol.* 217:4298-4313.

- Madey, P., and M. Melkonian. 1990. Flagellar Development During the Cell Cycle in *Chlamydomonas reinhardtii*. *Botanica Acta*. 103:97-102.
- Marshall, W.F., H. Qin, M. Rodrigo Brenni, and J.L. Rosenbaum. 2005. Flagellar length control system: testing a simple model based on intraflagellar transport and turnover. *Mol Biol Cell*. 16:270-278.
- Montenegro Gouveia, S., K. Leslie, L.C. Kapitein, R.M. Buey, I. Grigoriev, M. Wagenbach, I. Smal, E. Meijering, C.C. Hoogenraad, L. Wordeman, M.O. Steinmetz, and A. Akhmanova. 2010. In vitro reconstitution of the functional interplay between MCAK and EB3 at microtubule plus ends. *Curr Biol*. 20:1717-1722.
- Patzke, S., T. Stokke, and H.C. Aasheim. 2006. CSPP and CSPP-L associate with centrosomes and microtubules and differently affect microtubule organization. *J Cell Physiol*. 209:199-210.
- Perlaza, K., M. Mirvis, H. Ishikawa, and W. Marshall. 2022. The short flagella 1 (SHF1) gene in *Chlamydomonas* encodes a Crescerin TOG-domain protein required for late stages of flagellar growth. *Mol Biol Cell*. 33:ar12.
- Rezabkova, L., S.H. Kraatz, A. Akhmanova, M.O. Steinmetz, and R.A. Kammerer. 2016. Biophysical and Structural Characterization of the Centriolar Protein Cep104 Interaction Network. *J Biol Chem*. 291:18496-18504.
- Roostalu, J., C. Thomas, N.I. Cade, S. Kunzelmann, I.A. Taylor, and T. Surrey. 2020. The speed of GTP hydrolysis determines GTP cap size and controls microtubule stability. *eLife*. 9:e51992.
- Rosenbaum, J.L., and F.M. Child. 1967. Flagellar regeneration in protozoan flagellates. *J Cell Biol*. 34:345-364.
- Rosenbaum, J.L., J.E. Moulder, and D.L. Ringo. 1969. Flagellar elongation and shortening in *Chlamydomonas*. The use of cycloheximide and colchicine to study the synthesis and assembly of flagellar proteins. *J Cell Biol*. 41:600-619.
- Satish Tammana, T.V., D. Tammana, D.R. Diener, and J.L. Rosenbaum. 2013. Centrosomal protein CEP104 (*Chlamydomonas* FAP256) moves to the ciliary tip during ciliary assembly. *J Cell Sci*. 126:5018-5029.
- Shaheen, R., H.E. Shamseldin, C.M. Loucks, M.Z. Seidahmed, S. Ansari, M. Ibrahim Khalil, N. Al-Yacoub, E.E. Davis, N.A. Mola, K. Szymanska, W. Herridge, A.E. Chudley, B.N. Chodirker, J. Schwartzentruber, J. Majewski, N. Katsanis, C. Poizat, C.A. Johnson, J. Parboosingh, K.M. Boycott, A.M. Innes, and F.S. Alkuraya. 2014. Mutations in CSPP1, encoding a core centrosomal protein, cause a range of ciliopathy phenotypes in humans. *Am J Hum Genet*. 94:73-79.
- Srour, M., F.F. Hamdan, D. McKnight, E. Davis, H. Mandel, J. Schwartzentruber, B. Martin, L. Patry, C. Nassif, A. Dionne-Laporte, L.H. Ospina, E. Lemyre, C. Massicotte, R. Laframboise, B. Maranda, D. Labuda, J.C. Décarie, F. Rypens, D. Goldsher, C. Fallet-Bianco, J.F. Soucy, A.M. Laberge, C. Maftel, K. Boycott, B. Brais, R.M. Boucher, G.A. Rouleau, N. Katsanis, J. Majewski, O. Elpeleg, M.K. Kukulich, S. Shalev, and J.L. Michaud. 2015. Joubert Syndrome in French Canadians and Identification of Mutations in CEP104. *Am J Hum Genet*. 97:744-753.
- Tuz, K., R. Bachmann-Gagescu, D.R. O'Day, K. Hua, C.R. Isabella, I.G. Phelps, A.E. Stolarski, B.J. O'Roak, J.C. Dempsey, C. Lourenco, A. Alswaid, C.G. Bonnemann, L. Medne, S. Nampoothiri, Z. Stark, R.J. Leventer, M. Topcu, A. Cansu, S. Jagadeesh, S. Done, G.E. Ishak, I.A. Glass, J. Shendure, S.C. Neuhaus, C.R. Haldeman-Englert, D. Doherty, and R.J. Ferland. 2014. Mutations in CSPP1 cause primary cilia abnormalities and Joubert syndrome with or without Jeune asphyxiating thoracic dystrophy. *Nat Cell Biol*. 94:62-72.
- Van De Weghe, J.C., T.D.S. Rusterholz, B. Latour, M.E. Grout, K.A. Aldinger, R. Shaheen, J.C. Dempsey, S. Maddirevula, Y.-H.H. Cheng, I.G. Phelps, M. Gesemann, H. Goel, O.S. Birk, T. Alanzi, R. Rawashdeh, A.O. Khan, M.J. Bamshad, D.A. Nickerson, S.C.F. Neuhaus, W.B. Dobyns, F.S. Alkuraya, R. Roepman, R. Bachmann-Gagescu, and D. Doherty. 2017. Mutations in ARMC9, which Encodes a Basal Body Protein, Cause Joubert Syndrome in Humans and Ciliopathy Phenotypes in Zebrafish. *Nat Cell Biol*. 101:23-36.
- van den Berg, C.M., V.A. Volkov, S. Snorrenberg, H. Z., K.E. Stecker, I. Grigoriev, S. Patzke, T. Zimmermann, M. Dogterom, and A. Akhmanova. 2022. CSPP1 stabilizes growing microtubule ends and damaged lattices from the luminal side. *bioRxiv*. 2022.06.23.497320.
- Widlund, P.O., J.H. Stear, A. Pozniakovskiy, M. Zanic, S. Reber, G.J. Brouhard, A.A. Hyman, and J. Howard. 2011. XMAP215 polymerase activity is built by combining multiple tubulin-binding TOG domains and a basic lattice-binding region. *Proc Natl Acad Sci U S A*. 108:2741-2746.
- Witman, G.B. 1975. The site of in vivo assembly of flagellar microtubules. *Ann N Y Acad Sci*. 253:178-191.
- Yamazoe, T., T. Nagai, S. Umeda, Y. Sugaya, and K. Mizuno. 2020. Roles of TOG and jelly-roll domains of centrosomal protein CEP104 in its functions in cilium elongation and Hedgehog signaling. *J Biol Chem*. 295:14723-14736.
- Zanic, M., P.O. Widlund, A.A. Hyman, and J. Howard. 2013. Synergy between XMAP215 and EB1 increases microtubule growth rates to physiological levels. *Nat Cell Biol*. 15:688-693.

Supplementary figures

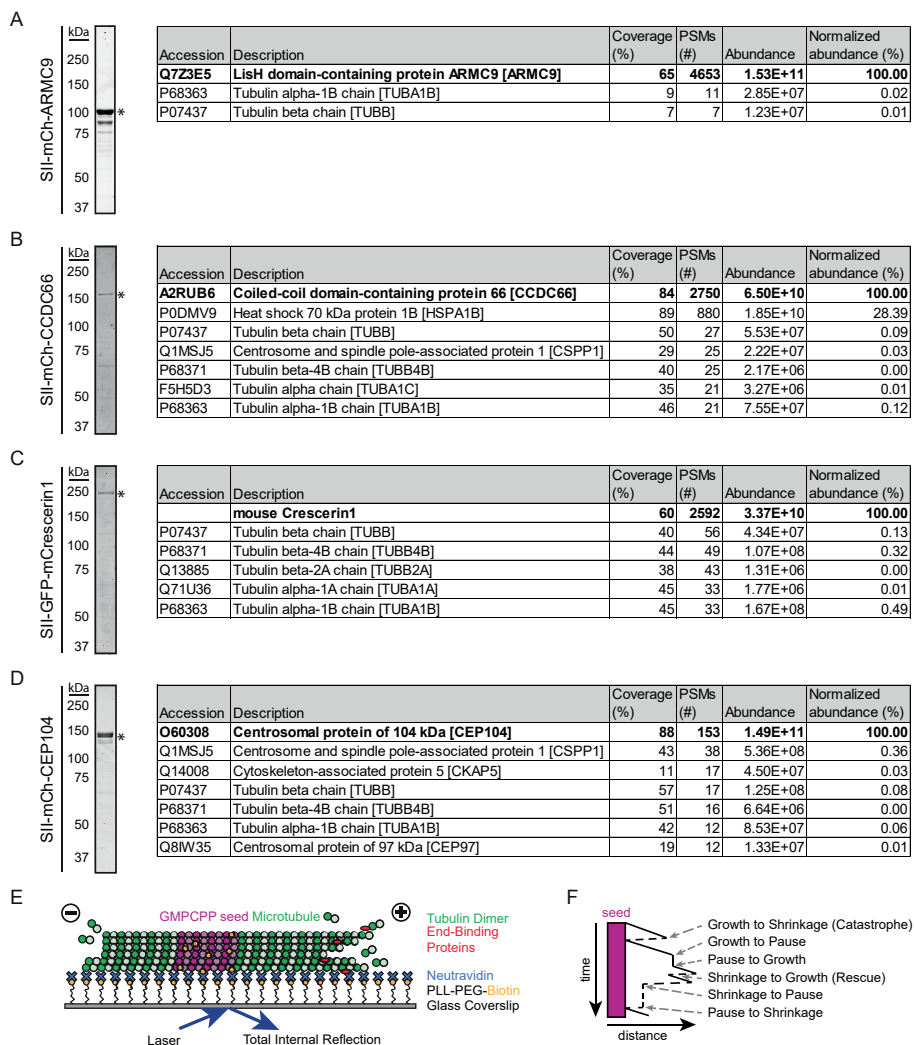


Figure S1, related to Figure 1: Characterization of purified ciliary tip module proteins.

(A-D) Analysis of the indicated proteins by SDS-PAGE and mass spectrometry analysis. Asterisk indicates the full-length protein band. Protein concentrations were determined from BSA standard. (E) Schematic representation of the *in vitro* reconstitution assays with dynamic microtubules for imaging with TIRF microscopy. GMPCPP-stabilized microtubule seeds containing fluorescent tubulin, such as rhodamine tubulin (for visualization) and biotinylated tubulin (for surface attachment via NeutrAvidin), are immobilized on a plasma-cleaned coverslip coated with biotinylated poly(L-lysine)-[g]-poly(ethylene glycol) (PLL-PEG-biotin), which is coupled to NeutrAvidin. Microtubule growth from GMPCPP-stabilized seeds is initiated and visualized by the addition of tubulin supplemented with fluorescently-labeled tubulin, or by the addition of unlabeled tubulin combined with fluorescently-tagged EB3. Microtubule plus ends and minus ends are indicated. (F) Schematic representation of a kymograph visualizing the various transition events observed and quantified in this paper. Panel E and F are from van den Berg et al, 2022.

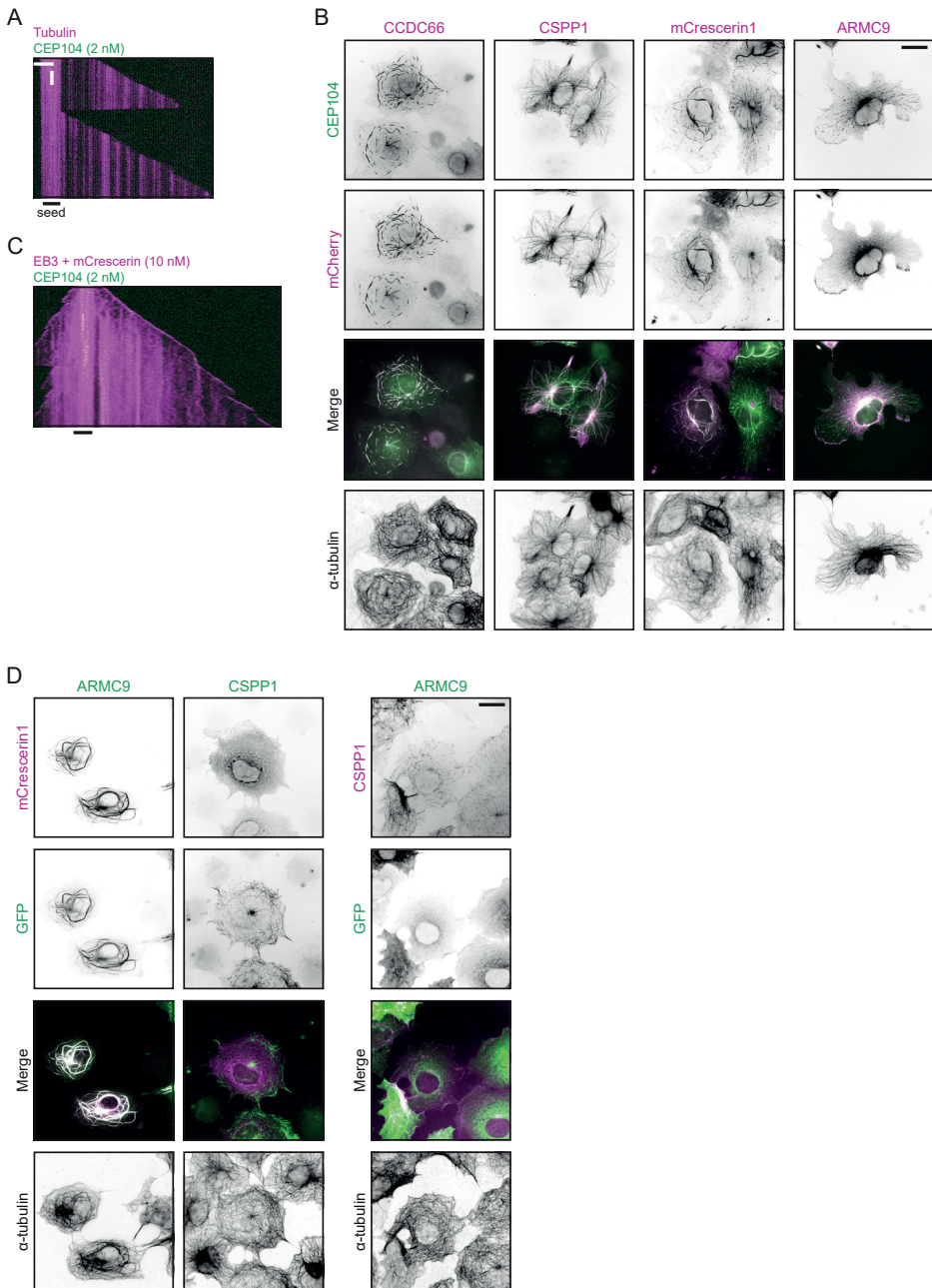


Figure S2, related to Figure 2 and 3: Co-expression of ciliary tip module proteins in COS-7 cells.

(A) Representative kymograph showing microtubule dynamics in the presence of Hilyte488-labeled tubulin supplemented with 2 nM SII-mCherry-CEP104. Scale bars, 2 μ m (horizontal) and 60 s (vertical). (B) Widefield fluorescence images of COS-7 cells overexpressing combinations of mCherry-tagged and GFP-tagged proteins and stained for α -tubulin. Scale bar, 20 μ m. (C) Representative

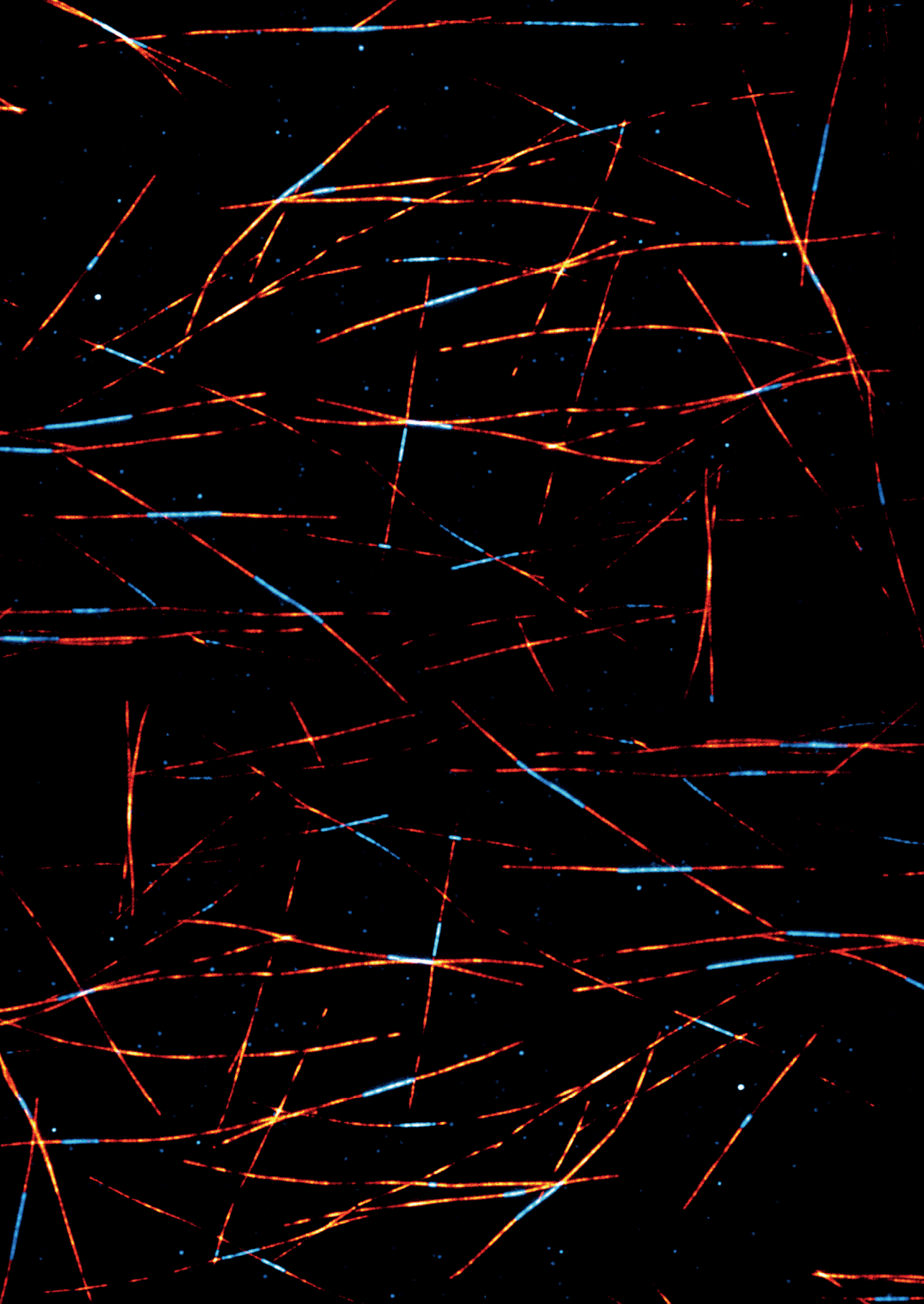
kymograph showing microtubule dynamics in the presence of 20 nM GFP-EB3 supplemented with 10 nM SII-GFP-mCrescerin1 and 2nM SII-mCherry-CEP104. **(D)** Widefield fluorescence images of COS-7 cells overexpressing combinations of mCherry-tagged and GFP-tagged proteins and stained for α -tubulin. Scale bar, 20 μ m.

Supplementary table

Table S1: Key resources table

REAGENT or RESOURCE	SOURCE	IDENTIFIER
Antibodies		
Rat anti-tyrosinated α -tubulin (Clone YL1/2)	Abcam	Cat# ab6160
Goat Anti-Rat IgG H&L (Alexa Fluor® 405) preadsorbed	Abcam	Cat# ab175673
Chemicals, Peptides, and Recombinant Proteins		
StrepTactin Sepharose High Performance	GE Healthcare	Cat# 28-9355-99
Polyethyleneimine	Polysciences	Cat# 24765-2
cOmplete™, EDTA-free Protease Inhibitor Cocktail	Roche	Cat# 4693116001
Tubulin protein: porcine brain	Cytoskeleton	Cat# T240
Tubulin protein (fluorescent HiLyte 488): porcine brain	Cytoskeleton	Cat# TL488M
Tubulin protein (rhodamine): porcine brain	Cytoskeleton	Cat# TL590M
Tubulin protein (biotin labeled): porcine brain	Cytoskeleton	Cat# T333P
PLL-PEG-biotin	Susos AG, Switzerland	PLL(20)-g[3.5]-PEG(2)/PEG(3.4)-biotin(50%)
Methyl cellulose, 4000 cp	Sigma-Aldrich	Cat# M0512
GMPCPP	Jena Biosciences	Cat# NU-405L
GTP	Sigma-Aldrich	Cat# G8877
Glucose oxidase	Sigma-Aldrich	Cat# G7141
Catalase	Sigma-Aldrich	Cat# C9322
DTT	Sigma-Aldrich	Cat# R0861
k-casein	Sigma-Aldrich	Cat# C0406
Neutravidin	Invitrogen	Cat# A-2666
d-Desthiobiotin	Sigma-Aldrich	Cat# D1411
StrepII-mCherry-ARMC9 full length	This study	N/A
StrepII-GFP-CCDC66 full length	This study	N/A
StrepII-GFP-mCrescerin1 full length	This study	N/A
StrepII-mCherry-mCrescerin1 full length	This study	N/A
StrepII-GFP-CSPP-L full length	(van den Berg et al., 2022)	N/A
StrepII-mCherry-CSPP-L full length	(van den Berg et al., 2022)	N/A
StrepII-mCherry-CEP104 full length	(Jiang et al., 2012)	N/A
mCherry-EB3 full length	(Montenegro Gouveia et al., 2010)	N/A
GFP-EB3 full length	(Montenegro Gouveia et al., 2010)	N/A
FuGENE6	Promega	Cat# E2691
Experimental Models: Cell Lines		
Human: HEK293T	ATCC	CRL-11268
Monkey: COS-7	ATCC	CRL-1651
Recombinant DNA		
StrepII-mCherry-ARMC9 full length	This study	N/A
StrepII-GFP-ARMC9 full length	This study	N/A
StrepII-GFP-CCDC66 full length	This study	N/A

StreptII-mCherry-mCrescerin1 full length	This study	N/A
StreptII-GFP-CSPP-L full length	(van den Berg et al., 2022)	N/A
StreptII-mCherry-CSPP-L full length	(van den Berg et al., 2022)	N/A
StreptII-mCherry-CEP104 full length	This study	N/A
StreptII-GFP-CEP104 full length	This study	N/A
Software and Algorithms		
ImageJ	NIH	https://imagej.nih.gov/ij/
Metamorph Version 7.8	Molecular Devices	https://www.moleculardevices.com/products/cellular-imaging-systems/acquisition-and-analysis-software/metamorph-microscopy
GraphPad Prism 9	GraphPad Software	https://www.graphpad.com/scientific-software/prism/
KymoResliceWide plugin	Eugene Katrukha	https://github.com/ekatrunkha/KymoResliceWide





General Discussion

Cyntha M. van den Berg¹

¹Cell Biology, Neurobiology and Biophysics, Department of Biology, Faculty of Science, Utrecht University, Padualaan 8, 3584 CH Utrecht, The Netherlands.

5

Microtubules are cytoskeletal polymers that can randomly switch between polymerization and depolymerization phases, also described as ‘dynamic instability’. However, for some cellular processes and cellular structures, microtubules should not exhibit dynamic instability and may need to be stabilized for shorter or longer periods of time. Microtubules can be stabilized by the incorporation of different tubulin isotypes, addition or removal of post-translational modifications (PTMs), presence of microtubule targeting agents (MTAs), or presence or absence of microtubule associated proteins (MAPs). In this thesis, we studied the components of two multi-protein assemblies which act on microtubule plus ends for stabilization. In **Chapter 1**, we provided an overview of tubulin isotypes, PTMs and MAPs known to directly or indirectly stabilize microtubules, as well as a detailed description of the components of the cortical microtubule stabilizing complex (CMSC) and ciliary tip module (CTM). In **Chapter 2**, we studied the role of the CMSC in insulin secretion in pancreatic β -cells. We showed that a combined complex of the CMSC and components from neuronal synapses participates in the regulation of the first wave of insulin secretion. In **Chapter 3**, we characterized the behavior of microtubule stabilizing CTM-protein CSPP1 in cells and *in vitro*. We showed that CSPP1 binds to the microtubule lumen and is able to stabilize microtubules that exhibit slow or perturbed growth or contain damaged lattices. Subsequently, we studied the effect of the other CTM components individually and collectively on reconstituted microtubules (**Chapter 4**). We showed that every component affected microtubule dynamics differently, and various combinations of proteins resulted in blocked or extremely slow growing microtubules. In this final chapter, we will further discuss our findings, put them in a broader context and provide suggestions for future research.

Effects of stabilization on microtubule plus ends

Microtubule stabilization commonly refers to changed microtubule plus-end dynamics. Minus ends are generally less dynamic, and in cells these are usually anchored at a microtubule organizing center. Growing microtubule plus ends are characterized by the presence of a GTP cap, which has stabilizing properties. In absence of MAPs, loss of the GTP cap leads to a switch from polymerization to depolymerization (called catastrophe). Microtubules that do not lose their GTP cap, for example by presence of a polymerization promoting factor or catastrophe inhibitor, are considered stable (**Fig. 1**). However, microtubules that do lose their GTP cap can also be stable when they are anchored, paused, or capped, which prevents depolymerization. Additionally, microtubules that undergo catastrophe, meaning they lose their GTP cap, can subsequently switch back to polymerization in presence of a rescue factor. However, they are only regarded as stable when the average microtubule length lost during depolymerization is shorter than the average length gained during polymerization (Akhmanova and Kapitein, 2022). Microtubule stabilization is not just achieved by factors which are acting directly on the microtubule end, but also changes in the microtubule lattice can facilitate rescues which can subsequently lead to net extension of microtubule length. For example, damages to the microtubule lattice can result in incorporation of GTP-tubulin to create stable ‘GTP-islands’, the formation of which can be affected by MAPs recruited to damage sites (de Forges et al., 2016; Dimitrov et al., 2008; Vemu et al., 2018). Furthermore, MAPs can be recruited to the microtubule lattice and act as rescue factors when microtubules undergo depolymerization.

Anchored microtubule plus ends

Microtubule plus-end anchoring usually occurs at the cell cortex and involves microtubule plus-end tracking proteins and cortical proteins (**Fig. 1**). In non-neuronal cells, the CMSC anchors microtubule plus ends in close proximity to focal adhesions (FAs) to facilitate processes such as localized secretion around FAs and FA turnover where connection between

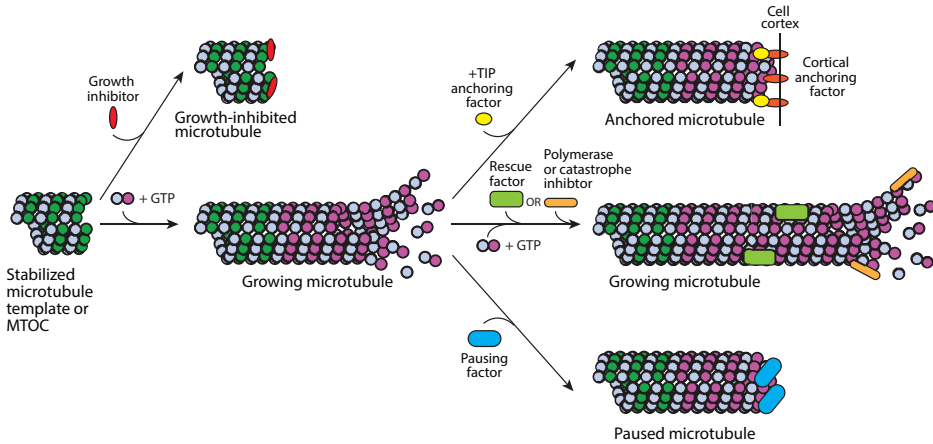


Figure 1: Microtubule stabilization at the plus ends. Scheme illustrating effects of microtubule-stabilizing factors affecting plus-end dynamics. MTOC, microtubule organizing center; +TIP, microtubule plus-end tracking protein.

cells and the extracellular matrix is required (Bouchet et al., 2016). The CMSC consists of the cortical proteins ELKS, LL5 β , liprin- α 1, liprin- β 1 and KANK1. Microtubule anchoring is enabled by the direct interaction of LL5 β at the cell cortex and CLASP family members at the microtubule plus end (Hotta et al., 2010; Lansbergen et al., 2006). Additionally, motor protein KIF21A cooperates with CLASP to promote microtubule stability at the cortex by inhibition of growth and catastrophes (van der Vaart et al., 2013). LL5 β recruits scaffolding protein ELKS to the cell cortex, and ELKS in turn recruits the other CMSC proteins (Lansbergen et al., 2006). KANK1 serves as the link between FAs and the CMSC (Bouchet et al., 2016). ELKS can also recruit other proteins to the CMSC clusters and has been shown to be important for Rab6-mediated exocytosis in non-neuronal cells (Grigoriev et al., 2007). In these cells, ELKS is not important for targeting of vesicles to the CMSC, but it is required for subsequent vesicle fusion.

ELKS, together with members of the liprin- α 1 family, has been identified as a component of the insulin exocytosis machinery in pancreatic β -cells (Gan et al., 2017; Low et al., 2014; Ohara-Imaizumi et al., 2019). Docking and secretion sites of insulin vesicles strongly colocalized with ELKS clusters, and ELKS depletion abolished glucose stimulated insulin secretion (Ohara-Imaizumi et al., 2005). Insulin secretion sites are enriched at the interface with vasculature, where pancreatic β -cells are in contact with the extracellular matrix (Low et al., 2014). Additionally, glucose stimulation results in FA enlargement (Arous and Halban, 2015; Arous et al., 2013; Gan et al., 2018; Rondas et al., 2011; Rondas et al., 2012). These findings suggest a direct link between insulin secretion sites and FAs. We were wondering if the insulin exocytotic machinery is linked to focal adhesions in a similar way as the constitutive exocytotic machinery in non-neuronal cells. In [Chapter 2](#), we showed that clusters of CMSC components LL5 β and KANK1 colocalized with components of the insulin secretion machinery RIM1/RIM2 and bassoon in pancreatic β -cells. LL5 β and KANK1 colocalized with the liprins and ELKS in these cells. Additionally, CLASP1 was enriched at regions with high LL5 β accumulation, indicating that microtubule plus ends may be anchored to the cell cortex via this known interaction. We also observed spatial proximity between microtubules and focal adhesions. We confirmed that glucose stimulation results in enlarged FAs and we showed increased recruitment of LL5 β to FAs. These data make it attractive to think that

enrichment of LL5 β at insulin secretion sites by glucose stimulation is contributing to efficient insulin vesicle transport and subsequent release at FA-rich secretory sites. Enrichment of LL5 β would then lead to increased microtubule density at secretion sites. However, the opposite is true. Studies have shown that microtubules are actually destabilized upon glucose stimulation and that the reduction of microtubule density increases insulin docking and secretion (Bracey et al., 2020; Ho et al., 2020; Zhu et al., 2015).

Apart from facilitating transport of insulin vesicles towards the plasma membrane, microtubules are also involved in insulin vesicle movement away from the plasma membrane. The microtubule network in β -cells is quite different than the radial network in mesenchymal (non-neuronal) cells. Microtubules in β -cells originate from the Golgi network and form an undirected random mesh (Zhu et al., 2015). Bi-directional transport in a random microtubule network limits the time for insulin vesicles to dock to the cell periphery for subsequent release. Glucose stimulation destabilizes microtubules which makes the cortical dwell time of insulin vesicles longer, allowing them to dock, thereby increasing insulin release (Bracey et al., 2020; Zhu et al., 2015). Thus, microtubule anchoring facilitates insulin vesicle transport towards, but also away from the plasma membrane. This mechanism of regulating the abundance of insulin vesicles at the cell cortex is important because β -cells need to be ready to release insulin, but only upon glucose stimulation. We showed that LL5 β is not required for insulin vesicle docking but knockdown of LL5 β attenuated the first wave of insulin vesicle release. The first wave of insulin secretion is characterized by the release of insulin vesicles that are already docked at the cell cortex and do not rely on microtubule transport anymore. So why is LL5 β knockdown leading to decreased insulin secretion? We observed that knockdown of LL5 β resulted in less efficient clustering of the exocytic machinery components RIM1/RIM2. Therefore, we think that clustering of LL5 β and its cortical interaction partners, is required for efficient insulin exocytosis by recruiting the fusion machinery. This mechanism is not surprising as the requirement of cortical clustering of factors required for vesicle fusion and release was also observed in non-neuronal cells (Bouchet et al., 2016; Lansbergen et al., 2006; van der Vaart et al., 2013). We hypothesize the following role of LL5 β in β -cells (Fig. 2). First, cortical anchoring of microtubules via the LL5 β -CLASP1 interaction regulates the number of insulin vesicles docking at the cell cortex under unstimulated conditions. Then, glucose stimulation destabilizes the microtubule network, and vesicles can dock at LL5 β -

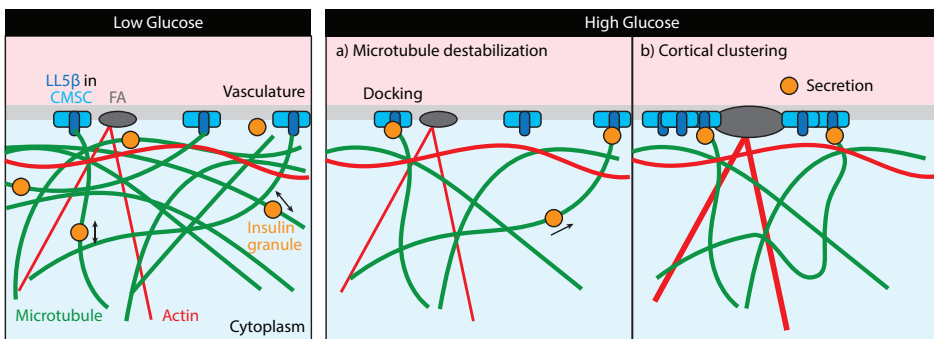


Figure 2: Proposed role for LL5 β in pancreatic β -cells. Under low glucose conditions, LL5 β captures CLASP-positive microtubule plus ends. The microtubule network is dense, regulating the balance between insulin granule transport towards and from the cell cortex. Upon stimulation with high glucose, the microtubule network is destabilized and insulin granules can dock more easily (a). Subsequently or simultaneously, actin stress fibers form, focal adhesions (FA) enlarge, and LL5 β is recruited to FAs to cluster the secretion machinery to promote insulin release towards the vasculature (b).

sites. Subsequently or simultaneously, released LL5 β molecules, their interaction partners and insulin vesicles, get recruited to FAs close to the vasculature to facilitate fusion towards the blood vessels. Future research is required to test this hypothesized role for LL5 β and to elucidate how cortical clustering exactly facilitates insulin release.

Blocked microtubule plus ends

Microtubule plus-end growth can be blocked by certain MAPs. MAPs can induce pauses during microtubule polymerization or depolymerization, and these MAPs are called pausing factors (Fig. 1). MAPs that block microtubule outgrowth from stabilized microtubules are referred to as growth inhibitors or capping proteins. Pausing factors are capable of preventing microtubule polymerization as well as depolymerization simultaneously, while growth inhibitors only prevent microtubule polymerization.

Microtubule pausing

In Chapter 3, we characterized the stabilizing behavior of ciliary protein CSPP1. We showed that CSPP1 binds to microtubule ends specifically when they undergo a growth perturbation. When this occurs, microtubules enter the pre-catastrophe state, which means that the stabilizing GTP cap is reduced. Upon binding, CSPP1 induces pausing, followed by microtubule growth. Thus, CSPP1 is stabilizing microtubules by inducing pauses and preventing depolymerization. In Chapter 4, we observed that the addition of CTM component ARMC9 resulted in increased pause duration.

Pausing factors have two simultaneous tasks, they have to prevent tubulin subunit addition and they have to prevent depolymerization. These two tasks usually require two separate domains as demonstrated for kinesin-4 KIF21B and centriolar protein CPAP (Sharma et al., 2016; van Riel et al., 2017). Therefore, we examined the different domains of the CSPP1 protein for their effects on microtubule dynamics. We show that indeed the interplay of two separate domains is responsible for CSPP1 behavior. One predicted helical region was sufficient for microtubule binding and stabilization and another helical region was responsible for the growth-inhibiting activity to induce pausing.

It is remarkable how CSPP1 can block tubulin subunit addition during pausing but allows microtubule growth at a later time point. However, we have not investigated the underlying mechanism. CSPP1 is also able to prevent microtubule depolymerization when it induces pausing. This is potentially achieved by preventing individual protofilaments from curling or promoting lateral interactions between multiple protofilaments such as has been observed for MTAs (Elie-Caille et al., 2007; Prota et al., 2013). To gain more insight into CSPP1 binding to microtubules, we turned to cryo-electron tomography experiments (Chapter 3). We found that CSPP1 binds to the luminal side of complete microtubules, making it a microtubule inner protein (MIP). Tomograms did not give any clues on how CSPP1 could block subunit addition, but they did show a reduction in microtubule tip raggedness. This suggests that CSPP1 might span several protofilaments at the luminal side. This idea is strengthened by the observation that CSPP1 was not found at protofilament flares. Proving that this is indeed the case and finding out how CSPP1 can block subunit addition without completely preventing microtubule regrowth would require additional structural studies.

CSPP1 recognizes microtubule ends that are in the pre-catastrophe state, which are characterized by the recent loss of their GTP cap and are on the verge of switching to disassembly (Duellberg et al., 2016). This suggests that CSPP1 might prefer to bind to microtubule ends that contain a small or no GTP cap. In agreement with this possibility, growing microtubule minus ends, which contain a short GTP cap, also showed strong CSPP1 accumulation. When we reduced the microtubule plus-end growth rate by reducing the tubulin concentrations in our assays, we also observed an increase in CSPP1 signal confirming that CSPP1 prefers

5 binding to perturbed or slow growing microtubule ends. This can be explained by the finding that CSPP1 is a MIP. CSPP1 was found to bind to the microtubule lumen, and for intact microtubule lattices, the only way to enter is via the microtubule end. At the microtubule end, tubulin subunits are added longitudinally to existing protofilaments which flare somewhat outward, slightly exposing the luminal side of tubulin dimers (Brouhard and Rice, 2018). These flared protofilaments close into a tube when more tubulin subunits are added, limiting luminal exposure. This process occurs faster when microtubule polymerization is fast because of rapid tubulin subunit addition. We suspect that CSPP1 has a slow on-rate for the luminal side of tubulin dimers, potentially explaining why CSPP1 does not bind to processive growing microtubules. When microtubules grow slowly or end up in the pre-catastrophe state, the luminal side of tubulin dimers is exposed for a longer time period and CSPP1 is able to bind. The binding profile of CSPP1 over time seems similar to that of taxanes, compounds that have also been localized to the microtubule lumen (Nogales et al., 1995; Rai et al., 2020; Steinmetz and Prota, 2018). After initiation of binding, the intensity of CSPP1 and taxanes rapidly increases, suggesting cooperative binding, and after a short while their intensity starts to diminish, suggesting dissociation from the microtubule (Rai et al., 2020). Modelling of taxane binding kinetics to microtubules proposed an autocatalytic step to account for the rapid and sustained increase in taxane intensity. Exposure of a few luminal binding sites on microtubules would recruit a few taxane molecules and their binding could then trigger the conversion of nearby sites into binding sites. Increased taxane binding could induce microtubule lattice alterations which would release the taxane molecules, matching with the decrease in signal over time. It is attractive to think that the microtubule binding kinetics of CSPP1 are similar to taxanes, but this remains to be confirmed. Additionally, it will be interesting to find out if CSPP1 also localizes to the lumen of axonemal microtubules in primary cilia and if the accessibility to its preferred binding site is similar to what we observed *in vitro*.

Microtubule growth inhibition

Cilia formation is highly regulated during the cell cycle because cilia can only be present in interphase (Breslow and Holland, 2019). Primary cilia are generated from the mother centriole, and during mitosis, this centriole is required for spindle formation. Therefore, plus ends of the microtubules of the mother centriole need to be blocked to prevent elongation. This block is achieved by a complex of centriolar capping proteins CPAP, CP110 and CEP97. CPAP contains microtubule lattice-binding domain and two tubulin-binding domains, one which mediates binding to the side of tubulin dimer, and another that binds to the exposed surface of β -tubulin to prevent the addition of new tubulin dimers (termed LID domain) (Campanacci et al., 2022; Sharma et al., 2016; Zheng et al., 2016). Counterintuitively, CPAP on its own cannot block microtubule growth. This was shown by *in vitro* experiments with reconstituted microtubules where a truncated version of CPAP did not block plus-end growth, but it slowed down the microtubule growth rate, inhibited catastrophes and promoted rescues (Sharma et al., 2016). Additionally, it was found that overexpression of CPAP led to elongated centrioles (Kohlmaier et al., 2009; Schmidt et al., 2009; Tang et al., 2009). Recently, CPAP was found to interact with CP110 (Ogunmolu et al., 2021). CP110, together with its interaction partner CEP97, was shown to block centriolar microtubule outgrowth and it needs to be removed to enable cilia formation (Spektor et al., 2007). CP110 blocks microtubule outgrowth from stabilized microtubule templates *in vitro*, and this is unaffected by the presence of CEP97 (Ogunmolu et al., 2021). However, presence of CPAP potentiated the ability of CP110 to block microtubule outgrowth. CPAP and CP110 do not compete with each other for microtubule tip localization but together they inhibit microtubule outgrowth (Ogunmolu et al., 2021). They bind to different regions of the microtubule tip. CPAP has been localized to the microtubule tip at the outside surface of tubulin dimers, where its LID domain binds to the exposed

surface of β -tubulin (Sharma et al., 2016). A chimera construct of CP110 and CEP97 has been localized at the luminal side of the microtubule plus end (Ogunmolu et al., 2021).

To initiate microtubule outgrowth, CP110 and CEP97 are required to be displaced from the mother centriole, as depletion of these proteins was shown to promote cilia formation (Spektor et al., 2007). Interestingly, CP110 and CEP97 both bind to CTM component CEP104, which for a long time was proposed to be involved in their removal (Jiang et al., 2012; Latour et al., 2020; Satish Tammana et al., 2013). However, a recent study showed that this is not the case. Knockdown of CP110 alone significantly increased the population of ciliated cells, but this increase was similar when CP110 and CEP104 were co-depleted (Yamazoe et al., 2020). This showed that CEP104 does not affect the inhibitory function of CP110 in ciliogenesis, and therefore, it is also not involved in the removal of the CP110-CEP97 complex from the mother centriole to allow cilia elongation. During ciliogenesis, CEP104 moves from the mother centriole to the ciliary tip, and this was shown to be important for cilia elongation (Satish Tammana et al., 2013). CP110 is not involved in this function of CEP104 because CEP104-mediated elongation occurs after CP110 is removed from the mother centriole (Yamazoe et al., 2020). CEP104 contains one TOG domain, and this domain on its own was shown to promote tubulin polymerization, like it has been described for other TOG domains (Yamazoe et al., 2020).

In **Chapter 4**, we studied the effect of CEP104 on *in vitro* reconstituted dynamic microtubules, when it is present alone or in combination with the other CTM components. We were surprised to find that CEP104 blocked microtubule plus-end growth, rather than promoted microtubule polymerization. This finding was unexpected because the TOG domain of CEP104 structurally resembles the TOG1 domain of yeast Stu2 (Al-Jassar et al., 2017; Rezabkova et al., 2016). Stu2 is a canonical microtubule polymerase which increases microtubule growth rate by promoting tubulin addition. Stu2 is part of the XMAP215/Stu2/ch-TOG family, which are the best studied polymerases. These proteins contain multiple TOG domains and localize to the growing microtubule plus end where they promote microtubule elongation by increasing the microtubule growth rate (Al-Bassam et al., 2006; Brouhard et al., 2008; Zanic et al., 2013). Another reason why the growth inhibition by CEP104 was unexpected is the previously mentioned study showing increased polymerization for the isolated TOG domain (Yamazoe et al., 2020). Why do we see blocked microtubule plus ends when CEP104 is present in our assays? We studied the behavior of full-length CEP104, so it could be possible that the additional domains of CEP104 are regulating microtubule polymerization by positioning the TOG domain a certain way. CEP104 contains a coiled-coil domain which can be used to induce dimerization. For Stu2 it was shown that dimerization was important for polymerase activity as well as end-binding affinity (Geyer et al., 2018). It could be that the opposite is true for CEP104. Dimerization of the full-length protein potentially positions the TOG domains in a way that that would prevent tubulin addition whereas a monomer or isolated TOG domain could promote polymerization. Specific positioning of the CEP104 TOG domain in relation to one or multiple other domains could also affect its function. For Stu2 it was also found that the position of TOG2 adjacent to the basic region, mediating microtubule lattice binding, was required for efficient polymerization (Geyer et al., 2018). The addition of a flexible linker between TOG2 and the basic region retained the ability to tip-track and stimulate elongation but to a substantially lesser extent. To study the effect of the additional CEP104 domains, it would be useful to perform *in vitro* experiments comparing the full-length protein with the isolated TOG domain and the full-length containing a mutation previously shown to abrogate the interaction of TOG domains with tubulin. Next, deletion of other CEP104 domains could reveal their specific role.

Difference in TOG domain availability and positioning would fit with the different localizations of CEP104 during the cell cycle and ciliogenesis. CEP104 is located on the

mother centriole when microtubule outgrowth needs to be prevented and it moves towards the ciliary tip during cilia elongation (Satish Tammana et al., 2013). On the mother centriole, CEP104 could assist in capping the centriolar microtubule plus ends by interacting with the CP110-CEP97-CPAP complex. Here, microtubule outgrowth needs to be prevented and the TOG domain could be positioned to block tubulin addition. Then, when cilia assembly is initiated, interaction with other proteins could affect the conformation or dimerization of CEP104 and result in promotion of microtubule polymerization, facilitating cilia elongation. It would be interesting to find out if this indeed explains the different localizations and behavior of CEP104. To start, it would be useful to determine the specific localization of CEP104 at (centriolar) microtubule ends in relation to CPAP and CP110. This could provide more insight into its role in centriolar capping and may give some hints if CEP104 could be conformationally regulated.

Structural studies showed that the CEP104 TOG domain is involved in binding of free tubulin which is in a curved state (Al-Jassar et al., 2017; Rezaczkova et al., 2016). How does this property match with its growth-inhibiting activity as well as its potential polymerization activity? One possibility is that CEP104 stabilizes a tubulin intermediate state. This characteristic has been observed for XMAP215. XMAP215 was found to act as a catalyst which stabilizes an intermediate tubulin conformation which promotes microtubule plus-end polymerization in presence of soluble tubulin, while it promotes microtubule plus-end depolymerization in absence of soluble tubulin (Brouhard et al., 2008). This shows that TOG domain proteins identified as polymerases can also be involved in microtubule depolymerization. We have not observed depolymerization of the GMPCPP-stabilized seeds, which was previously shown for XMAP215, but we have not tried the experiment in absence of soluble tubulin. However, we did observe slow depolymerization of microtubules that were blocked mid-growth when CEP104 was combined with CSPP1, and occasionally with CCDC66, in absence of End Binding proteins (EBs). Another possibility is that CEP104 could destabilize the microtubule end. XMAP215 binds to soluble tubulin and has also been shown to increase the catastrophe frequency while simultaneously promoting microtubule polymerization (Farmer et al., 2021). It has been shown that microtubule ends grown in presence of XMAP215 are less stable and this is suggested to be due to XMAP215 promoting formation of tapered microtubule ends. Reduced end stability can lead to growth inhibition in the case of CEP104, which can be counteracted by presence or interaction with other proteins. Both possibilities require further investigation.

Stabilization by reduction of microtubule plus-end shrinkage length

Microtubules are also considered stable in presence of factors which reduce the net microtubule shrinkage length. This can be achieved by the presence of a factor enhancing polymerization or inhibiting catastrophes (Fig. 1). Additionally, shrinking microtubules can switch to growth in presence of a rescue factor, and these microtubules are considered stable when the length lost during shrinkage is shorter than the length gained during polymerization. In Chapter 4, we studied mCrescerin1, the mouse homolog of the human CTM component TOGARAM1. We expected that mCrescerin1 would also increase the microtubule growth rate, based on the presence of multiple TOG domains and a basic microtubule binding region (Das et al., 2015), for the same reasons as described above for CEP104. However, we found that mCrescerin1 slowed down microtubule polymerization and induced rescues. It is not the first time that a member of a family of TOG domain proteins was shown to decrease the microtubule polymerization rate. *In vitro* studies of mammalian CLASPs also showed that it reduces microtubule growth rate, and its main effect is catastrophe suppression rather than acceleration of microtubule polymerization (Aher et al., 2018).

We investigated the role of TOGARAM1 in the CTM by studying the effect of protein

combinations on microtubule dynamics *in vitro*. TOGARAM1 was described to recruit ARMC9 to microtubules (Latour et al., 2020), and we confirmed this finding *in vitro* by combining mCrescerin1 and ARMC9. Increasing concentrations of ARMC9 did not affect microtubule dynamics compared to mCrescerin1 alone. Combination of mCrescerin1 with the growth inhibiting activity of CEP104, resulted in a reduced microtubule growth rate compared to mCrescerin1 alone. Presence of both mCrescerin1 and CSPP1 resulted in the reduction in the number and duration of pauses compared to CSPP1 alone and reduced the microtubule growth rate compared to mCrescerin1 alone. Blocked and paused microtubules have a small or absent GTP cap, and slower microtubule polymerization also leads to a smaller GTP cap. The finding that mCrescerin1 is able to overcome growth inhibition by CEP104 and CSPP1, allowing slow polymerization, suggests that mCrescerin1 can potentiate polymerization when the GTP cap is small or absent. Thus, it seems that mCrescerin1 TOG domains can promote tubulin addition like those in canonical polymerases, but in a different way. mCrescerin1 alone specifically affected microtubule plus-end dynamics and it bound to regions on the microtubule lattice that were already polymerized for some time. Microtubule lattices that are formed by growth of the microtubule plus end are longer-lived, potentially explaining why stronger signal is observed on these ends. Combination of mCrescerin1 and CEP104 increased the binding of both proteins on the lattice formed by minus-end elongation and stabilized these lattices by inducing many rescues. CSPP1 alone binds to both growing microtubule ends, and even though mCrescerin1 and CSPP1 do not colocalize, we observed increased binding of mCrescerin1 to the lattices formed by minus-end growth in presence of CSPP1. CSPP1 stabilizes minus ends, and thereby also the lattice formed by minus-end elongation, generating longer-lived lattices for mCrescerin1 to bind. To distinguish if mCrescerin1 binds to the microtubule lattice with a slow on-rate and therefore binds longer-lived lattices, or if it recognizes a specific microtubule lattice structure requires additional investigation.

When we combined mCrescerin1, ARMC9, CSPP1, EB3 and CEP104 in the same assay, we observed extremely slow but persistent microtubule growth. This is also a mechanism of microtubule stabilization because the microtubule keeps growing. It is fascinating that the combination of a rescue factor, a scaffolding protein, a pause factor, a catastrophe inducer and a growth inhibitor can create stable, slowly growing microtubules *in vitro*. Importantly, this is achieved in an environment of a high soluble tubulin concentration which usually results in fast microtubule growth. Our findings fit well with what is generally known about cilia formation. Cilia are microtubule-based structures which are assembled very slowly and must reach a certain length to be able to function. The CTM proteins localize at the tip of primary cilia, and they are found to be important in the regulation of ciliary length. Most CTM components are associated with a ciliopathy called Joubert syndrome, where patient-derived cells often contain shorter cilia. We were not able to compare our microtubule growth rate with primary cilium elongation speed because this is unknown, but the values we obtained *in vitro* do fall nicely within the range of the measured initial growth rates of regenerating flagella (a type of motile cilia) in single-celled organisms (Marshall et al., 2005; Rosenbaum et al., 1969; Rosenblatt, 2005; Witman, 1975). It will be interesting to find out if axonemal microtubules grow slowly due to low tubulin concentration and require stabilization of MAPs and MIPs to grow while there is no significant GTP cap. Or, if the tubulin concentration is actually high, and slow growth is caused by the presence of MAPs and MIPs. Until now, soluble tubulin concentration in primary cilia is unknown because tubulin can both diffuse in and be transported into the cilium (Craft et al., 2015; Hao et al., 2011; Luo et al., 2017).

In our *in vitro* assays, we combined certain concentrations of each protein to generate extremely slow growing microtubules. It will be interesting to find out how the concentration and stoichiometry of the CTM proteins are controlled in cells, because this regulation will be

quite complicated. CTM proteins are very potent in their ability to bind to microtubules, but under native conditions they have not been observed to localize to cytoplasmic microtubules. In ciliated cells, the CTM proteins will most likely be directly imported into the cilia resulting in a low cytoplasmic concentration. When proteins are required in the cilium, they are trafficked to the transition zone. There, they must enter the cilium via active transport. This is facilitated by intraflagellar transport (IFT) (Pigino, 2021). In non-ciliated cells, some CTM proteins have been found to localize to centrosomes or centriolar satellites (Conkar et al., 2017; Jiang et al., 2012; Patzke et al., 2010; Patzke et al., 2006). Aside from microtubule binding domains, these proteins contain domains with affinity for these other cellular structures, potentially to concentrate them near the location for subsequent cilia assembly. The specific affinity of the various domains for certain cellular structures can be tuned by PTMs or complex formation with other proteins, like trafficking proteins. This could explain why the CTM proteins have not been localized to cytoplasmic microtubules. Within cilia, it will also be interesting to study the stoichiometry of CTM proteins at the tip of axonemal microtubules. So far, it is unclear whether all five components form one big complex or some transient assemblies. The latter could be regulated by addition or removal of PTMs, binding and unbinding to other proteins, or even by the amount of available tubulin. These types of regulation are difficult or impossible to reconstitute *in vitro*. However, it would be possible to study the effects of changing tubulin concentration, and mutation or deletion constructs on the contribution of each protein to the collective effect of generating processive, slowly growing microtubules.

Microtubule inner proteins

Until recently, studies of microtubule stabilization have been mainly focused on proteins that are binding to the microtubule outer surface. Now, it is becoming increasingly clear that MIPs also contribute to microtubule stability. Historically, globular densities inside microtubules have been observed by conventional electron microscopy studies, but their level of detail was not sufficient for identification. Early technical advances using cryo-electron tomography and image processing revealed MIPs in both tubules of axonemal doublets in motile cilia such as in sperm of sea urchins and axonemes of *Chlamydomonas reinhardtii*, and cytoplasmic microtubules in mammalian cells such as neurons and astrocytes (Garvalov et al., 2006; Nicastro et al., 2006; Sui and Downing, 2006). Low resolution density maps combined with biochemical techniques such as mass spectrometry analysis and the use of mutants revealed the identity of some MIPs (Ichikawa et al., 2019; Kirima and Oiwa, 2018; Owa et al., 2019; Stoddard et al., 2018). Increase in the resolution of density maps revealed an additional class of MIPs termed filamentous MIPs (Ichikawa et al., 2017). More recent advances in structural analysis generated density maps with nanometer and sub-nanometer resolution, which enabled the identification of MIPs, particularly in motile cilia and flagella (Gui et al., 2021; Ma et al., 2019). These studies only revealed MIPs that are present in a repetitive pattern, usually referred to as structural MIPs, as non-repetitive MIPs were lost during subtomogram averaging needed to increase the resolution of the density maps. Compared to motile cilia and flagella, MIPs in primary cilia were only found sporadically and their identity is unknown (Kiesel et al., 2020). The difference between the number of luminal densities between primary and motile cilia could be due to two reasons. First, motile cilia need to generate and withstand more force and therefore microtubules are required to be more stable. Stability can be provided by MIPs, by binding between protofilaments or bridging two tubulin subunits, and by recruiting of stabilizing MAPs on the microtubule surface (Ichikawa et al., 2019; Ichikawa et al., 2017; Maheshwari et al., 2015). Second, the majority of the axonemal length in motile cilia consists of microtubule doublets, while primary cilia have recently been shown to mainly consist of microtubule singlets (Kiesel et al., 2020). MIPs that specifically bind to

the B-tubule lumen or are in the A-tubule to support B-tubule formation and stabilization are less important in primary cilia. Nevertheless, primary cilia need to be stabilized to reach the correct length for their role in signal processing.

In **Chapter 3**, we studied ciliary protein CSPP1 and found that its localization and behavior on reconstituted microtubules was similar to a class of microtubule stabilizing agents called taxanes. Taxanes have been identified to bind to the luminal side of microtubules and we investigated if this was also true for CSPP1 (Nogales et al., 1995; Steinmetz and Prota, 2018). We used cryo-electron tomography and MINFLUX microscopy techniques on *in vitro* reconstituted microtubules to show that CSPP1 indeed binds to the microtubule lumen. We observed globular densities inside fully closed tubes, and microtubule tip raggedness was reduced, suggesting that CSPP1 might stabilize lateral interactions between protofilaments. These results, together with our observation that CSPP1 accumulations occurred at microtubules that undergo growth perturbations, suggest that CSPP1 only affects the microtubule tip. Additionally, we did not observe alterations in the microtubule lattice structure in presence of CSPP1. This is different from a neuronal MIP MAP6. MAP6 has been known to stabilize neuronal microtubules against drug- and cold-induced depolymerization (Delphin et al., 2012; Guillaud et al., 1998; Job et al., 1987). Investigation of MAP6 using *in vitro* reconstituted microtubules revealed that it alters the microtubule lattice by triggering microtubule coiling and induces lattice apertures (Cuveillier et al., 2020). CSPP1 and MAP6 do share similarities as well. Similar to CSPP1, MAP6 reduces microtubule shrinkage, promotes rescues, and contains a short domain that can perturb processive microtubule growth (Cuveillier et al., 2020). For MAP6, the deletion of this short domain resulted in binding to the microtubule outer surface, while we have not seen any indications that CSPP1 can bind to the microtubule outer surface. It is still possible that some parts of CSPP1 are extending out of microtubules, like has been shown for some MIPs in motile cilia and flagella (Gui et al., 2021; Ichikawa et al., 2019; Ichikawa et al., 2017; Ma et al., 2019). This could be a mechanism to connect to proteins that are located at the microtubule outer surface.

In **Chapter 4**, we studied the combined effects of CSPP1 and its interaction partners of the CTM. CSPP1 and CEP104 were previously shown to interact directly, and their intraciliary interaction is required for the control of ciliary length and functional Hedgehog signaling (Frikstad et al., 2019). As discussed above, we found that CEP104 can block microtubule plus-end outgrowth, and this could be potentiated by EBs and CSPP1. EBs localize to the outer microtubule surface (Maurer et al., 2012; Zhang et al., 2015), also confirmed in primary cilia (Kiesel et al., 2020), and CEP104 could potentially bind to the outer microtubule surface based on the presence of a TOG domain. TOG domain proteins usually contain a positively charged domain which is proposed to be interacting with the negatively charged C-terminal tails on the microtubule outer surface (Al-Bassam et al., 2010; Brouhard et al., 2008). However, there is no structural evidence for this, and our results showed that CEP104 is not acting like a traditional TOG domain protein. Additionally, we showed that CSPP1 is binding to the microtubule lumen (**Chapter 3**). Thus, CEP104 could be binding to the microtubule lumen, to the outer surface or span both. This raises the question whether CEP104 can bind to CSPP1 and EBs simultaneously. If this is the case, and CEP104 would bind on the outer microtubule surface, this could potentially be in a similar fashion as the interaction between centriolar capping proteins CPAP and CP110. CPAP contains two tubulin-binding domains, one that binds to the exposed surface of β -tubulin to prevent the addition of new tubulin dimers (termed LID domain) and another one that mediates binding to the outer surface of microtubule plus ends (Sharma et al., 2016; Zheng et al., 2016). CPAP interacts with CP110, and it has been shown to potentiate microtubule growth inhibition by CP110 (Ogunmolu et al., 2021). CP110 has been localized at the luminal side of the microtubule plus end (Ogunmolu et al., 2021). Both proteins bind to the microtubule tip, but at different regions. The binding

site of CPAP for CP110 is at the end of the LID domain that extends in the direction of the microtubule lumen, likely facilitating the interaction of two proteins binding on the opposite sides of the microtubule wall. Comparing this interaction with CEP104 and CSPP1, CEP104 could be localizing like CPAP to inhibit tubulin addition or facilitate tubulin removal, and CSPP1 would then be localizing like CP110 (Fig. 3A). However, we previously observed CSPP1 deeper into the microtubule lumen compared to CP110. Therefore, it is also possible that the CEP104-binding domain of CSPP1 could protrude through the microtubule wall (Fig. 3B). Interactions of MIP domains with MAPs across the tubulin lattice have previously been shown for certain MIPs in doublets of motile cilia (Gui et al., 2021; Ichikawa et al., 2019; Ichikawa et al., 2017; Ma et al., 2019). Another possibility is that CEP104 binds at the luminal side, but potentially mirrored compared to CPAP binding (Fig. 3C). This way, CEP104 could reach CSPP1 for interaction after it has been recruited to the microtubule tip by EBs. CSPP1 also directly interacts with ARMC9 (Latour et al., 2020), and we showed that presence of ARMC9 extends the duration of CSPP1-induced pauses. ARMC9 interacts with the other TOG domain protein of the CTM, TOGARAM1 (Latour et al., 2020). Is one of the scenarios described above for CEP104 also fitting for the combination of these three proteins? If so, can they bind simultaneously to CEP104 as well? We found that the fifth member of the CTM, CCDC66, potentiates growth inhibition of CEP104. On which side of the microtubule does CCDC66 bind, and can all five proteins form one big complex? Structural information will hopefully provide more understanding about the geometry of the CTM at microtubule plus

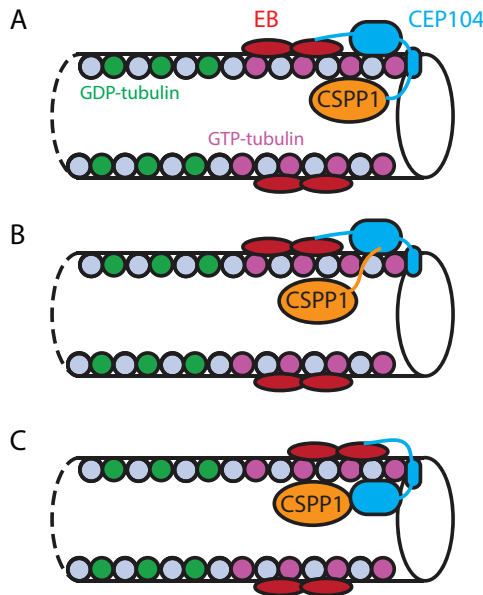


Figure 3: Potential configurations of simultaneous binding between EB, CEP104 and CSPP1.

CEP104 localizes to the microtubule to prevent tubulin addition and potentially blocks tubulin addition at the exposed β -tubulin site. It can bind to EB with its C-terminal 5xIP-domain and to CSPP1 with its N-terminal domain. (A,B) CEP104 potentially binds to the microtubule outer surface and reaches CSPP1 around the tip (A) or binds to CSPP1 via the CSPP1-domain that is protruding through the microtubule lattice (B). (C) CEP104 could also bind to the inner surface, where it binds CSPP1 in the lumen and binds to EBs around the tip.

ends. Moreover, it will be interesting to find out the exact arrangement of CTM proteins in primary cilia.

Interestingly, some orthologs of the CTM proteins have been localized to a specific tubule in microtubule doublets in motile cilia of *Tetrahymena thermophila*. The orthologs of ARMC9 and TOGARAM1, ARMC9A and CHE-12 respectively, have been localized near the ends of B-tubules (Louka et al., 2018). This indicates that they prefer binding to the incomplete microtubules. The ortholog of CEP104, FAP256A, localizes to the ends of A-tubules and the central pair, indicating its preference for complete microtubules (Louka et al., 2018). ARMC9A and CHE-12 are spatially separated from FAP256A, suggesting they do not form a stable complex, or at least not in steady-state cilia. However, in the primary cilium they are found to be part of one complex localized at the ciliary tip. Additionally, the tips of primary cilia only contain A-tubules, indicating that the preference of ARMC9A and CHE-12 for B-tubules in motile cilia may be regulated by other factors. CSPP1 has also been localized to the tip of motile cilia, but its preference for any of the tubules is not known (Frikstad et al., 2019). Nothing is known about the presence of CCDC66 in motile cilia. It will be interesting to investigate whether the complete CTM is present during doublet elongation. Additionally, more research is required to find out if CSPP1 localizes to one or both doublet microtubules in motile cilia. It has not been identified as a MIP in the two recent MIP mapping studies (Gui et al., 2021; Ma et al., 2019), but it is possible that CSPP1 does not bind in a repetitive pattern, and therefore was lost during subtomogram averaging, or CSPP1 could be only present at the ciliary tip. Advances in microscopy and structural analysis are desired to meet the required resolution to identify other ciliary proteins that do not bind in a repetitive pattern.

Microtubule damage and repair

MIPs need to access the microtubule lumen for binding and to execute their function. They can enter microtubules at the growing ends, or they can move through regular lattice fenestrations if they are small enough. Bigger proteins can also enter the lumen when one or more tubulin dimers are missing in the lattice, for example due to a damage event. Loss of microtubule lattice integrity can be caused by spontaneous tubulin dissociation, severing enzymes, molecular motors, protofilament number mismatch, or mechanical stress (Andreu-Carbó et al., 2022; Aumeier et al., 2016; Budaitis et al., 2022; de Forges et al., 2016; Rai et al., 2021; Schaedel et al., 2015; Schaedel et al., 2019; Triclin et al., 2021; Vemu et al., 2018). Microtubules with damage sites can become unstable and undergo catastrophe quickly, or damage sites can get stabilized or repaired and this increases the lifetime of the microtubule. Microtubules get repaired by the incorporation of GTP-tubulin, which creates a so-called GTP-island (de Forges et al., 2016; Dimitrov et al., 2008; Vemu et al., 2018). Tubulin incorporation can occur spontaneously or be facilitated by MAPs (Aher et al., 2020; Aumeier et al., 2016; Schaedel et al., 2015; Schaedel et al., 2019). Depolymerizing microtubules can get rescued at these repair sites and start re-growing.

Microtubule damage sites can be compared to microtubule plus ends, because in both cases, microtubule protofilament ends are exposed for the addition of new GTP-tubulin dimers. Similar to microtubule plus-end elongation, lattice repair only requires the presence of tubulin, but MAPs can promote or regulate the repair. Plus-end tracking proteins like CLIP-170 and EB1 have been shown to be recruited to the damage sites (de Forges et al., 2016; Vemu et al., 2018). In [Chapter 3](#), we found that CSPP1 accumulated at microtubule ends which grow slowly or undergo growth perturbations. Additionally, we discovered that CSPP1 binds to the microtubule lumen. Therefore, we wondered if CSPP1 specifically binds to exposed luminal sites. To answer this question, we investigated if CSPP1 could enter the lumen at microtubule damage sites. We showed that CSPP1 prefers binding to Taxol-

5

stabilized microtubules which are known to have large defects when incubated without soluble tubulin (Aher et al., 2020; Arnal and Wade, 1995). Laser microsurgery experiments both *in vitro* and cells showed strong accumulation of CSPP1 signal at the illuminated sites. Next, we wondered if CSPP1 would be involved in the stabilization or repair of the induced damages. Comparison of microtubule lattices grown in the presence of vinblastine with or without CSPP1 by cryo-electron tomography showed many defects in the absence of CSPP1, but hardly any defects were observed in presence of CSPP1. Additionally, CSPP1 densities were mainly observed within complete tubes. This shows that CSPP1 does not stabilize lattice defects, like has been shown for Taxol (Rai et al., 2020), but promotes lattice repair. In absence of soluble tubulin, CSPP1 was not able to prevent the erosion of Taxol-stabilized seeds, but presence of low tubulin concentrations (2-5 μM) prevented depolymerization and even facilitated microtubule outgrowth. We think that CSPP1 is not directly adding tubulin dimers to the exposed microtubule ends, otherwise it would not induce pauses upon binding to the pre-catastrophe state. Instead, we think that it promotes microtubule lattice integrity by stabilizing protofilament ends close to the damage site or pre-catastrophe state. Tubulin dimers in a microtubule lattice can interact longitudinally, meaning the head-to-tail interaction between the α -tubulin of one tubulin dimer to the β -tubulin of another tubulin dimer within the same protofilament (Brouhard and Rice, 2018). Additionally, tubulin dimers of one protofilament can interact laterally with tubulin dimers of the neighboring protofilament. This creates a well-organized tube of protofilaments to achieve microtubule lattice integrity. In the case of microtubule damage or pre-catastrophe state, lateral contacts between protofilaments are weakened or lost which leads to a decrease in microtubule lattice integrity. Because we observed a reduction of protofilament raggedness, a measure for the heterogeneity in the positions where protofilaments at the microtubule tip start curving away from the tube, we think that CSPP1 could span multiple protofilaments on the luminal side to promote lateral interactions. It will be interesting to determine how CSPP1 is binding to the protofilaments at the luminal side to provide stability.

To date, only a few proteins have been identified to be involved in damage site recognition or microtubule lattice repair. Apart from its role in microtubule anchoring at the cell cortex (described in [Chapter 2](#)), mammalian CLASPs are capable of mediating microtubule repair by regulating tubulin incorporation (Aher et al., 2020). CLASPs are TOG domain proteins, which, like CEP104 and TOGARAM1 discussed above ([Chapter 4](#)), do not match the standard characteristics of canonical microtubule polymerases. Like TOGARAM1, CLASPs have been shown to slow down microtubule growth rate (Aher et al., 2018). Additionally, a single TOG domain of CLASP2 α was sufficient to suppress microtubule catastrophes. However, unlike TOG domains from canonical microtubule polymerases, this domain does not bind to free tubulin dimers (Aher et al., 2018). Catastrophe inhibition is achieved by the ability of CLASPs to stabilize an incomplete set of protofilaments to promote recovery into a complete tube (Aher et al., 2018). Experiments where microtubule damage was induced by laser ablation or where Taxol-stabilized microtubules were used, showed increased length of new tubulin incorporation areas at damage sites in the presence of CLASP2 α (Aher et al., 2020). This indicates that CLASP2 α mediates the complete closure of lattice defects, potentially via a mechanism similar to that of catastrophe inhibition. CLASPs and CSPP1 show similar mechanisms of stabilization of incomplete sets of protofilaments. However, CSPP1 induces stabilization from luminal side, while CLASPs probably act at the outer microtubule surface, because their recruitment to microtubules is promoted by EBs. Additionally, their microtubule localization pattern in cells is very distinct as CSPP1 localizes to ciliary microtubules while CLASPs localize to cytoplasmic microtubules (Ishikawa et al., 2012).

SSNA1 is a protein which localizes to the ciliary axoneme, and it is required for proper cilium assembly and intraflagellar transport, and it also functions in dividing cells and

developing neurons (Basnet et al., 2018; Lawrence et al., 2021). It is a small, fibrillar protein which can assemble in large fibrils which have been proposed to be important for microtubule branching (Basnet et al., 2018), although it is uncertain that microtubules can indeed branch in cells. Additionally, SSNA1 has recently been shown to detect microtubule damages which occur naturally, or those that are induced by severing enzymes like spastin (Lawrence et al., 2021). Damage recognition of SSNA1 has only been shown *in vitro*, while we have shown that CSPP1 can recognize damages in cells as well. The main difference between SSNA1 and CSPP1 is that CSPP1 is much more potent in damage recognition as low concentrations of 5-10 nM already showed strong effects, while SSNA1 required concentrations of 0.5-5 μM for detection. Additionally, it is not known yet if SSNA1 also mediates microtubule repair or if it is stabilizing the damage sites. We showed that CSPP1 promotes microtubule repair *in vitro*, but it remains to be determined if it can exert a similar activity in cells.

The ability of CSPP1 to recognize damage sites in cells might provide an opportunity to use it as a marker for damage and repair sites. As mentioned above, there are many different ways in which microtubule damage can occur in cells. However, inducing and detecting microtubule damage and potential repair in live cells is challenging. Damage can be induced by laser irradiation, which we have done for CSPP1 (Chapter 3), but this approach can also damage other cellular components resulting in artefacts. Overexpression of severing enzymes is another possibility, but this usually results in the generation of new microtubule ends. Recently, a kinesin-1 variant was shown to induce microtubule damage while stepping along tubulin subunits (Budaitis et al., 2022). High expression of this motor protein resulted in microtubule breakage and appearance of small microtubule fragments, but at low expression it could be employed to induce microtubule damage without disrupting other cellular compartments. Microtubule repair in cells has been demonstrated with the use of a photoconvertible fluorescent probe to be able to distinguish polymerized dimers from free soluble tubulin dimers that can incorporate (Aumeier et al., 2016). Conversion of the probe in a small region in the cytoplasmic showed that differently colored spots appeared on pre-existing microtubules suggesting the incorporation of new tubulin dimers. This was repeated *in vitro* where, in the absence of MAPs, occasional incorporation of new tubulin dimers was observed along the microtubule. Thus, tubulin incorporation in the microtubule lattice can occur in the absence of MAPs, which makes it difficult to determine in cells when specific MAPs are involved in this process. Additionally, it is not possible to distinguish the size of the damage or incorporation site due to the resolution limit of light microscopy. CSPP1 could potentially be used to address some of the questions on microtubule damage and repair. CSPP1 is a large protein which can only bind to the microtubule lumen if the damage is sufficiently large for it to enter. Combination of photoconvertible tubulin and CSPP1 could show a distinction between smaller and large defects.

Microtubule damage and repair is not limited to cytoplasmic microtubules, but potentially also occurs in cilia. As described before, ciliary microtubules contain many MIPs. These MIPs are identified to be structural MIPs, and they probably reach the microtubule lumen via the tip during cilia assembly. However, there are also non-structural MIPs that gain access to the lumen via the ciliary tip but have also been shown to be able to enter by travelling across the microtubule lattice wall. One example is the enzyme αTAT1 , which catalyzes the addition of an acetyl group to a specific lysine at the luminal side of α -tubulin. Ciliary microtubules are strongly acetylated, and αTAT1 specifically modifies α -tubulins in polymerized microtubules, meaning it has to be able to access the microtubule lumen (Shida et al., 2010). It was shown that αTAT1 can enter the microtubule lumen through the microtubule ends, as well as through bends or breaks in the microtubule lattice (Coombes et al., 2016). Thus, apart from entry via the ciliary tip, αTAT1 might enter axonemal microtubules via damage sites. This could be particularly relevant for motile cilia, as these cilia bend extensively to generate movement.

Axonemal microtubule damage could also be induced by motor proteins. Motor proteins have been shown to induce damage to the microtubule lattice when they use them as tracks for cargo transport. In cilia, virtually all components must be transported inside and along axonemal microtubules. This is mediated by intraflagellar transport, specifically by kinesin-2 and cytoplasmic dynein (Pigino, 2021). Whether these motor proteins can indeed induce damage to axonemal microtubules remains to be determined. To function properly, cilia need to be stable, and the preceding examples show why presence of ciliary proteins, which can stabilize and repair microtubules like CSPP1 and potentially SSNA1, could be important. It remains to be investigated if CSPP1 can recognize microtubule defects in cilia and if it can promote lattice integrity. Additionally, studying the occurrence of lattice defects and their correlation with mutations in ciliopathy-linked proteins could provide more insight into disease mechanism and potential remedies.

Scaffolding proteins

5 Protein complexes contain components with highly variable functions and often contain proteins that connect the other complex components together and insure complex stability. Such proteins are often referred to as scaffolds. Scaffolds can play a role in the regulation of signaling pathways or by recruitment of interaction partners to specific cellular compartments. In **Chapter 2**, we studied the clustering of secretory complexes at the cell cortex in insulin secreting cells by investigating the dynamics of a multivalent protein ELKS. ELKS was previously found to localize at the cytomatrix at the active zone in neurons and at the cell cortex as part of the cortical microtubule stabilizing complex (CMSC) (Bouchet et al., 2016). Studies showed that interaction of ELKS with LL5 β is essential for its cortical recruitment, but ELKS is required for the clustering of LL5 β and the other members of the CMSC (Lansbergen et al., 2006; van der Vaart et al., 2013). In neurons, it has been suggested that the cytomatrix at the active zone could be formed by liquid-liquid phase separation (LLPS), driven by the key players including ELKS (Emperador-Melero et al., 2021; Liang et al., 2021; Sala et al., 2019; Wu et al., 2019; Wu et al., 2021). LLPS leads to the formation of membraneless organelles, also called condensates or droplets, where multicomponent cellular mixtures de-mix into two distinct liquid phases with different compositions. Condensate components can be broadly divided into scaffolds and clients, where the former can self-associate into condensates, and the latter are dispensable for condensate formation but are recruited through their interactions with the scaffolds (Banani et al., 2016). We investigated whether the clustering of cortical complexes in pancreatic β -cells was driven by LLPS. We isolated pancreatic islets from mice bearing a GFP knock-in in the gene encoding ELKS and studied the dynamics of ELKS at the cell cortex in live islets. We showed that ELKS-cluster turnover was stimulated after glucose addition and that individual ELKS molecules moved at the same rate as the clusters which were much slower than cytoplasmic diffusion. This suggests that ELKS molecules at the cell cortex bind to a low-mobility scaffold rather than form liquid condensates. Additionally, we found the majority of clusters consisted of only two to four ELKS-dimers and thus are too small to constitute condensates. We have not investigated the nature of the low-mobility scaffold, so future research is required for its identification and its implications in insulin secretion.

In **Chapter 4**, we studied the components of the CTM, some of which have been shown to localize to centriolar satellites. Centriolar satellites are non-membranous structures which localize close to the centrosome and play a role in the regulation of cargo trafficking to the centrosome and the primary cilium. The main component of centriolar satellites is PCM1, because knockdown of PCM1 results in the absence of centriolar satellites (Hori and Toda, 2017). Increasing numbers of proteins have been identified to localize to centriolar satellites, including CCDC66 and CSPP1 (Conkar et al., 2017; Patzke et al., 2010; Quarantotti et al., 2019).

For these proteins, localizing to centriolar satellites could have a dual role: it could prevent them from binding to cytoplasmic microtubules and provide storage to the components that can be mobilized to initiate cilia assembly. ARMC9, CEP104 and TOGARAM1 were not found to be part of centriolar satellites (Gheiratmand et al., 2019; Quarantotti et al., 2019). Centriolar satellite formation may involve LLPS, as satellite dispersal in mitosis is driven by the kinase DYRK3 which was shown to promote dissolution of multiple membraneless organelles (Rai et al., 2018; Zwicker et al., 2014). Proteins that have been found to induce LLPS often contain intrinsically disordered regions (IDRs) which can self-assemble (Boeynaems et al., 2018; Holehouse and Pappu, 2018). Structure prediction showed that CCDC66 contains multiple intrinsically disordered regions, indicating it has potential to induce LLPS (Hu et al., 2021). Knockdown of CCDC66 resulted in smaller and more dispersed satellites, contributing to this idea (Conkar et al., 2022). Interestingly, CSPP1 does not contain IDRs suggesting that it gets assembled into centriolar satellites via interaction partners.

CCDC66 has the potential to induce LLPS and it could act as a scaffold in the CTM. CCDC66 was previously shown to directly interact with ARMC9, but not with the other CTM components. However, both *in vitro* experiments and co-overexpression of ARMC9 and CCDC66 in COS-7 cells, did not show interaction or colocalization between the two proteins. Interestingly, we found that CCDC66 is linked to the other CTM proteins via its interaction with CEP104. CCDC66 potentiated the microtubule growth inhibiting activity of CEP104, similar to CSPP1, and microtubule growth inhibition was even more pronounced when the three proteins were mixed together. CSPP1 and TOGARAM1 were previously identified to directly interact with ARMC9 (Latour et al., 2020). We confirmed that ARMC9 cannot bind to microtubules on its own, but it can be recruited to microtubules by mCrescerin1 and CSPP1. ARMC9 did not affect the behavior of mCrescerin1 but increased the duration of CSPP1-induced pauses. mCrescerin1 and CSPP1 did not directly interact, but their combined presence slowed down microtubule growth rate compared to mCrescerin1 alone and reduced the number and duration of CSPP1-induced pauses compared to CSPP1 alone. Microtubule growth rate was slowed down even further when ARMC9 was added, showing it potentially links CSPP1 and mCrescerin1 thereby acting like a scaffold. Alternatively, ARMC9 could directly affect microtubule dynamics but requires a specific recruitment factor to execute its function.

CCDC66 and ARMC9 have the potential to act as scaffolds within the CTM. As the CTM has been localized to the tip of primary cilia, it will be interesting to elucidate the CTM protein interactions at the tip as well as the tip structure. Condensate formation at dynamic microtubule ends has recently been shown for microtubule end-binding proteins CLIP-170 and EB3 (Miesch et al., 2022). Experiments *in vitro* and in cells showed that CLIP-170 can induce LLPS and co-condense tubulin on its own, while for EB3 this was only shown *in vitro* (Miesch et al., 2022). Together, these proteins increased microtubule growth rate and reduced catastrophe and pausing frequencies at the microtubule plus end *in vitro* (Miesch et al., 2022). In contrast, we observed reduction in catastrophe and pausing frequencies as well as slow microtubule growth rates in the presence of CTM proteins. It is possible that tubulin is excluded from CTM condensates. We currently do not have evidence that the CTM can form condensates, but this could be studied by experiments using Fluorescence Recovery after Photobleaching (FRAP). Alternatively, microtubules themselves could act like a scaffold to recruit the different components, and complex formation could be strengthened by inter-protein interactions. Microtubules could act as low-mobility scaffolds, similar to the unidentified scaffold recruiting ELKS and the other CMSC components as described above. Future studies will reveal the structure and composition of ciliary tips and show whether LLPS plays a role in the formation of protein complexes controlling the dynamics of axonemal microtubules.

Concluding remarks

In this thesis, we studied two multi-protein assemblies which are involved in microtubule plus-end stabilization in cells and *in vitro*. We showed that individual proteins are involved in microtubule plus-end anchoring, pausing, rescue, growth or catastrophe inhibition, but their function depends on their collective action. This illustrates why a single mutation in one of the complex components can result in diseases with symptoms ranging from very mild to extremely severe. Together, our studies contribute to the understanding how individual proteins and their complexes interacting with microtubules regulate insulin secretion and ciliary length. In addition to fundamental insights, our work can contribute to devising new strategies to treat type 2 diabetes and Joubert syndrome.

References

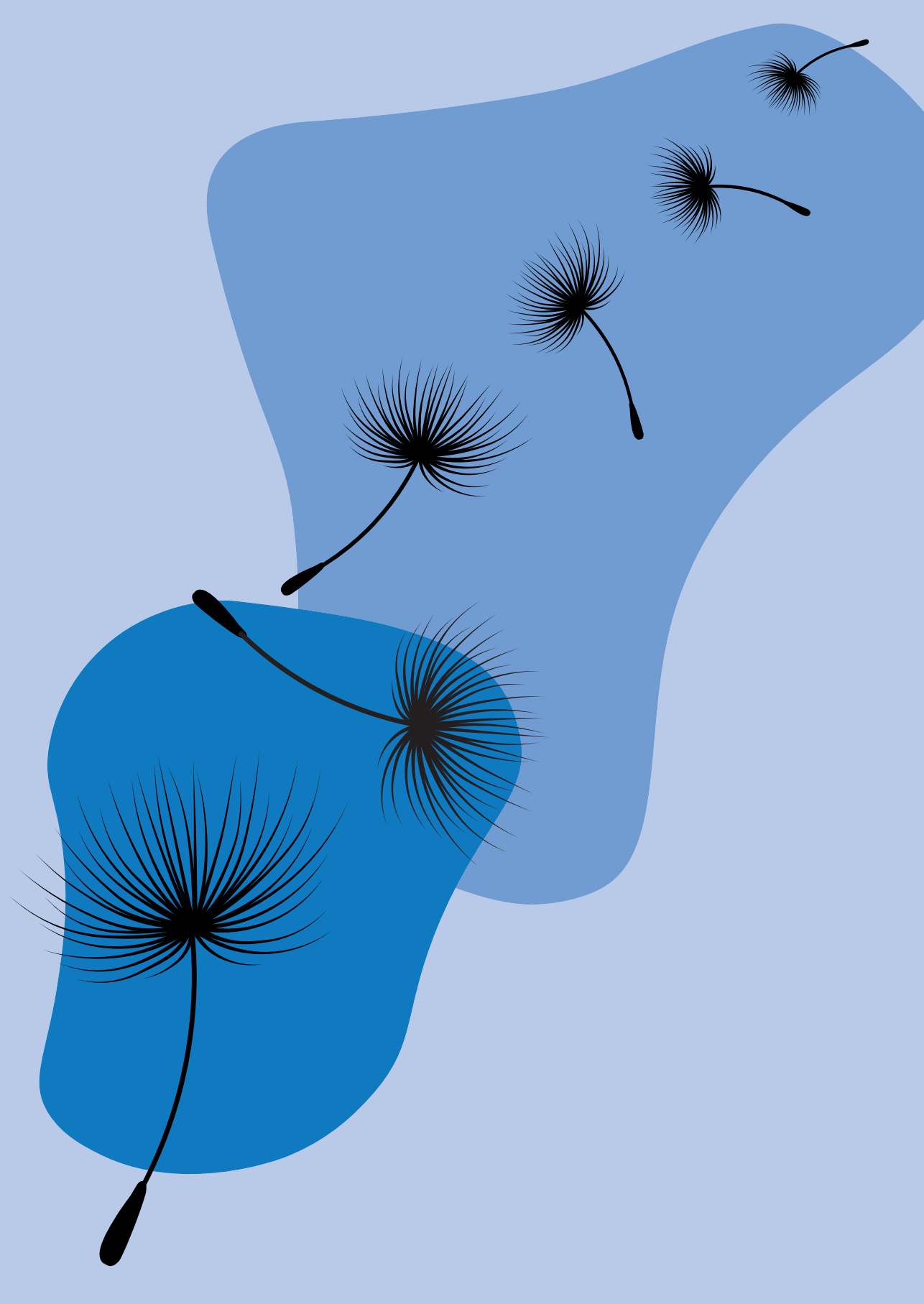
- Aher, A., M. Kok, A. Sharma, A. Rai, N. Olieric, R. Rodriguez-Garcia, E.A. Katrukha, T. Weinert, V. Olieric, L.C. Kapitein, M.O. Steinmetz, M. Dogterom, and A. Akhmanova. 2018. CLASP Suppresses Microtubule Catastrophes through a Single TOG Domain. *Dev Cell*. 46:40-58.
- Aher, A., D. Rai, L. Schaedel, J. Gaillard, K. John, Q. Liu, M. Altelaar, L. Blanchoin, M. Thery, and A. Akhmanova. 2020. CLASP Mediates Microtubule Repair by Restricting Lattice Damage and Regulating Tubulin Incorporation. *Curr Biol*. 30:2175-2183.
- Akhmanova, A., and L.C. Kapitein. 2022. Mechanisms of microtubule organization in differentiated animal cells. *Nat Rev Mol Cell Biol*. 23:541-558.
- Al-Bassam, J., H. Kim, G. Brouhard, A. van Oijen, S.C. Harrison, and F. Chang. 2010. CLASP promotes microtubule rescue by recruiting tubulin dimers to the microtubule. *Dev Cell*. 19:245-258.
- Al-Bassam, J., M. van Breugel, S.C. Harrison, and A. Hyman. 2006. Stu2p binds tubulin and undergoes an open-to-closed conformational change. *J Cell Biol*. 172:1009-1022.
- Al-Jassar, C., A. Andreeva, D.D. Barnabas, S.H. McLaughlin, C.M. Johnson, M. Yu, and M. van Breugel. 2017. The Ciliopathy-Associated Cep104 Protein Interacts with Tubulin and Nek1 Kinase. *Structure*. 25:146-156.
- Andreu-Carbó, M., S. Fernandes, M.C. Velluz, K. Kruse, and C. Aumeier. 2022. Motor usage imprints microtubule stability along the shaft. *Dev Cell*. 57:5-18.e18.
- Arnal, I., and R.H. Wade. 1995. How does taxol stabilize microtubules? *Curr Biol*. 5:900-908.
- Arous, C., and P.A. Halban. 2015. The skeleton in the closet: actin cytoskeletal remodeling in beta-cell function. *Am J Physiol Endocrinol Metab*. 309:E611-620.
- Arous, C., D. Rondas, and P.A. Halban. 2013. Non-muscle myosin IIA is involved in focal adhesion and actin remodeling controlling glucose-stimulated insulin secretion. *Diabetologia*. 56:792-802.
- Aumeier, C., L. Schaedel, J. Gaillard, K. John, L. Blanchoin, and M. Thery. 2016. Self-repair promotes microtubule rescue. *Nat Cell Biol*. 18:1054-1064.
- Banani, S.F., A.M. Rice, W.B. Peeples, Y. Lin, S. Jain, R. Parker, and M.K. Rosen. 2016. Compositional Control of Phase-Separated Cellular Bodies. *Cell*. 166:651-663.
- Basnet, N., H. Nedozralova, A.H. Crevenna, S. Bodakuntla, T. Schlichthaerle, M. Taschner, G. Cardone, C. Janke, R. Jungmann, M.M. Magiera, C. Biertumpfel, and N. Mizuno. 2018. Direct induction of microtubule branching by microtubule nucleation factor SSNA1. *Nat Cell Biol*. 20:1172-1180.
- Boeynaems, S., S. Alberti, N.L. Fawzi, T. Mittag, M. Polymenidou, F. Rousseau, J. Schymkowitz, J. Shorter, B. Wolozin, L. Van Den Bosch, P. Tompa, and M. Fuxreiter. 2018. Protein Phase Separation: A New Phase in Cell Biology. *Trends Cell Biol*. 28:420-435.
- Bouchet, B.P., R.E. Gough, Y.C. Ammon, D. van de Willige, H. Post, G. Jacquemet, A.M. Altelaar, A.J. Heck, B.T. Goult, and A. Akhmanova. 2016. Talin-KANK1 interaction controls the recruitment of cortical microtubule stabilizing complexes to focal adhesions. *eLife*. 5:e18124.
- Bracey, K.M., K.H. Ho, D. Yampolsky, G. Gu, I. Kaverina, and W.R. Holmes. 2020. Microtubules Regulate Localization and Availability of Insulin Granules in Pancreatic Beta Cells. *Biophys J*. 118:193-206.
- Breslow, D.K., and A.J. Holland. 2019. Mechanism and Regulation of Centriole and Cilium Biogenesis. *Annu Rev Biochem*. 88:691-724.
- Brouhard, G.J., and L.M. Rice. 2018. Microtubule dynamics: an interplay of biochemistry and mechanics. *Nat Rev Mol Cell Biol*. 19:451-463.
- Brouhard, G.J., J.H. Stear, T.L. Noetzel, J. Al-Bassam, K. Kinoshita, S.C. Harrison, J. Howard, and A.A. Hyman. 2008. XMAP215 is a processive microtubule polymerase. *Cell*. 132:79-88.
- Budaitis, B.G., S. Badiyan, Y. Yue, T.L. Blasius, D.N. Reinemann, M.J. Lang, M.A. Cianfrocco, and K.J. Verhey. 2022. A kinesin-1 variant reveals motor-induced microtubule damage in cells. *Curr Biol*. 32:2416-2429.e2416.
- Campanacci, V., A. Urvoas, L. Ammar Khodja, M. Aumont-Nicaise, M. Noiray, S. Lachkar, P.A. Curmi, P. Minard, and B. Gigant. 2022. Structural convergence for tubulin binding of CPAP and vinca domain microtubule inhibitors. *Proc Natl Acad Sci U S A*. 119:e2120098119.
- Conkar, D., E. Culfa, E. Odabasi, N. Rauniyar, J.R. Yates, and E.N. Firat-Karalar. 2017. The centriolar satellite protein CCDC66 interacts with CEP290 and functions in cilium formation and trafficking. *J Cell Sci*. 130:1450-1462.
- Conkar, D., E. Odabasi, J. Deretic, U. Batman, K.M. Frikstad, S. Patzke, and E.N. Firat-Karalar. 2022. CCDC66 regulates primary cilium length and signaling competence via multi-site interactions with transition zone and axonemal proteins. *bioRxiv*. 2022.04.10.487777.
- Coombes, C., A. Yamamoto, M. McClellan, T.A. Reid, M. Plooster, G.W. Luxton, J. Alper, J. Howard, and M.K. Gardner. 2016. Mechanism of microtubule lumen entry for the alpha-tubulin acetyltransferase enzyme alphaTAT1. *Proc Natl Acad Sci U S A*. 113:E7176-E7184.
- Craft, J.M., J.A. Harris, S. Hyman, P. Kner, and K.F. Lechtreck. 2015. Tubulin transport by IFT is upregulated during ciliary growth by a cilium-autonomous mechanism. *J Cell Biol*. 208:223-237.

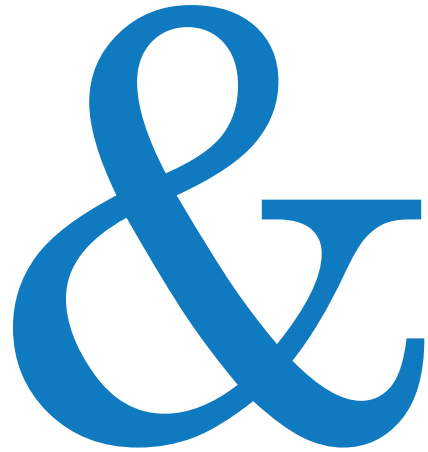
- Cuveillier, C., J. Delaroche, M. Seggio, S. Goryfaure, C. Bosc, E. Denarier, M. Bacia, G. Schoehn, H. Mohrbach, I. Kulic, A. Andrieux, I. Arnal, and C. Delphin. 2020. MAP6 is an intraluminal protein that induces neuronal microtubules to coil. *Sci Adv.* 6:eaz4344.
- Das, A., D.J. Dickinson, C.C. Wood, B. Goldstein, and K.C. Slep. 2015. Crescerin uses a TOG domain array to regulate microtubules in the primary cilium. *Mol Biol Cell.* 26:4248-4264.
- de Forges, H., A. Pilon, I. Cantaloube, A. Pallandre, A.M. Haghiri-Gosnet, F. Perez, and C. Pous. 2016. Localized Mechanical Stress Promotes Microtubule Rescue. *Curr Biol.* 26:3399-3406.
- Delphin, C., D. Bouvier, M. Seggio, E. Couriol, Y. Saoudi, E. Denarier, C. Bosc, O. Valiron, M. Bisbal, I. Arnal, and A. Andrieux. 2012. MAP6-F is a temperature sensor that directly binds to and protects microtubules from cold-induced depolymerization. *J Biol Chem.* 287:35127-35138.
- Dimitrov, A., M. Quesnoit, S. Moutel, I. Cantaloube, C. Pous, and F. Perez. 2008. Detection of GTP-tubulin conformation in vivo reveals a role for GTP remnants in microtubule rescues. *Science.* 322:1353-1356.
- Duellberg, C., N.I. Cade, D. Holmes, and T. Surrey. 2016. The size of the EB cap determines instantaneous microtubule stability. *eLife.* 5:e13470.
- Elie-Caille, C., F. Severin, J. Helenius, J. Howard, D.J. Muller, and A.A. Hyman. 2007. Straight GDP-tubulin protofilaments form in the presence of taxol. *Curr Biol.* 17:1765-1770.
- Emperador-Melero, J., M.Y. Wong, S.S.H. Wang, G. de Nola, H. Nyitrai, T. Kirchhausen, and P.S. Kaeser. 2021. PKC-phosphorylation of Liprin-alpha3 triggers phase separation and controls presynaptic active zone structure. *Nat Commun.* 12:3057.
- Farmer, V., G. Arpağ, S.L. Hall, and M. Zanic. 2021. XMAP215 promotes microtubule catastrophe by disrupting the growing microtubule end. *J Cell Biol.* 220.
- Frikstad, K.M., E. Molinari, M. Thoresen, S.A. Ramsbottom, F. Hughes, S.J.F. Letteboer, S. Gilani, K.O. Schink, T. Stokke, S. Geimer, L.B. Pedersen, R.L.H. Giles, A. Akhmanova, R. Roepman, J.A. Sayer, and S. Patzke. 2019. A CEP104-CSPP1 Complex Is Required for Formation of Primary Cilia Competent in Hedgehog Signaling. *Cell Rep.* 28:1907-1922. e1906.
- Gan, W.J., O.H. Do, L. Cottle, W. Ma, E. Kosobrodova, J. Cooper-White, M. Bilek, and P. Thorn. 2018. Local Integrin Activation in Pancreatic beta Cells Targets Insulin Secretion to the Vasculature. *Cell Rep.* 24:2819-2826.
- Gan, W.J., M. Zavortink, C. Ludick, R. Templin, R. Webb, W. Ma, P. Poronnik, R.G. Parton, H.Y. Gaisano, A.M. Shewan, and P. Thorn. 2017. Cell polarity defines three distinct domains in pancreatic beta-cells. *J Cell Sci.* 130:143-151.
- Garvalov, B.K., B. Zuber, C. Bouchet-Marquis, M. Kudryashev, M. Gruska, M. Beck, A. Leis, F. Frischknecht, F. Bradke, W. Baumeister, J. Dubochet, and M. Cyrklaff. 2006. Luminal particles within cellular microtubules. *J Cell Biol.* 174:759-765.
- Geyer, E.A., M.P. Miller, C.A. Brautigam, S. Biggins, and L.M. Rice. 2018. Design principles of a microtubule polymerase. *eLife.* 7.
- Gheiratmand, L., E. Coyaud, G.D. Gupta, E.M. Laurent, M. Hasegan, S.L. Prosser, J. Gonçalves, B. Raught, and L. Pelletier. 2019. Spatial and proteomic profiling reveals centrosome-independent features of centriolar satellites. *Embo J.* 38:e101109.
- Grigoriev, I., D. Splinter, N. Keijzer, P.S. Wulf, J. Demmers, T. Ohtsuka, M. Modesti, I.V. Maly, F. Grosveld, C.C. Hoogenraad, and A. Akhmanova. 2007. Rab6 regulates transport and targeting of exocytotic carriers. *Dev Cell.* 13:305-314.
- Gui, M., H. Farley, P. Anujan, J.R. Anderson, D.W. Maxwell, J.B. Whitchurch, J.J. Botsch, T. Qiu, S. Meleppattu, S.K. Singh, Q. Zhang, J. Thompson, J.S. Lucas, C.D. Bingle, D.P. Norris, S. Roy, and A. Brown. 2021. De novo identification of mammalian ciliary motility proteins using cryo-EM. *Cell.* 184:5791-5806.
- Guillaud, L., C. Bosc, A. Fourest-Lieuvin, E. Denarier, F. Pirollet, L. Lafanechère, and D. Job. 1998. STOP proteins are responsible for the high degree of microtubule stabilization observed in neuronal cells. *J Cell Biol.* 142:167-179.
- Hao, L., M. Thein, I. Brust-Mascher, G. Civelekoglu-Scholey, Y. Lu, S. Acar, B. Prevo, S. Shaham, and J.M. Scholey. 2011. Intraflagellar transport delivers tubulin isoforms to sensory cilium middle and distal segments. *Nat Cell Biol.* 13:790-798.
- Ho, K.H., X. Yang, A.B. Osipovich, O. Cabrera, M.L. Hayashi, M.A. Magnuson, G. Gu, and I. Kaverina. 2020. Glucose Regulates Microtubule Disassembly and the Dose of Insulin Secretion via Tau Phosphorylation. *Diabetes.* 69:1936-1947.
- Holehouse, A.S., and R.V. Pappu. 2018. Functional Implications of Intracellular Phase Transitions. *Biochemistry.* 57:2415-2423.
- Hori, A., and T. Toda. 2017. Regulation of centriolar satellite integrity and its physiology. *Cell Mol Life Sci.* 74:213-229.
- Hotta, A., T. Kawakatsu, T. Nakatani, T. Sato, C. Matsui, T. Sukezane, T. Akagi, T. Hamaji, I. Grigoriev, A. Akhmanova, Y. Takai, and Y. Mimori-Kiyosue. 2010. Laminin-based cell adhesion anchors microtubule plus ends to the epithelial cell basal cortex through LL5alpha/beta. *J Cell Biol.* 189:901-917.
- Hu, G., A. Katuwawala, K. Wang, Z. Wu, S. Ghadermarzi, J. Gao, and L. Kurgan. 2021. fIDPnn: Accurate intrinsic disorder prediction with putative propensities of disorder functions. *Nat Commun.* 12:4438.
- Ichikawa, M., A.A.Z. Khalifa, S. Kubo, D. Dai, K. Basu, M.A.F. Maghrebi, J. Vargas, and K.H. Bui. 2019. Tubulin lattice in cilia is in a

- stressed form regulated by microtubule inner proteins. *Proc Natl Acad Sci U S A.* 116:19930-19938.
- Ichikawa, M., D. Liu, P.L. Kastritis, K. Basu, T.C. Hsu, S. Yang, and K.H. Bui. 2017. Subnanometre-resolution structure of the doublet microtubule reveals new classes of microtubule-associated proteins. *Nat Commun.* 8:15035.
- Ishikawa, H., J. Thompson, J.R. Yates, 3rd, and W.F. Marshall. 2012. Proteomic analysis of mammalian primary cilia. *Curr Biol.* 22:414-419.
- Jiang, K., G. Toedt, S. Montenegro Gouveia, N.E. Davey, S. Hua, B. van der Vaart, I. Grigoriev, J. Larsen, L.B. Pedersen, K. Bezstarosti, M. Lince-Faria, J. Demmers, M.O. Steinmetz, T.J. Gibson, and A. Akhmanova. 2012. A Proteome-wide screen for mammalian SxIP motif-containing microtubule plus-end tracking proteins. *Curr Biol.* 22:1800-1807.
- Job, D., C.T. Rauch, and R.L. Margolis. 1987. High concentrations of STOP protein induce a microtubule super-stable state. *Biochem Biophys Res Commun.* 148:429-434.
- Kiesel, P., G. Alvarez Viar, N. Tsoy, R. Maraspini, P. Gorilak, V. Varga, A. Honigsmann, and G. Pigino. 2020. The molecular structure of mammalian primary cilia revealed by cryo-electron tomography. *Nat Struct Mol Biol.* 27:1115-1124.
- Kirima, J., and K. Oiwa. 2018. Flagellar-associated Protein FAP85 Is a Microtubule Inner Protein That Stabilizes Microtubules. *Cell Struct Funct.* 43:1-14.
- Kohlmaier, G., J. Loncarek, X. Meng, B.F. McEwen, M.M. Mogensen, A. Spektor, B.D. Dynlacht, A. Khodjakov, and P. Gönczy. 2009. Overly long centrioles and defective cell division upon excess of the SAS-4-related protein CPAP. *Curr Biol.* 19:1012-1018.
- Lansbergen, G., I. Grigoriev, Y. Mimori-Kiyosue, T. Ohtsuka, S. Higa, I. Kitajima, J. Demmers, N. Galjart, A.B. Houtsmuller, F. Grosveld, and A. Akhmanova. 2006. CLASPs attach microtubule plus ends to the cell cortex through a complex with LL5beta. *Dev Cell.* 11:21-32.
- Latour, B.L., J.C. Van De Weghe, T.D.S. Rusterholz, S.J.F. Letteboer, A. Gomez, R. Shaheen, M. Gesemann, A. Karamzade, M. Asadollahi, M. Barroso-Gil, M. Chitre, M.E. Grout, J. van Reeuwijk, S.E.C. van Beersum, C.V. Miller, J.C. Dempsey, H. Morsy, M.J. Bamshad, D.A. Nickerson, S.C.F. Neuhaus, K. Boldt, M. Ueffing, M. Keramatipour, J.A. Sayer, F.S. Alkuraya, R. Bachmann-Gagescu, R. Roepman, and D. Doherty. 2020. Dysfunction of the ciliary ARMC9/TOGARAM1 protein module causes Joubert syndrome. *J Clin Invest.* 130:4423-4439.
- Lawrence, E.J., G. Arpag, C. Arnaiz, and M. Zanic. 2021. SSNA1 stabilizes dynamic microtubules and detects microtubule damage. *eLife.* 10:e67282.
- Liang, M., G. Jin, X. Xie, W. Zhang, K. Li, F. Niu, C. Yu, and Z. Wei. 2021. Oligomerized liprin-alpha promotes phase separation of ELKS for compartmentalization of presynaptic active zone proteins. *Cell Rep.* 34:108901.
- Louka, P., K.K. Vasudevan, M. Guha, E. Joachimiak, D. Wloga, R.F.-X. Tomasi, C.N. Baroud, P. Dupuis-Williams, D.F. Galati, C.G. Pearson, L.M. Rice, J.J. Moresco, J.R. Yates 3rd, Y. Jiang, K. Lechtreck, W. Dentler, and J. Gaertig. 2018. Proteins that control the geometry of microtubules at the ends of cilia. *J Cell Biol.* 217:4298-4313.
- Low, J.T., M. Zavortink, J.M. Mitchell, W.J. Gan, O.H. Do, C.J. Schwiening, H.Y. Gaisano, and P. Thorn. 2014. Insulin secretion from beta cells in intact mouse islets is targeted towards the vasculature. *Diabetologia.* 57:1655-1663.
- Luo, W., A. Ruba, D. Takao, L.P. Zweifel, R.Y.H. Lim, K.J. Verhey, and W. Yang. 2017. Axonemal Lumen Dominates Cytosolic Protein Diffusion inside the Primary Cilium. *Sci Rep.* 7:15793.
- Ma, M., M. Stoyanova, G. Rademacher, S.K. Dutcher, A. Brown, and R. Zhang. 2019. Structure of the Decorated Ciliary Doublet Microtubule. *Cell.* 179:909-922.
- Maheshwari, A., J.M. Obbineni, K.H. Bui, K. Shibata, Y.Y. Toyoshima, and T. Ishikawa. 2015. α - and β -Tubulin Lattice of the Axonemal Microtubule Doublet and Binding Proteins Revealed by Single Particle Cryo-Electron Microscopy and Tomography. *Structure.* 23:1584-1595.
- Marshall, W.F., H. Qin, M. Rodrigo Brenni, and J.L. Rosenbaum. 2005. Flagellar length control system: testing a simple model based on intraflagellar transport and turnover. *Mol Biol Cell.* 16:270-278.
- Maurer, S.P., F.J. Furniol, G. Bohner, C.A. Moores, and T. Surrey. 2012. EBs recognize a nucleotide-dependent structural cap at growing microtubule ends. *Cell.* 149:371-382.
- Miesch, J., R.T. Wimbish, M.C. Velluz, and C. Aumeier. 2022. Phase separation of +TIP-networks regulates microtubule dynamics. *bioRxiv.* 2021.09.13.459419
- Nicastro, D., C. Schwartz, J. Pierson, R. Gaudette, M.E. Porter, and J.R. McIntosh. 2006. The molecular architecture of axonemes revealed by cryoelectron tomography. *Science.* 313:944-948.
- Nogales, E., S.G. Wolf, I.A. Khan, R.F. Ludueña, and K.H. Downing. 1995. Structure of tubulin at 6.5 Å and location of the taxol-binding site. *Nature.* 375:424-427.
- Ogunmolu, F.E., S. Moradi, V.A. Volkov, C. van Hoorn, J. Wu, N. Andrea, S. Hua, K. Jiang, I. Vakonakis, M. Potočnjak, F. Herzog, B. Gigant, N. Gudimchuk, K.E. Stecker, M. Dogterom, M.O. Steinmetz, and A. Akhmanova. 2021. Microtubule plus-end regulation by centriolar cap proteins. *bioRxiv.* 2021.12.29.474442.
- Ohara-Imaizumi, M., K. Aoyagi, H. Yamauchi, M. Yoshida, M.X. Mori, Y. Hida, H.N. Tran, M.

- Ohkura, M. Abe, Y. Akimoto, Y. Nakamichi, C. Nishiwaki, H. Kawakami, K. Hara, K. Sakimura, S. Nagamatsu, Y. Mori, J. Nakai, M. Kakei, and T. Ohtsuka. 2019. ELKS/Voltage-Dependent Ca(2+) Channel-beta Subunit Module Regulates Polarized Ca(2+) Influx in Pancreatic beta Cells. *Cell Rep.* 26:1213-1226.
- Ohara-Imaizumi, M., T. Ohtsuka, S. Matsushima, Y. Akimoto, C. Nishiwaki, Y. Nakamichi, T. Kikuta, S. Nagai, H. Kawakami, T. Watanabe, and S. Nagamatsu. 2005. ELKS, a protein structurally related to the active zone-associated protein CAST, is expressed in pancreatic beta cells and functions in insulin exocytosis: interaction of ELKS with exocytotic machinery analyzed by total internal reflection fluorescence microscopy. *Mol Biol Cell.* 16:3289-3300.
- Owa, M., T. Uchihashi, H.A. Yanagisawa, T. Yamano, H. Iguchi, H. Fukuzawa, K.I. Wakabayashi, T. Ando, and M. Kikkawa. 2019. Inner lumen proteins stabilize doublet microtubules in cilia and flagella. *Nat Commun.* 10:1143.
- Patzke, S., S. Redick, A. Warsame, C.A. Murga-Zamalloa, H. Khanna, S. Doxsey, and T. Stokke. 2010. CSPP is a ciliary protein interacting with Nephrocystin 8 and required for cilia formation. *Mol Biol Cell.* 21:2555-2567.
- Patzke, S., T. Stokke, and H.C. Aasheim. 2006. CSPP and CSPP-L associate with centrosomes and microtubules and differently affect microtubule organization. *J Cell Physiol.* 209:199-210.
- Pigino, G. 2021. Intraflagellar transport. *Curr Biol.* 31:R530-r536.
- Prota, A.E., K. Bargsten, D. Zurwerra, J.J. Field, J.F. Diaz, K.H. Altmann, and M.O. Steinmetz. 2013. Molecular mechanism of action of microtubule-stabilizing anticancer agents. *Science.* 339:587-590.
- Quarantotti, V., J.X. Chen, J. Tischer, C. Gonzalez Tejedo, E.K. Papachristou, C.S. D'Santos, J.V. Kilmartin, M.L. Miller, and F. Gergely. 2019. Centriolar satellites are acentriolar assemblies of centrosomal proteins. *Embo J.* 38:e101082.
- Rai, A., T. Liu, S. Glauser, E.A. Katrukha, J. Estevez-Gallego, R. Rodriguez-Garcia, W.S. Fang, J.F. Diaz, M.O. Steinmetz, K.H. Altmann, L.C. Kapitein, C.A. Moores, and A. Akhmanova. 2020. Taxanes convert regions of perturbed microtubule growth into rescue sites. *Nat Mater.* 19:355-365.
- Rai, A., T. Liu, E.A. Katrukha, J. Estevez-Gallego, S.W. Manka, I. Paterson, J.F. Diaz, L.C. Kapitein, C.A. Moores, and A. Akhmanova. 2021. Lattice defects induced by microtubule-stabilizing agents exert a long-range effect on microtubule growth by promoting catastrophes. *Proc Natl Acad Sci U S A.* 118:e2112261118.
- Rai, A.K., J.X. Chen, M. Selbach, and L. Pelkmans. 2018. Kinase-controlled phase transition of membraneless organelles in mitosis. *Nature.* 559:211-216.
- Rezabkova, L., S.H. Kraatz, A. Akhmanova, M.O. Steinmetz, and R.A. Kammerer. 2016. Biophysical and Structural Characterization of the Centriolar Protein Cep104 Interaction Network. *J Biol Chem.* 291:18496-18504.
- Rondas, D., A. Tomas, and P.A. Halban. 2011. Focal adhesion remodeling is crucial for glucose-stimulated insulin secretion and involves activation of focal adhesion kinase and paxillin. *Diabetes.* 60:1146-1157.
- Rondas, D., A. Tomas, M. Soto-Ribeiro, B. Wehrle-Haller, and P.A. Halban. 2012. Novel mechanistic link between focal adhesion remodeling and glucose-stimulated insulin secretion. *J Biol Chem.* 287:2423-2436.
- Rosenbaum, J.L., J.E. Moulder, and D.L. Ringo. 1969. Flagellar elongation and shortening in *Chlamydomonas*. The use of cycloheximide and colchicine to study the synthesis and assembly of flagellar proteins. *J Cell Biol.* 41:600-619.
- Rosenblatt, J. 2005. Spindle assembly: asters part their separate ways. *Nat Cell Biol.* 7:219-222.
- Sala, K., A. Corbetta, C. Minici, D. Tonoli, D.H. Murray, E. Cammarota, L. Ribolla, M. Ramella, R. Fesce, D. Mazza, M. Degano, and I. de Curtis. 2019. The ERC1 scaffold protein implicated in cell motility drives the assembly of a liquid phase. *Sci Rep.* 9:13530.
- Satish Tammana, T.V., D. Tammana, D.R. Diener, and J.L. Rosenbaum. 2013. Centrosomal protein CEP104 (*Chlamydomonas* FAP256) moves to the ciliary tip during ciliary assembly. *J Cell Sci.* 126:5018-5029.
- Schaedel, L., K. John, J. Gaillard, M.V. Nachury, L. Blanchoin, and M. Théry. 2015. Microtubules self-repair in response to mechanical stress. *Nat Mater.* 14:1156-1163.
- Schaedel, L., S. Triclin, D. Chrétien, A. Abrieu, C. Aumeier, J. Gaillard, L. Blanchoin, M. Théry, and K. John. 2019. Lattice defects induce microtubule self-renewal. *Nat Physics.* 15:830-838.
- Schmidt, T.I., J. Kleylein-Sohn, J. Westendorf, M. Le Clech, S.B. Lavoie, Y.D. Stierhof, and E.A. Nigg. 2009. Control of centriole length by CPAP and CP110. *Curr Biol.* 19:1005-1011.
- Sharma, A., A. Aher, N.J. Dynes, D. Frey, E.A. Katrukha, R. Jaussi, I. Grigoriev, M. Croisier, R.A. Kammerer, A. Akhmanova, P. Gonczy, and M.O. Steinmetz. 2016. Centriolar CPAP/SAS-4 Imparts Slow Processive Microtubule Growth. *Dev Cell.* 37:362-376.
- Shida, T., J.G. Cueva, Z. Xu, M.B. Goodman, and M.V. Nachury. 2010. The major alpha-tubulin K40 acetyltransferase alphaTAT1 promotes rapid cilogenesis and efficient mechanosensation. *Proc Natl Acad Sci U S A.* 107:21517-21522.
- Spektor, A., W.Y. Tsang, D. Khoo, and B.D. Dynlacht. 2007. Cep97 and CP110 suppress a cilia assembly program. *Cell.* 130:678-690.
- Steinmetz, M.O., and A.E. Prota. 2018. Microtubule-Targeting Agents: Strategies To

- Hijack the Cytoskeleton. *Trends Cell Biol.* 28:776-792.
- Stoddard, D., Y. Zhao, B.A. Bayless, L. Gui, P. Louka, D. Dave, S. Suryawanshi, R.F. Tomasi, P. Dupuis-Williams, C.N. Baroud, J. Gaertig, M. Winey, and D. Nicastro. 2018. Tetrahymena RIB72A and RIB72B are microtubule inner proteins in the ciliary doublet microtubules. *Mol Biol Cell.* 29:2566-2577.
- Sui, H., and K.H. Downing. 2006. Molecular architecture of axonemal microtubule doublets revealed by cryo-electron tomography. *Nature.* 442:475-478.
- Tang, C.J., R.H. Fu, K.S. Wu, W.B. Hsu, and T.K. Tang. 2009. CPAP is a cell-cycle regulated protein that controls centriole length. *Nat Cell Biol.* 11:825-831.
- Triclin, S., D. Inoue, J. Gaillard, Z.M. Htet, M.E. DeSantis, D. Portran, E. Derivery, C. Aumeier, L. Schaedel, K. John, C. Leterrier, S.L. Reck-Peterson, L. Blanchoin, and M. Thery. 2021. Self-repair protects microtubules from destruction by molecular motors. *Nat Mater.* 20:883-891.
- van der Vaart, B., W.E. van Riel, H. Doodhi, J.T. Kevenaar, E.A. Katrukha, L. Gummy, B.P. Bouchet, I. Grigoriev, S.A. Spangler, K.L. Yu, P.S. Wulf, J. Wu, G. Lansbergen, E.Y. van Battum, R.J. Pasterkamp, Y. Mimori-Kiyosue, J. Demmers, N. Olieric, I.V. Maly, C.C. Hoogenraad, and A. Akhmanova. 2013. CFEOM1-associated kinesin KIF21A is a cortical microtubule growth inhibitor. *Dev Cell.* 27:145-160.
- van Riel, W.E., A. Rai, S. Bianchi, E.A. Katrukha, Q. Liu, A.J. Heck, C.C. Hoogenraad, M.O. Steinmetz, L.C. Kapitein, and A. Akhmanova. 2017. Kinesin-4 KIF21B is a potent microtubule pausing factor. *eLife.* 6:e24746.
- Vemu, A., E. Szczesna, E.A. Zehr, J.O. Spector, N. Grigorieff, A.M. Deaconescu, and A. Roll-Mecak. 2018. Severing enzymes amplify microtubule arrays through lattice GTP-tubulin incorporation. *Science.* 361:eaau1504.
- Witman, G.B. 1975. The site of in vivo assembly of flagellar microtubules. *Ann N Y Acad Sci.* 253:178-191.
- Wu, X., Q. Cai, Z. Shen, X. Chen, M. Zeng, S. Du, and M. Zhang. 2019. RIM and RIM-BP Form Presynaptic Active-Zone-like Condensates via Phase Separation. *Mol Cell.* 73:971-984.
- Wu, X., M. Ganzella, J. Zhou, S. Zhu, R. Jahn, and M. Zhang. 2021. Vesicle Tethering on the Surface of Phase-Separated Active Zone Condensates. *Mol Cell.* 81:13-24.
- Yamazoe, T., T. Nagai, S. Umeda, Y. Sugaya, and K. Mizuno. 2020. Roles of TOG and jelly-roll domains of centrosomal protein CEP104 in its functions in cilium elongation and Hedgehog signaling. *J Biol Chem.* 295:14723-14736.
- Zanic, M., P.O. Widlund, A.A. Hyman, and J. Howard. 2013. Synergy between XMAP215 and EB1 increases microtubule growth rates to physiological levels. *Nat Cell Biol.* 15:688-693.
- Zhang, R., G.M. Alushin, A. Brown, and E. Nogales. 2015. Mechanistic Origin of Microtubule Dynamic Instability and Its Modulation by EB Proteins. *Cell.* 162:849-859.
- Zheng, X., A. Ramani, K. Soni, M. Gottardo, S. Zheng, L. Ming Gooi, W. Li, S. Feng, A. Mariappan, A. Wason, P. Widlund, A. Pozniakovskiy, I. Poser, H. Deng, G. Ou, M. Riparbelli, C. Giuliano, A.A. Hyman, M. Sattler, J. Gopalakrishnan, and H. Li. 2016. Molecular basis for CPAP-tubulin interaction in controlling centriolar and ciliary length. *Nat Commun.* 7:11874.
- Zhu, X., R. Hu, M. Brissova, R.W. Stein, A.C. Powers, G. Gu, and I. Kaverina. 2015. Microtubules Negatively Regulate Insulin Secretion in Pancreatic beta Cells. *Dev Cell.* 34:656-668.
- Zwicker, D., M. Decker, S. Jaensch, A.A. Hyman, and F. Jülicher. 2014. Centrosomes are autocatalytic droplets of pericentriolar material organized by centrioles. *Proc Natl Acad Sci U S A.* 111:E2636-2645.





Addendum

Nederlandse samenvatting

Curriculum Vitae

List of publications

Dankwoord

Nederlandse samenvatting

Cellen worden ‘de bouwstenen van het leven’ genoemd en om goed te kunnen functioneren hebben ze een cytoskelet nodig. In eukaryote cellen bestaat het cytoskelet uit vier grote netwerken: F-actine, microtubuli, intermediaire filamenten en septins. Deze netwerken zijn betrokken bij cellulaire processen zoals het tot stand brengen en onderhouden van celpolariteit en celvorm, transport van organellen en celmigratie. In dit proefschrift richten we ons op microtubuli. Microtubuli worden opgebouwd uit tubuline-eiwitten en ze zijn van nature erg dynamisch. Dit houdt in dat ze snel kunnen vormen, maar ook snel uit elkaar kunnen vallen. Deze dynamiek is voor diverse processen juist niet wenselijk en daarvoor is het belangrijk dat microtubuli kunnen worden gestabiliseerd. Dit kan bereikt worden door het aanbrengen van modificaties direct op de tubuline-eiwitten of door andere eiwitten of eiwitcomplexen die binden aan microtubuli. In dit proefschrift hebben we twee eiwitcomplexen bestudeerd die belangrijk zijn bij het stabiliseren van microtubuli.

In **Hoofdstuk 2** hebben we ons gericht op de rol van het eiwitcomplex dat microtubuli stabiliseert aan het plasmamembraan. Dit complex bestaat uit eiwitten LL5 β , ELKS, liprin- α 1, liprin- β 1 en KANK1 en verankert microtubuli nabij focale adhesies. Eerdere studies hebben aangetoond dat verankering van microtubuli aan de celperiferie essentieel is voor het uitscheiden van verschillende stoffen naar het extracellulaire milieu. We hebben aangetoond dat insulinesecretie in β -cellen in de alvlesklier wordt gereguleerd door een gecombineerd complex van het microtubuli-stabiliserende complex en eiwitten die zorgen voor afgifte van neurotransmitters in de presynaptische actieve zone in neuronen. We hebben ontdekt dat zowel een tekort aan eiwit LL5 β als afbraak van focale adhesies ervoor zorgden dat insulinesecretie werd verzwakt. We hebben ook de dynamische organisatie bestudeerd van de eiwitcomplexen die betrokken zijn bij insulinesecretie. Op basis van eerder werk van andere groepen hadden we verwacht dat deze complexen door vloeistof-vloeistof fasescheiding zouden vormen. Dit bleek echter niet waar te zijn, want deze complexen blijken te bestaan uit een kleine aantal moleculen die uitwisselen op immobiele bindingsplaatsen.

Microtubuli kunnen ook dienen als fysieke ondersteuning in stabiele celstructuren zoals cilia, ook wel trilhaartjes genoemd. Cilia hebben een kern van microtubuli en kunnen betrokken zijn bij het verplaatsen van slijm in de luchtpijp (bewegende cilia) of ze fungeren als een soort antenne om signalen door te geven (primaire cilia). Het is belangrijk dat cilia de correcte lengte hebben, omdat te korte of te lange cilia worden geassocieerd met ziekten die meerdere orgaansystemen aantasten, gezamenlijk ciliopathieën genaamd. In **Hoofdstuk 3** en **Hoofdstuk 4** hebben we componenten bestudeerd van het complex dat zich bevindt aan het uiteinde van primaire cilia. De kerncomponenten van dit complex zijn de eiwitten ARMC9, CSPP1, CEP104, CCDC66 en TOGARAM1. Mutaties in vier van deze eiwitten zijn gelinkt aan een ciliopathie (een aandoening aan het cilium) genaamd Joubert syndroom.

In **Hoofdstuk 3** hebben we de microtubuli-stabiliserende eigenschappen van het eiwit CSPP1 gekarakteriseerd. We hebben aangetoond dat CSPP1 microtubuli stabiliseert die langzaam groeien, groeiverstoringen ondergaan of beschadigd zijn. Deze stabilisatie wordt bereikt door het samenspel van twee afzonderlijke domeinen. Door middel van cryo-elektronentomografie en MINFLUX-microscopie hebben we onthuld dat CSPP1 aan de binnenkant van een microtubulus bindt. In **Hoofdstuk 4** hebben we het individuele en collectieve gedrag van de andere ciliaire complex componenten op dynamische microtubuli onderzocht. We hebben aangetoond dat alle componenten kunnen worden gezuiverd en gebruikt in experimenten met *in vitro* gereconstitueerde microtubuli. We hebben aangetoond dat CEP104 de groei van microtubuli verhindert en dit effect werd versterkt door de aanwezigheid van Eind-Bindende eiwitten, CSPP1 of CCDC66. TOGARAM1 werkt de verandering juist tegen en zorgde voor langzaam groeiende microtubuli in aanwezigheid van

CEP104. De groei van microtubuli was nog sterker verminderd wanneer ARMC9 en CSPP1 aan de mix werden toegevoegd. Met deze bevindingen hopen we een basis te hebben gelegd voor het begrijpen van het mechanisme achter lengtere regulatie door eiwitten in cilia.

Het stabiliseren van microtubuli speelt een belangrijke rol in veel cellulaire processen. Wanneer dit om de een of andere reden niet goed gaat in een cel, kan dit zich uiten in diverse ziekten. Met het onderzoek in dit proefschrift hopen we bij te dragen aan de opheldering van de mechanismen achter microtubulistabilisatie. Dit zou de diagnose en ontwikkeling van behandelingsstrategieën kunnen bevorderen voor aandoeningen die gelinkt zijn aan één of meer componenten van microtubuli-stabiliserende complexen zoals diabetes type 2 en Joubert syndroom.

Curriculum Vitae

Cyntha van den Berg was born on the 9th of July 1994 in Gouda, The Netherlands. In 2012, she obtained her high school degree (Atheneum) at 'De Goudse Scholengemeenschap (GSG) Leo Vroman' in Gouda. She continued her education by choosing the Bachelor's program 'Chemistry' at Utrecht University and obtained her bachelor's degree in 2015. Driven by her interest for the biological questions in the chemistry field, Cyntha entered the Master's program Molecular and Cellular Life Sciences, again at Utrecht University. For her major internship, she joined the lab of Prof. Dr. Jos van Strijp at the Department of Medical Microbiology at the University Medical Centre Utrecht (UMCU). There, she studied secreted proteins from the human intestinal microbiome and their role in intestinal homeostasis and inflammation. Cyntha learned many different biochemical techniques such as protein purification and immunoprecipitation assays. To continue learning biochemical techniques, she joined the group 'Plasma Proteins' of Prof. Dr. Koen Mertens at the research division of Sanquin in Amsterdam. Her project was about the identification of receptors responsible for FVIII uptake using proximity-dependent biotin labeling. Here, she learned more techniques such as molecular cloning. Cyntha obtained her Master's degree in 2017 and was looking for a position to use biochemical techniques and learn to work with light microscopes. She started a PhD position under the supervision of Prof. Dr. Anna Akhmanova at Utrecht University and the results Cyntha obtained during her research projects are described in this dissertation.



List of publications

Published

Organization and dynamics of the cortical complexes controlling insulin secretion in β -cells.

Noordstra, I.* , van den Berg, C.M.*, Boot, F. W. J., Katrukha, E. A., Yu, K.L., Tas, R.P., Portegies, S., Viergever, B.J., de Graaff, E., Hoogenraad, C.C., de Koning, E. J. P., Carlotti, F., Kapitein, L.C., Akhmanova, A.

J Cell Sci. 2022 Feb 03; 135(3)

Preprint

CSPP1 stabilizes growing microtubule ends and damaged lattices from the luminal side.

van den Berg, C.M., Volkov, V. A., Schnorrenberg, S., Huang, Z., Stecker, K.E., Grigoriev, I., Patzke, S., Zimmermann, T., Dogterom, M., Akhmanova, A.

bioRxiv; <https://doi.org/10.1101/2022.06.23.497320>

* These authors contributed equally

Dankwoord

Daar is ie dan, mijn proefschrift! Toen ik tien jaar geleden het ‘Utrecht Science Park’ (toen nog gewoon ‘de Uithof’) opkwam om met mijn mede-eerstejaarsstudenten ‘Scheikunde’ op introductiekamp te gaan, had ik niet gedacht dat ik ooit een eigen proefschrift zou schrijven. Dit proces begon vijf jaar geleden en wat was het een avontuur! Van vrijdagavond laat nog achter de microscoop, naar ineens drie maanden thuis aan de keukentafel achter mijn laptop vanwege de corona-lockdown tot het met droogijs in de trein reizen naar Duitsland. Ik heb enorm veel geleerd en beleefd en dit had ik niet kunnen doen zonder de mensen om mij heen.

Allereerst wil ik mijn promotor, **Anna**, enorm bedanken. Ik bewonder je hoeveelheid kennis en je duidelijke visie. Ik had me geen beter supervisor kunnen voorstellen. Je hebt me de kans gegeven om veel verschillende technieken te leren en liet me mijn gang gaan totdat ik zelf behoefte had aan een bespreking. Ondanks dat je megadruk bent, maakte je snel tijd vrij wanneer ik daarom vroeg. Na zo’n bespreking kon ik altijd weer vooruit. Een van mijn leukste herinneringen is toen ik net een paar weken was begonnen in het lab. Door mijn scheikunde-achtergrond had ik nog weinig kennis hoe cellen en hun organellen er in het echt uit zien en kende alleen de schematische afbeeldingen in lesboeken. Toen ik de lokalisatie van een bepaald eiwit in een cel moest bepalen met fluorescentie microscopie, en bij meerdere werkbesprekingen vertelde dat het eiwit in gekke kronkels lokaliseerde, stelde je voor om samen achter de microscoop te gaan zitten. We hebben toen samen naar de cellen kunnen kijken en die kronkels waren blijkbaar mitochondriën (die er dus niet uitzien als kleine, gekke boontjes). Ook toen ik mijn proefschrift aan het schrijven was, ontving ik binnen een paar dagen feedback terwijl je op vakantie was in Thailand (en jij je nog verontschuldigde dat je lui was...). Bedankt voor alles!

Ik wil graag alle leden van mijn leescommissie bedanken voor het lezen en beoordelen van mijn proefschrift: **Ronald Roepman**, **Friedrich Förster**, **Susanne Lens**, **Geert Kops** en **Mike Boxem**.

Lukas, **Harold**, **Martin**, **Ginny**, **Florian**, **Corette**, **Paul**, **Sabrina**, **Frederik**, **Agathe**, **Casper** and **Sander**, thank you all for your questions and input during the weekly meetings.

Tijdens mijn PhD heb ik voor mijn diverse projecten mogen samenwerken met leuke en gemotiveerde mensen en de resultaten zijn te vinden in dit proefschrift. **Ivar**, jij was mijn gids toen ik net begon aan mijn PhD in het Akhmanovalab, zowel op logistiek als op experimenteel gebied. In een korte tijd heb jij mij veel geleerd zodat ik het insulineproject kon afmaken omdat jij een paar maanden later voor je postdoc naar Australië ging verhuizen. We konden goed kletsen en hadden plezier samen in het lab. Ik zie ons nog samen als een malle buizen staan shaken met geïsoleerde alvleeskliertjes van muizen! Het insulineproject nam toch wat meer tijd in beslag dan we hadden ingeschat, maar ondanks dat we inmiddels aan twee kanten van de wereld aan het werk waren, konden we heel goed samenwerken. Eigenlijk was dat extreem efficiënt, want wanneer jij ging slapen kon ik verder werken en andersom. Het is heel leuk om te zien hoe enthousiast jij bent over de wetenschap en jouw onderzoek en ik heb er alle vertrouwen in dat je een mooie onderzoeksgroep gaat leiden! **Fransje**, ook jij werd betrokken bij het insulineproject. Waar insuline voor ons lab een uitstapje was, was dit het hoofdonderwerp in jouw lab in het LUMC. Het was erg waardevol om naast muis- en ratcellen ook humane cellen te kunnen bestuderen. Het was leuk om bij jou op het lab mee te kunnen kijken, maar ook om jou te laten zien hoe wij experimenten doen. Op een gegeven moment hadden we een goed protocol waarbij jij de coverslips met cellen

voorbereidde, ik naar Leiden ging met de trein om deze te fixeren en ze dan meenam naar Utrecht om er verder mee te gaan. In het begin was een leuk en gezellig bezoekje, maar met de coronamaatregelen mocht ik helaas niet zomaar meer het LUMC in. Toen moesten we buiten, naast het LUMC gebouw, afspreken waarbij je mij dan snel de plaat met gefixeerde coverslips gaf en ik dan gelijk weer naar de trein ging. Gelukkig was het door de maatregelen juist vrij rustig buiten, anders zouden mensen nog kunnen denken dat we een drugsdeal aan het doen waren..! Bedankt voor je bijdrage aan dit project en ik wens je veel succes met het afronden van je PhD. **Eugene**, you were a big help in data collection and analysis to advance the insulin project. I admire how you manage to keep calm and do your thing while everybody seems to need your help with data analysis at the same time. Thanks for taking the time and having the patience to explain what you did or needed to be done. I wish you the best with your career and your family! **Vladimir**, the microtubule guy. You were an enormous help in driving the CSPP1 project forward. We suspected CSPP1 was binding at the luminal side of microtubules, but we did not have the tools to confirm this. Your cryo-ET experiments and generation of beautiful images and renderings really showed and confirmed that CSPP1 is binding to the inside of microtubules. We did not meet or talk often, but it was fun when we did. Thank you very much for your contribution and insights and I wish you the best of luck in London! **Sebastian**, you were also a big help in confirming that CSPP1 is binding to the inside of microtubules. Our collaboration started as a pilot to find out if we could achieve sufficient resolution with fluorescence microscopy to distinguish proteins binding to the inside or outside of microtubules. We started with me sending fixed cells on coverslips over to you in Heidelberg, where you imaged them on the MINFLUX microscope. This was quite successful, but it became difficult when we wanted to study smaller protein constructs. Luckily, the corona measures were gradually being lifted and I could visit you in Heidelberg to set up a new protocol to use in vitro microtubules for this. I had a lot of fun during my visits and I especially remember our hunt for food while working on Sunday. I still wonder whose spaghetti bolognese we ate and very glad we didn't get sick afterwards. We managed to create a working protocol and during my second visit we generated quite some data. Together with the help of **Ziqiang**, the data analysis master, we managed to finish the CSPP1 manuscript at that time as well. Thank you both very much for this and I wish you both the best. **Harriet**, you were such a big help in creating a solid chapter in a short amount of time. Thank you so much for doing many in vitro reconstitution assays, helping with the analysis and giving feedback on my writing. Our conversations in the lab were a nice mix between serious and fun. I am amazed by your ability and enthusiasm to work on the complex reconstitutions of the ciliary tip module. I have no doubt that it will be a beautiful paper and I wish you the best. **Ilya**, thanks so much for all the help with microscope. This ranged from aligning lasers and correcting wrong settings, to the microscope just needing your presence or 'magic hands'. I enjoyed our conversations in the hallway or when you came to visit in my office.

Ik wil ook graag de mensen achter de schermen van de afdeling Celbiologie, Neurobiologie en Biofysica bedanken. **Phebe**, jij bent echt onmisbaar op de afdeling! Jij zorgt ervoor dat wij ons kunnen bezig houden met onze experimenten en geen zorgen hoeven te maken of alle benodigdheden er wel zijn. En wanneer er toch tekorten van plastics, handschoenen of ander labspullen dreigden te ontstaan of al ontstonden, was jij 24/7 bezig om deze toch te bemachtigen of alternatieven te regelen. En bij problemen en vragen kon ik ook altijd bij jou terecht. Jouw organisatieskills komen niet alleen tot uiting gerelateerd aan werk, door jou hebben we ook ontspannen en sociale dingen als labouting, borrels en barbecues. Tijdens deze events kletsten we gezellig over van alles en nog wat. Bedankt voor alles! **Bart** en **René**, jullie ook bedankt voor alle hulp in het draaide houden van de afdeling. Daarnaast wil ik jullie ook bedanken voor tijd vrij maken om te helpen met de muizen voor mijn experimenten.

Esther en **Lena**, ook jullie hebben mij geholpen met de muizen en daarnaast zetten jullie je enorm in voor praktische onderwijs voor bachelorstudenten en activiteiten voor het PhD programma voor het Institute of Biomembranes, waar ik bij hoorde. **Ron**, **Laurens** en **Jan Andries**, zonder jullie zouden de studenten die bij ons stage gaan lopen een stuk minder celbiologische kennis hebben. Dank daarvoor. **Wilco**, elke keer verbaasde ik me weer over wat voor coole technieken jij gebruikt en wat voor prachtige images je laat zien. Bedankt voor je goeie vragen en suggesties tijdens werkbijeenkomsten en jouw mooie verhalen tijdens borrels ga ik zeker missen.

Vervolgens wil ik iedereen die het Akhmanovalab inmiddels heeft verlaten bedanken voor de fijne tijd. **Peter Jan**, we waren eerst huisgenoten, vervolgens collega's en nu vrienden. Als huisgenoten aten we af en toe samen en deden we activiteiten met onze huisgenoten. Vooral je zoete aardappelfrietjes en zelfgemaakt ijs zijn me bijgebleven uit die tijd. Door jou wist ik dat er een PhD positie beschikbaar kwam in het Akhmanovalab en toen ik die kreeg, werden we collega's. Gelukkig waren we toen allebei al verhuisd, anders was het waarschijnlijk wel intens om elkaar zoveel te zien. Bedankt voor je betrokkenheid, dat je altijd bereid was te helpen, ervaringen te delen, geklaag aan te horen of juist mee te juichen. Jij was één van de initiatiefnemers van sociale activiteiten met het lab en we waren vaak samen aanwezig bij borrels en activiteiten van de hele afdeling. Ondanks dat je nu al een tijdje niet meer in het Akhmanovalab werkt, hebben we regelmatig contact en hebben we veel mooie gesprekken. Ik vond het een eer om bij de bruiloft van jou en Rosanna te zijn. **York**, we hadden in het begin niet veel contact, maar dit veranderde toen ik verhuisde naar het kantoor waar jij ook zat en we burens werden op het lab. We hadden het daar goed voor elkaar door alle benodigde apparaten en vriezers om ons heen te verzamelen en te labelen. Je vroeg of ik alleen maar in het Nederlands tegen je wilde praten, omdat je de taal aan het leren was en alle andere collega's standaard in het Engels begonnen. Ik vind het knap hoe snel en hoe goed je het Nederlands oppakte, al hadden we af en toe wel de slappe lach wanneer een uitspraak of vertaling niet helemaal klopte. Ook jij was altijd bereid te helpen als ik weer een vraag had over kloneren of de celkweek en we konden elkaar goed motiveren. Jij hield je bezig met de organisatie van het lab en bestellingen en dat deed je heel goed. Heel erg bedankt hiervoor. Ook buiten het lab spraken we af om samen te eten, te gaan wandelklimmen of wandelen met je hond Ollie. Ik vond het bijzonder om je paronymph te zijn tijdens je verdediging en getuigen tijdens je bruiloft. Ook nadat je een andere baan kreeg, zijn we in contact gebleven en eten we af en toe samen met onze partners. Ik wens jou, Elodie en Ollie veel geluk, ook met jullie nieuwe puppy Mephi. **Chiung-Yi**, we were also sharing the same office. Thanks for helping me out when I was having trouble with the TIRF microscope or the in vitro assays themselves. You were always up for a chat and many thanks for sharing bits of your home-cooked food at lunchtime. I still have to laugh at the time you, your husband George, and me were helping Dipti move to her new home and had to put together furniture. Dipti left to do something in the lab, so the three of us were left to put together Dipti's furniture.... Luckily, she invited us for a nice Indian dinner to make up for this. It is fun to keep in touch and I wish you and your husband the best with your son Liam and your careers. **Ankit**, you were my in vitro hero! Almost every Tuesday morning, we were doing in vitro assays at the same time but on different microscopes. Thanks for teaching me all the different kinds of experiments with in vitro microtubules. It was never a bother when I was doubting my (control) experiments. Even when you were not in the lab, I could message you whenever, also when you started your own lab back in India. I wish you the best of luck with your research. **Babet**, ik vind het heel knap hoe jij zo'n lastige cellijn hebt weten op te zetten in ons lab. Het was altijd heel cool om kloppende hartcellen te zien in een culture dish, maar de cellen konden ook erg frustrerend zijn. We konden elkaar goed motiveren wanneer we weer orgaanisolaties uit muizen moesten doen en waren heel blij

wanneer dit succesvol was. Ik vind het knap hoe je bleef doorzetten met je experimenten en je daarnaast ook bezig hield met het organiseren van het lab. Het was fijn om een maatje te hebben om alle antilichamen te organiseren in de vriezers. Ik wens je veel plezier bij je nieuwe baan. **Funso**, thanks for being my corona-buddy. During the time when only a few people were allowed in the lab at the same time, we were very good in scheduling our respective allowed times in the lab. When the measures were loosened a bit and we could actually be in the office at the same time we had nice chats and you showed me handy tools like Alphafold and Grammarly. I wish you good luck with your career. **Amol**, when I joined the lab I was amazed by the amount of time you put into your work. You did many experiments while also supervising several master students simultaneously. Your CLASP papers inspired many in vitro reconstitution experiments that I did in my projects. Good luck with the rest of your career. **Chao**, when I think of you, I always see a smiling face. You were very enthusiastic about your research and happy to help when I had a question. Thanks a lot for showing me how to image condensates in cells, which was very helpful a couple of years later for the insulin project. I wish you the best with your family and career. I also want to thank **Maud**, **Ruddi** and **Kyle** for the time we shared in the lab and the nice chats that we had.

Ook wil ik graag iedereen bedanken die momenteel deel uitmaakt van het Akhmanovalab. **Dipti**, we started our PhDs around the same time (only two weeks apart), so you were there for the whole run. Therefore, I am very happy that you are my paronymph. I am amazed by your work ethic, lab skills and your knowledge. You taught me how to do in vitro assays and whenever there was something wrong, missing or if I needed to do a new kind of experiment, you were willing to help and explain. Our work schedules were quite different but that came in handy when wanting to use the microscope on the same day. I took the morning slots while you came in in the afternoon to take the slot after me. When we were present at the same time we could talk about science, but about many other things as well. I learned a lot about Indian traditions and food from you and I am very happy I could taste many things (even though most of them were very spicy...). It was also fun to do things outside the lab, such as travelling to Heidelberg twice to join the microtubule conference. I am still (not really) sorry for convincing you to walk downhill to the city center at the end of the conference, which turned out to have quite some uphill stretches... I wish you all the best with finishing your PhD (which is soon) and with the next steps in your career. **Milena**, thanks for being my other paronymph. When you moved to my office after the covid measures, we started talking and getting to know each other better. Somehow, we did not really need each other's help science-wise but we could talk often about PhD-related things or just in general about life. I especially enjoyed our banter. It was always fun to walk into the office and secretly check out your computer screen. We laughed so hard when you realized I saw you were practicing the lyrics of an Eminem song... I wish you the best during the rest of your PhD. **Fangrui**, I am amazed at all the different knockout cell lines you created during your PhD and all the stainings that you did. We shared an office for a short while where you showed me many places in China on Google Maps. I still have to laugh so much when I think about that time that you tried to change something in one of the Dutch government portals for your wife. Your wife's last name kept being changed to 'Cheek' instead of 'Wang' and we didn't understand why. I then tried to call to ask why this was happening and during my waiting time on the phone, I realized that your internet browser automatically translated Dutch words to English and 'wang' is the Dutch word for cheek. In the lab you were always happy to answer questions, explain concepts or find reagents. Thank you so much. We also had fun together at the conferences in Lisbon and Heidelberg. Good luck with finishing your PhD and deciding your next step. **Hugo**, toen ik mijn PhD begon, was jij de masterstudent van Peter Jan en later kwam je terug als PhD student. Het is echt bizar goed hoe jij de hele expansie microscopietechniek hebt

opgezet en images zijn altijd supermooi. Bedankt voor je hulp voor het opzetten van expansie microscopie voor mijn projecten en je was altijd bereid om mee te kijken als ik weer geen cellen kon vinden op de microscoop. Ik vind het mooi om te zien dat je een gericht doel hebt voor je carrière en ik wens je alle goeds. **Emma**, jij bestudeert eiwitten daadwerkelijk in gecilieerde cellen terwijl ik ciliaire eiwitten bestudeerde in cellen zonder cilia of op in vitro microtubuli. Ik vind het knap hoe je met deze cellen kunt werken en ik verwacht dat je mooie resultaten zult verkrijgen. Bedankt voor het organiseren van leuke activiteiten buiten het lab zoals diners en het IB retreat. Ook heb ik een aantal keer mogen genieten van je bakkunsten. Veel succes met je PhD. **Lilian**, ik vind knap hoe je lastige projecten aanpakt en overneemt. Je bent altijd vrolijk, overal voor in en je kunt het met iedereen goed vinden. We hadden vooral leuke gesprekken over van alles wanneer we allebei vroeg in het lab waren. Succes met je PhD en veel woonplezier in je nieuwe huis. **Saishree**, it was fun to share an office with you. I enjoyed helping you move to a new place and thanks very much for the nice dinner afterwards. We had a good time sharing a room during the microtubule meeting in Heidelberg, although I still don't understand why you wanted to get up soooo early. Thanks for taking the initiative to organize social outings with the lab. Good luck with all your projects. **Joyce**, dankjewel voor jouw enthousiasme over je onderzoek. Ik kon altijd bij je terecht met vragen over kloneren, microscopie of om gewoon gezellig te kletsen. Ook je suggesties tijdens werkbesprekingen waren erg nuttig. Het was leuk om samen aanwezig te zijn bij het Bijvoet symposium om onze projecten te presenteren. Het was vooral grappig dat we dachten dat we de enigen zouden zijn die over microtubuli zouden praten, bleek bijna de helft van de presentaties hierover te gaan. Ik weet zeker dat je een mooie carrière tegemoet gaat. **Boris**, I am amazed about all the imaging of muscle cells you can do with many different microscopes. It was fun to talk about climbing (sorry, but not actually sorry, that I did not join bouldering). Thanks for allowing me to taste your food when you were experimenting with a food dryer, or when you were almost 'selling' how good the couscous was you were buying. I wish you all the best with your career. **Yinlong**, you recently joined our lab and have taken on the heroic task of continuing Fangrui's work with all the different cell lines. I wish you the best of luck and I hope you enjoy living in Nieuwegein. **Robin**, jij ben net begonnen als PhD-student in het Akhmanovalab, maar eigenlijk lijkt het alsof je helemaal niet bent weggeweest. Als masterstudent van Dipti was het altijd gezellig als je er was en daarin is niks veranderd. Het is leuk om te zien hoe geïnteresseerd jij bent en ik wens je veel plezier met de diverse projecten tijdens je PhD. **Charlotte, Elena, Sacha, Ivo, Joyce en Rick**, ik wil jullie bedanken voor jullie inzet tijdens de bachelor eindprojecten. Het was leuk en leerzaam om jullie te begeleiden. **Jari**, bedankt dat je voor je grote masterstage mijn project hebt gekozen. Het was voor mij erg leerzaam om een student voor langere tijd te begeleiden en daarnaast was het ook gezellig in het lab. We konden veel dingen testen en je hebt veel verschillende experimenten gedaan. Ik hoop dat je het naar je zin hebt gehad in Zweden en ik ben benieuwd wat je hierna gaat doen.

Het voordeel van een onderzoeksgroep binnen een afdeling met meerdere groepen is dat je makkelijk andere mensen tegenkomt aan wie je dingen kunt vragen en waar je wat van kunt leren. Dit heeft een fijne werkomgeving gecreëerd en daarom wil ik ook graag mensen bedanken van de diverse buurlabs op de vijfde verdieping van het Kruytgebouw. **Desiree, Riccardo, Anna, Mithila, Yolanda, Arthur, Eitan, Sofia, Amélie, Bart, Max, Josiah, Jey, Feline, Dennis, Robin, Sybren, Katharina, Anne, Roderick, Sara, Jian, Yujie, Xingxiu, Marjolein, Jessica, Lisa, Marijn, Robbelien, Nicky, Jelmer, Klara, Manon, Ate, Carlijn, Lotte, Liu, Daphne, Derk, Wouter, Malina, Nazmiye, Giel, Albert, Chun Hei, Ha, Mai Dan, Noortje, Anna and Elly**. Thanks to each of you for the chats in the hallway and during borrels, and for the fun times at lab outings and IB evenings.

Tijdens mijn PhD zijn ook mensen buiten mijn werkomgeving belangrijk geweest voor afleiding en ontspanning. **Yoni, Maartje, Saydi, Melanie, Veerle** en **Riande**, we hebben elkaar ongeveer tien jaar geleden leren kennen bij de studievereniging 'Proton' en waren daar geregeld te vinden bij borrels, activiteiten, commissievergaderingen en studiereizen. Ondanks dat we inmiddels verspreid door het land wonen en iedereen ergens anders werkt, ben ik blij dat we na al die tijd nog steeds geregeld afspreken voor een etentje, verjaardag, weekendje weg, dagje sauna of bruiloft. **Helma, Ronald, Peter** en de rest van mijn schoonfamilie, bedankt voor jullie Limburgse gastvrijheid, interesse, steun en natuurlijk de kilo's vlaai. Ik wil ook graag mijn eigen familie bedanken waarvan een paar mensen in het bijzonder. **Papa**, voor jou is niets te veel moeite. Of het nu gaat om gordijnen vermaken, spontaan taxi spelen in Brussel of manuscripten doorlezen, je maakt snel tijd vrij en je doet het met enthousiasme. Je weet precies wat je moet zeggen (of juist niet moet zeggen) zodat ik weer verder kan wanneer ik ergens in ben vastgelopen. Ik vind het heel tof dat we in 2019 samen de Nijmeegse Vierdaagse hebben uitgelopen, jij voor je 10^{de} medaille en ik voor mijn 1^{ste}. **Mama**, wij kunnen uren kletsen over van alles en nog wat. Wanneer mijn hoofd maar niet wil stoppen met denken, word ik altijd rustiger wanneer we gebeld hebben. Ik vind het leuk als we samen ergens naartoe gaan, maar ik hou ook van het tegen elkaar aan zitten op de bank, zoals we vroeger vaak zaten. Jouw knuffels zijn onmisbaar! Voor feestdagen en verjaardagen kom je altijd met creatieve ideeën die een leuke afleiding zijn in ieders drukke leven. **Myrthe**, de laatste jaren zijn we steeds hechter geworden. Bedankt voor de goede gesprekken, lieve berichtjes en grappige plaatjes en kaartjes. Ik vind onze zussendagjes heel leuk en onwijs vet dat we gewoon voor één nachtje naar Birmingham zijn gevlogen voor een concert! Onze geplande zonvakantie was door het coronavirus vervangen door een paar weekendjes in eigen land, wat evengoed heel gezellig was. Die zonvakantie gaan we zeker nog een keer doen!

Lieve **Irene**, ik had deze jaren niet zonder jou willen doen. Je springt en juicht met me mee wanneer experimenten en presentaties goed gingen en kwam met een lief kaartje of een knuffel wanneer het even tegengat. Je voelt goed aan wanneer je me even moet laten of me juist kan afleiden. Ik vind het leuk hoe enthousiast jij kan zijn over zowel grote als kleine dingen en dat werkt erg aanstekelijk. We kunnen samen lekker gek doen en ik voel me thuis bij jou. Ik ben trots dat ik je binnenkort mijn vrouw mag noemen en ik kijk uit naar alles wat we samen gaan beleven. Ik hou van jou!

Cyntha

